LARGE SCALE SURVEYS AT 408 MHz

A Thesis submitted for the degree of
Doctor of Philosophy
in the University of Sydney

by Warwick Edward Wilson, B.Sc., B.E.
School of Electrical Engineering
University of Sydney

March, 1975

PREFACE

Since the very early days of Radio Astronomy, much work has been done towards measuring the large scale structure of the galactic radio continuum radiation. However, in recent years, owing to the advent of short centimeter wave receivers on large dishes, and the techniques of aperture synthesis, interest has turned to studying fairly small regions of the sky, with the highest possible resolution. The result has been that many questions pertaining to the large scale structure of our galaxy, particularly at high galactic latitudes, have remained unanswered. There is still much work to be done in this field, but when one examines the observational evidence available, a glaring omission is apparent. There exists no complete, consistent survey of the whole sky with a resolution suitable for the study of the structure of the high latitude galactic radio radiation. This thesis describes steps that have been made, and are being made, to provide such a survey.

The first stage of the all sky survey was begun by Dr. C.G.T. Haslam and his co-workers at Jodrell Bank in 1966 (Haslam et al. (1970)). They chose a frequency of 408 MHz, which was a compromise between the higher resolutions available at higher frequencies, and the better sensitivity obtainable at lower frequencies. The work described in this thesis follows on from this earlier work, and comprises stages 2 and 3 of the all sky survey at 408 MHz. Stage 4, covering the north polar cap region, will complete the survey. This survey will then provide complete coverage of the sky with a resolution of approximately 50 arc minutes, and a sensitivity approaching the confusion limit.

This thesis is mainly concerned with the techniques involved in producing large scale surveys. Particular emphasis is given to the data reduction methods that are needed to handle the large amount of data collected in such surveys.

The author began work towards a Ph.D. in January 1969, but for the first two years was involved in research in the topic of 'Absolute Calibrations of the Galactic Background Radiation' (see Appendix 1). The work described in this thesis was completed in the period from January, 1971, to March, 1975. During this time, the author was the recipient of a research scholarship from the Max-Planck-Institut für Radioastronomie in Bonn, West Germany.

Chapter 1 describes a survey of a large area of the northern sky, at 408 MHz. Chapter 2 describes the computer reduction techniques used to reduce the data from this survey, to maps. Chapter 3 describes the methods used to calibrate the intensity scale of these maps. The accuracy of the final survey maps is also investigated. Chapter 4 describes the techniques and first observations of a survey of the complete southern sky, at 408 MHz. The results of Chapter 3 have been used, together with surveys at other frequencies, to obtain information on the spectral index of the galactic background radiation. The results are presented in Chapter 5. Chapter 6 contains a discussion of the structure of the radio sky at 408 MHz, as revealed from the results of Chapters 3 and 4.

No part of this thesis has been submitted to any other university, and no part has been incorporated into any previous thesis by the author. The work described is that of the author, assisted by others as outlined in this preface.

The work described in Chapter 1 was done by the author in collaboration with Dr. C.G.T. Haslam and Dr. D.A. Graham. Mr. G.C. Hunt provided valuable assistance in the area of data collection in the early days of the survey. The programs described in Chapter 2 were written by the author and Dr. C.G.T. Haslam. The work described in Chapter 3 is that of the author, assisted by Dr. C.G.T. Haslam. The work described in Chapter 4 was done by the author in close collaboration with Dr. C.G.T. Haslam. Chapters 5 and 6 are the work of the author.

Appendix 1 contains two papers describing work done by the author in the first two years of his canditure. 1. "Radio Sky Background Measurements using the Moon as a Screen" by K.S. Stankevich, R. Wielebinski and W.E. Wilson. In this experiment, the author was responsible for the building of the 408 MHz receiver, and took part in the observations and first stages of the data reduction. 2. "Das Spectrum der Radiostrahlung" by R. Wielebinski and W.E. Wilson. The absolutely calibrated horn measurements at 716.5 MHz and 1424 MHz described in this paper, were made by the author, at the Fleurs Field Station of the University of Sydney, Department of Electrical Engineering.

Appendix 2 comprises of two papers in which the author collaborated. 1. "Radio Observations of the

Cygnus Loop at 2.7 and 10.7 GHz" by N.J. Keen, W.E. Wilson, C.G.T. Haslam, D.A. Graham and P. Thomasson. 2. "High Resolution Measurements of the Supernova Remnant HB 21 at a Frequency of 2.7 GHz" by C.G.T. Haslam, N.J. Keen, W.E. Wilson, D.A. Graham, P. Thomasson. The author assisted in the observations of these experiments and was responsible for the data reduction, using the techniques and programs described in Chapter 2.

The work described in Chapters 1, 2 and 3 has been published as "A Further 408 MHz Survey of the Northern Sky" by C.G.T. Haslam, W.E. Wilson, D.A. Graham and G.C. Hunt (1974) (see reference list).

During the first three years of my canditure, I was the recipient of a Commonwealth Postgraduate Studentship.

I wish to express my gratitude to Dr. R. Wielebinski, who has acted as my supervisor throughout the course of this work. Without his support, the work described in this thesis would not have been possible. I consider myself extremely fortunate to have had Dr. C.G.T. Haslam as my friend, co-worker and teacher during the course of this work. The success of this project is due largely

to his unfailing ingenuity. I wish to express my gratitude to the many members of the Max-Planck-Institut fürRadioastronomie who provided assistance in the production of the Bonn survey, and to the members of the C.S.I.R.O. Division of Radiophysics who assisted with the southern sky survey. I would also like to thank Dr. D.A. Graham for his helpful advice throughout the course of this work.

The following abbreviations are used in this thesis:

Right Ascension - R.A.
Declination - dec.
Sidereal time - S.T.
New galactic longitude - l^{II}
New galactic latitude - b^{II}

TABLE OF CONTENTS

Page

CHAPTER 5 THE SPECTRAL INDEX OF GALACTIC RADIO RADIATION

CHAPTER 6 THE STRUCTURE OF GALACTIC RADIO RADIATION AT 408 MHz

The 100 M Radiotelescope of the MPIfR at Effelsberg, near Bonn, W. Germany

CHAPTER 1

THE BONN 408 MHZ SURVEY

1.1 Introduction

This chapter describes the equipment and techniques used to collect the data for the Bonn 408 MHz survey. This survey was made with the 100 metre radiotelescope of the Max-Planck-Institut für Radioastronomie at Effelsberg, West Germany. Beginning in June, 1971, it became the first astronomical program to be carried out with the new instrument.

The 408 MHz measurements were intended to fulfil two main purposes. The first was to complete Stage 2 of the proposed all sky 408 MHz survey, begun at Jodrell Bank in 1966 (Haslam, Quigley and Salter (1970)). The second purpose of the experiment was to provide a first experiment that required the minimum performance from the telescope, and that could be used to test the various receiver and data collecting systems being developed for later use with the higher frequency parametric amplifiers, for which the telescope was primarily intended. The experiment was conceived to use any spare time that was available during the completion of the telescope's construction.

1.2 The Observations

The observing technique used in this survey was the "nodding scan" technique (Large, Quigley and Haslam (1966)). In this method, the telescope is kept at a constant azimuth, usually along the meridian, whilst it is driven up and down in elevation at a constant speed. As the telescope is driven in elevation, the sky moves through the elevation axis at drift rate, thereby producing the oblique scan tracks on the sky shown in Figure 1.1. If the same scan program is repeated one day later, starting at a slightly different time, then tracks are produced adjacent to the first night's tracks. If this time difference is chosen such that adjacent tracks are always less than one half of one beamwidth apart, then two fully sampled maps of the region can be constructed from a number of days of observations. One map is constructed from the set of upscans, the other from the set of downscans. The declination coverage of such a survey is wholly determined from the limits, in elevation, of the scans,

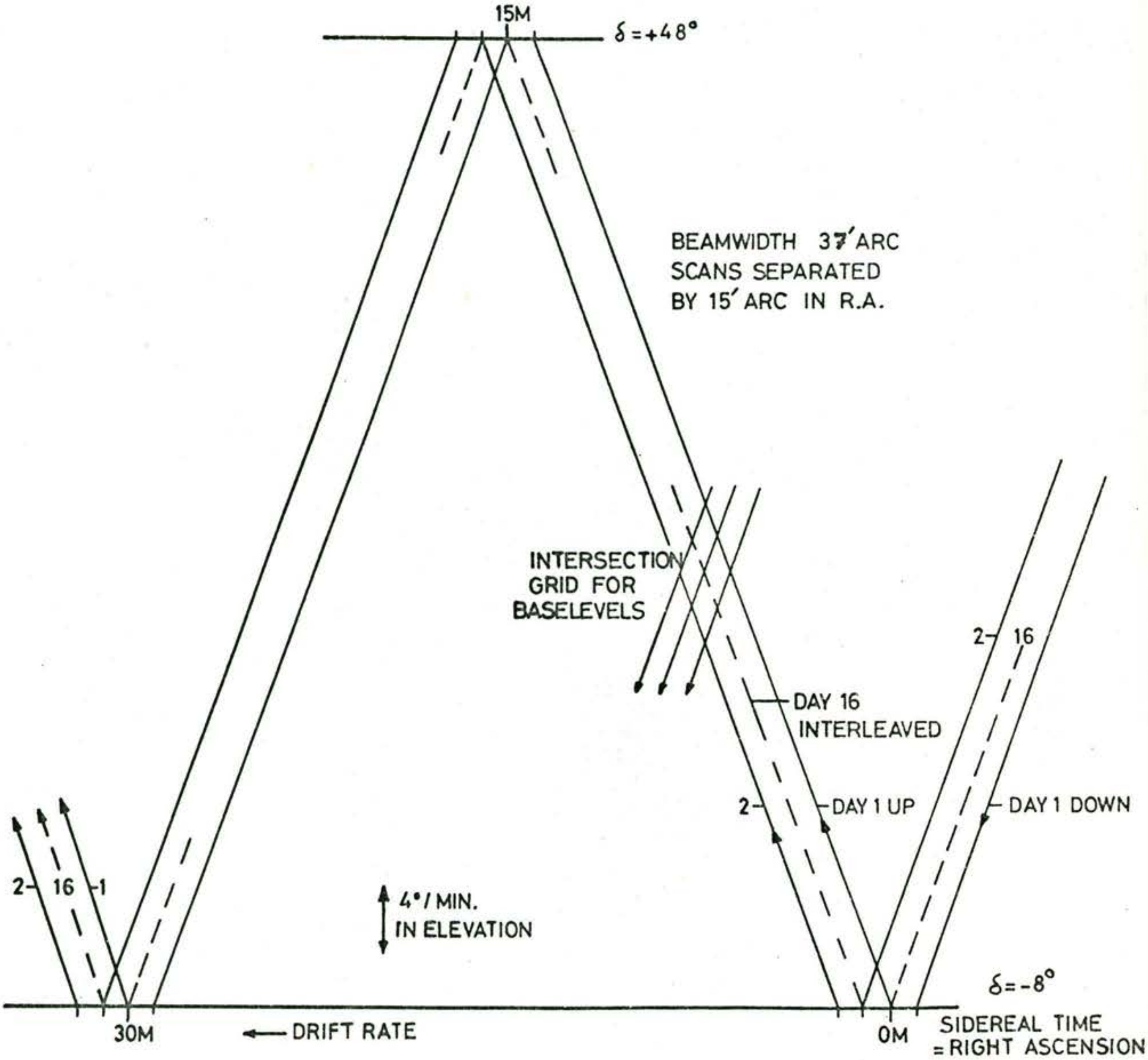

408 MHZ SURVEY NODDING SCAN PROGRAMME

FIGURE 1.1

whilst the right ascension coverage is approximately equal to the sidereal time spent observing on any one day.

This technique of surveying large regions of the sky has the following advantages over other methods:

1. The position of the telescope in celestial coordinates is determined simply from the elevation of the telescope and the sidereal time. No spherical transformation is required.
2. Two surveys of the region are produced, one comprising the down scans, one comprising the upscans.
3. Any contribution to the maps from ground radiation picked up by the sidelobes of the antenna, appears only as an elevation (i.e. declination) dependent term. Correction for this effect is, therefore, made easier.
4. As shown in Figure 1.1, each upscan is cut by many downscans, and vice versa. This property can be used to determine a consistent baselevel for each scan (see Section 2.7).

One disadvantage of this method is that the survey is less well sampled at low declinations, so that, if the observations are not confusion limited, a varying noise level across the map is obtained.

The scanning program used during the survey is shown in Figure 1.1. A time interval of one minute between starting times of adjacent scans gave a 15 arc min. sampling interval at dec. = 0°. This was sufficient for the 37 arc min. beamwidth of the telescope at 408 MHz. At the time of the start of observations the maximum driving speed of the telescope was limited to 4° per minute. It was, therefore, decided to restrict the declination coverage of the survey so as to complete the desired R.A. range in a reasonable time.

The observations were begun in June, 1971, but were not finally completed until February, 1972. The program, which should ideally have taken 30 days of observing, finally took over 70 days, spread out during this period. It was initially intended to cover the R.A. range 12 hours to 24 hours. However, when more time became available, this was extended from 00 hours to 04 hours, thereby covering the region missing from the survey of Haslam et al. (1970).

1.3 The Feed Antenna

Because the 408 MHz receiver at all times occupied a low priority on the 100 M telescope, it was necessary in the design to ensure that any equipment installed did not interfere with the 11 cm test receiver that was at that time operating on the telescope. This was particularly the case with the feed system, where an aerial was required that would not cause any degradation in performance of the 11 cm feed horn. This was achieved by the use of a "boxing ring" type aerial, which was made up of four half-wave dipoles, arranged in a square around the 11 cm horn.

Each dipole was fed by a cable balun, i.e. each half of the dipole is fed from a common source, through 50 ohm coaxial cables of lengths $\lambda/4$ and 3 $\lambda/4$, whose shields are connected together at the centre of the dipole. The length of the dipole and its height above the backing plate were then adjusted to give a 50 ohm input impedance to the balun. The two parallel dipoles were then joined to the common input by 3 $\lambda/4$ lengths of 70 ohm coaxial cable, which formed the required transformers to give an input impedance to the two dipole array of 50 ohms, assuming no reaction between the dipoles.

The distance between parallel dipoles is required to be as small as practicable to give a circular feed pattern. However, this is limited by the reaction with the orthogonal dipoles. The distance finally used, based on an experimental determination of this reaction effect, was 0.54 λ. Once the complete feed was assembled around the 11 cm horn, fine tuning was accomplished by slight changes in the length of the dipoles, the final V.S.W.R. obtained from both pairs being 1.07. All measurements were made with the use of a General Radio Admittance Bridge.

As circular polarisation was required for the survey, the two outputs from the feed were fed through two lengths of 50 ohm coaxial cable, one of which was λ/4 longer than the other, to a ring hybrid, which produced right and left-handed circular polarisation components. These were then fed to the top of the 11 cm receiver box, where the required sense of circular polarisation was fed through a large diameter, low loss coaxial cable to the receiver which stood in a rack some 5 metres above the focus of the dish. The overall loss from the feed to the receiver was approximately 1.0 dB, which was unfortunately large, but nevertheless necessary so as not to affect the operation of the 11 cm receiver.

1.4 The Receiver

The receiver used for the survey was a dual channel correlation radiometer as shown in Figure 1.2. It was conceived as a general purpose receiver which could be remotely switched between two basic modes of operation. In one mode it accepts either of the two inputs and measures this relative to a standard reference load. The second mode provides direct through paths for the two inputs, thereby allowing polarisation measurements to be made. Throughout the survey, the first mode of operation was used exclusively, the input being the left-hand circularly polarised signal from the feed system.

A noise diode calibration signal was added to the input by means of a 20 dB directional coupler. A pin diode switch was used to switch the noise from the diode on and off at a frequency equal to half the phase switching frequency of the correlator (see below). This allowed a continuous monitor to be kept on the gain of the receiver.

During the first sixteen days of the survey, a well insulated room temperature termination was used as the reference load. A thermistor connected to the load

408 MHz RECEIVER

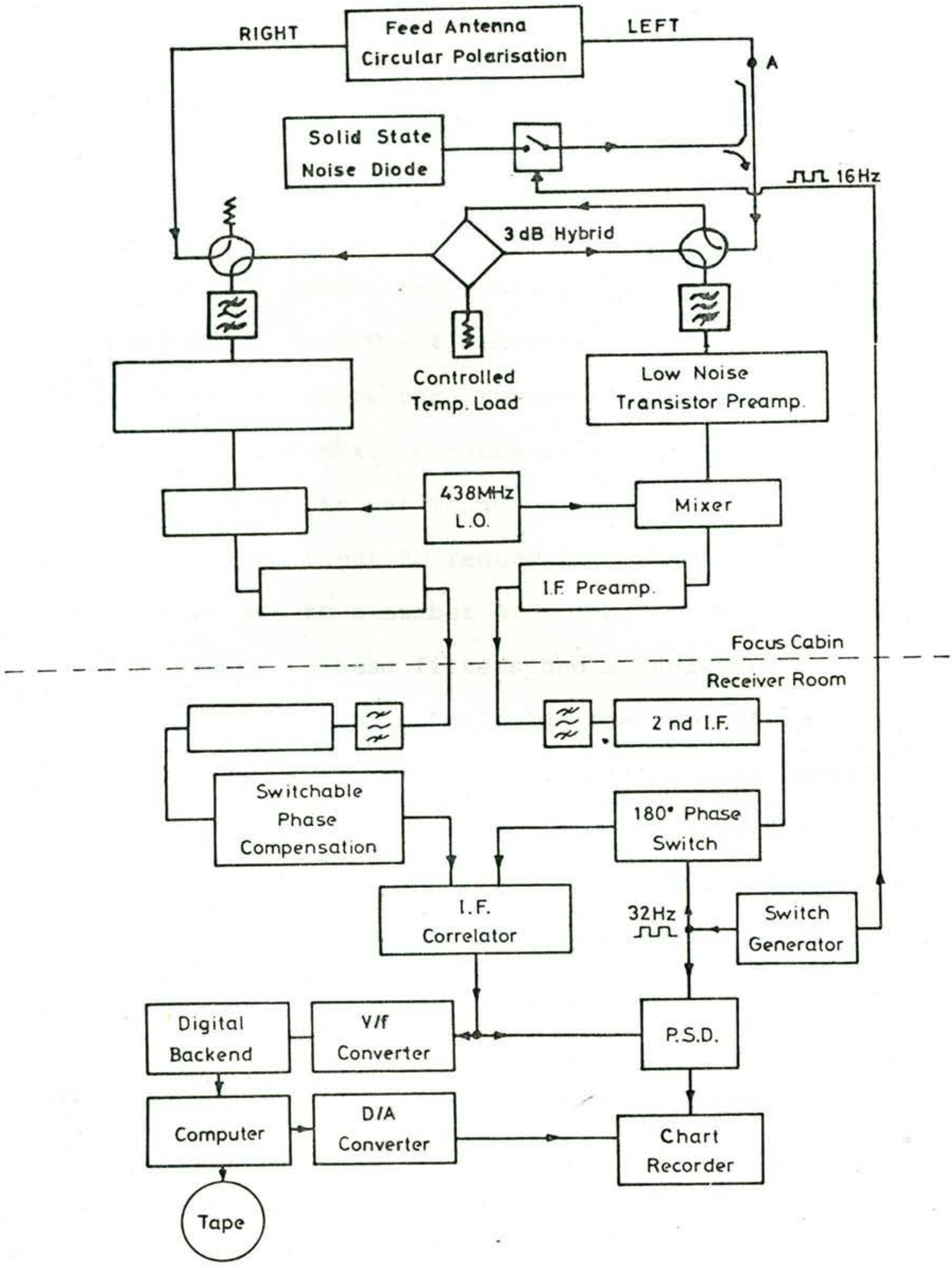

FIGURE 1.2

allowed remote monitoring of its temperature. After this, a servo-controlled heated load held at a constant temperature of about 30 °C was substituted. Once again its temperature was monitored by a thermistor thermometer.

The R.F. amplifiers used in the receiver were AVANTEK model AK-500B-14 wideband transistor amplifiers with an excess noise temperature of 120 K and a gain of 30 dB at 408 MHz. Because of the wide bandwidth of the amplifiers, it was found necessary to place R.F. filters on the input to reduce intermodulation distortion due to a number of strong interfering signals in the region. These filters had a bandwidth of 3.5 MHz and a loss of 0.4 dB. Following the amplifiers were balanced crystal mixers, fed by a transistor local oscillator set at 438 MHz resulting in a 30 MHz I.F. frequency. After 45 dB of amplification, the two I.F. signals were fed into the telescope cables to the receiver room.

In the receiver room, the signals first passed through matched I.F. filters, which were used to define the overall bandwidth. These filters had a 3 dB bandwidth of 3.5 MHz and a high selectivity, thereby reducing the overall bandwidth to 3.0 MHz. A weak interfering signal on the skirts of the primary band was completely removed by these filters. The signals then passed through a further 45 dB of amplification before being fed into the phase switched I.F. correlator. The correlator circuit was developed from the designs of Frater (1964). 180° phase switching was used in one arm of the input to the correlator so that any direct squared terms of the inputs reaching the output could be removed by the subsequent subtraction required in the demodulation process. By this means, a receiver dynamic range in excess of 45 dB was obtained. Compensation for any phase difference in the paths of the two signals was achieved by sections of delay cable inserted in one of the I.F. signal paths and switchable in steps of $\lambda/64$ from zero to $\lambda/2$. The output of the correlator was then split into two paths. One was used as the input to an analogue synchronous demodulator, the output of which was displayed on a pen-recorder to provide an analogue record of the observations. The second output of the correlator was fed into a voltage to frequency converter and thence to a "digital back-end" of the type described by Zinz and Haslam (1972) which provided the required inputs to the ARGUS 500 computer.

1.5 Temperature Scale Calibration

The temperature scale of the receiver output was calibrated relative to the injected calibration noise signal. The effective temperature of this noise signal was measured in the following way.

The servo-controlled heated load, used as a reference load during observations, was placed at point A in Figure 1.2. Its temperature was monitored by an accurately calibrated thermistor type thermometer. By comparing the step in the receiver output produced by the noise signal with that from heating the controlled load by a known temperature, the effective temperature of the noise signal was determined, with reference to the point A. This type of measurement was made three times covering the whole course of the observations, and the noise output of the calibration signal was found to be 88 K and was constant to within 2% during this period.

With knowledge of the effective temperature of the injected noise signal, receiver output deflections could be expressed in units of antenna temperature, assuming zero losses in the feed and receiver up to the point A.

1.6 Data Collection

Two different methods of data collection were used during the survey.

The method used during the first eight days of the survey (METHOD A) was a standby system, written by colleagues of the author (see acknowledgements) when it was discovered that the standard data collecting system (METHOD B) would not be ready by the time observations were to begin.

In the data collecting process itself, no attempt was made to do the required arithmetic on the separate switch phases to produce outputs representing signal and gain. A direct recording was made of each of the four switch phases which were contained in the basic cycle of the receiver. These four switch phases and the values they represent are:

P1: Antenna - Reference; Positive correlation
P2: Antenna - Reference; Negative correlation
P3: Antenna + Calibration - Reference; Positive correlation
P4: Antenna + Calibration - Reference; Negative correlation

With a switch rate of 31 Hz, each phase was approximately 16 mS long and each cycle approximately 64 mS long.

The required outputs of signal and calibration are obtained by performing the following sums:

$$2 \times \text{SIGNAL (+ CALIBRATION)} = P1 - P2 + P3 - P4$$

$$\text{CALIBRATION} = P3 - P1 + P2 - P4$$

The signal, as in a Dicke switched receiver, is antenna minus reference. As the level of the injected calibration noise signal is kept constant, the calibration, as calculated above, is a direct measure of the gain of the receiver.

METHOD A: Each of the four phases were integrated together in the computer for sixteen cycles. These four values were then written on paper tape together with the local zone time and telescope elevation, which were read by the computer midway through the integration. This process led to a data sampling rate of approximately one second.

METHOD B: In this case no on-line integration was performed, each single phase being directly written onto magnetic tape. Every sixteen cycles, the local sidereal time and telescope elevation of the preceding cycle was also written onto the magnetic tape.

In both of the above methods, two outputs were provided from the computer representing the final value of the signal and calibration. The two sums giving signal and calibration were performed on-line and integrated for sixteen cycles. They were then fed to a digital to analogue converter and thence to the second channel of the pen-recorder to be displayed alongside the analogue record. This provided a check on the data being collected. An example of one of these records is shown in Figure 1.3.

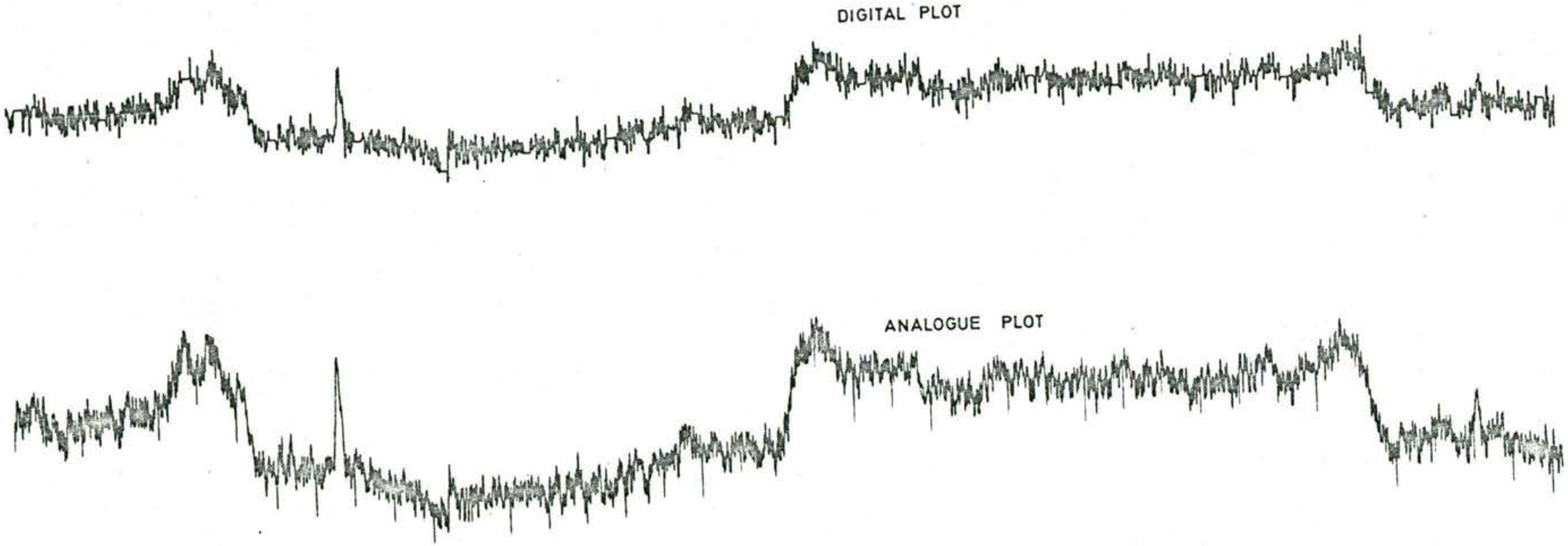

FIGURE 1.3

CHAPTER 2.

THE BONN SURVEY COMPUTER REDUCTION

2.1 Introduction

The computer analysis of the Bonn 408 MHz survey was carried out using the CDC 3300 computer of the Max-Planck-Institut für Radioastronomie in Bonn. A block diagram of the basic steps taken in the analysis of the data from the telescope tapes through the final maps, is shown in Figure 2.1. A description of the stages in the analysis follows. As the bulk of the data was recorded on magnetic tape, the analysis used for processing this data will be described first. Methods peculiar to the paper tape data will be described when necessary.

2.2 Initial Reading of Tapes

Because this survey was the first experiment to make use of the magnetic tape facilities at the Effelsberg observatory, it acted as a test for both the hardware and software associated with these facilities. As a result, as might be expected, it was found that in the early days of the survey, there were many and varied errors written

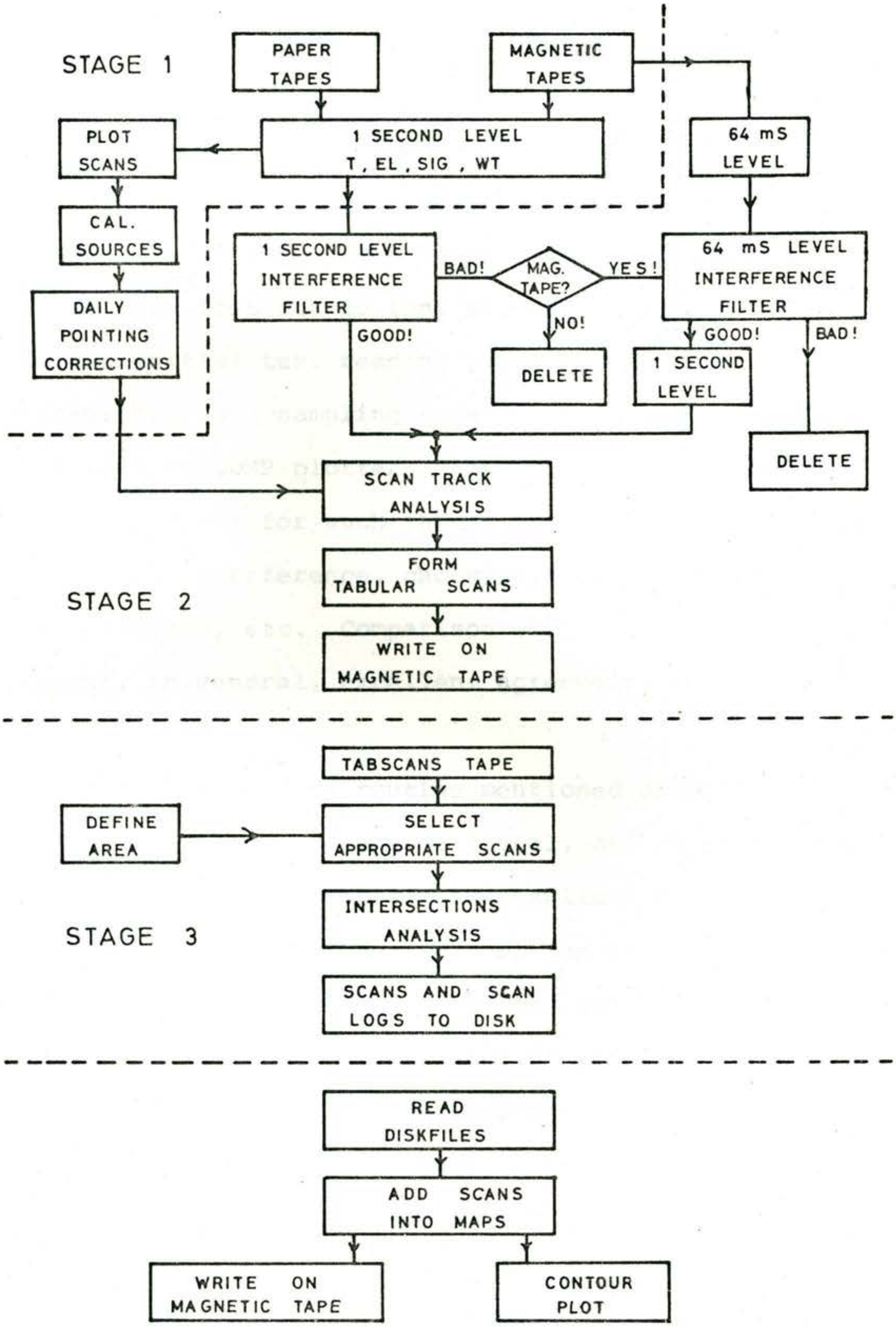
STAGE 1
PAPER TAPES
MAGNETIC TAPES
PLOT SCANS
1 SECOND LEVEL T, EL, SIG, WT
64 mS LEVEL
CAL. SOURCES
1 SECOND LEVEL INTERFERENCE FILTER
BAD!
MAG. TAPE?
YES!
64 mS LEVEL INTERFERENCE FILTER
DAILY POINTING CORRECTIONS
GOOD!
NO!
DELETE
GOOD!
1 SECOND LEVEL
BAD!
DELETE
SCAN TRACK ANALYSIS
FORM TABULAR SCANS
STAGE 2
WRITE ON MAGNETIC TAPE
TABSCANS TAPE
DEFINE AREA
SELECT APPROPRIATE SCANS
INTERSECTIONS ANALYSIS
STAGE 3
SCANS AND SCAN LOGS TO DISK
READ DISKFILES
ADD SCANS INTO MAPS
WRITE ON MAGNETIC TAPE
CONTOUR PLOT

FIGURE 2.1

onto the magnetic tapes. Because of this, the first task in the analysis was to write a general program which could read over all the different types of errors present on the tapes. In almost every case the data could be salvaged, and in the entire survey, comprising of some 2,000 scans, only approximately eight scans were lost due to tape errors. During the process of the initial test reading of the tapes, the data was integrated to a sampling rate of one second and plotted out on a CALCOMP plotter. These plots were used later in the process for such things as picking out obvious bursts of interference, choosing sources for pointing calibrations, etc. Comparison with the analogue charts showed, in general, excellent agreement.

The tape reading routine mentioned above had a basic output of signal, weight of signal, and calibration, integrated for sixteen receiver switching cycles, i.e. about one second. The weight of the signal was set equal to the number of cycles integrated together to give the signal, and had a nominal value of sixteen. The local sidereal time and the telescope elevation associated with the data point were also given. This routine was slightly modified for the final "production" run in that the 64 mS (one cycle) level data was also stored away, in case it was found necessary to return to this level from the next stage in the analysis.

A different reading routine was required for the data collected on paper tape. This data was collected together onto one magnetic tape, and then a routine to read this tape was written which gave the same output format as the magnetic tape data reading routine. The weight of each data point was given the full value of sixteen.

2.3 Telescope Pointing Corrections

During the course of the observations, construction work was continuing in the prime focus cabin of the 100 M telescope. This meant that the position of the 408 MHz feed with respect to the telescope focus might be changed from day to day. As the control room readouts of focal position were not, at that stage, in operation, it was impossible to find out, directly, whether any changed had been made since the previous night's observations. For this reason, it was necessary to obtain, from the observations, a measure of the day to day pointing of the telescope.

A measure of the azimuth pointing errors could only be obtained from the occasional test drift scans made during the survey period. In spite of the fact that there was no azimuth encoder for the first period of observations, so that the telescope had to be placed in the South position by aligning a plumb line with a marker driven into the ground under the telescope, measurements on these drift scans showed that there were no significant azimuth pointing errors. This is understandable in terms of the fact that the main movement in feed position is in the elevation plane, so that any changes made should not affect the azimuth pointing.

Information on daily pointing errors in elevation could be obtained by measurements on those scans passing close to point sources whose positions were accurately known. For each day's observations, pointing sources were chosen from the scan plots for that day. In the region of these sources, the scans were plotted out with an expanded elevation scale, and the elevation of the source peak was calculated. If the scan did not pass directly through the source, a small correction was necessary to allow for the fact that the scans were not parallel to a line of constant R.A. This correction was calculated assuming no azimuth pointing errors.

For the first two sessions of observations (before 20.9.71) elevation pointing errors of less than 3 arc minutes were found. However, for the final session (after 22.11.71) a consistent error of 6 arc minutes was found. Seventeen sources were measured covering this period, giving an elevation pointing error of 6' ± 2' (R.M.S.).

The pointing errors obtained from this analysis were used in corrections applied to the data during the scan tracking routine (Section 2.5).

2.4 Impulsive Interference Rejection

The next stage in the analysis was the beginning of Stage 2, and was aimed at finding and rejecting any data affected by impulsive interference.

A high pass filter technique (Salter (1970)) was used, whereby all frequencies that could be due to the convolution of the telescope beam with any time independent brightness distribution in the sky, were rejected, leaving only higher frequency components, which could only be due to interference. Because one of the reasons for collecting data with such high redundancy was to give better protection against interference, a filter was developed which would work on the basic 64 mS data samples. However, as any such filter would need to inspect each point at this level, this would lead to a large amount of computing time. As a result, it was decided to run an initial "finding" filter on the data integrated to one second samples. Once this filter had detected interference, the program would revert to the 64 mS level, using the higher level filter, and select the points unaffected by this interference.

Figure 2.2A shows the Fourier transform of time independent astronomical signals which are passed by the telescope moving at the 4°/minute speed of the observations. An ideal filter for removing any impulsive interference is also shown.

The finding filter is formed in the following way. The Fourier transform of a group of three delta functions with separation P, as shown in Figure 2.2B is:

$$2P \sin^2 (\pi f/2Q) \qquad \ldots (2.1)$$

where $Q = 1/2\,P$

for P in seconds and Q in Hertz. This function, in time space, will be henceforth called a "3DELTA" function.

It is seen from the right-hand side of Figure 2.2B that if P is so chosen such that Q is much greater than

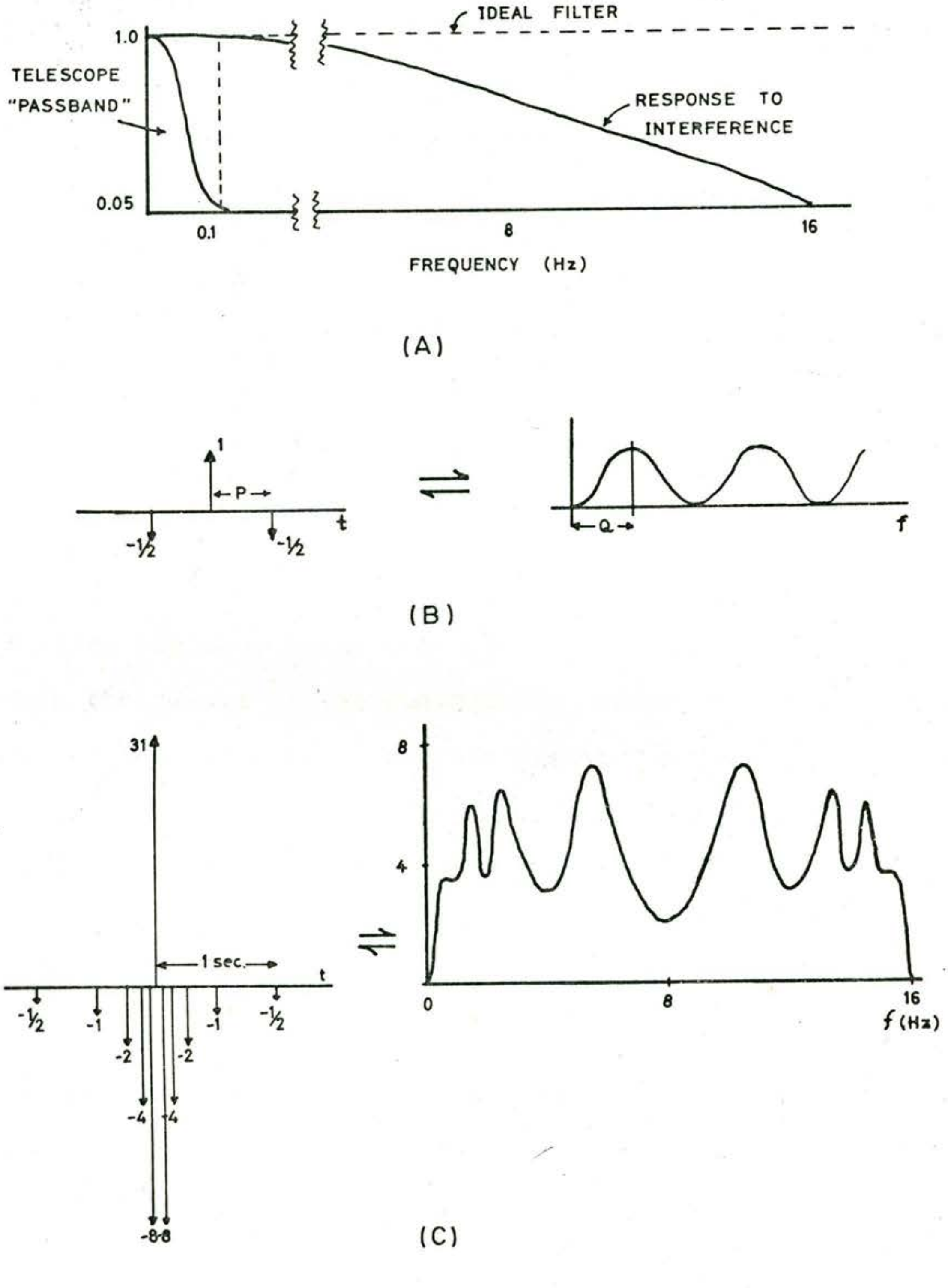
IDEAL FILTER
1.0
TELESCOPE
"PASSBAND"
RESPONSE TO
INTERFERENCE
0.05
0.1
8
16
FREQUENCY (Hz)
(A)
1
P
t
-½
-½
Q
f
(B)
31
1 sec.
t
-½
-1
-2
-4
-8
-8
-4
-2
-1
-½
8
4
0
8
16
f (Hz)
(C)

FIGURE 2.2

the maximum frequency passed by the telescope, then this filter will successfully reject the astronomical frequencies. As the sampling interval is one second, it is required that P is an integral number of seconds. With P equal to one second, Q becomes 0.5 Hz and the rejection is quite acceptable. Increasing P leads to unacceptable rejection. Any frequencies above 0.7 Hz are severely attenuated by the one second integration process, and so the minimum in the filter at 2Q = 1 Hz has no effect.

Such a filter was used as the interference finding filter, the data being convolved by the 3DELTA function. When the result of the convolution centred at a certain data point was below a certain preset value, this data point was assumed to be free of interference, and proceeded to the next stage of processing. When a data point did not pass this test, it was passed through the higher level filter described below. The upper limit for the result of the point by point convolution was determined from an examination of the maximum value of the convolution, when the radio source Virgo A was passed through the filter. In the region surveyed, this is the strongest unresolved radio source that did not overload the receiver. Hence the highest frequencies passed by the telescope beam should appear at this point.

As the data collected on paper tape did not contain information at the 64 mS level, no higher level filter could be used on this data. Therefore, if the above filter registered the presence of interference in a data point, it was rejected by setting its weight to zero.

At the 64 mS level, frequencies up to about 16 Hz can be present, and so the high level filter must more closely approach the ideal filter shown in Figure 2.2A. Such a filter was constructed from a superposition of a number of 3DELTA functions of differing heights and separations.

The first minimum in the response of the first look filter can be filled by the addition of a similar filter whose width to first maximum is 1 Hz. The superposition of the two filters leaves a zero at 2 Hz, which can be filled by the addition of a filter whose width to first maximum is 2 Hz. By adding five such filters together, each one being twice as large as the one before, the result is a filter whose first zero is at 16 Hz. This filter, shown in Figure 2.2C, is by no means flat up to 16 Hz, but in a frequency range of 0.5 Hz to 16 Hz it never falls below a value of 2.0, and has a maximum value of approximately 8.0. It was decided, therefore, to use this as the high level filter. The inverse Fourier transform of this function is a set of 11 delta functions of varying heights, as shown on the left hand side of Figure 2.2C.

In the computer analysis, if the prescence of interference was signalled by the first look filter, the higher order filter was successively centred on each of the 16, 64 mS samples of the data point in question. For this purpose, the data points to either side were also available at the 64 mS level. If the result of the convolution at any point was above a certain preset level, the sample was rejected. All the good samples were added together and then normalised, the weight of the resulting 1 sec. sample being set equal to the number of 64 mS samples that had been retained.

The limit for the result of the point by point convolution of this filter with the 64 mS level data, was determined from the level of noise expected at the sampling rate. This proved to be a more important effect than the prescence of any radio source in the data.

2.5 Scan Tracking Routine

The next stage in the analysis was aimed at choosing from the recorded data, only that data that lay along one of the prescribed scan tracks. Ideally this stage should have preceded the interference filter routines, which are specifically designed to work on data collected at the scanning speed. However, this would have meant that the scan tracking routine would have to work at the 64 mS level, which would lead to a large increase in computing time. As a result, it was decided to place the routines in the order shown in Figure 2.1. As 95% of the data collected was taken while scanning, this leads to only a small amount of unnecessary processing by the interference filter routines.

The scan tracking routine began by placing the data in a 5 deep, "pushdown" store, and examining the top two data points until their elevations differed by more than 2' arc. Once this condition was satisfied, the theoretical track was computed from the elevations and sidereal times of the top two data points. The five stored data points, and each succeeding data point, were then examined to see if they lay within 20 seconds of time of the theoretical track, and if so, were placed in a large scan array containing the sidereal time, elevation (corrected for any predetermined pointing error), signal, calibration, and weight of signal for each point. If a point was found which did not satisfy this condition, its weight was set to zero in the scan array, and it was stored in an auxiliary array with full weight. If five such points in succession were found, the scan array was temporarily closed, and control returned to the initial procedure of finding the theoretical scan track of the latest data points. If the new theoretical track differed from that of the previous one, the scan array was considered as complete, and was passed on to the next stage of the analysis. Otherwise, it was opened again for incoming data satisfying the tracking condition. On return from the following stage of the analysis, the process was begun again on the data stored in the auxiliary array.

This process was found to be extremely efficient in choosing data applicable to the survey from tapes which often contained many different types of observations, and discontinuities in scans.

2.6 Formation of Tabular Scans

The final part of Stage 2 of the analysis was the formation of scans, tabulated at specific points in declination. The spacing of the tabular points must be somewhat less than the half power beamwidth of the telescope. With a beamwidth of 37 arc min., a spacing of 12 arc min. in declination was chosen.

At each declination, the right ascension (1950.0), signal, calibration and weight of signal, was stored, whilst the position in the array defined the declination. The interpolation of the irregularly spaced data onto a regular grid was achieved by convolving the data with a truncated SIN X/X function. With a suitable selection of the width of this function, the form of the signal in frequency space remains unaltered, except that the higher frequency components, due to noise, are suppressed. The width of the function used was 16 minutes of arc to first zero. It was truncated at 64 minutes of arc from the centre.

The function was successively centred at each position on the tabular scan grid, and a weighted average was taken of all data points within 64 minutes of arc of this position. The weight of each data point was taken as the value of the SIN X/X function at the declination of the data point, multiplied by its own weight. The sum of the weights of all data points used then became the weight of this tabular scan grid point. The calibration value at each tabular scan grid point was formed by a simple average of all data points within 6' arc of the grid position. The sidereal time of the closest data point was used as the sidereal time of each grid point. This leads to a maximum error of 0.5 sec. in right ascension.

Declination precession was achieved by precessing the standard grid in 1950.0 coordinates, to epoch date, and performing the convolution onto this precessed grid. The sidereal time (i.e. right ascension) associated with each grid point was then precessed to 1950.0 coordinates. As the survey did not go below 30^{o} elevation, it was not necessary to apply any correction for refraction.

Each tabular scan contained a header block, with information pertaining to the scan. In particular, information on the variation in gain of the receiver, and the baselevel across the scan was stored in the form of a start timeand a stop time, and the value of the calibration and the baselevel at these two times. The calibration values were obtained from a straight line fit to the values in the scan. The values of the baselevel were determined from measurements of the variation of the temperature of the reference load. Also contained in the header block was a parameter representing the overall weight of the scan. This allowed all points in a particular scan to be given less weight if there was any reason to believe that it contained less reliable data.

The tabular scans so formed were then written onto a magnetic tape in preparation for Stage 3. of the analysis.

2.7 Formation of Log and Baselevel Optimisation

One of the main problems involved in making a survey of such a large area, is the need to define a consistant zero level to scans which have been made over a long period of time. The method of solution used in this survey invoked the property of the observing procedure, that any one upscan is intersected by many downscans, and vice versa (see Figure 1.1).

To determine the baselevel corrections to be supplied to any one, for example, upscan, all the downscans which cut it were selected, and the values of the "intersection errors" determined. The intersection error at a crossing point is defined as:-

$$\text{Intersection error} = T_c(t)\ (\text{upscan}) - T_c(t)\ (\text{downscan}) \qquad \ldots (2.2)$$

where $T_c(t)$ = calibrated signal value at S.T. t (K)

and t = S.T. (i.e. R.A.) of crossing point

The calibrated signal at any point in a scan is given by:-

$$T_c(t) = \frac{S(t) \cdot T_{cal}}{C(t)} - B(t) \qquad \ldots (2.3)$$

where $S(t)$ = Scan signal value at S.T. t (digitised units)

$C(t)$ = Scan calibration value at S.T. t (digitised units)

$B(t)$ = Scan baselevel value at S.T. t (K)

T_{cal} = Measured value of calibration noise signal (K)

Once all the intersection errors for the particular upscan in question had been determined, along with the sidereal times at which they occurred and their weights, a linear weighted least mean squares fit was made. The values of the line of best fit at the scan start time and scan stop time were then assumed to be the corrections to be made to the baselevels of the scan. By processing each scan in this way, and then updating the baselevels of all scans and repeating the whole procedure a number of times, the mean intersection error for all intersections was found to decrease and converge to a solution which gave a consistent zero level to all scans. A description of the way in which this method was implemented in the computer, now follows.

To facilitate the use of the baselevel optimising process, the concept of the scans "log" was introduced. This log contains a number of entries for each scan, representing the scan number, start S.T., stop S.T., gain at start, gain at stop, baselevel at start, baselevel at stop, and overall weight of scan. During the baselevel optimising process, only the log entries for a particular scan are changed, the original scan being kept as a record of the initial state. Also, by printing out the log, a convenient way of showing the state of the calibration of all scans at that point, was available.

Because of the large area covered in the complete survey, it was impossible to process all the data at one time. Based on the amount of computer store available, it was decided that Stage3 of the reduction should work on blocks of one hour of right ascension at a time. So that adjacent blocks would line up satisfactorily, the

the block size was made to be one hour plus four minutes on either side, so that there was an overlap region with the adjacent blocks of eight minutes of R.A.

Stage 3 of the computer reduction began by choosing from the tabular scan tape only those scans which cut the area of the particular hour of R.A. chosen, plus the eight minute overlap regions. Each scan was then written to one of two disk files, depending on whether it was an upscan or downscan. As each scan was read in it was entered in either the uplog or the downlog. At the completion of the input, the uplog and the downlog were written to spaces reserved for them at the beginning of each disk file. Each upscan was then compared with all downscans, and wherever an intersection was found it was entered in the upscan intersections log, which contained for each intersection a combined code indicating which upscan and which downscan intersected, the sidereal time, t, of the intersection, the value of S(t) (Equation 2.3) for the upscan, the value of S(t) for the downscan, and the weight of the intersection. As the intersection point did not in general correspond to a tabulated point (see Figure 1.1) a four point interpolation was necessary to find the value of t and hence the value of S(t) in the two scans.

An interpolation was also used to find the weights of S(t), the weight of the intersection being defined as the product of the weight of the upscan S(t) and the weight of the downscan S(t). The downscans intersections log was similarly produced by comparing each downscan with all upscans.

The next step in the process was to determine the intersection errors for each upscan against all downscans. At this stage, all the information required to calculate the intersection error of any intersection was available in the intersections log and the scans logs. To calculate the calibrated signal values (Equation 2.3) of the upscan and the downscan, the value of S(t) and t were stored in the intersections log, whilst the values of C(t) and B(t) could be calculated from a linear interpolation from the values in the scan logs. A linear weighted least mean squares fit was made to the intersection errors of each upscan, and the values of this line of best fit at the start and stop time of the scan were stored in an auxiliary array. This was repeated for each downscan against all upscans. The appropriate entries in the auxiliary array were then used to correct the baselevels of each scan in the scans log.

This step was then repeated a number of times, using the intersections logs in conjunction with the updated scans logs, each time producing new base-level corrections for every scan. In a similar, but less rigorous application of this method to a similar problem, Salter (1970) found that the convergence of the solution was greatly aided by applying a fraction, k, of the corrections in each step, where $k \leq 0.7$. This factor, k, can be considered as analogous to the damping coefficient in a mechanical servo. By adopting this procedure, it was found that after each cycle of the iteration, the mean intersection error of all intersections decreased, finally converging after only a few cycles.

2.8 Results of Baselevel Optimisation Process

The effectiveness of the above baselevel optimisation process can be gauged from the values of the mean intersections error and the mean modulus intersection error of all intersections, after each successive iteration.

Figure 2.3 shows the results of the process operating on 175 scans covering the right ascension range 15 56 to 17 04. There were 2274 scan inter-

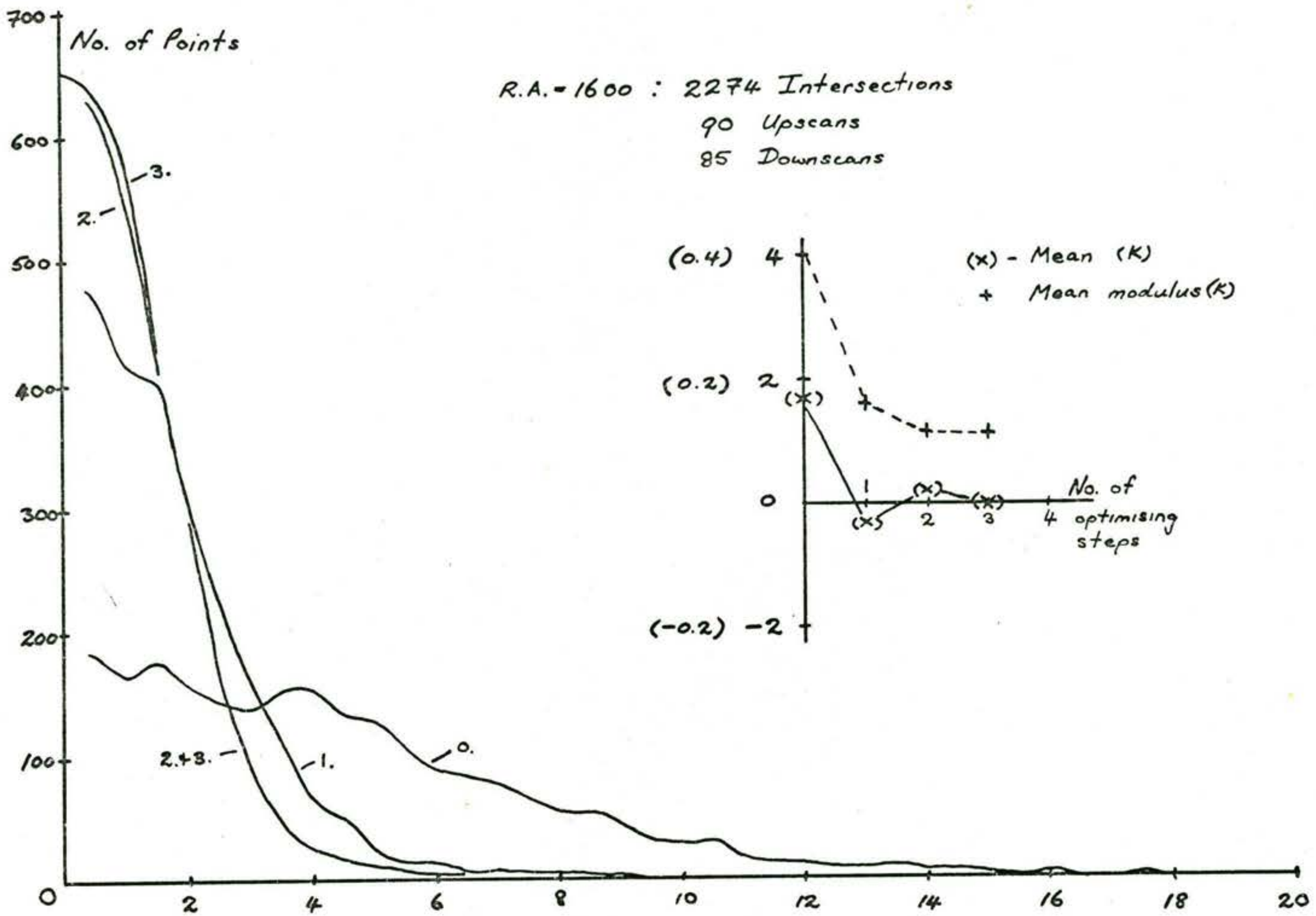
No. of Points
700
600
500
400
300
200
100
0
2
4
6
8
10
12
14
16
18
20
Temperature Differences (K)
R.A. = 1600 : 2274 Intersections
90 Upscans
85 Downscans
3.
2.
2.+3.
1.
0.
(0.4) 4
(0.2) 2
0
(−0.2) −2
(×) - Mean (K)
+ Mean modulus (K)
No. of optimising steps
1
2
3
4

FIGURE 2.3

sections in this region. This example, which is typical of the whole survey, shows the final distribution of intersection errors is approximately gaussian and has a standard deviation of 1.6 K (referred to the noise calibration signal).

2.9 Formation of Maps

At the completion of the intersection analysis, two disk files had been formed containing all the scans applicable to the area being analysed, and the upscans log and downscans log containing the fully optimised baselevels for these scans. Stage 4 of the analysis was aimed at forming the final map arrays from these diskfiles.

Because of limitations in computer storage space available, it was impossible to form a map of the whole 56° of declination. Instead, the area was divided into six sections, each covering 12° of declination, beginning at -11°, and with an overlap of 2° into the next highest section.

The map arrays were stored in the NOD2 format (Haslam (1974)). This comprises of a block of information words pertaining to the data which follows.

Included in the information block are the coordinates of the bottom left hand corner of the map, the tabular interval in the X and Y coordinates, and the number of rows and columns included in the map. The data is stored by rows, beginning at the bottom left hand corner. The coordinates of any point in the map can then be found from its position in the array.

As in the formation of the tabular scans, each scan data point was added into the map by the use of SIN X/X interpolation function. For the map arrays, a tabular interval of 12 minutes of arc was used in both R.A. and declination. Because the scan was tabulated at the declination (1950.0) positions of the rows in the final maps, it was only necessary to perform this interpolation along the right ascension (1950.0) coordinate. In the formation of the maps, the calibrated signal value of each data point was used (Equation 2.3), with the values of calibration and baselevel interpolated from the optimised values stored in the updated logs.

It was possible at this stage to make maps from only downscans, or only upscans, or from both types of scans combined. These maps could then be displayed using the line printer contour plotting facility of the

NOD2 compiler (Haslam (1974)). Because of the baselevel optimising process used, the maps made with different types of scans were not entirely independent. However, by comparing them, a measure of the reliability of each map was obtained. The maps were then edited, based on information obtained from the comparison. Any structure not common to both types of maps was traced to a bad scan, which was then given lower weight for the final production run of Stages 2 and 3. A routine was also written which could reject part of a scan on input to Stage 2. This was necessary owing to the appearance of low level interference at low elevations towards the end of the observing period. This effect was only discovered after examination of the maps and, fortunately, only affected a few days of observing.

After all maps had been edited for bad scans, the final production run of Stages 2 and 3 of the analysis was carried out. This entailed running both stages for each of the 16 hours of right ascension covered by the survey, each time producing six maps covering the complete declination range and using all scans. The result was 96 maps, each of area 17° in R.A. by 12° in dec. and containing 5,300 elements. The maps had a consistent but arbitrary zero level, and were in units of antenna temperature, not including losses in the feed antenna and feed cables. These maps were all stored on magnetic tape.

CHAPTER 3.

THE BONN 408 MHZ SURVEY MAPS

3.1 Introduction

This chapter begins with a description of the methods used to determine a brightness temperature scale and zero level for the uncalibrated survey maps. An evaluation is then made of the properties and accuracy of the final survey maps as presented in Appendix 3.

3.2 Determination of Temperature Scale and Zero Level

The temperature scale of the maps produced in Stage 3 of the survey computer analysis was calibrated in terms of the continuously injected noise signal at the input to the receiver. No attempt was made during the survey to make the measurements that were necessary to convert these maps to the required absolute full beam brightness temperatures. It was not possible to install the complex matching techniques required to determine an accurate zero level for the survey, nor was it possible to obtain an accurate measure of the antenna effective area (including feed losses) that would have been necessary to determine a brightness temperature scale. For this reason, an attempt was made to absolutely calibrate the survey maps by comparison with a lower resolution, absolutely calibrated survey at 404 MHz by Pauliny-Toth and Shakeshaft (1962). This survey, henceforth known as the "PTS" survey, presents measurements of absolute full beam brightness temperatures on a somewhat undersampled grid covering the whole Northern sky. The resolution of the antenna used was 6.5° in elevation by 8.5°.

The measured temperatures in the uncalibrated 408 MHz maps are given by:-

$$T_A(\Theta,\phi) = L \cdot \beta \cdot \bar{T}_B(\Theta,\phi) + L \cdot (1-\beta)\bar{T}_S(\Theta,\phi) + + L \cdot T_{EL}(\Theta) \qquad \ldots (3.1)$$

where L = loss in system up to point where temperature calibration was made.

β = fraction of power in the main beam if the antenna were placed within an isotropic radiation field.

$\bar{T}_B(\Theta,\phi)$ = full beam brightness temperature.

$\bar{T}_S(\Theta,\phi)$ = anisotropic and non-elevation dependent sidelobe contribution averaged over all sidelobes.

$T_{EL}(\Theta)$ = elevation dependent term, mainly due to ground radiation and atmospheric radiation.

To determine the values of full beam brightness temperatures, the values of L, β, $\bar{T}_S(\Theta,\phi)$ and $T_{EL}(\Theta)$ must be found.

If the survey maps are convolved by a suitable convolving function, resulting in a final resolution equal to the PTS survey, then the result is:-

$$T_{conv}(\Theta_o,\phi_o) = L \cdot \beta \cdot \frac{1}{C_o} \int C(\Theta-\Theta_o,\phi-\phi_o)\, \bar{T}_B\,(\Theta,\phi)\, d\Omega$$

$$+\ L \cdot (1-\beta) \cdot \frac{1}{C_o} \int C(\Theta-\Theta_o,\phi-\phi_o)\, \bar{T}_S(\Theta,\phi)\, d\Omega$$

$$+\ L \cdot \frac{1}{C_o} \cdot \int C\,(\Theta-\Theta_o,\phi-\phi_o)\, T_{EL}\,(\Theta)\, d\Omega \quad \ldots(3.2)$$

where $C(\Theta,\phi)$ is the convolving function and

$$C_o = \int_{4\pi} C(\Theta,\phi)\, d\Omega\ .$$

This reduces to

$$T_{conv}(\Theta,\phi) = L \cdot \beta \cdot \bar{T}'_B(\Theta,\phi) + S(\Theta,\phi) + L \cdot T'_{EL}(\Theta) \quad \ldots \text{ (3.3)}$$

where $\bar{T}'_B(\Theta,\phi)$ = new resolution full beam brightness temperature.

$\equiv$ PTS full beam brightness temperature.

$S(\Theta,\phi)$ = sidelobe term, in general small compared to other terms.

$T'_{EL}(\Theta)$ = elevation dependent term averaged over the new beamwidth.

If a plot is made of $T_{conv}(\Theta,\phi)$ against $\bar{T}'_B(\Theta,\phi)$, at constant elevation (declination), a straight line should result, any deviations from it being due to the term $S(\Theta,\phi)$ in Equation 3.3. The slope of this line is $L \cdot \beta$, while the intercept on the $T_{conv}(\Theta,\phi)$ axis is $L \cdot T'_{EL}(\Theta)$. As $T_{EL}(\Theta)$ should be a smoothly varying function of declination, its value at any declination is determined from interpolating between the values of $T'_{EL}(\Theta)$, found at the declinations at which the PTS survey is listed.

This method was used to determine all the unknowns in Equation 3.1, assuming that the term due to sidelobe contribution was negligible. With the low sidelobe level of the antenna (see Section 3.5), this is probably a reasonable assumption. It should be noted that this term does not include any isotropic or elevation dependent sidelobe contributions, both of which are included in $T'_{EL}(\theta)$. Approximate calculations show that this term is at most only a few percent of the main beam temperature.

The first step in the process was to convolve the uncalibrated maps down to a resolution of $8.5^\circ \times 6.5^\circ$. This was done in a number of steps, firstly to $2.5^\circ \times 2.5^\circ$ then to $5^\circ \times 5^\circ$, and finally to $8.5^\circ \times 6.5^\circ$, so as to minimise any errors that might have been introduced when the convolving function approached the edges of the component maps. With each step, the number of component maps was reduced, finally the whole survey being accommodated in one fully sampled map at a resolution of $8.5^\circ \times 6.5^\circ$.

A large majority of the points observed in the PTS survey, were taken at meridian transit. However, a number of points were observed off the meridian, with the result that the elliptical beam was at various parallactic angles on the sky. To take this effect into account, the final step in the convolution of the 408 MHz survey maps was performed a number of times, with various skewed beams, to produce maps with the beam in the various position angles used in the PTS survey.

For each point in the PTS survey, a 408 MHz map was selected, depending on the position angle used for that point. The 408 MHz temperature at this point was then found by a three dimensional interpolation from the grid points. The 404 MHz full beam brightness temperature was then calculated from published values, and a correction was made for the frequency difference, assuming a temperature spectral index of 2.7 from 404 MHz to 408 MHz. So as to bring the comparison more closely to a brightness temperature comparison, an initial scaling and baselevel subtraction was performed on the 408 MHz temperatures. The factors used, based on a first look analysis of the temperature pairs, were:-

Scaling factor = 1/0.7
Baselevel term = 159 such that:

$$T' = T_{MAP} / 0.7 - 159 \qquad \ldots (3.4)$$

where T' = 408 MHz temperatures used in comparison
T_{MAP} = 408 MHz temperatures from convolved map.

Plots were then made of these corrected 408 MHz temperatures against the 404 MHz values, at constant declination. The results of the straight line fits are shown in Table 3.1. The valuesof A (Table 3.1) obtained, showed a scatter of over 20%. Using the number of points at each declination as a weighting parameter, a weighted average of the values of A gave a value of 1.05 ± 0.05. The values of T' were corrected by dividing by this average value of A, and a new comparison was made. A close examination of these plots showed that at certain declinations, there was a large scatter of points about the line of best fit. This was traced to the fact that there was a marked discontinuity in zero level of one, or both, of the temperatures, between points observed at different parallactic angles. A comparison ofthe convolved 408 MHz maps at different parallactic angles showed significant differences only at the largest parallactic angle (52°). Hence this effect could not have been due to errors in the convolution process. Also, the fact that this only occurred at certain declinations, and also over relatively flat regions (e.g. at dec. 0°, R.A. 15 21 - 15 36) ruled out the possibility that the inconsistencies were solelydue to sidelobe contributions to the 408 MHz temperatures (i.e. the term $S(\theta,\phi)$ in Equation 3.3).

TABLE 3.1

$$T_{408} = A \cdot T_{404} + B$$

Declination	A	B	No. of points	Temperature Range (K)
-5°	1.18	2.9	7	29 - 40
0°	1.02	7.0	26	23 - 178
5°	1.09	3.1	12	23 - 89
10°	1.05	1.6	24	24 - 145
15°	1.10	-2.2	12	22 - 57
20°	1.04	-0.3	24	19 - 81
25°	0.94	1.9	9	19 - 33
30°	0.97	1.0	25	18 - 71
40°	1.13	-3.9	18	17 - 72

The conclusion must be that errors exist in the published 404 MHz temperatures, such that points observed off transit, at declinations 0° and 10°, have a different zero level to points observed at meridian transit. This is probably due to an incorrect estimate of the contribution from ground radiation at certain azimuth angles. Owing to the doubt raised as to the accuracy of the PTS survey, an independent method of calibrating the 408 MHz survey was sought for.

In the right ascension range, 00 - 04 hours, the present 408 MHz survey has a region of overlap with the Jodrell Bank 408 MHz anticentre survey. This survey was absolutely calibrated by two independent methods, one of which was a comparison with the PTS survey. The comparison in this case gave good results, but it must be noted that in the anticentre region, the PTS survey was observed always at meridian transit. Also, the temperature range in this region is much smaller than in the region overlapping with the present survey. In an attempt to define the brightness temperature scale of the present survey, sources common to both 408 MHz surveys were chosen, and the temperature deflections caused by these sources were compared. As the resolution of the two surveys differed, it was necessary, as a first step, to convolve the Bonn maps down to the 44 x 47 arc minutes resolution of the Jodrell Bank survey. The convolved Bonn maps were also given the initial calibration, as described in Equation 3.4. The results of this comparison are shown in Table 3.2. It should be noted that some unpublished data from the Jodrell Bank survey was used in this comparison (Haslam, private communication)

TABLE 3.2

Source	R.A.	Declination	K
3C66	02 20 10	$+42^{\circ}\ 46'$	1.00 ± 0.11
3C40	01 23 24	$-01^{\circ}\ 37'$	1.07 ± 0.15
3C47	01 33 38	$+20^{\circ}\ 42'$	1.06 ± 0.26
3C65	02 20 39	$+39^{\circ}\ 46'$	1.19 ± 0.35
3C31	01 04 42	$+32^{\circ}\ 08'$	1.07 ± 0.18
3C55	01 54 20	$+28^{\circ}\ 36'$	1.08 ± 0.32

Table 3.2 gives the values obtained for the quantity $K = T'(\text{Bonn}) / T_B(\text{Jodrell})$ and the probable errors in these values. The errors arise from errors

in measuring the height of the sources from the contour plots produced. Using the percentage error in each value for K as a weighting parameter, the weighted average value of K was found to be 1.08 with an error of 20%.

Using this value to correct the 408 MHz temperatures, a further comparison with the PTS survey was made. In this case, a number of points which appeared to be inconsistant with surrounding points, were discarded. This included the points in the PTS survey, observed off transit at declinations 0° and 10°. The results of this comparison are shown in Table 3.3.

TABLE 3.3

Declination	A	B
-5°	1.10 ± 0.09	2.7 ± 2.3
0°	0.86 ± 0.09	5.9 ± 2.3
5°	1.03 ± 0.02	2.3 ± 0.8
10°	1.03 ± 0.07	-1.6 ± 2.0
15°	1.00 ± 0.04	-1.1 ± 1.5
20°	1.03 ± 0.03	-2.3 ± 1.0
25°	0.85 ± 0.04	2.3 ± 1.1
30°	0.87 ± 0.03	1.75 ± 1.0
40°	1.02 ± 0.03	-3.1 ± 0.8

An average value of A was determined from a weighted average of the values in Table 3.3. In determining the weight of each value, account was taken of the error in that value, found from the goodness of the straight line fit, and the range of temperatures of the points used. The resulting average value of A was found to be 0.99 with an error of approximately 5%. The brightness temperature scale was, therefore, considered to be determined.

The values of B shown in Table 3.3 seem not to follow the expected smoothly varying curve that could be used to correct the survey for any elevation dependent sidelobe contribution. However, if the average value of the temperature differences ($T_{408} - T_{404}$) are plotted against declination, a reasonable curve results. As the temperature scales are nominally the same, this curve can be used to correct the 408 survey temperatures. The curve used in the correction is shown in Figure 3.1. During the comparison of the present survey with the Jodrell Bank Survey, values were obtained for the background temperatures around the sources used in the comparison. These points are also shown plotted on Figure 3.1, and tend to confirm the validity of the results.

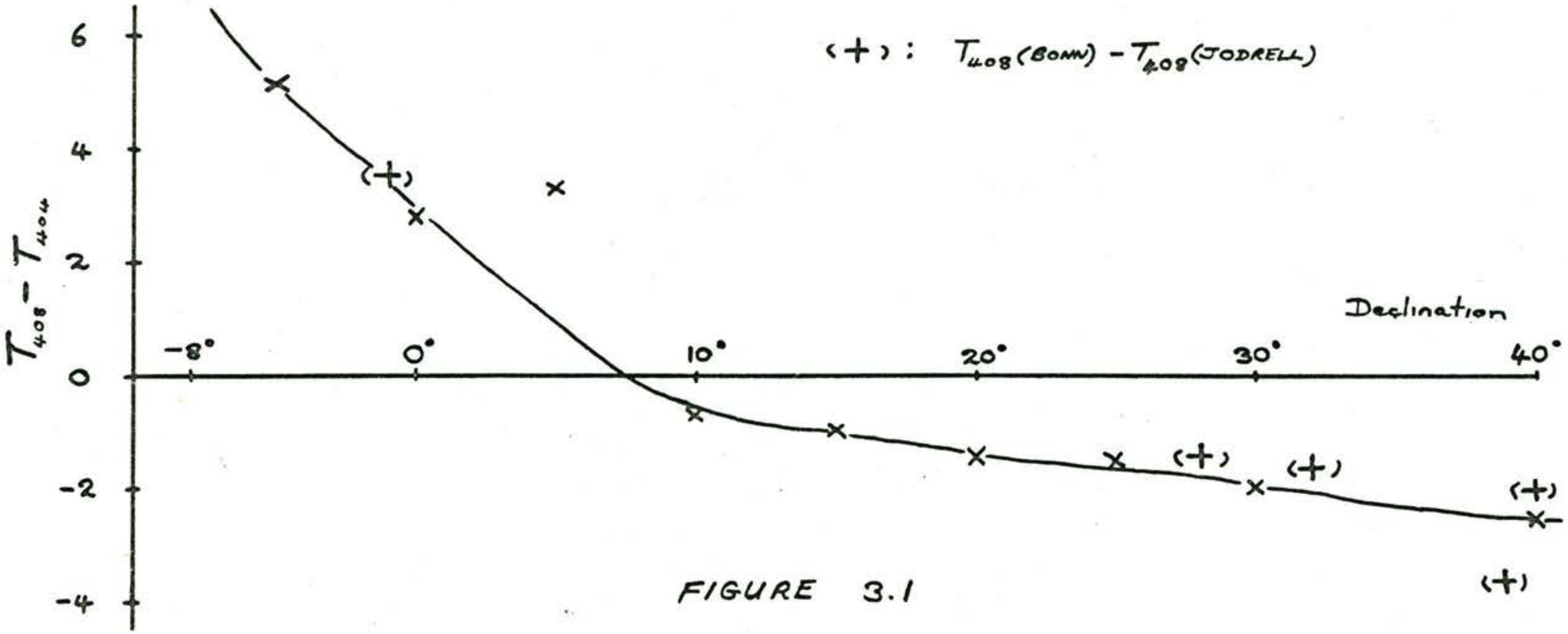
(+) : T_{408}(BONN) - T_{408}(JODRELL)
$T_{408} - T_{404}$
6
4
2
0
-2
-4
Declination
-8°
0°
10°
20°
30°
40°

FIGURE 3.1

The temperatures contained in the final maps were obtained from the initial uncalibrated maps by applying the following equation:-

$$T_B = 1.32 \times T_{MAP} - 147 - T(EL) \quad \ldots (3.5)$$

where T_B = Final brightness temperature

T_{MAP} = Uncalibrated map temperature

$T(EL)$ = Function shown in Figure 3.1.

The accuracy of the calibration can be gauged from a combination of the errors in the comparison surveys and the errors found in the comparison itself. Based on this, the brightness temperature scale has a probable error of about 10%, whilst the zero level is considered to be accurate to ± 3 K.

3.3 Comparison with Absolute Horn Measurement

During the course of work on another experiment, (Stankevich et al. (1969)), an absolute measurement of the background radiation at 408 MHz was made by the author of the position (00 00, 0°). This was made with a horn antenna whose gain and sidelobe structure were accurately known (Price (1969), Landecker (1969)), so that an absolute temperature could be directly obtained. The value obtained was 20 ± 1 K. By comparison, the average temperature at this position from the calibrated 408 MHz maps, averaged over the horn beam (H.P.B.W. = 15°) is 19 K. The good agreement between the two measurements would tend to further confirm the validity of the calibration procedure described in the previous section.

3.4 Accuracy of Survey Temperatures

As explained earlier, one of the advantages of the nodding scan technique is that two complete surveys of the region are produced, one from the set of upscans, and one from the set of downscans. A measure of the internal consistancy of the final maps may be obtained from an analysis of the temperature differences in the two component surveys.

At a number of sample right ascensions, component map pairs were made, each being made from only one type of scans. The point by point differences were then taken and a statistical analysis carried out on the values obtained. An example of the results obtained is shown in Table 3.4. The results in the region R.A. 02-03 hours are typical of those obtained in areas away from the galactic plane, whilst the results in the region R.A. 18-19 hours include the most intense region of the galactic plane, with the steepest gradients.

These values are to be compared with the mean intersection errors obtained from the baselevel optimisation process (see Figure 2.3). The intersection errors are a measure of the consistency of the two surveys before the scan points were added into the maps, whilst the values shown in Table 3.4 represent the differences between the final maps. The values obtained should be approximately equal, as, on the average, only one scan point was added into each map point, the scans being at approximately half beamwidth intervals. The slightly smaller differences at high declinations are due to the fact that the maps are better sampled in this region.

A measure of the errors in the temperatures of the final maps may be obtained from this analysis. If the standard deviation of the differences of two maps is σ, then the standard deviation of temperatures in each map

TABLE 3.4

	Declination					
R.A.	-5°	$+5^{\circ}$	$+15^{\circ}$	$+25^{\circ}$	$+35^{\circ}$	$+45^{\circ}$
12 30	2.0 3.2	1.8 2.6	2.1 7.4	1.6 2.0	1.6 2.0	1.7 2.2
13 30	1.7 2.3	1.8 3.2	1.7 2.6	1.6 2.2	1.5 1.9	1.5 2.0
16 30	1.5 2.0	1.5 2.1	1.4 1.8	1.3 1.6	1.2 1.6	1.3 1.7
17 30	1.7 2.2	1.6 2.3	1.5 1.9	1.4 1.8	1.3 1.8	1.4 1.8
18 30	3.5 6.3	2.5 6.1	1.6 2.6	1.3 1.7	1.3 1.7	1.2 1.6
02 30	1.4 1.8	1.3 1.7	1.3 1.7	1.3 1.6	1.3 1.6	1.2 1.6

For each map two values are given. The top figure is the mean of the moduli point by point differences of the upscan map and the downscan map. The bottom figure is the R.M.S. of these differences. Each map is specified by the coordinates of its centre. The map centred at (12 30, $+15^{\circ}$) is seen to have a relatively large R.M.S. value. This is due to the radio source Virgo A.

is $\sigma/\sqrt{2}$. When the two maps are added together, a further improvement to $\sigma/2$ is obtained. This leads to a value of approximately 1 K for the standard deviation of temperature errors in the survey maps.

These errors are most likely to have been caused by:-

1. Receiver noise. The fluctuations due to receiver noise, in the final maps, had a standard deviation of approximately 0.2 K.
2. Receiver gain variations. As the receiver operated, in general, a long way from balance, any deviations in the receiver gain from the straight line approximation (over onescan) would lead to errors in the calculated temperatures. In the colder regions, a 1% error in gain would lead to a 2 K error in the temperature. Measurements on the tabular scans indicated that the gain was generally constant over a scan to better than 1%. Nevertheless, this effect is an important one, and may explain a large part of the errors found.

3. Low level interference. An exhaustive editing process was carried out in an attempt to remove the effects of interference from the final maps. However, the possibility that very low level interference remains must not be overlooked.

4. Variations in ambient temperature. Because of the approximately 1 dB cable loss from antenna to receiver, a change in the ambient temperature would produce a similar change in antenna temperature, down by a factor of 0.2.

3.5 The Antenna Beam

An investigation was made of the telescope beam pattern by making a series of drift scans through the radio source Cassiopeia A at a number of different azimuths. Three of these scans are shown in Figure 3.2. This gave cuts through the telescope beam at various angles to the elevation axis. The main beam of the telescope was found to be a good approximation to a circular gaussian of half width 37 arc minutes. This is

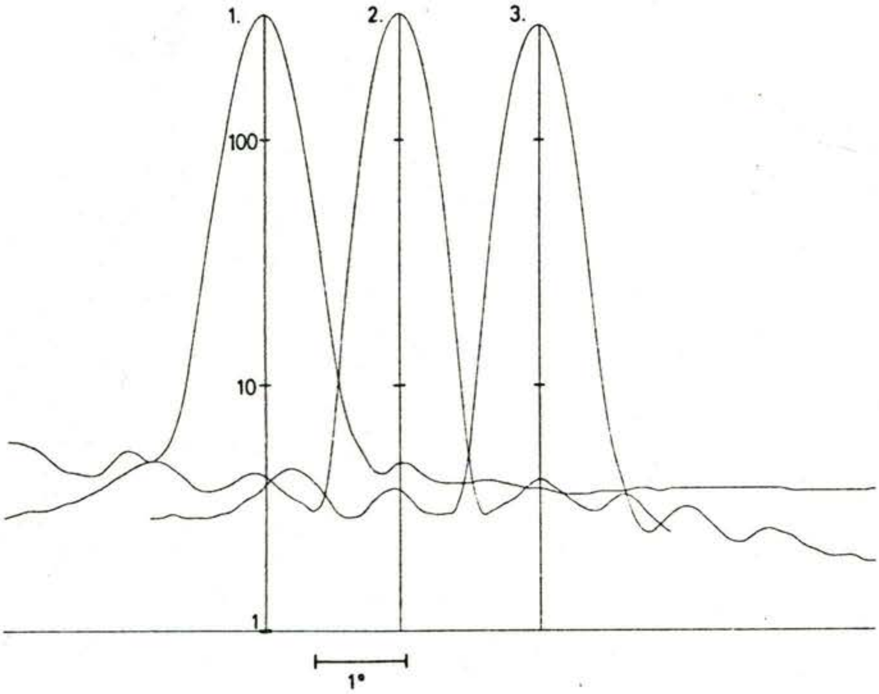

FIGURE 3.2

Three drift scans through CAS A at different azimuths. Scans 1.,2., and 3. cut the beam at angles of 40°,0°, and 90° respectively to the elevation plane. The large sidelobe, 2.7° to the left of beam centre in all three scans, is in fact the radio source CTB 109.

somewhat wider than the theoretically attainable value for a 100 M diameter of 31 arc minutes, due to the fact that the dish was somewhat underilluminated by the feed. This in turn led to a low sidelobe level, and good rejection to interference, which are important features in a survey such as this, where absolute maximum resolution is not of prime importance.

Unfortunately it was not possible, with the time available, to make an accurate map of the sidelobe distribution of the antenna beam. However, some conclusions as to the sidelobe pattern may be drawn from the final survey map, and the drift scans mentioned above. A sidelobe pattern can be seen around the source Cygnus A, at (R.A., dec.); (19 57, +40.5°), although parts of it merge into the nearby Cygnus X region. The main features revealed are narrow sidelobes in planes parallel and perpendicular to the elevation plane and extending out to approximately 6° from beam centre. In addition, there appears to be a ring of sidelobes at a radius of 2.5° from beam centre. These features can also be seen on the three drift scans shown in Figure 3.2, and appear symmetrically placed around the beam centre. Small scale structure closer in to the main beam on the Cygnus A map is due to the SIN X/X convolving function used. The first sidelobes appear at a level of approximately 25 dB down from the maximum, the second at approximately -28 dB. The ring of sidelobes appears from the map to be at a varying level, but always below -28 dB. There is no other structure apparent above the -30 dB level. This low sidelobe level is consistent with the broadening of the beam due to underillumination of the dish. The effects of sidelobes are not apparent in any other survey map. In particular, around the source Virgo A, there is only slight evidence of sidelobes and only in the elevation plane. The expected peak brightness temperature of Virgo A is approximately 750 K, so that any sidelobes whose level is higher than -25 dB should be visible.

The negative sidelobes which appear close to some of the stronger point sources (e.g. around Hercules A at (16 48, $+05^{\circ}$) and 3C 353 at (17 18, -1°) are due to the fact that the SIN X/X convolving function used in the analysis was truncated at the sixth zero.

3.6 Positional Accuracy of Survey

A measure of the positional accuracy of the survey was obtained by comparing the measured positions of certain small diameter radio sources with the accurately determined positions of Adgie and Gent (1966).

Sources which gave a 408 MHz brightness temperature deflection greater than 10 K were chosen from the list of Adgie and Gent. For each of these sources, an area 4° square, centred on the nominal position, was taken from the survey maps. A baselevel was then subtracted from this area. This baselevel was in the general form of a sloping plane, determined from three of the corners of the area. This method was found to give good results for sources which, in general, were in regions where background variations were small compared to the source height. A two dimensional Gaussian fit was then made to the area, the results being displayed in the form of absolute position in R.A., dec., and source height in brightness temperature. The results of this procedure, for all sources, are shown in Table 3.5. The fluxes are taken from Horton et al. (1969).

The mean positional errors of the survey have been calculated from the values shown in Table 3.5. The flux of a source was used as a weight of the offsets found for the source. The results, given as survey position minus nominal position, are:-

TABLE 3.5

3C	R.A.$_o$	δ_o	$\alpha - \alpha_o$	$\delta - \delta_o$	Flux (400 MHz)
48	01 35	+33	- 3 s	0'	34.0
63	02 18	-02	- 7 s	0'	11.4
65	02 21	+39	-34 s	0'	11.6
71	02 40	-00	+11 s	+0.5'	10.4
78	03 06	+04	- 9 s	-1'	13.1
CTA21	03 16	+16	- 6 s	-1.5'	8.9
273	12 27	+02	+ 4 s	-1.5'	54.2
279	12 54	-05	- 7 s	+2'	13.8
286	13 29	+31	-11 s	+1.5'	22.6
287	13 28	+25	- 2 s	-2.5'	12.8
298	14 17	+07	- 7 s	+0.5'	22.5
317	15 14	+07	- 5 s	-0.5'	22.4
338	16 27	+40	0 s	-0.5'	18.9
388	18 43	+46	-12 s	+0.5'	14.4
409	20 12	+23	- 3 s	+0.5'	43.6
410	20 18	+29	- 2 s	+0.5'	22.4
433	21 21	+25	-12 s	0'	31.6
438	21 54	+38	+ 1 s	0'	22.9
459	23 14	+04	- 9 s	-0.5'	13.5

Right Ascension: -4 secs. ± 6 secs. (collimation error)

Declination: 0.0' ± 1.0'

Any positional errors in the survey are, therefore, very small compared to the 37 arc minute beamwidth.

3.7 The Calibrated Survey Maps

The complete calibrated survey maps are presented in Appendix 3, in the form of contour maps in equatorial coordinates, Epoch 1950.0. The maps are drawn in blocks of 2 hours right ascension by 20° declination, and are each formed from four of the basic map blocks as stored on magnetic tape.

In certain low level areas of the map, and particularly at low declinations, structure parallel to the scan direction may be due to a badly determined baselevel for a particular scan, and should not be trusted. An example is the region around (14 05, $+01^{\circ}$).

Appendix 3 also contains a number of maps in galactic coordinates. These were produced from the R.A., dec. maps by use of the RETABULATE facility of the NOD2 compiler (Haslam (1974)).

The quantity represented in the contour maps is the absolute full beam brightness temperature, as determined by the methods described above.

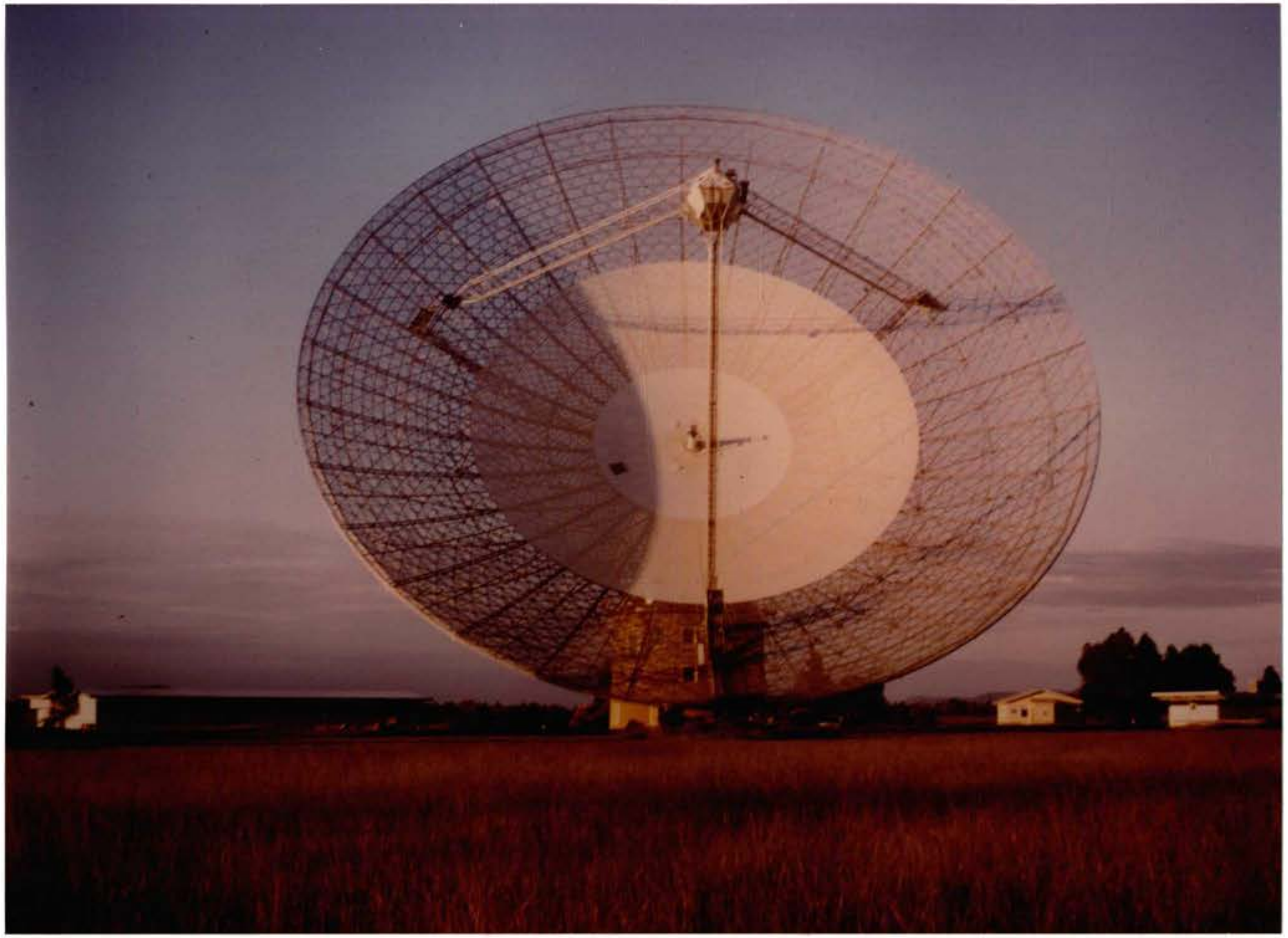

The 64 M Radiotelescope of the CSIRO at Parkes, N.S.W., Australia

CHAPTER 4

408 MHZ SOUTHERN SKY SURVEY

4.1 Introduction

This chapter describes the third stage in the proposed All Sky 408 MHz Survey. This stage comprises of a survey of the Southern Sky, using the C.S.I.R.O. Division of Radiophysics 64 meter radiotelescope at the A.N.R.A.O., Parkes, Australia. The equipment and data collecting facilities, as well as the first observations and results are described. At the time of writing, observations are continuing to complete coverage of the whole sky visible with the Parkes radiotelescope.

It was initially intended to transfer all equipment and techniques used in the Bonn 408 MHz Survey directly to Parkes. This, in fact was done, but in the process a number of fundamental changes and improvements were made to the Bonn System.

The major change to the equipment was the addition of a third channel to the receiver, thereby allowing polarisation information to be collected. Also, it was possible at Parkes to complete a large part of the data reduction on-line, thereby significantly reducing the time required for off-line reduction of the survey.

4.2 The Southern Sky Survey

A survey of the southern sky with a resolution of the order of one degree has long been required to complement the existing surveys of the northern sky. Until now, the highest resolution accurate survey of the galactic background in the southern sky is the 85 MHz survey of Yates, Wielebinski and Landecker (1967), which has a resolution of 3.6°. Higher resolution surveys have either not been attempted, or not completed, because of the formidable problem of reducing the huge amount of data collected in such a survey. With the application of computer-aided reduction techniques it has been shown (Salter (1970), this thesis, chapt. 3) that such a project is feasible.

A large amount of telescope time is required to complete such a project, and to use this time efficiently, the maximum amount of information should be collected. For this reason it was decided to attempt the first combined total power - polarisation survey of the galactic background emission.

Previous galactic background polarisation surveys of the southern sky (Mathewson and Milne (1965), Mathewson, Broten and Cole (1966)) have measured the linear polarisation temperatures and polarisation angles of discrete points on an undersampled grid covering a large portion of the southern sky. Because of the lack of a total power survey of this region, no information is available on the percentage polarisation at these points. It is the aim of the present experiment to simultaneously measure the total power and linear polarisation components of the galactic background emission, in a fully sampled survey of the southern sky.

4.3 Measuring the Polarisation of Cosmic Radio Emission

The polarisation properties of a quasi-monochromatic, partially polarized electromagnetic wave are completely described by the four Stokes Parameters, I, Q, U, V.

These can be defined in terms of E_x and E_y, the transverse electric field in two orthogonal directions, and the phase difference between them, δ. Alternatively, they can be described in terms of E_r and E_l, the right- and left-handed circularly polarised components, and their phase difference, ε (Kraus, 1966).

$$I = \frac{<E_x^2>}{z} + \frac{<E_y^2>}{z} = \frac{<E_r^2>}{z} + \frac{<E_1^2>}{z} \qquad \ldots\ 4.1$$

$$Q = \frac{<E_x^2>}{z} - \frac{<E_x^2>}{z} = \frac{<2\,E_r\,E_1>}{z} \cos\varepsilon \qquad \ldots\ 4.2$$

$$U = \frac{<2\,E_x\,E_y>}{z} \cos\delta = \frac{<2\,E_r\,E_1>}{z} \sin\varepsilon \qquad \ldots\ 4.3$$

$$V = \frac{<2\,E_x\,E_y>}{z} \sin\delta = \frac{<E_r^2>}{z} - \frac{<E_1^2>}{z} \qquad \ldots\ 4.4$$

where z is the intrinsic impedance of the propagation medium.

The Stokes parameter I is the total intensity which is the sum of two orthogonal intensities, say I_0 and I_{90}. Q is then $I_0 - I_{90}$. It can be shown from a simple translation of axes that U is in fact equal to $I_{45} - I_{135}$. Q and U together completely describe the linear polarisation properties of the radiation, because for a linear polarisation intensity I_L at a polarisation angle, θ,

$$Q = I_0 - I_{90} = I_L \cos 2\theta \qquad \ldots\ 4.5$$

$$U = I_{45} - I_{135} = I_L \sin 2\theta \qquad \ldots\ 4.6$$

The Stokes parameter V is seen to describe the circular polarisation properties of the radiation.

It is well known, and can be seen from equations 4.1 - 4.4 that if two receivers are set up to measure either E_x and E_y or E_r and E_l, then the four Stokes parameters can be formed simultaneously from the two outputs of these receivers. Two of the parameters are obtained from the sum and difference of the power-detected outputs, the remaining parameters being formed from the in-phase and quadrature phase analogue correlation of the two receiver outputs.

The problem that arises in applying this method to large scale survey observations, is that the total power term, I, contains the receiver noise from both receivers, and is not measured relative to a fixed reference as in a Dicke switched receiver, or a correlation radiometer of the type described in Section 1.4. The power difference term (i.e. either Q or V) is also very sensitive to receiver noise variations. To overcome these difficulties the three channel receiver shown in Figure 4.1 was developed.

The receiver is seen to be the receiver of Section 1.4, with a third channel added. As in the Bonn 408 MHz Survey, and the Jodrell Bank 408 MHz Survey, the left-hand circularly polarised component of the celestial radiation is measured in relation to a fixed reference, by the use of a standard two channel correlation radio-

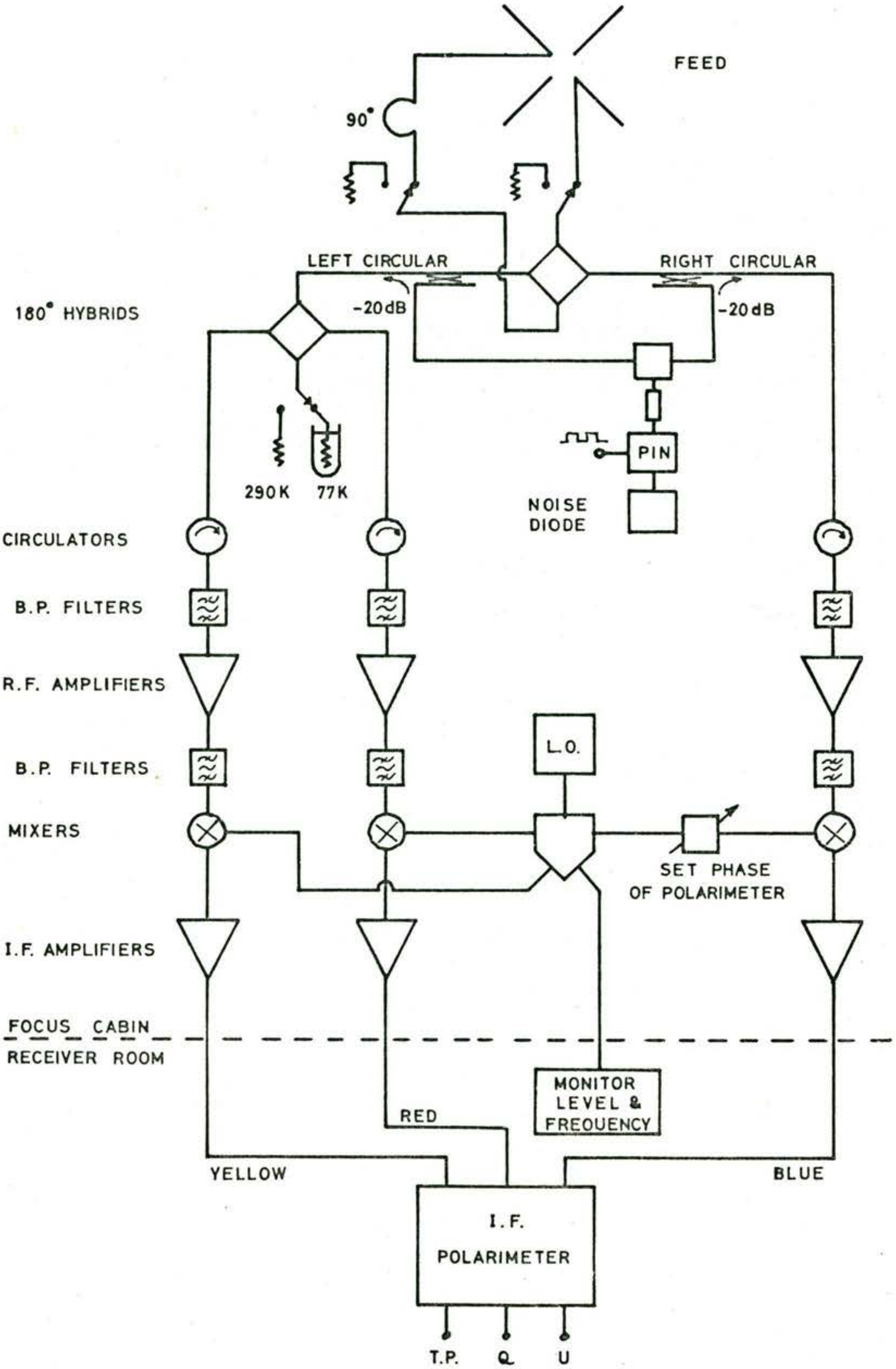
FEED
90°
LEFT CIRCULAR
RIGHT CIRCULAR
-20dB
-20dB
180° HYBRIDS
290K
77K
PIN
NOISE DIODE
CIRCULATORS
B.P. FILTERS
R.F. AMPLIFIERS
B.P. FILTERS
L.O.
MIXERS
SET PHASE OF POLARIMETER
I.F. AMPLIFIERS
FOCUS CABIN
RECEIVER ROOM
MONITOR LEVEL & FREQUENCY
RED
YELLOW
BLUE
I.F. POLARIMETER
T.P.
Q
U

FIGURE 4.1

meter. The third channel is used to receive the right-hand circularly polarised component. In-phase and quadrature phase correlations of one of the radiometer channels with the third channel produce outputs proportional to the Stokes Parameters Q and U, which describe the linear polarisation properties of the received radiation. The fact that all three outputs are formed from the correlation of the outputs of two different receivers assures that they are not sensitive to receiver noise variations.

By the use of this novel three channel receiver it has been possible to make simultaneous surveys of the total power and linear polarisation components of the galactic background radiation. The assumption made is that the Stokes Parameter, V, describing the circular polarisation properties, is zero. This assumption was also made in the Bonn and Jodrell Bank Surveys and seems justified in light of the fact that circular polarisation has not, as yet, been detected in the galactic background radiation.

4.4 Equipment

This section describes the details of the equipment used in the Southern Sky Survey.

4.4.1 Feed Antenna

Following the normal method used to feed the Parkes antenna at decimetre wavelengths, a "boxing ring" feed, similar to that used in Bonn, was constructed. Each dipole was constructed as shown in Figure 4.2. The length of the dipole, the height above the ground plane, and the length of the 70 ohm cable was adjusted to give an input impedance of 100 ohm (resistive). Each parallel pair of dipoles was then connected together in a T-piece, and the length and height of each dipole was trimmed to give a 50 ohm impedance at the T-piece. This was necessary to compensate for the mutual coupling of the four dipoles. Circular polarisation was then produced by use of a 180° hybrid and two 50 ohm coaxial cables whose lengths differed by a quarter wavelength.

4.4.2 Front-end

The front-end configuration of the receiver is shown in Figure 4.1. The components used were generally the same as those used in the Bonn receiver, however there

408 MHz DIPOLE

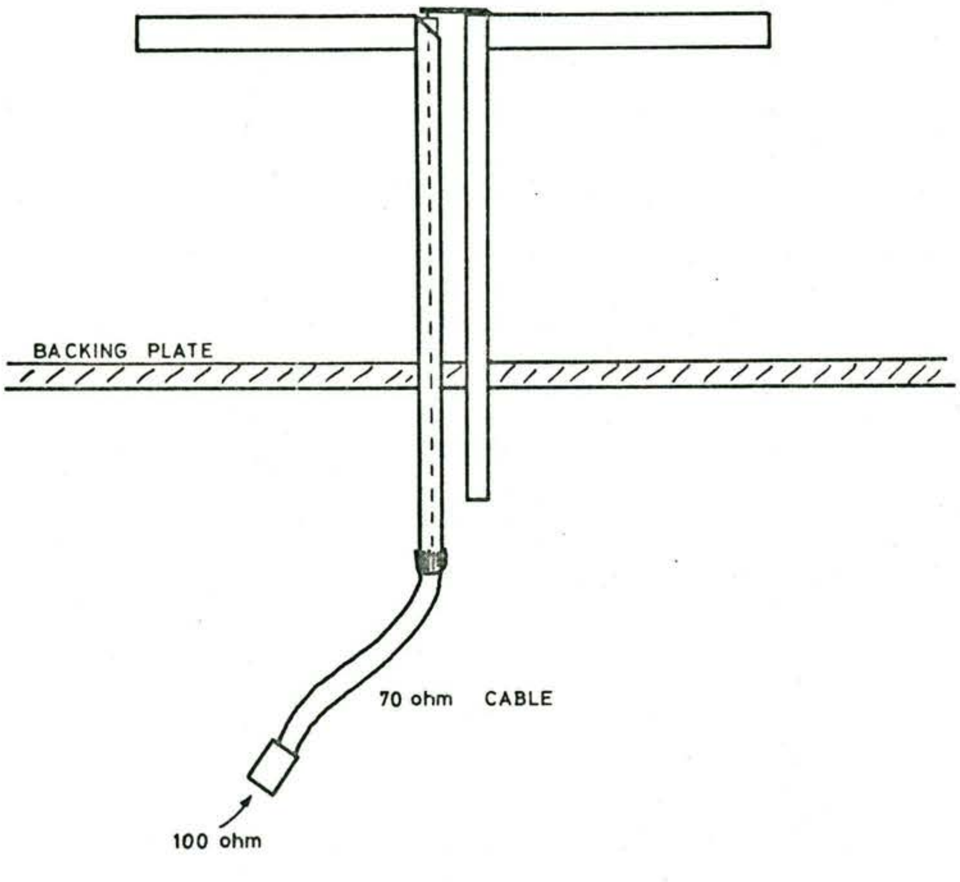

FIGURE 4.2

were some changes and additions which will be described in this section.

The two coaxial switches in the aerial lines were used to decouple the receiver from the antenna for stability tests and as a check on possible interference. Also, the fact that each pair of dipoles could be switched out independently, proved useful in comparing the two polarisations for equality and interference.

The switched calibration signal was added to both circular polarisation channels. The cables from the power divider to the directional couplers were cut so as to give an approximate 45° phase difference in the injected noise signals. This ensured that when the receiver was correctly phased, a calibration signal would appear on both polarimeter outputs, as well as in the radiometer output.

The reference termination used in the survey was a 50 ohm termination immersed in liquid nitrogen, hence giving a reference temperature of the order of 80 $^{\circ}$K. For purposes of testing, a coaxial switch in the reference line was used to allow the substitution of a room temperature reference. These coaxial switches were remotely controlled from the observers room.

The original Bonn R.F. filters were replaced by three two-element coaxial cavity filters having a 3 dB bandwidth of approximately 25 MHz and a loss of 0.2 dB. As the interference problem at Parkes was not as serious as in Bonn, the wider bandwidth could be tolerated. In addition, three R.F. filters fabricated in stripline technique were placed after the low noise amplifiers. These filters had a 20 MHz bandwidth and a loss of approximately 2 dB. These filters ensure that the noise produced by the R.F. amplifiers at the image frequency, is removed. This should lead to an improvement of the noise temperature of the receiver of the order of 3 dB, depending on the input impedance seen by the amplifiers at the image frequencies. The example shown in Figure 4.3 illustrates the improvement in noise figure achieved by the use of these filters. The relatively high loss of the filters is not important, following, as they do, the 30 dB gain R.F. amplifiers.

Local oscillator signal was distributed through a four way power divider, thereby allowing a continuous remote monitor to be kept on the local oscillator frequency and power level. A coaxial line stretcher in the L.O. line to the third channel was used to set up and retain the correct phase relationship between the polarimeter channels. A photograph of the receiver package is shown in Figure 4.4.

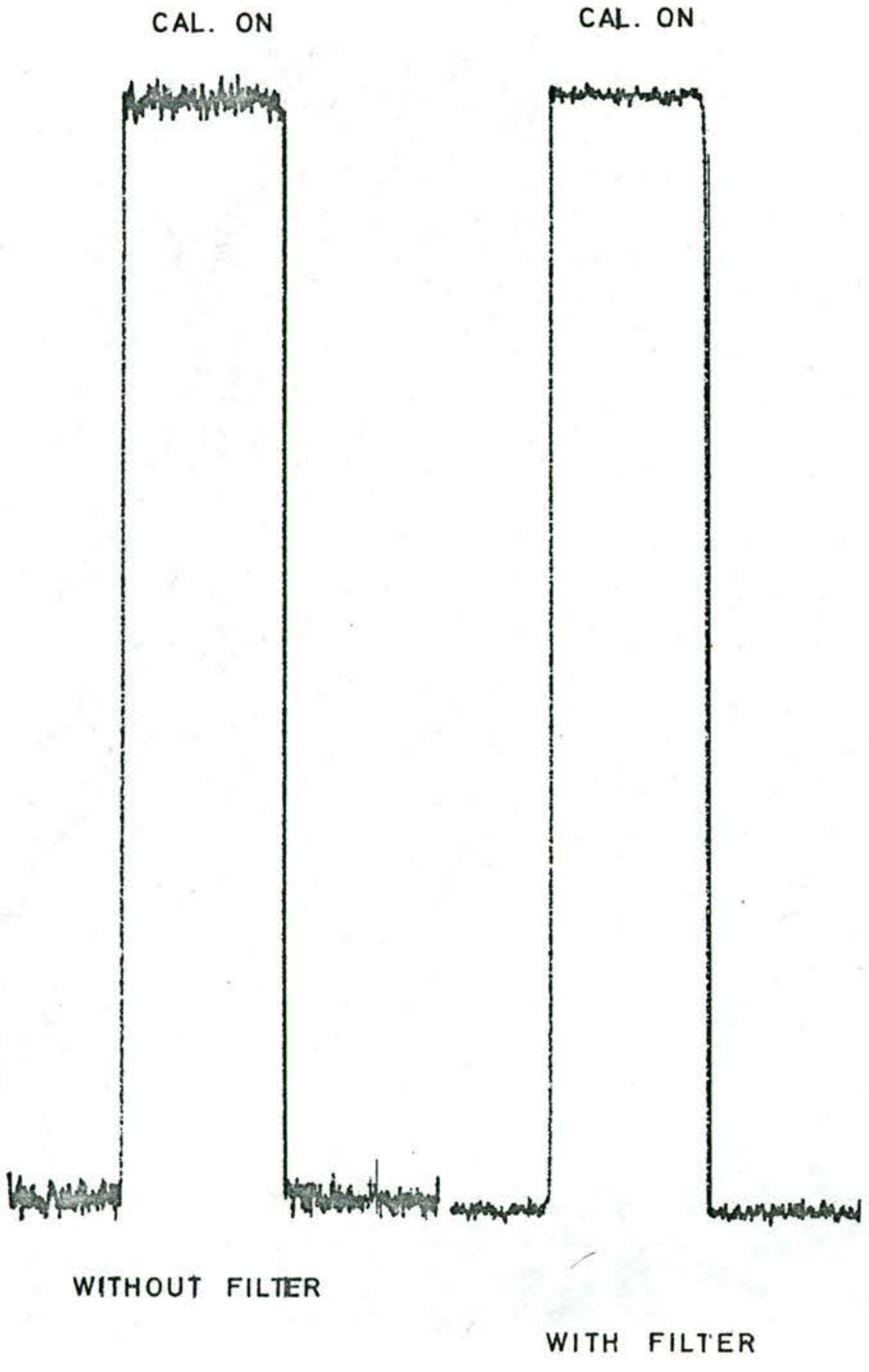

FIGURE 4.3

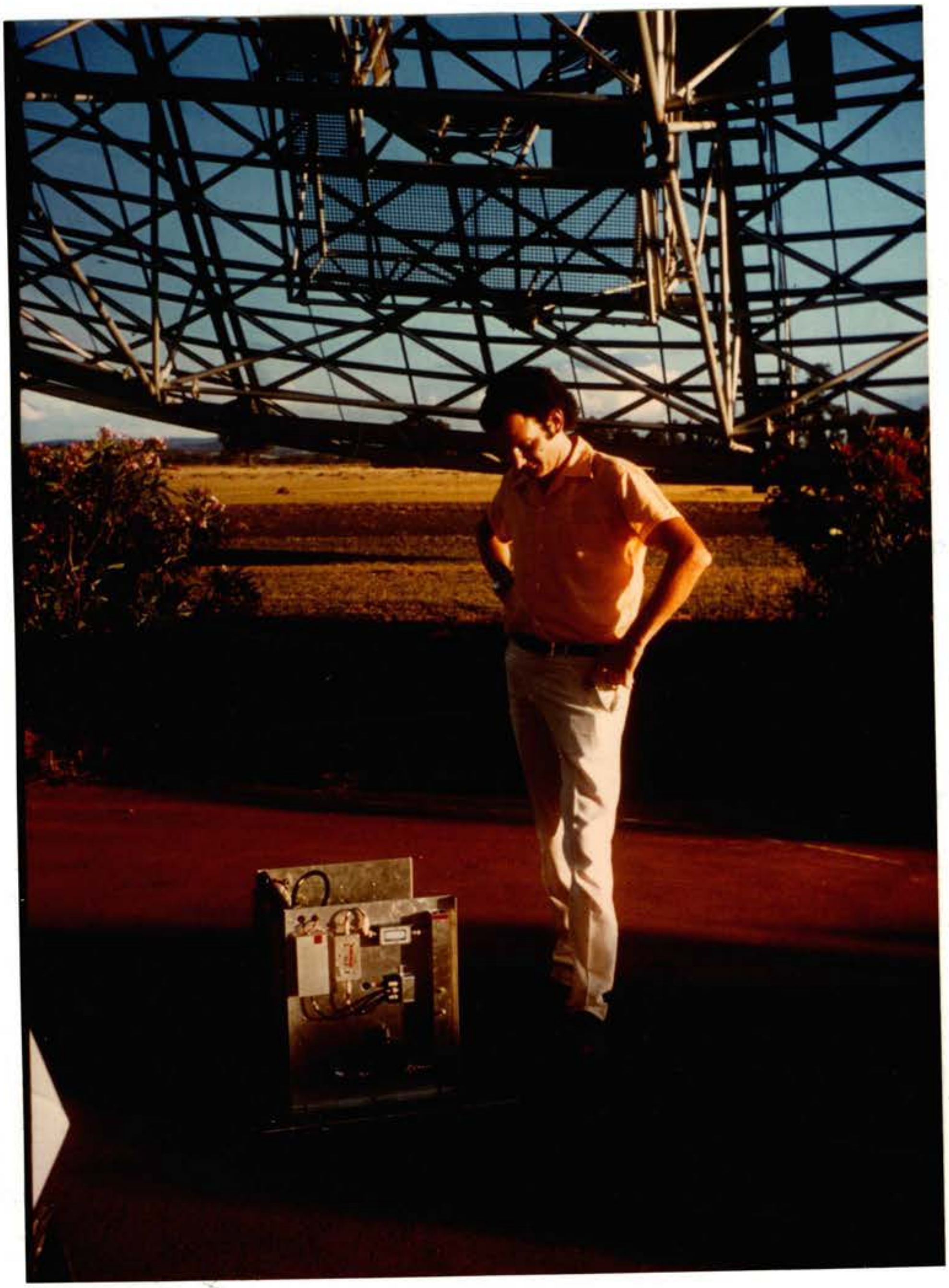

FIGURE 4.4

4.4.3 Intermediate Frequency Polarimeter

The three intermediate frequency signals from the receivers were carried from the focus cabin to the observers room on three identical low loss cables. Each signal then passed through an I.F. filter, with a 3.5 MHz, 3dB bandwidth at 30 MHz, before entering the I.F. Polarimeter. These filters were used to define the overall system bandpass.

The I.F. Polarimeter was required to produce the three outputs, total power, Q and U, from the three I.F. inputs. A circuit diagram of the polarimeter is shown in Figure 4.5.

The three input signals first pass through variable attenuators and wideband, 50 dB gain I.F. amplifiers. A portion of the signal is coupled off into high input impedance detectors whose outputs are connected to front panel meters. The attenuators, which are variable in 1 dB steps from 0 - 60 dB, can then be used to set the required I.F. levels.

The RED channel (see Figure 4.1), which is the common channel to all three outputs, then passes through a 180° phase switch. This ensures that all three output multipliers operate in the phase switched mode.

I.F. POLARIMETER

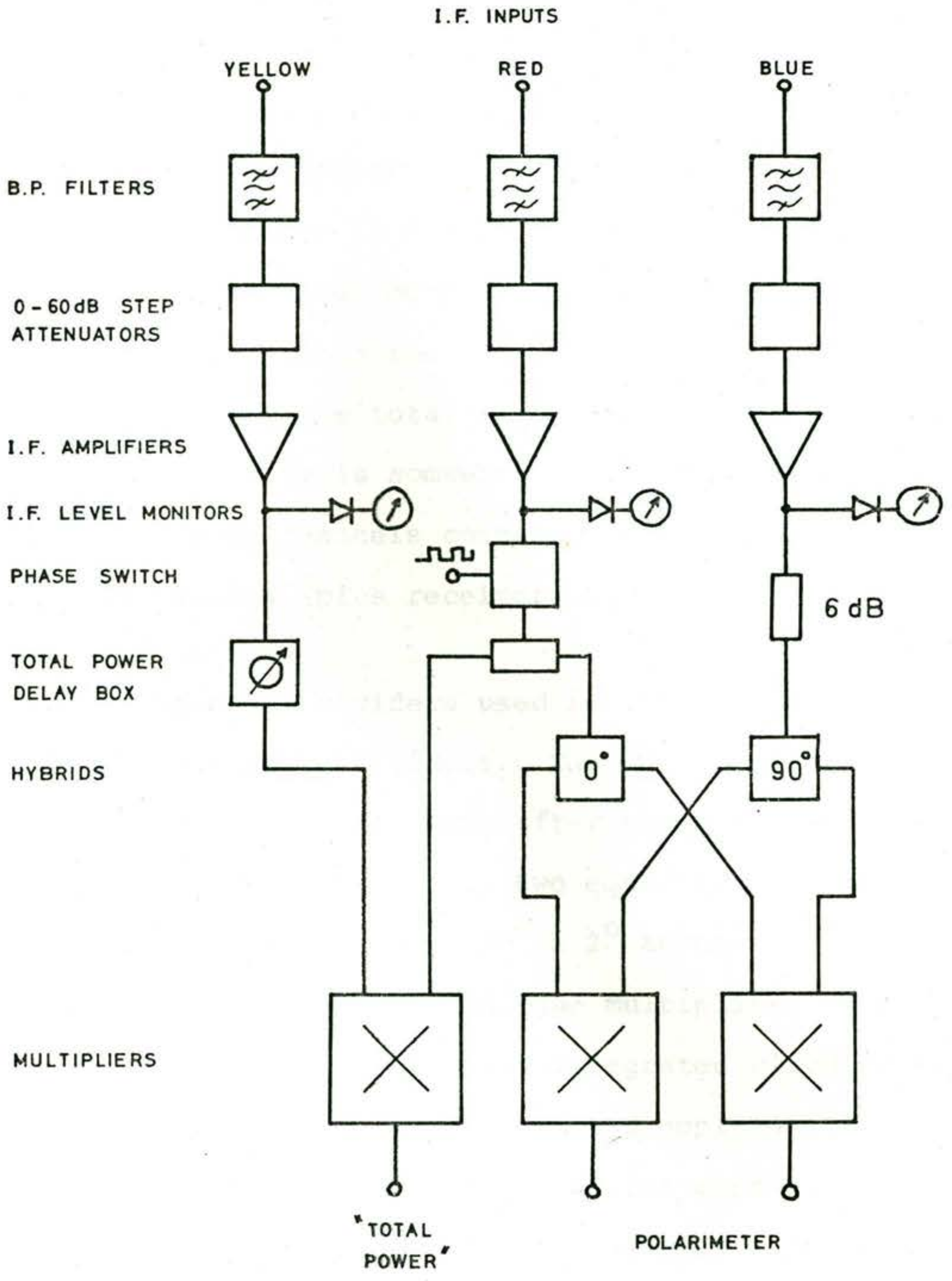

FIGURE 4.5

The total power (radiometer) output is then formed from the in-phase correlation of the YELLOW and RED channels. The outputs representing the Stokes parameters Q and U are formed from the in-phase and quadrature-phase correlation of the RED and BLUE channels. Contributions from the reference termination are present only in one of these channels and therefore form no correlated output. However, because the required signal in the RED channel is a smaller percentage of the total signal in this channel, the signal to noise is somewhat smaller than would be the case if both channels contained only the circular polarisations (plus receiver noise).

The power dividers used in the polarimeter were simple resistive dividers. The 90° power splitter was a quadrature hybrid, made after the design of Fisher (1973). This device gave two equal (± 0.1 dB) outputs whose phase differed by $90^{\circ} \pm 2^{\circ}$ across an 8 MHz bandwidth at 30 MHz. The analogue multipliers were constructed from commerical integrated circuits (LM 1496). By operating at a low current and applying delay compensation to one input, a useful bandwidth of over 200 MHz was obtained with this circuit. The dynamic range of the multipliers, when operated in the phase switched mode, with two correlated noise signals as inputs, was approximately 40 dB.

4.5 Receiver Alignment

The output of an analogue multiplier of the type used in the receiver is given by

$$V = \overline{\nu_1 \cdot \nu_2}$$

$$= (\overline{\nu_{c1}^2} \cdot \overline{\nu_{c2}^2})^{\frac{1}{2}} \cdot \cos \Theta \qquad \ldots 4.7$$

where $\nu_1(t)$ and $\nu_2(t)$ are the input voltages containing components from the same origin, $\nu_{c1}(t)$ and $\nu_{c2}(t)$, whose phase difference at the input to the multiplier is Θ. The averaging is over a time interval determined by the output bandwidth of the multiplier. Components of $\nu_1(t)$ and $\nu_2(t)$ which are not from a common origin produce multiplication products whose average values are zero. Equation 4.7 can be easily shown to hold for monochromatic sinusoidal voltages $\nu_1(t)$ and $\nu_2(t)$. For the present case, where the inputs are band-limited noise voltages, the output becomes an average over all frequencies in the band.

For the radiometer channel, it is required that maximum correlated output is obtained, to maintain maximum signal to noise ratio. This can only be achieved if $\cos\left[\Theta(\omega)\right] = 1$ for all frequencies in the band, which is only possible if the delay through each radiometer R.F./I.F. channel is the same.

The polarimeter produces outputs proportional to the average values over all frequencies in the band of the quantities $\cos\left[\phi + \delta_1(\omega)\right]$ and $\sin\left[\phi + \delta_2(\omega) + \varepsilon(\omega)\right]$, when ϕ is the average phase difference between the received signals and $\delta_i(\omega)$ is the differential phase shift through the two R.F./I.F. paths to the inputs of a multiplier. $\varepsilon(\omega)$ is a term representing errors in the 90° phase shifting network. From these outputs, it is required to calculate the value of ϕ, which is directly related to the average polarisation angle of the linear polarisation component of the received signals. As these outputs are intended to provide direct measurement of the Stokes parameters Q and U, it is required that $\delta_1(\omega) = \delta_2(\omega)$ and $\varepsilon(\omega) = 0$. Also, although it is not essential, it is desirable that $\delta_1(\omega)$ and $\delta_2(\omega)$ are constant with frequency. If this were not the case, but instead $\delta_i(\omega)$ varied linearly with frequency across the band, both outputs would be reduced by a factor $(\sin(KF/2)/(KF/2))$, where K is the differential delay (in degrees/Hz) and F is the bandwidth (in Hz). For the small bandwidths used in this receiver, a very large differential delay is required before this effect becomes important. More important is that if narrow band measurements of the polarisation angle are made at different frequencies in the band, a differential delay will give rise to a frequency dependent offset. To overcome this effect, the delay in all R.F./I.F. paths from antenna to the two polarimeter multipliers must be equal.

It is, therefore, seen that the successful operation of such a receiver relies heavily on the phase tracking of components used in the different channels. For this reason each channel was constructed from identical components which had previously been adjusted to give both amplitude and phase tracking across the full useful bandwidth.

The differential delay at the inputs to the three multipliers was then set to zero by the addition of delay compensation cables in all three channels. The need for such compensation can be seen by the fact that, for example, the RED channel passes through a phase switch and two resistive power dividers to the polarimeter multipliers, whereas the BLUE channel passes through a 90° hybrid. The delay (i.e. path length) through these two paths will not be equal, but can be compensated for by a length of cable. In general compensating for delay differences also sets the phase difference to zero. However, this does not apply to the hybrid used in the polarimeter. The input is not only delayed by an equal amount to the two outputs, but it is also phase shifted by approximately 22° to one output and 112° to the other output. This is a true phase shift, remaining constant with frequency. The phase difference between the two outputs remains at 90° across the band, as required. The result of this property of the hybrid is that the polarimeter, when used to measure the phase difference of the two input signals, has a constant zero offset of 22°. Input signals with a phase difference ϕ° will give polarimeter outputs consistent with two signals with a phase difference of $(\phi + 22)^{\circ}$. However, as this term is constant, it can be either corrected for or calibrated out.

An example of the phase and amplitude tracking achieved with the receiver is shown in Figure 4.6. The measurements were made with a Hewlett-Packard Model 8407A Network Analyser. Signal was injected into the frontend hybrid and the phase and amplitude differences between the inputs to each polarimeter multiplier were measured. Also shown is the effect of switching the $0^{\circ}/180^{\circ}$ phase switch. For these measurements the I.F. filters were removed, so the full 8 MHz bandwidth is shown. Only the middle 3.5 MHz were used in the observations. The measurements show that across the observation bandwidth the phase difference was constant to within 1°. The error in the phase switch was of the order of 1°.

PHASE AND AMPLITUDE DIFFERENCES OF INPUTS TO MULTIPLIERS

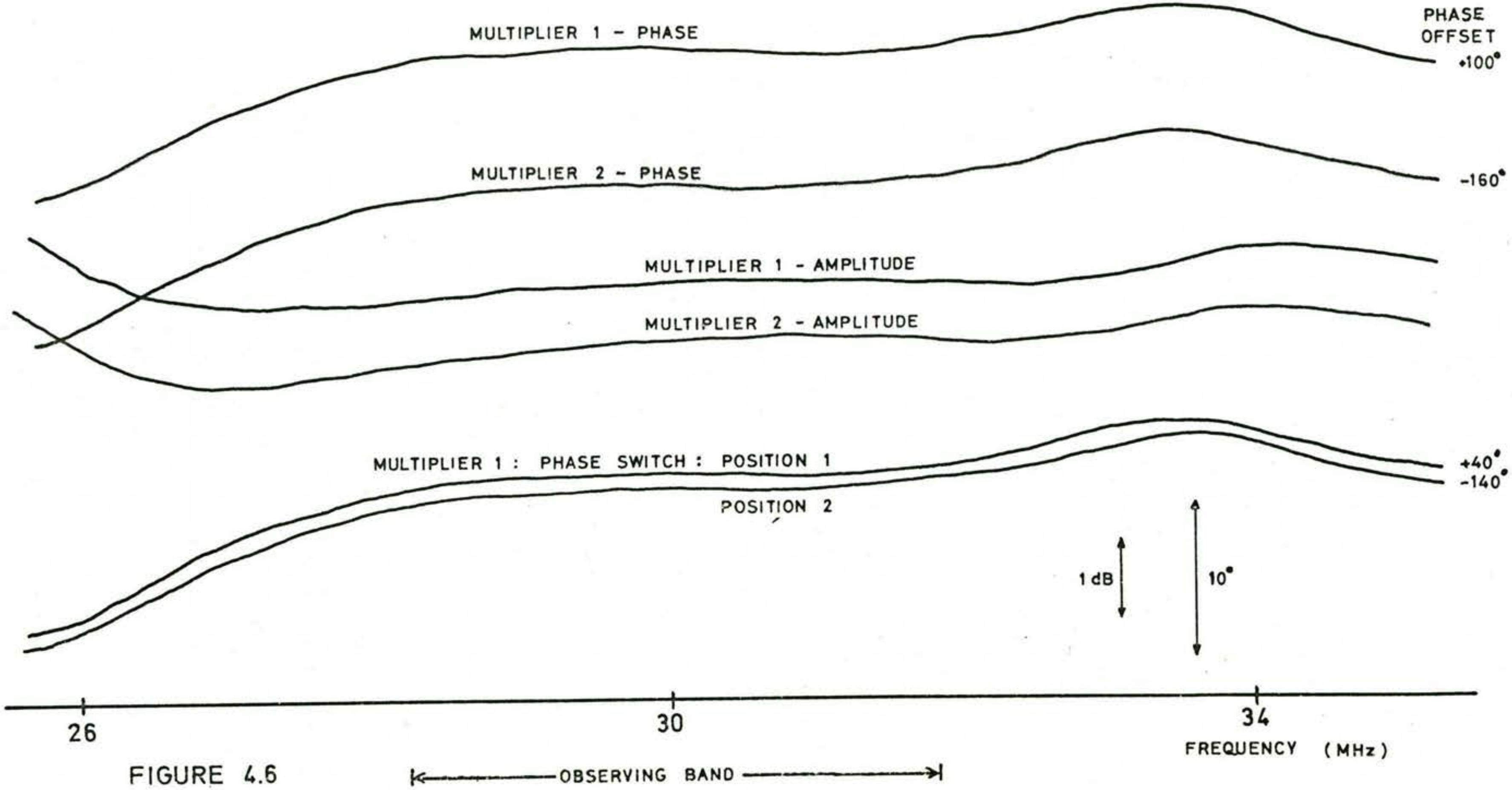

FIGURE 4.6

Figure 4.7 shows theoverall receiver bandpass of all three channels. Figure 4.8 shows the two polarimeter multiplier outputs corresponding to the inputs shown in Figure 4.6. In this case the local oscillator phase shifter was used to set one output to zero at the midband. Once again, the action of the $0^o/180^o$ phase switch is shown.

4.6 Observations

The observations described in this section form only the first part of the proposed all sky survey. They were completed in the period 24. 1. 1974 to 2. 2. 1974. Once again the nodding scan technique was used. The scan limits were from zenith angle 2^o to 57^o, with azimuth in the south. The latitude at Parkes is -33^o so that the scan limits in declination were from -35^o to -90^o. With a scanning speed of 6^o/minute, each scan lasted 9 min 10 sec. The interval of right ascension between adjacent upscans (or downscans) was chosen to be 3 minutes, so that at declination -35^o, the scans are approximately 36' arc apart, and below -63^o are closer than 20' arc. This means that below about -60^o declination, a fully sampled survey is produced of the right ascensions covered. The region above -60^o declination

RECEIVER BANDPASSES

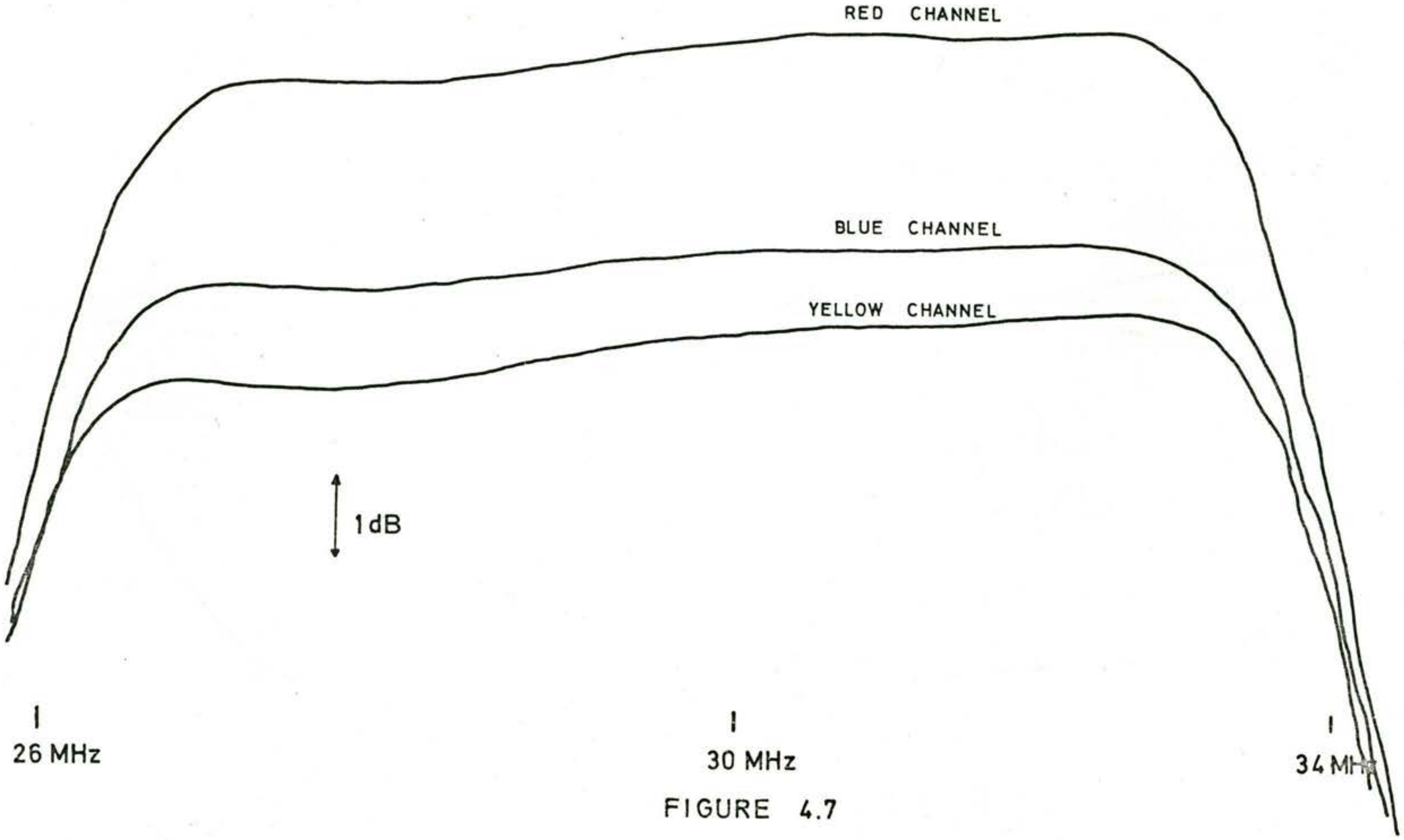

FIGURE 4.7

POLARIMETER MULTIPLIER OUTPUTS

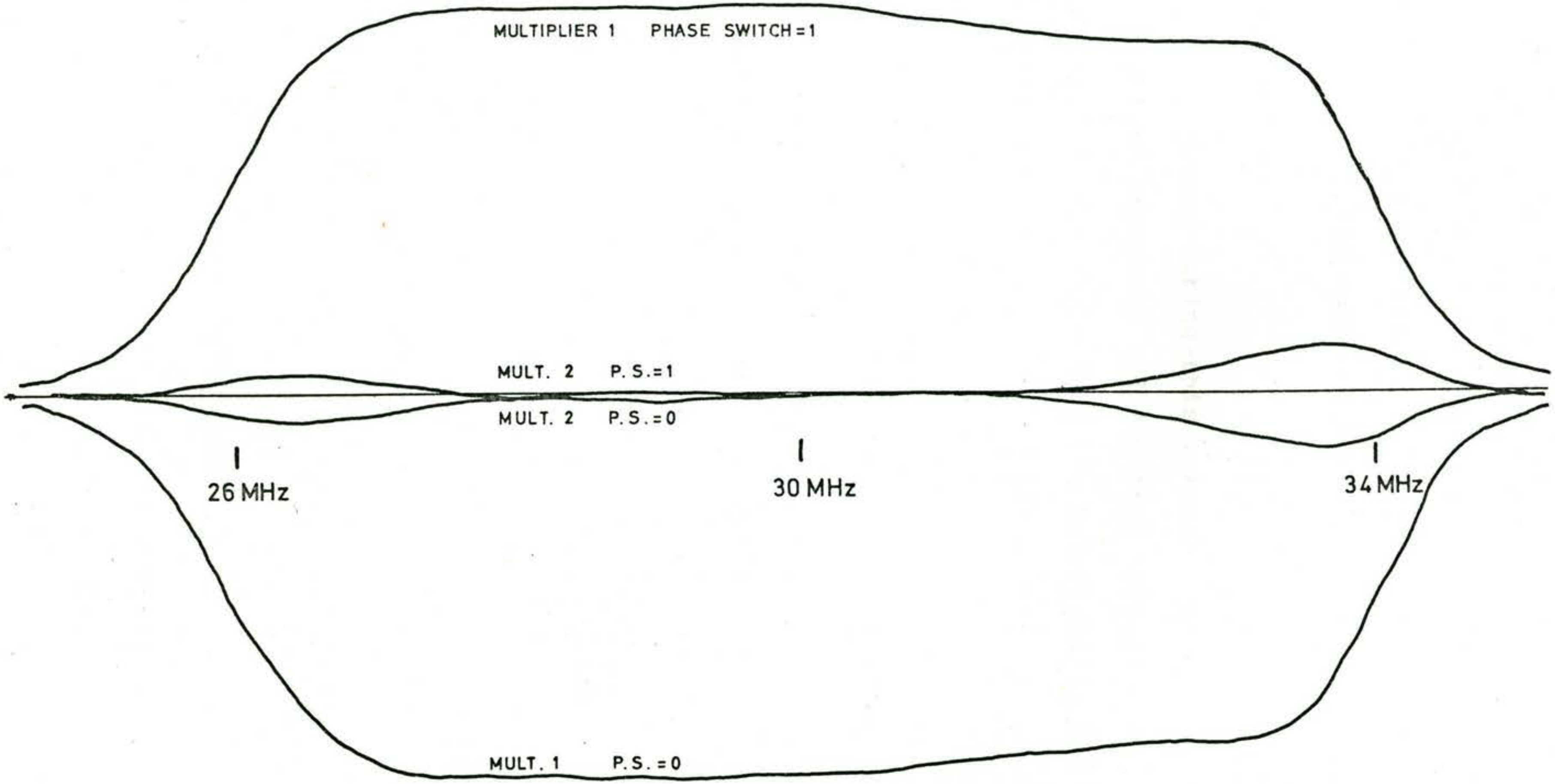

FIGURE 4.8

was not fully sampled in this first observing session, but has been completed in later sessions. Right ascensions in the range 22 00 through 00 00 to 15 00 were covered.

On each day during this session, observations began in the late afternoon and finished around 0900 the next morning. It is likely that the polarisation information collected before sunset and after sunrise will not be useable due to the large change in Faraday rotation in the ionosphere as the sun rises and sets. Each afternoon, before observations began, the delay and phase shift through each receiver to the polarimeter were equalised. One of the aerials was disconnected from the circularising hybrid and replaced by a swept R.F. signal source. The delay and phase was then adjusted to give zero output from the "SINE" correlator. After the initial setting up of the receiver, the required delay compensation remained fixed throughout the session. Only very small adjustments in phase were necessary.

4.7 On-line Computer Analysis

Experience gained during the reduction of the Bonn 408 MHz survey, showed that a great deal of time could be saved if as much as possible of the initial data reduction could be done on-line. In the Bonn survey, information was collected at the maximum possible rate, thereby allowing data that had been affected by various forms of interference, to be "cleared up" to the extent that it could be used in the later stages of reduction. In practise, the amount of data saved by this technique was minimal, and did not justify both the devotion of the large data storage area required to hold all this information and the off-line computer time required to reduce the data to the redundancy limit. For this reason, it was decided that for the Southern Sky Survey the first stage of the reduction should be done on-line. The availability of a PDP-9 computer at Parkes made this step possible.

It was envisaged that the same basic techniques would be used in the analysis of the Parkes survey as were used for the Bonn survey. That is, each nodding scan would be formed into a tabular scan and then these tabular scans would be added into the final maps. The first step of this process, the formation of tabular scans, reduces the data close to the redundancy limit.

The amount of on-line reduction possible depends only on the incoming information rate, and the amount of fast access storage available. A feasibility study showed that with the facilities available and with a telescope driving speed of 6°/minute, a tabular scan of length 60° could be produced directly from the incoming data. This array could be kept in memory until the end of the scan at which time a limited amount of processing could be done on it before it was written onto some form of mass storage. A description of the methods used in this analysis now follows.

4.7.1 Data Collection

All three outputs of the I.F. polarimeter are, in general, square waves, with a switching rate equal to that of the I.F. phase switch. This was set at 16 msec, so that a complete cycle of four phases lasts 64 msec. The calibration signal was switched on for half a cycle. The state of the receiver in any one phase was the same for all three outputs (see Section 1.6). The signals were fed from the polarimeter output, through voltage to frequency converters to a three channel "digital back-end" (Zinz and Haslam (1972)). This device counts each signal for one switch phase, at the end of which it transfers the result to a buffer and resets the counter for the next switch phase. The contents of the three buffers were then available as parallel 16 bit words which could be connected directly to the three input registers of the PDP-9 computer. As only 14 bits of each word were used, the top two bits of the first word could be used to transmit information on the state of the two switching waveforms being sent out to the receiver. Hence, in any one phase, the state of the receiver could be determined in the computer.

4.7.2 On-line Computer Program

The flow diagram of the on-line computer program is shown in Figure 4.9. The program makes use of the multi levelled interrupt capability of the PDP-9 computer, working in the Automatic Priority Interrupt mode. There are two basic types of interrupt in this mode, one being a hardware initiated interrupt, the other, a software initiated interrupt.

The program is controlled from an active field (AFIELD) array. Most of the subroutines in the program are controlled by parameters contained in this active field. These are set, on entry, to default values, which can be changed, at will, from the teletype input.

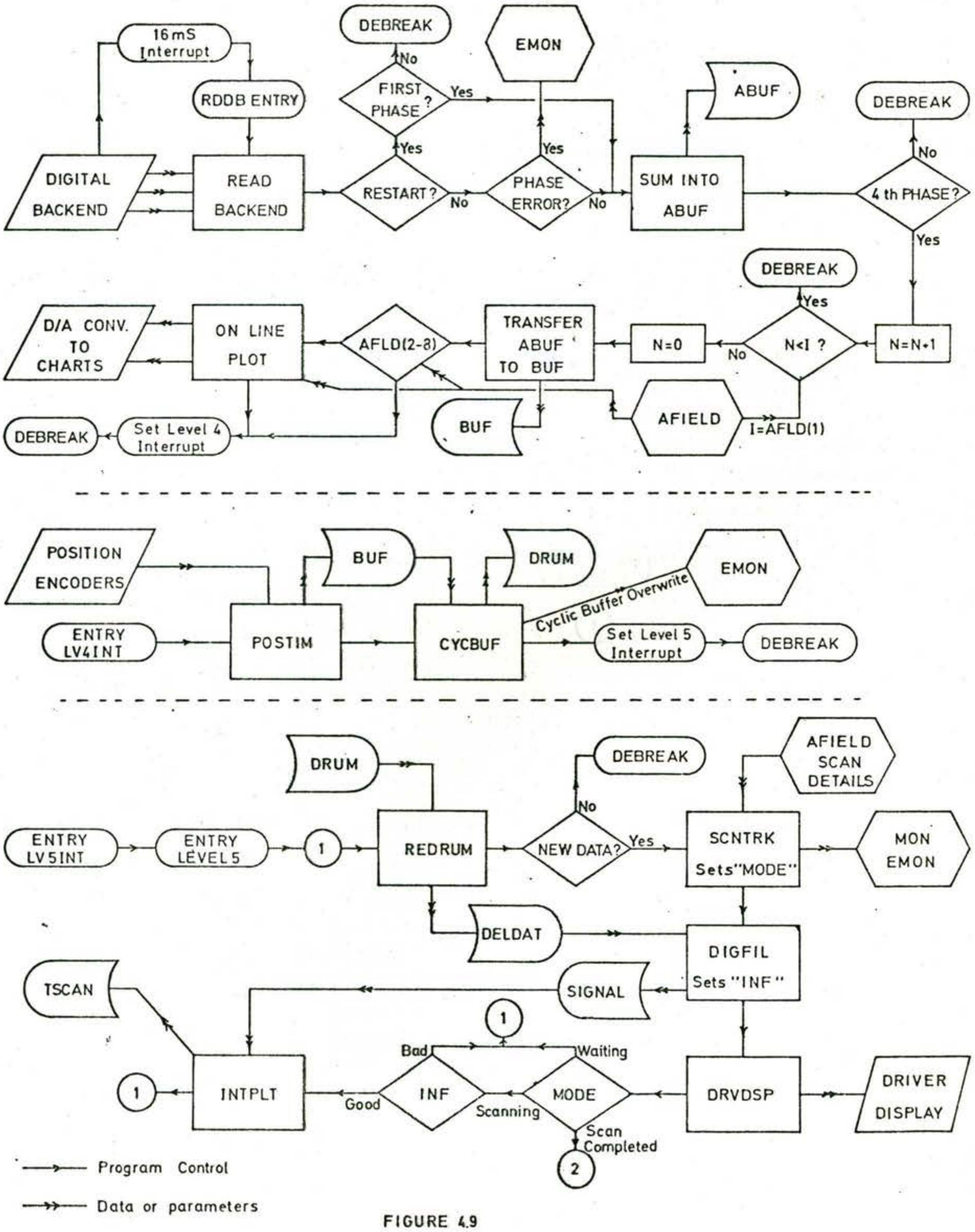
16mS Interrupt
RDDB ENTRY
DIGITAL BACKEND
READ BACKEND
DEBREAK
No
FIRST PHASE ?
Yes
Yes
RESTART?
No
EMON
Yes
PHASE ERROR?
No
ABUF
SUM INTO ABUF
DEBREAK
No
4 th PHASE?
Yes
DEBREAK
Yes
N<I ?
No
N=N+1
N=0
TRANSFER ABUF TO BUF
AFLD(2-8)
ON LINE PLOT
D/A CONV. TO CHARTS
BUF
AFIELD
I=AFLD(1)
DEBREAK
Set Level 4 Interrupt
POSITION ENCODERS
ENTRY LV4INT
POSTIM
BUF
CYCBUF
DRUM
Cyclic Buffer Overwrite
EMON
Set Level 5 Interrupt
DEBREAK
DRUM
ENTRY LV5INT
ENTRY LEVEL5
1
REDRUM
DEBREAK
No
NEW DATA?
Yes
AFIELD SCAN DETAILS
SCNTRK Sets "MODE"
MON EMON
DELDAT
DIGFIL Sets "INF"
SIGNAL
TSCAN
1
Bad
Waiting
INTPLT
1
Good
INF
Scanning
MODE
Scan Completed
2
DRVDSP
DRIVER DISPLAY
Program Control
Data or parameters

FIGURE 4.9

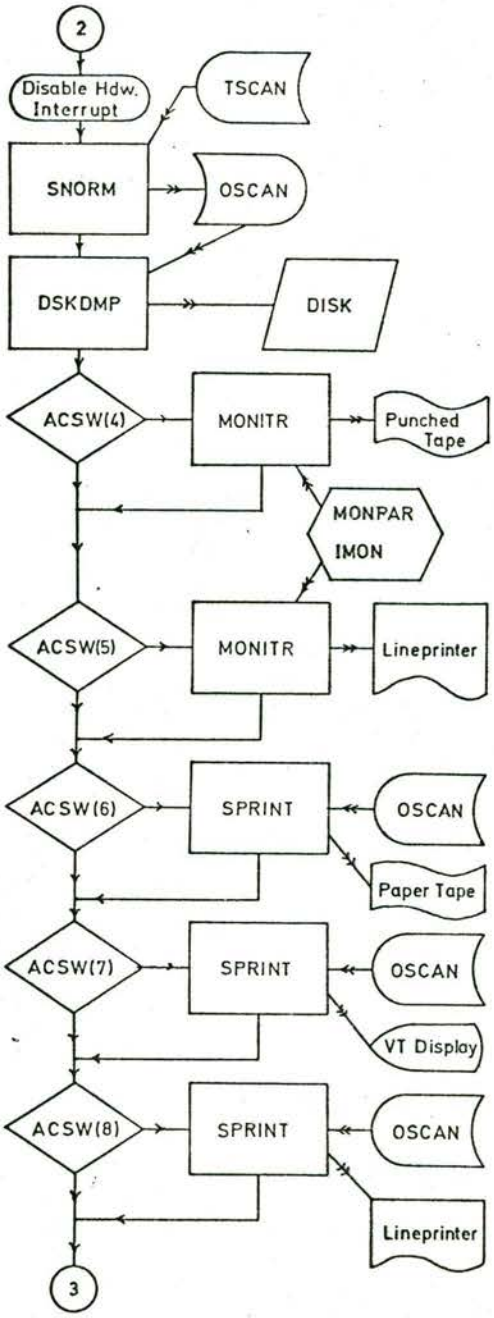

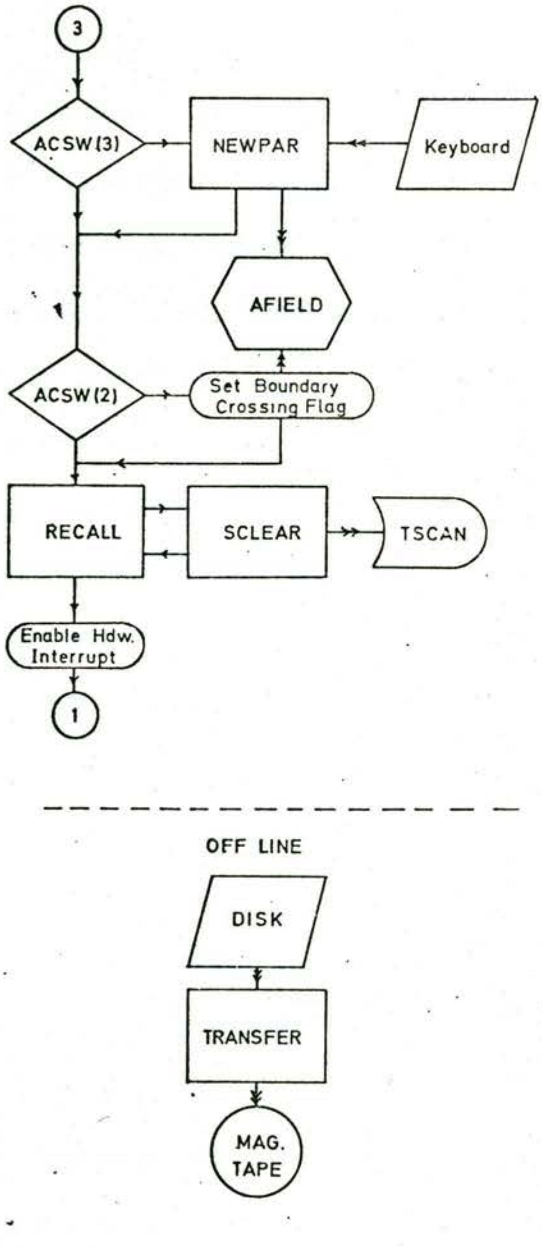

FIGURE 4.9 (Cont'd)

The highest level hardware interrupt is produced by the digital backend, and signals to the computer that the output buffers contain a new set of data, that of the previous 16 ms phase. This interrupt causes suspension of any lower priority program, and control is passed to the hardware interrupt service routine RDDB. This routine first reads the three outputs of the digital backend and determines, from the top two bits in the first word, the state of the receiver in the previous 16 ms. If this is the first entry to RDDB, a check is made to ensure that this is the first phase of the four phase switching cycle of the receiver. If this is not the case, control is returned to the interrupted program (DEBREAK). If it is the first phase of a cycle, the data is added into a 12 word buffer array (ABUF), one word for each phase of each of the three inputs. Control is then returned to the interrupted program. Each interrupt produces a new phase and new data which are added into their respective buffer locations. This continues until a complete cycle of four phases has been recorded. The operation of the program now depends on the selected on-line integration time, which is contained in the active field array as an integral number (N) of receiver cycles. If this number of cycles has not yet been attained, control is returned to the interrupted program. This integration process continues until the required number of cycles have been summed together. The data buffer area (ABUF) is then transferred to an external array (BUF) which is accessible from routines at lower priority levels.

Depending on the values of parameters set into the active field, an on-line plot of the data being collected can be made. The plot routine calculates the signal and/or gain of any of the three channels from the data contained in ABUF, and outputs this value to D/A converters. There are two output channels available so that two quantities can be simultaneously displayed. The quantities to be displayed (e.g. cal.-channel 1 : signal-channel 3) and the gains and D.C. offsets of each output channel are selected by setting various parameters in the active field.

At the end of the plot routine, the ABUF array is cleared to zero in preparation for the next integration period. Before debreaking, a software interrupt at level 4 (LV4INT) is set. This places the Level 4 programs on the waiting list. When control is returned to the System Organiser after a DEBREAK command, this will give control to the Level 4 programs, as they have the highest priority of those waiting. Only the hardware interrupt service routine (RDDB) has a higher priority.

During the observations, an integration period of 8 receiver cycles was used. This meant that the level 4 programs were entered once every 1/2 second. There were 32 hardware interrupts (i.e. entries to RDDB) during each integration period.

On each entry to RDDB a check is made to ensure that the correct phase sequence is maintained. If a phase error occurs then the integration is restarted with the next first phase of a cycle. The error is recorded in an error monitor array (EMON).

The first task of the Level 4 software interrupt service routine (LV4INT) is to read the sidereal time, azimuth and zenith angle encoders. This gives the position of the data point contained in BUF. The encoders are read a few milliseconds after the end of the integration period and so are in error by approximately 1/4 sec, or 1.5' arc in zenith angle at the 6°/minute observing speed. However, the mean of this position and the position of the previous data point gives the correct values.

The subroutine CYCBUF takes the incoming data point and adds it into a "cyclic buffer" (DRUM). The purpose of this cyclic buffer is to delay the incoming data, so that later stages of the program have access to a number of data points simultaneously. This was necessary to implement the digital filter technique described in Section 2.4. Data points are added sequentially into a one dimensional array until it is full. The next data point should then go into the first location, but this will only happen if the later stages of the program have already processed the very first data point and have cleared this location. This also allows later stages of the program to work asynchronously with the incoming data. However, it is still necessary that the average time taken to process a single datapoint is less than the time taken to collect that data. Before writing the data to DRUM, CYCBUF performs the demodulation process necessary to give the signal and gain of each channel. On the completion of CYCBUF, a Level 5 software interrupt is set and then control is returned to the system organiser.

The Level 5 interrupt service routine, LV5INT, calls the level 5 main program, LEVEL5, which begins by calling the subroutine REDRUM. This routine forms a delayed data array, DELDAT, from DRUM. This is a fixed length array, with the current data point in the middle position. If no new data or not enough data is available in DRUM, then Level 5 debreaks. Otherwise, the next step is the scan tracking routine, SCNTRK.

The routine SCNTRK determines the scanning state of the telescope (from the position information in DELDAT) i.e. beginning scanning program, scanning up, scanning down, waiting at the top, finished at the bottom etc. The integer variable MODE describes this state, and is set by SCNTRK. Declination precession to 1950.0 coordinates is also performed in SCNTRK.

The routine DIGFIL convolves the data in DELDAT by a simple interference filter of the type used at the 1 second level in the Bonn Survey (see Section 2.4). If the data is affected by interference, the switch INF is set. The current data point is also written from DELDAT into array SIGNAL.

The routine DRVDSP compares the actual scan path with the theoretical path and outputs the tracking error to a display which is used by the telescope driver to keep in track. If the telescope is waiting at the top or bottom for a scan to begin, a count down to the start time is given in this display.

The information required by SCNTRK and DRVDSP to specify the scan (e.g. top and bottom scan limits, time between scans, scanning speed, etc.), is obtained from the active field.

If the current data point was taken in scanning mode, and was free of interference, then it is interpolated into the tabular scan array, TSCAN, using the same techniques as in Section 2.5. All three signal channels are treated in the same way in this process.

When a scan finishes, by crossing one of the boundaries, or by being aborted, then the program enters the scan logging phase. During this part of the program a number of operations can be performed, in order, on the scan data. As each of the programs performing these operations requires a relatively large amount of storage space, an overlay structure is used to fit the program into the 16 K of storage available. The logging program only operates in the time between scans, so it is not necessary to collect data, nor to use the programs DIGFIL, INTPLT and DRVDSP. The collection of data is suspended by disabling the hardware interrupt. The data in TSCAN is then normalised into the array OSCAN by the routine SNORM which overlays the three routines above.

When normalising is complete, the space occupied by TSCAN (and therefore SCNTRK, which contains TSCAN) and SNORM become free to be overlayed by the various output routines which follow. The first of these output routines is DSKDMP, which transfers the completed normalised tabular scan in OSCAN to disk storage.

The remaining logging operations are optional, and are chosen by setting hand switches which are read from LEVEL 5. The options available are shown in Figure 4.9. The routine MONITR outputs the error information contained in MONPAR, IMON and EMON. The routine SPRINT outputs OSCAN to punched tape, VT cathode ray screen display or lineprinter. The routine NEWPAR has the teletype as input and is used to change the values of parameters contained in the active field. When logging is completed, the routine RECALL rearranges the overlay structure to contain the data collecting routines and then the hardware interrupt is re-enabled. The driver display then begins to count down to the correct scan starting time.

With the scanning program used in the first observing session, a period of 80 seconds was available between the end of a scan and the beginning of the next scan. This was sufficient to complete a disk transfer and a MONITR and SPRINT output to lineprinter, leaving approximately 30 seconds during which time active field parameters could be changed.

When the program is first started, it remains in a waiting mode until the telescope is driven from a position outside the scan limits across the boundary. This is done in the routine SCNTRK which then calculates which of the correct scan starting times is closest to the actual boundary crossing time. By this method the theoretical scan track of the first scan is determined. The scanning program, the details of which are contained in the active field, is then followed automatically. If during a scan a particular hand switch is thrown, on completion of that scan the program waits for a boundary crossing to determine the next scan. By the use of this switch the scanning program can be changed. Another hand switch can be used to abort a scan. The program then immediately enters the logging phase and the scan observed up to that point is recorded. A boundary crossing is necessary to restart scanning after an abort command.

4.8 Off-line Reduction

The off-line reduction procedure used for the southern sky survey is only slightly modified from that used in the Bonn survey. Small modifications were necessary to accomodate the polarisation data, but otherwise the same computer programs were used.

The two extra channels, representing the Stokes parameters Q and U, can be treated in the same way as the radiometer channel, except that account must be taken of scan to scan variations in the position angle of the reference plane relative to which Q and U are measured. This is illustrated in the following analysis of the operation of the receiver and data collection.

A simplified block diagram of the polarimeter is shown in Figure 4.10. The two input signal voltages are the left and right handed circularly polarised components $R \sin \omega t$ and $L \sin (\omega t + \theta)$. To these are added calibration signal voltages $C \sin \omega t$ and $\alpha C \sin(\omega t + \phi)$. The factor α takes into account the different coupling of the directional couplers. G_1 and G_2 represent the R.F./I.F. gains of the polarimeter channels up to the splitters in the I.F. polarimeter. G_1 then includes the loss in the radiometer hybrid.

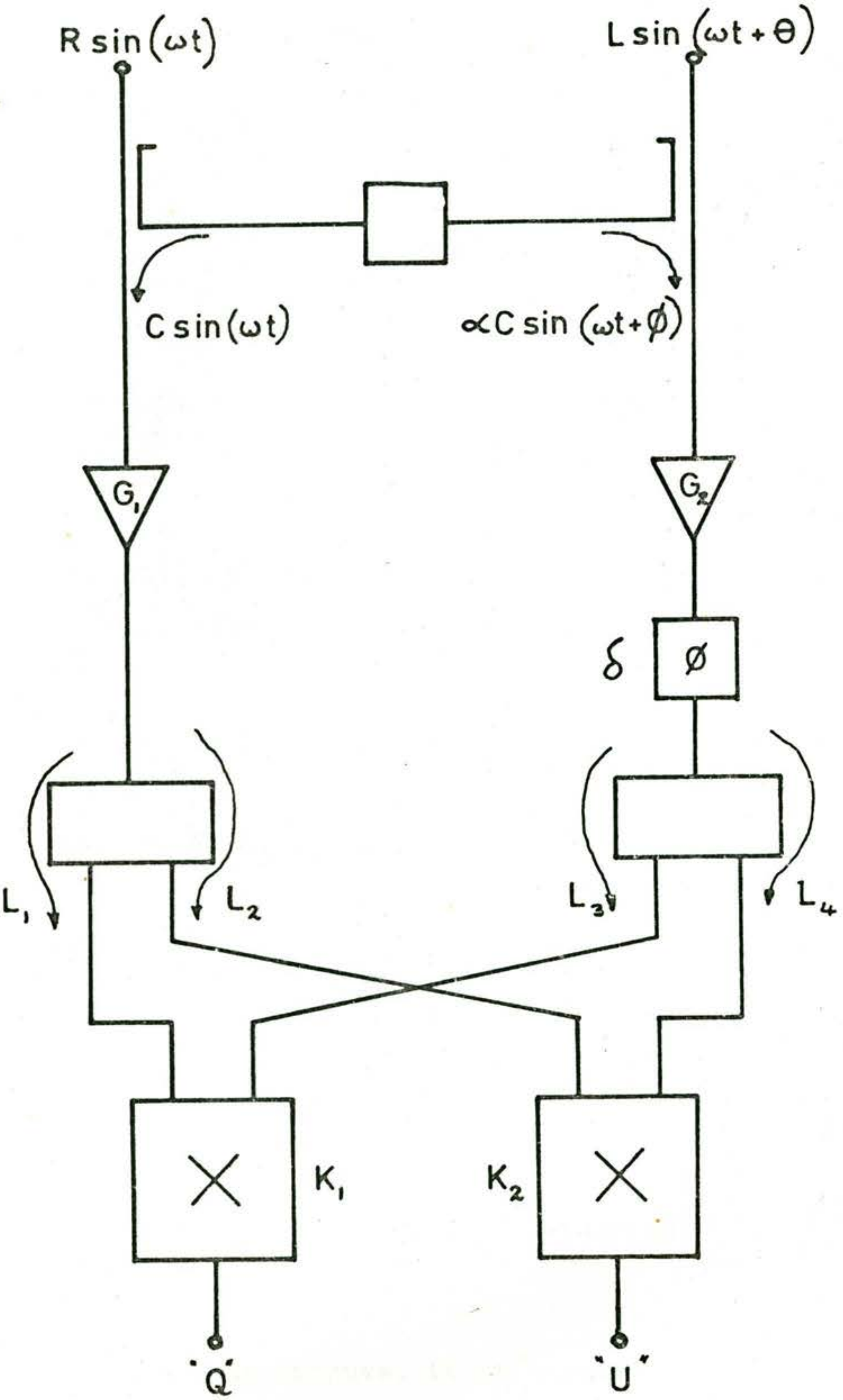

FIGURE 4.10

δ is the differential phase shift through the two channels. The delays through the two channels are considered to be equal. L_1, L_2, L_3 and L_4 represent the losses through each arm of the splitters to the multipliers, and K_1 and K_2 combine the gains of the multipliers and the conversion factors of the V/f converters.

The quantities recorded in the computer as polarimeter outputs due to the input signals are:

$$SQ = K_1 \; L_1 \; L_3 \; G_1 \; G_2 \; R\,L \cos(\Theta + \delta) \qquad \ldots \; 4.8$$

and

$$SU = K_2 \; L_2 \; L_4 \; G_1 \; G_2 \; R\,L \sin(\Theta + \delta) \qquad \ldots \; 4.9$$

The outputs due to the calibration signals are:

$$CQ = K_1 \; L_1 \; L_3 \; G_1 \; G_2 \; \alpha \; C^2 \cos(\phi + \delta) \qquad \ldots \; 4.10$$

and

$$CU = K_2 \; L_2 \; L_4 \; G_1 \; G_2 \; \alpha \; C^2 \sin(\phi + \delta) \qquad \ldots \; 4.11$$

From these four outputs, is is required to find the Stokes parameters

$$Q = 2\,R\,L \cos\Theta = I_L \cos 2\varepsilon \qquad \ldots \; 4.12$$

and $$U = 2RL\sin\theta = I_L \sin 2\varepsilon \qquad \ldots 4.13$$

where I_L is the intensity of the linearly polarised component and ε is the polarisation angle (see Equations 4.5, 4.6) and,

$$I_L = (Q^2 + U^2)^{\frac{1}{2}} \qquad \ldots 4.14$$

$$\varepsilon = \tfrac{1}{2}\cdot\tan^{-1}(U/Q) = \tfrac{1}{2}\cdot\theta \qquad \ldots 4.15$$

The outputs SQ and SU can be expressed in the following way

$$SQ = g\cdot(Q\cos\delta - U\sin\delta) \qquad \ldots 4.16$$

$$SU = x\cdot g\cdot(U\cos\delta + Q\sin\delta) \qquad \ldots 4.17$$

where $x = K_2 L_2 L_4 / K_1 L_1 L_3$, $g = K_1 L_1 L_3 G_1 G_2$

They contain a mixture of Q and U, depending on the value of δ. As δ will in general differ from scan to scan, due to phase instability of the receiver, the quantities recorded in SQ and SU will differ from scan to scan. As a phase change, δ, is equivalent to a polarisation angle change of $\tfrac{1}{2}\cdot\delta$ (Equation 4.13), different scans will, in general, have different polarisation angle reference planes.

To produce maps of Q and U using the programs developed for the Bonn 408 MHz survey it is necessary to have tabular scans containing independent channels representing Q and U. Hence the first step in the off-line analysis is to correct SQ and SU for δ, using Equations 4.16 and 4.17.

A measure of δ can be obtained from the ratio of CU and CQ

$$CU/CQ = x \cdot \tan(\phi + \delta) \qquad \ldots\ 4.18$$

If x and ϕ are known, then δ is determined. In practise, the phase change during a scan was very small so that it was sufficient to take a single value of δ for a complete scan.

New tabular scans are produced with channels containing SQ' and SU' where

$$SQ' = g \cdot Q = SQ \cdot \cos\delta + (SU/x) \cdot \sin\delta \qquad \ldots\ 4.19$$

and
$$SU' = g \cdot U = -SQ \cdot \sin\delta + (SU/x) \cdot \cos\delta \qquad \ldots\ 4.20$$

A single calibration, C', is sufficient to calibrate both polarimeter outputs. This is given by

$$C' = (CQ^2 + (CU/x)^2)^{\frac{1}{2}} = g \cdot \alpha c^2 \qquad \ldots 4.21$$

and provides the required measure of overall gain, g. As the later analysis only uses the values of the calibrations at the scan start and stop times (see Section 2.7), it is necessary only to change these four values.

Once the corrections for δ have been made, the analysis proceeds in exactly the same way for all three channels. The baselevel optimising procedure is first used to determine consistant baselevels for all scans. This operates on each of the three channels in turn. The result is a calibration log (Section 2.7) containing the updated baselevels. The map making routine uses this log in conjunction with the scans to produce maps of I, Q or U.

It is seen from the above discussion that it is necessary to obtain a value for the quantity, x. This was done by the use of a vertex calibration system. A noise diode was used as the signal source for a dipole transmitter placed at the vertex of the telescope. As the dipole was slowly rotated a sine wave output was produced in each of the polarimeter outputs. This was recorded into the normal tabular scan format using the normal on-line analysis, with the "dummy telescope" option. This technique allows the on-line analysis to continue with a stationary telescope so that drift scans and program tests can be made without requiring that the telescope be driven. The ratio of the peak values of the sine waves in the two channels then gave a direct measurement of x.

These off-line reduction techniques have been used to obtain maps of selected regions from the first observing session. A discussion of the results obtained now follows.

4.9 The Antenna Beam

A measure of the polarisation properties of the antenna beam was obtained by making observations of the strong radio source, Virgo A. The region 12 18 < R.A. (1974.1) < 12 42, 10.0° < dec. (1974.1) < 15.0° was mapped, using declination scans with a scanning speed of approximately 4°/minute. The scans were spaced 80 seconds apart in R.A. The data was collected using the normal on-line data collection programmes, modified so that the R.A. and declination encoders were read instead of the azimuth and zenith angle encoders, as in the normal survey program. The map was made about two hours after transit so that the parallactic angle changed by only 2° during the observations. The results are shown in Figure 4.11 in the form of maps of the left handed circularly polarised component (assumed to be the Stokes parameter, I), and the Stokes parameters, Q and U.

These measurements can be understood in terms of the radiating properties of a paraboloid reflector, when illuminated by a short electric dipole feed. For this case, Condon (1941) has calculated the electric field in the aperture of the paraboloid. Using this expression for the aperture field, Jones (1954) gives approximate solutions to the integral expressions for the far field diffraction patterns of the parabola. He found that the normalised far-zone electric field is given by:

$$\bar{E} = \bar{x}\left[f_1(\phi) + f_2(\phi)\cos 2\varepsilon\right] + \bar{y}\left[f_2(\phi)\sin 2\varepsilon\right] \quad \ldots \; 4.22$$

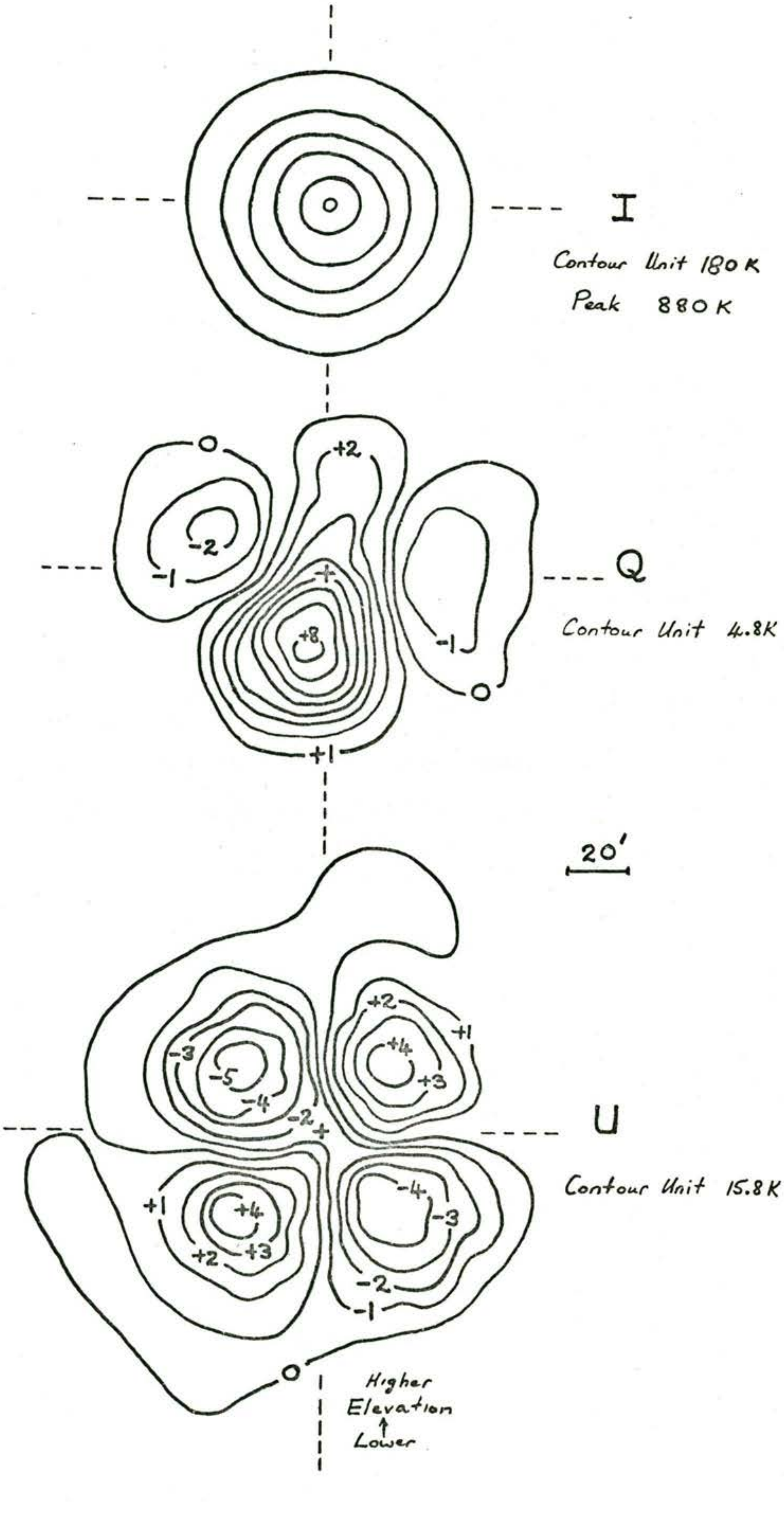
I
Contour Unit 180 K
Peak 880 K
0
+2
-2
-1
+
+8
-1
0
+1
Q
Contour Unit 4.8K
20′
+2
+1
-3
+4
-5
+3
-4
-2
+
U
-4
+1
+4
-3
+2
+3
-2
-1
Contour Unit 15.8K
0
Higher
Elevation
Lower

FIGURE 4.11

where ϕ and ε are defined in Figure 4.12 A. $\bar{x}$ and $\bar{y}$ are unit vectors parallel to the x and y axes, and the feed lies along the x axis. $f_1(\phi)$ and $f_2(\phi)$ are complicated functions of ϕ, and $f_1(\phi) > f_2(\phi)$.

Equation 4.22 shows that the diffraction pattern contains two components, the principal polarisation pattern (parallel to the feed polarisation) and the cross polarisation pattern (perpendicular to the feed). $f_2(\phi)$ can be thought of as a perturbation on $f_1(\phi)$, tending to make the principal polarisation pattern widths in the x and y planes unequal. The cross polarisation term is seen to be zero on the x and y axes, and maximum at 45° to these axes (for a fixed ϕ). Furthermore, the form of $f_2(\phi)$ is such that the maxima occur at approximately the first zero of the principal polarisation pattern, so that four cross polarised sidelobes appear as shown in Figure 4.12 B. Because of the dependence on sin 2ε, the cross polarised electric fields in adjacent quadrants are in magnitude symmetrical, but in the opposite directions.

For the case where the antenna is fed by a crossed dipole feed, the response of the paraboloid to a randomly polarised signal, and hence the Stokes parameters polar patterns can be calculated by the use of Equation 4.22.

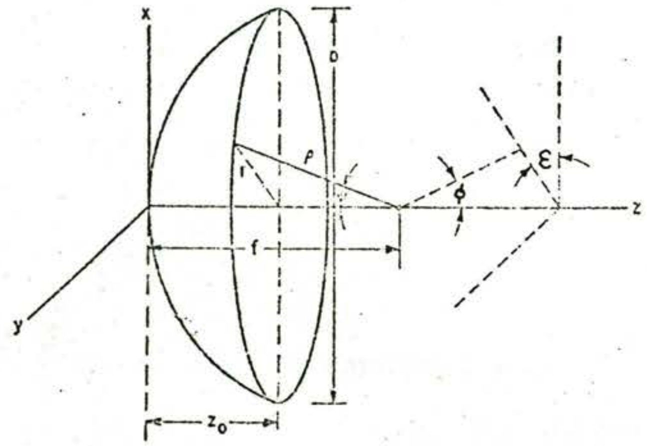

FIGURE 4.12 A

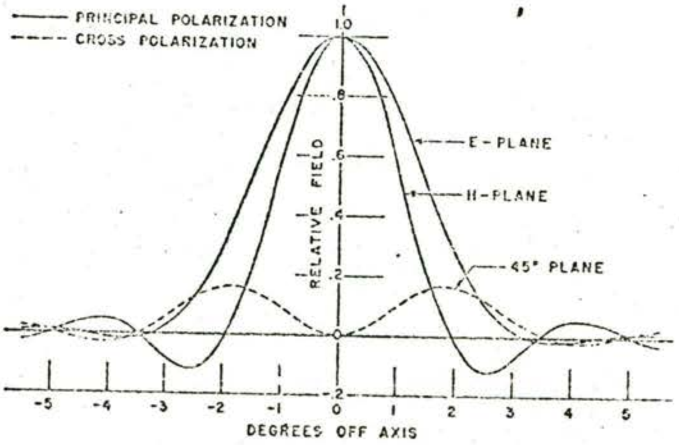

FIGURE 4.12 B

The time varying field due to a randomly polarised source at position (ϕ,ε) can be expressed in the following way

$$\bar{E}_s(t) = E_{sx}(t) \cdot \bar{x} + E_{sy}(t) \cdot \bar{y} \qquad \ldots\ 4.23$$

Because the source is randomly polarised, $E_{sx}(t)$ and $E_{sy}(t)$ are equal in amplitude, but uncorrelated.

The voltage induced into the dipole in x axis is:

$$\nu_x(t) \propto E_{sx}(t)\left[f_1(\phi) + f_2(\phi)\cos 2\varepsilon\right] + $$

$$+ E_{sy}(t)\left[f_2(\phi)\sin 2\varepsilon\right] \qquad \ldots\ 4.24$$

Relative to the dipole in the y axis, the source is at a position $(\phi, \varepsilon-90)$, and the field has the following form:

$$\bar{E}_s(t) = -E_{sy}(t) \cdot \bar{x}_1 + E_{sx}(t) \cdot \bar{y}_1 \qquad \ldots\ 4.25$$

where $\bar{x}_1$ and $\bar{y}_1$ are unit vectors parallel and perpendicular to the y dipole, and $\bar{x}_1 = -\bar{y}$, $\bar{y}_1 = \bar{x}$. The voltage induced is:

$$\nu_y(t) \propto -E_{sy}(t)\ \left[f_1(\phi) + f_2(\phi)\ \cos 2(\varepsilon-90)\right] +$$

$$+ E_{sx}(t)\ \left[f_2(\phi)\ \sin 2(\varepsilon-90)\right]$$

or

$$\nu_y(t) \propto -E_{sy}(t)\ \left[f_1(\phi) - f_2(\phi)\ \cos 2\varepsilon\right] -$$

$$- E_{sx}(t)\ \left[f_2(\phi)\ \sin 2\varepsilon\right]$$

The Stokes parameters, Q and U, are obtained from following relationships:

$$Q \propto < \nu_x^2 > - < \nu_y^2 >$$

$$U \propto 2 < \nu_x \cdot \nu_y > \cdot \cos \delta$$ (see Equations 4.2 and 4.3)

The symbol < > represents a time average.

The result is:

$$Q \propto 4\ E_o^2\ f_1(\phi)\ f_2(\phi)\ \cos 2\varepsilon \qquad \ldots\ 4.26$$

and

$$U \propto 4\ E_o^2\ f_1(\phi)\ f_2(\phi)\ \sin 2\varepsilon \qquad \ldots\ 4.27$$

where $E_o^2 = < E_{sx}(t)^2 > = < E_{sy}(t)^2 >$.

Both Q and U are seen to have "clover leaf" patterns, the sense of adjacent lobes being opposite. For Q, the pattern lies on the principal axes, and for U the pattern lies on the 45° axes, as was the case for the cross polarisation lobes (Figure 4.12).

The basic form of the measured patterns shown in Figure 4.11 are in agreement with these results. However, a number of important features are not explained by Equations 4.26 and 4.27. The large positive lobe appearing on the Q pattern can be probably explained in terms of the tripod mast of the Parkes antenna. This lobe occurs at the position where the source is looking through the mast which lies in the elevation plane. It is likely that orthogonal polarisations are affected differently by this mast, giving rise to differences in the principal polarisation lobes. Any such differences would be shown directly in Q. The fact that the Q pattern is slightly skewed cannot be explained. The U pattern is well lined up with the 45° planes. The U pattern has precisely the predicted form, showing very good symmetry. The fact that the Q and U patterns are not of equal height is most likely explained by the fact that the feed was a double dipole array, and not a short dipole as used in the theory above. It can be shown that the Q lobes arise mainly from the non-circularity of the principal polarisation pattern. With a short dipole feed, this non-circularity is rather severe, but with the feed used in the observations, the principal polarisation pattern is much more circular. This should lead to smaller Q lobes, which is what in fact is observed.

At the beam centre, there is seen to be a small residual polarisation, which amounts to 3% of the source height $((Q^2 + U^2)/I^2)$.

4.10 The Large Magellanic Cloud

Maps have been prepared of the region R.A. = 04 45 to 06 00, dec. -77° to -62°, which contains the large extended radio source due to the Large Magellanic Cloud (L.M.C.). Maps of the Stokes parameters I, Q and U, are shown in Figure 4.13. The maps are in units of antenna temperature, obtained by measuring the strength of the calibration noise signal with a hot-cold load method. The scale of I is defined in terms of the total intensity emitted from a black body at the same temperature. The units of Q and U have been chosen so that the polarisation percentage can be calculated directly from the values shown in the maps, using the

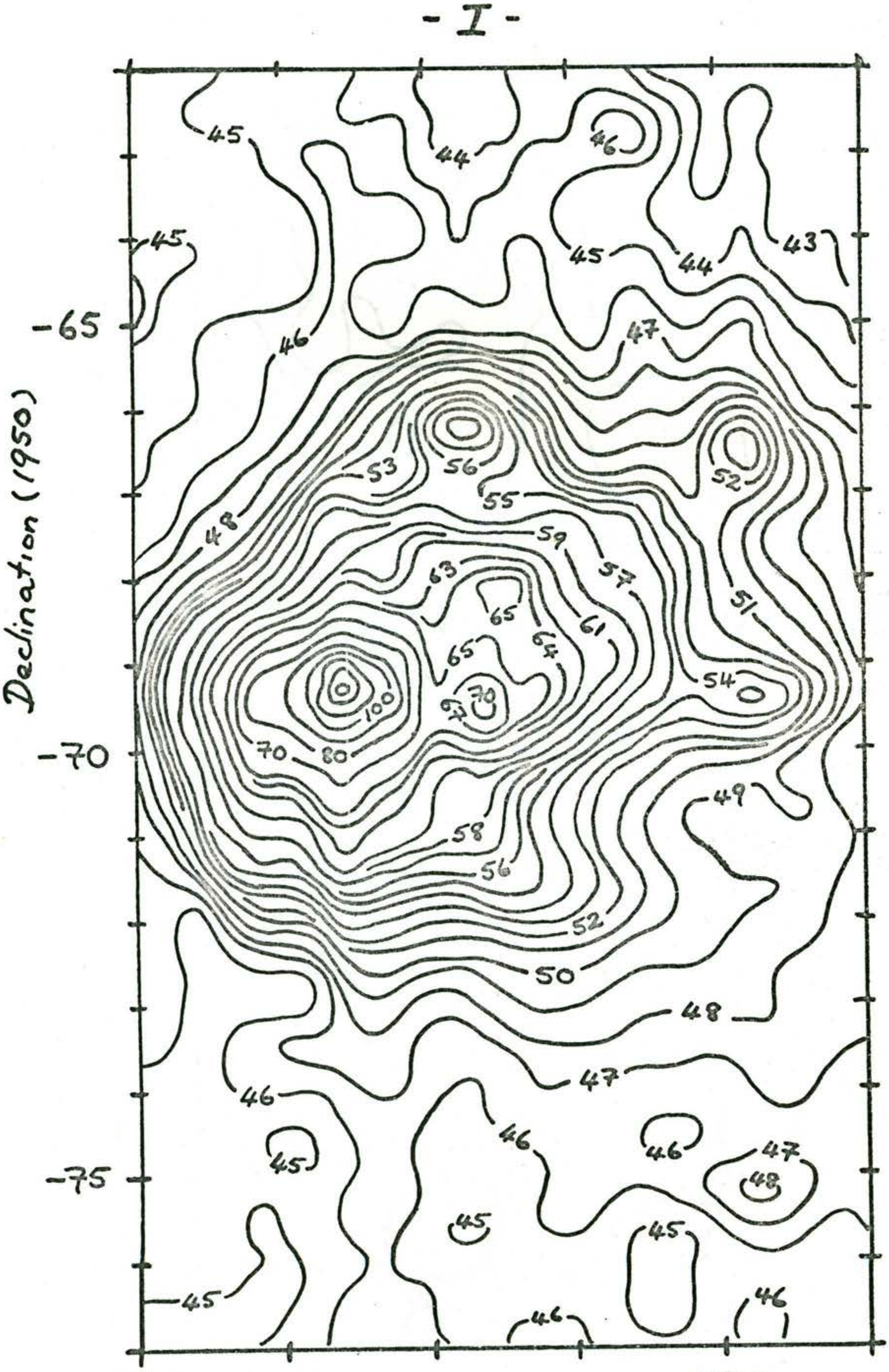
- I -
Declination (1950)
-65
-70
-75
0600
0500
R.A. (1950)
45
44
46
45
45
44
43
46
47
53
56
55
52
48
59
57
63
65
51
61
64
65
54
100
70
97
70
80
49
58
56
52
50
48
47
46
46
46
45
47
48
45
45
45
46
46

FIGURE 4.13

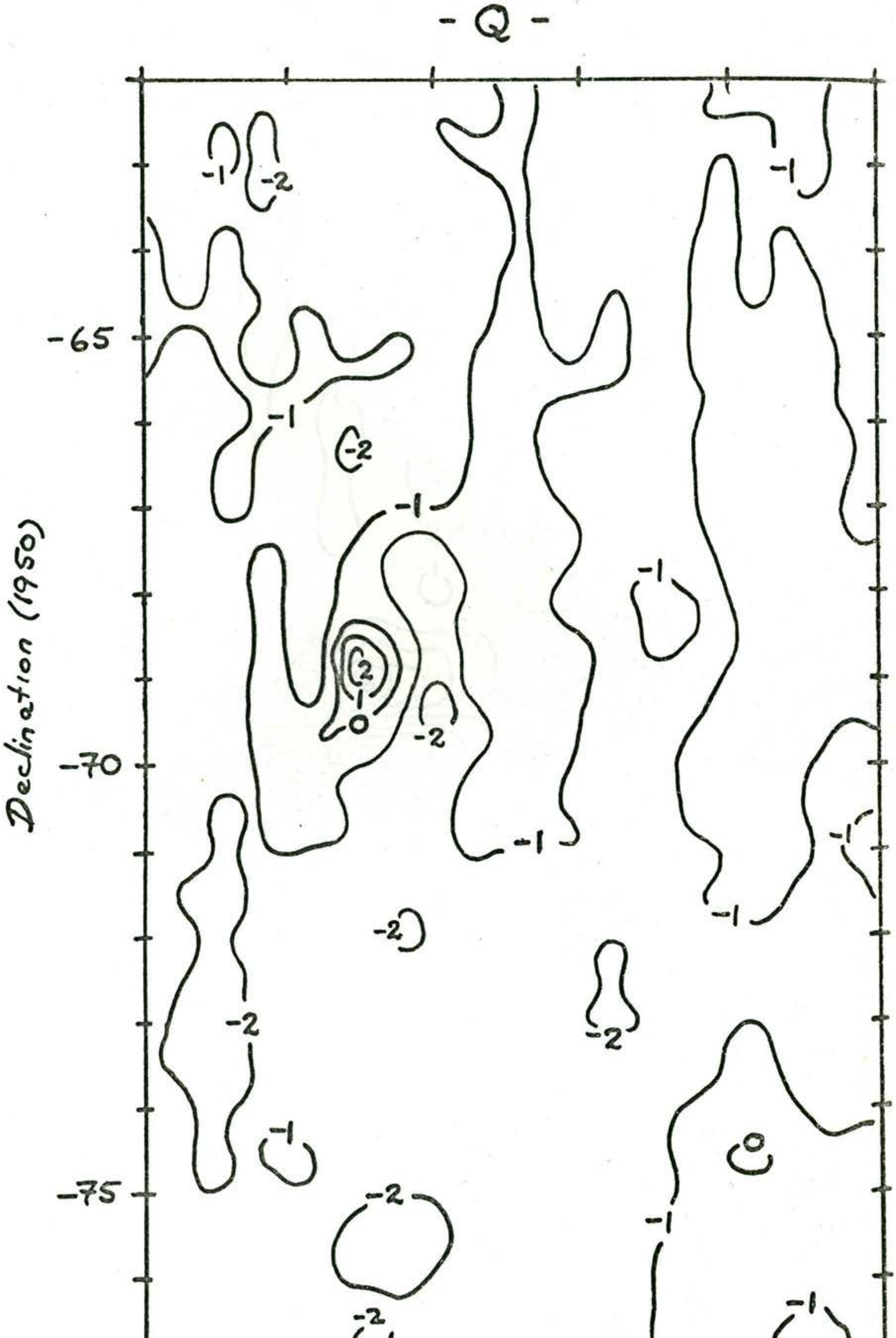

FIGURE 4.13 (Cont'd)

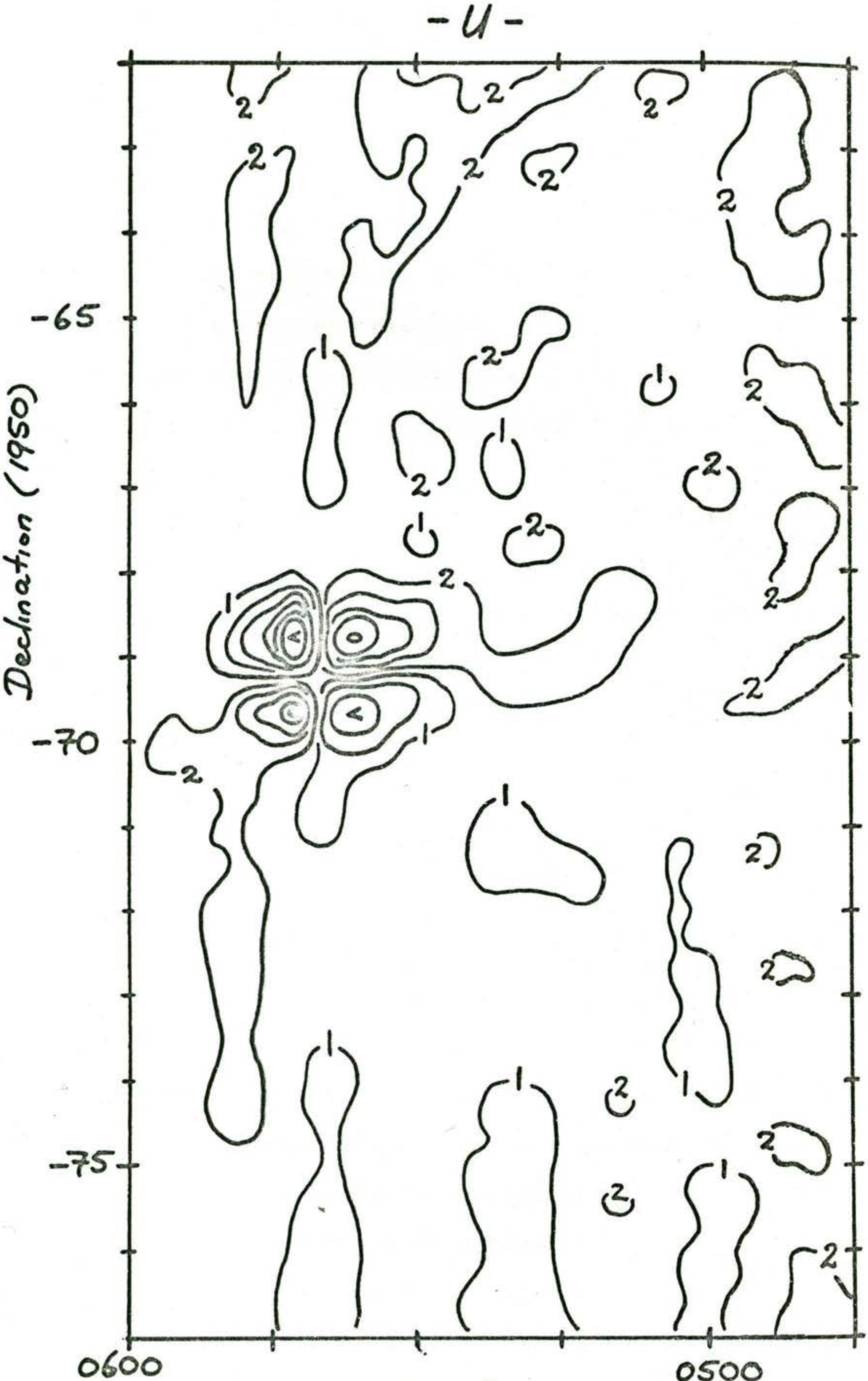

FIGURE 4.13 (Cont'd)

relationship:

$$\text{Polarisation percentage} = (Q^2 + U^2)^{\frac{1}{2}}/I.$$

The base level of the L.H. circular polarisation component map was obtained by adopting 80 K as the temperature of the liquid nitrogen reference load. This map shows excellent agreement with the 408 MHz map of this region made by Mathewson and Healey (1963) with the Parkes telescope.

The maps of Q and U show very little detail except in the neighbourhood of the strong radio source, 30 Doradus, at (05 39, -69° 20'), where the structure is obviously due to the polarised sidelobes, discussed in Section 4.9.

There is seen to be a general background of (Q, U) = (-1.5, +1.5) across the region. Initial maps have been made of most of the area covered in the first observing session, south of declination -55°, and these show that this background term is always present and is very constant. This would indicate that it is due to some form of coupling between the two receivers, giving correlated outputs from the two multipliers. More investigations are necessary to determine the origin of this term. The fact that it is a constant term means that it can be treated as a baselevel to be subtracted from the maps of Q and U.

4.11 Further Results

Figure 4.14 contains an example of the results obtained from a combination of observations described in this chapter, and later observations. These two maps were produced by Dr. G. Haslam, using the techniques described in this chapter. The polarization data is not yet available. The maps cover the region R.A. = 08 00 to 10 00, dec. -35° to -70°. The contours are in arbitrary units with an arbitrary baselevel. The maps are intended to show the quality of the results being obtained from the techniques described in this chapter.

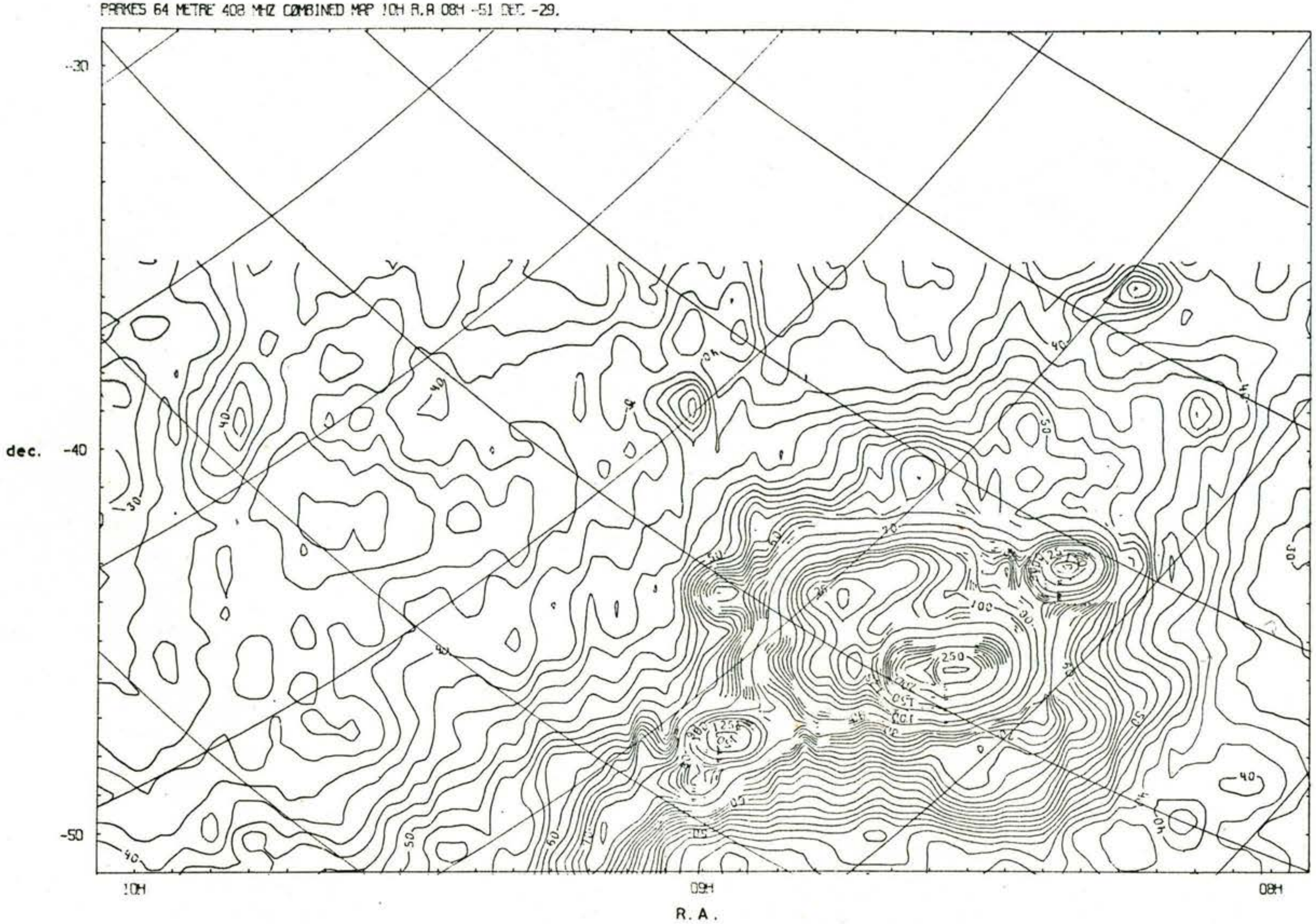
PARKES 64 METRE 408 MHZ COMBINED MAP 10H R.A 08H -51 DEC -29.
dec.
-30
-40
-50
10H
09H
08H
R.A.
30
40
50
70
100
125
150
200
250

FIGURE 4.14

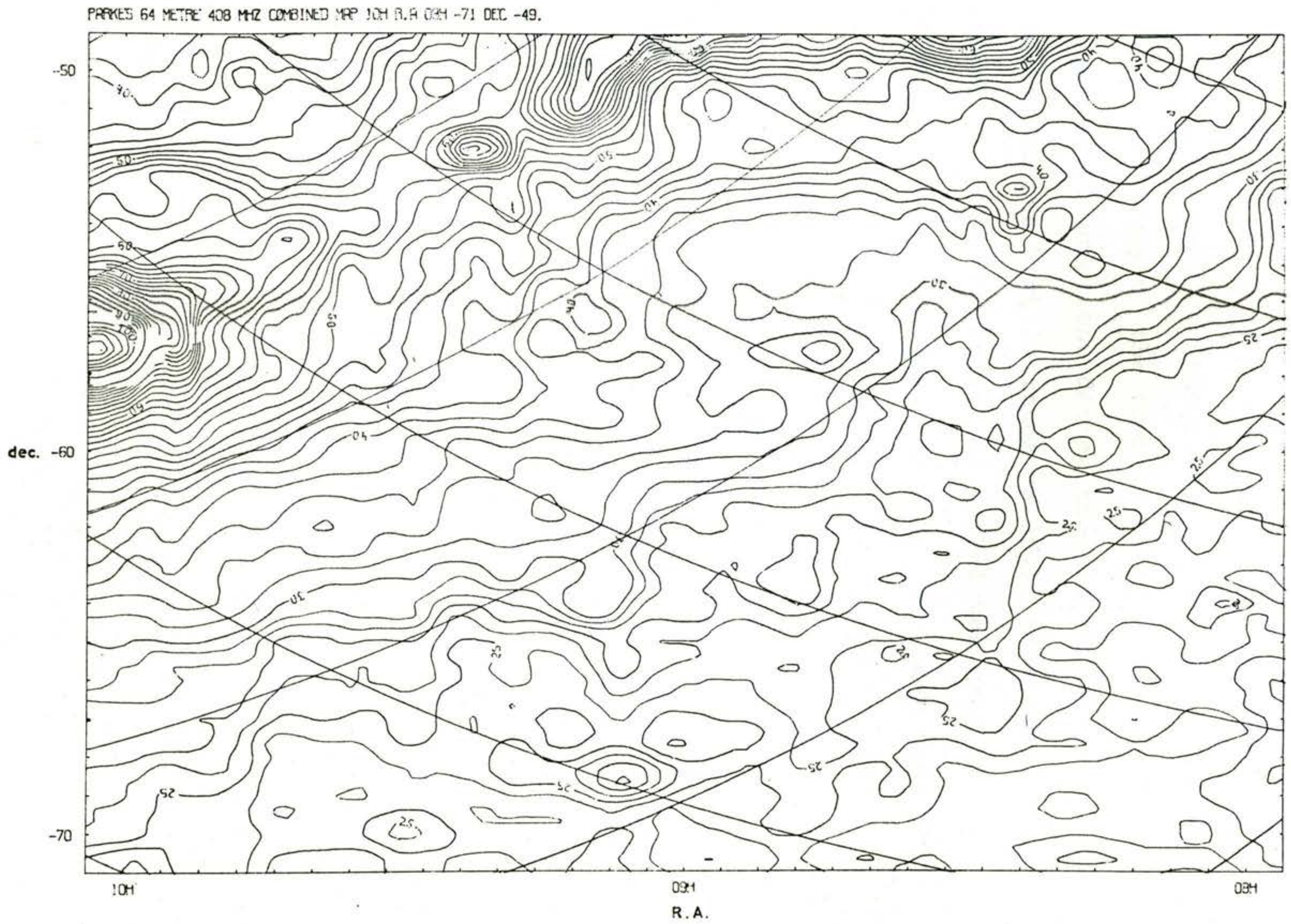

FIGURE 4.14 (Cont'd)

4.12 Summary

A new survey of the southern sky at 408 MHz is in the process of being completed. This will be the first survey of the complete southern sky with a resolution under one degree that is suitable for studies of the high latitude galactic continuum radiation. The equipment and techniques used in collecting and processing the data have been described. It is thought that this is the first occasion on which the complete linear polarisation parameters of the background radiation have been measured simultaneously in a large survey. Initial results of the first observations have been presented as evidence of the effectiveness of the methods used.

CHAPTER 5

THE SPECTRAL INDEX OF GALACTIC RADIO RADIATION

5.1 Introduction

The way in which the intensity of radio radiation from a particular source varies with frequency is an important factor in determining the mechanism producing that radiation, and hence the physical conditions existing within the source. In this chapter, the new Bonn 408 MHz survey data is used in conjunction with surveys at other frequencies, to study the variation, with frequency, of radiation from some of the large scale structures in the galaxy.

5.2 Definition

Because the variation with frequency of cosmic radio radiation follows, in general, a power law, the concept of the spectral index is usually used to express this variation. The spectral index is defined in the following way

$$S \propto f^{-\alpha} \qquad \ldots\ 5.1$$

where S = flux density from source at frequency f (watts m^{-2} Hz^{-1})
f = frequency (Hz)
α = spectral index

For large extended sources, a more convenient expression is

$$T(\alpha,\delta) \; \alpha \; f^{-\beta} \qquad \ldots\ 5.2$$

where $T(\alpha,\delta)$ = brightness temperature at point (α,δ) and at frequency f
β = temperature spectral index

Through the Rayleigh-Jeans radiation law, the following relation between α and β exists at radio wavelengths.

$$\beta = 2 + \alpha \qquad \ldots\ 5.3$$

Over a wide frequency range, most radio sources show a curved spectrum i.e. the variation with frequency does not follow a simple power law. However, the spectral index remains a convenient way of expressing the variation of intensity between two neighbouring observing frequencies. In this case the following equations hold

$$T(f_1)/T(f_2) = (f_1/f_2)^{-\beta(f_m)} = K(f_m) \qquad \ldots\ 5.4$$

where

$T(f)$ = brightness temperature of source at frequency f

$\beta(f_m)$ = temperature spectral index at frequency f_m

f_m = midpoint frequency

$$\equiv \sqrt{f_1 \cdot f_2} \qquad \ldots\ 5.5$$

$K(f_m)$ ≡ spectral ratio between f_1 and f_2

Deviations from the simple power law can then be expressed in terms of variations in β with frequency.

If brightness temperatures are available at two different observing frequencies, equation 5.4 may be used to find the spatial variation of spectral index across an extended source. However, two further points need to be taken into consideration. Errors may result from using different resolutions at the two observing frequencies, particularly if the source has temperature variations on the same scale as the smaller beam. To obtain the correct results identical beams should be used at both frequencies. Furthermore, as it is often difficult to determine a background level for a large extended source, the question arises as to whatpart of the received radiation emanates from the source under consideration.

5.3 The Galactic Spectrum between 408 MHz and 820 MHz

By making use of the Bonn 408 MHz survey and the Leiden 820 MHz survey (Berkhuijsen (1972)) it became possible to make spectral index studies with an angular resolution which is better than any previous work in this field.

The 820 MHz is an absolutely calibrated survey with a resolution of 1.2°. It was therefore necessary to make allowance for the different beam sizes of the two surveys. This was done by convolving the 408 MHz survey by a suitable smoothing function, resulting in a convolved 408 MHz map with an effective resolution of 1.2°. The convolution was made using the NOD2 smoothing facility (Haslam (1974), Salter (1970)). For this process, the 408 MHz survey beam was assumed to be a circular gaussian, and a gaussian smoothing function was used.

The 820 MHz data was available in BCD format, on magnetic tape. It was necessary at first to translate these data into a standard NOD2 document. This resulted in the production of 75 maps in galactic coordinates, each map being 30° x 20° in area, and tabulated at 0.5°

intervals, in l and b. The NOD 2 retabulate facility was also used to convert these maps in galactic coordinates into maps in equatorial coordinates (1950.0). The convolved 408 MHz maps were then combined into maps of the same size and tabular interval and centred at the same positions as the 820 MHz maps. The maps were then in a suitable format for a point by point determination of the spectral index.

The brightness temperatures at the two frequencies are made up of a number of components, these being

a) galactic radiation
b) nonthermal extragalactic radiation and
c) the thermal extragalactic component, the 3 K blackbody radiation.

As the aim of this study was to determine the spectral index of the galactic component, it was necessary to separate out this component from the others. According to Bridle (1967), the nonthermal extragalactic component has a value of about 3 K at 408 MHz, and a temperature spectral index of 2.75, giving a value of 0.4 K at 820 MHz. As these values are small compared to the average temperatures at the two frequencies, it was decided not to make any corrections for this component.

The thermal extragalactic component, on the other hand, is a significant proportion of the 820 MHz temperatures and warrants correcting for. Its value was taken at 2.7 K, from Thaddeus (1972).

Spectral index maps were produced by subtracting 2.7 K from the brightness temperatures at each tabular point, and then solving Equation 5.4 for β. These maps are shown in Figure 5.1, and cover the regions:

1. $15^{\circ} < l^{II} < 75^{\circ}$ & $-10^{\circ} < b^{II} < +10^{\circ}$
2. $15^{\circ} < l^{II} < 45^{\circ}$ & $+10^{\circ} < b^{II} < +70^{\circ}$
3. $13\ 00 < \mathrm{R.A.} < 14\ 00$ & $+10^{\circ} < \mathrm{dec.} < +30^{\circ}$

To aid in interpretation of these maps, the convolved 408 MHz maps of the same regions are given in Figure 5.2. The units are brightness temperature.

In low intensity regions at high galactic latitudes, an upper limit is given for the spectrum. This is necessary due to the fact that the spectrum is very noisy in these regions. This is caused mainly by errors in the 820 MHz maps, particularly "scanning" effects. These effects are pointed out by Berkhuijsen (1972) and become very important for the spectrum determination in cold regions.

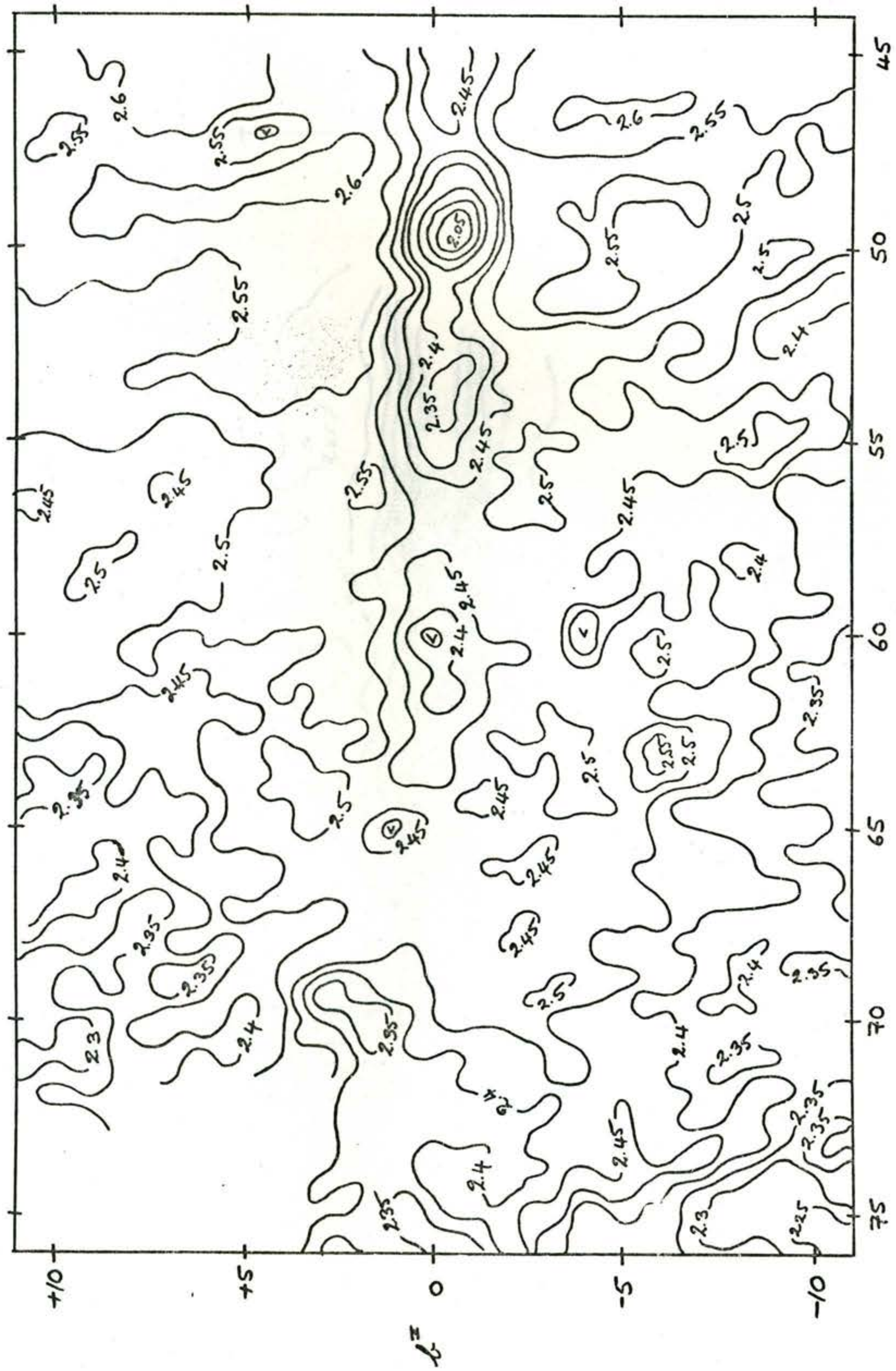

FIGURE 5.1

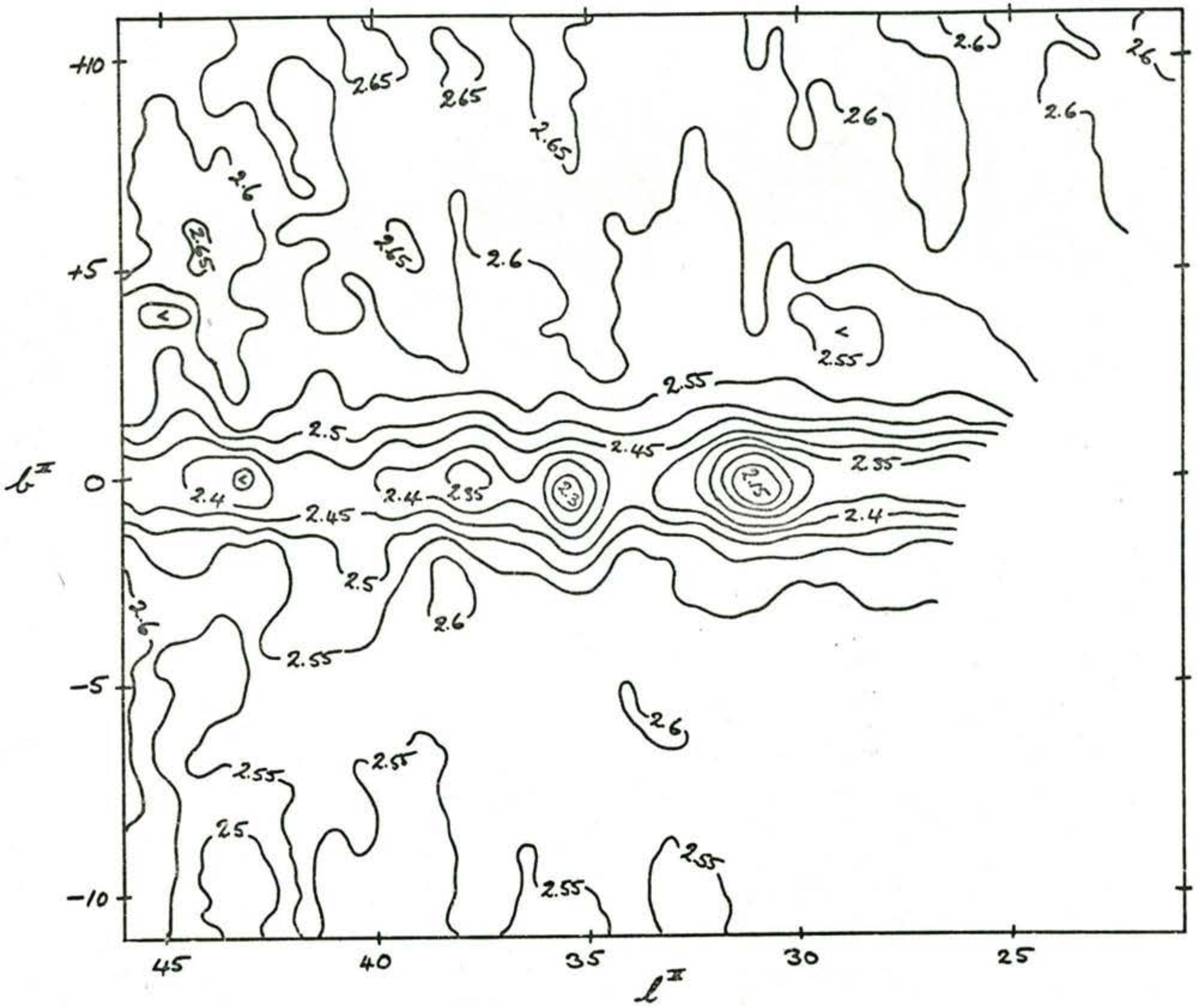

FIGURE 5.1 (Cont'd)

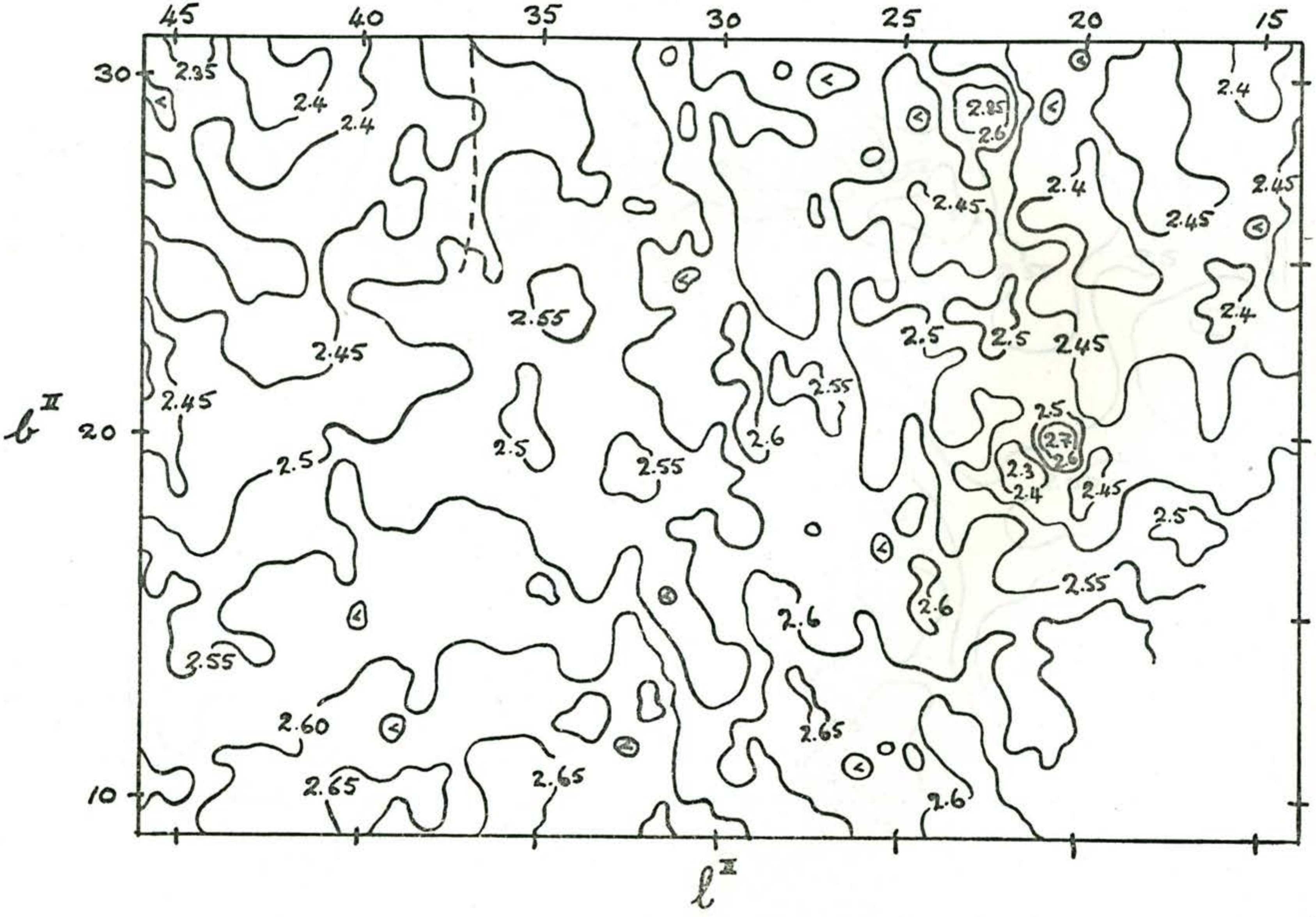

FIGURE 5.1 (Cont'd)

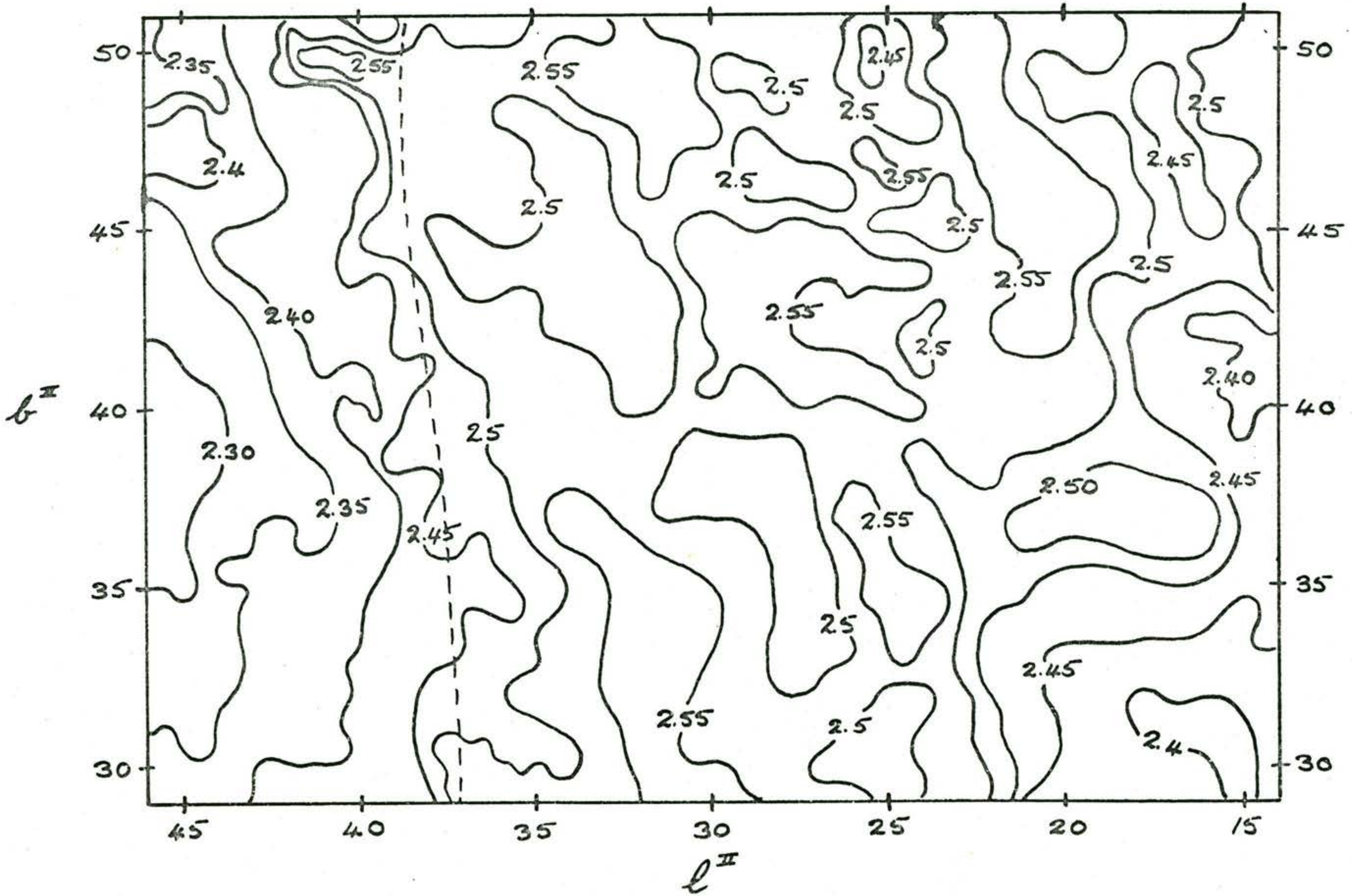

FIGURE 5.1 (Cont'd)

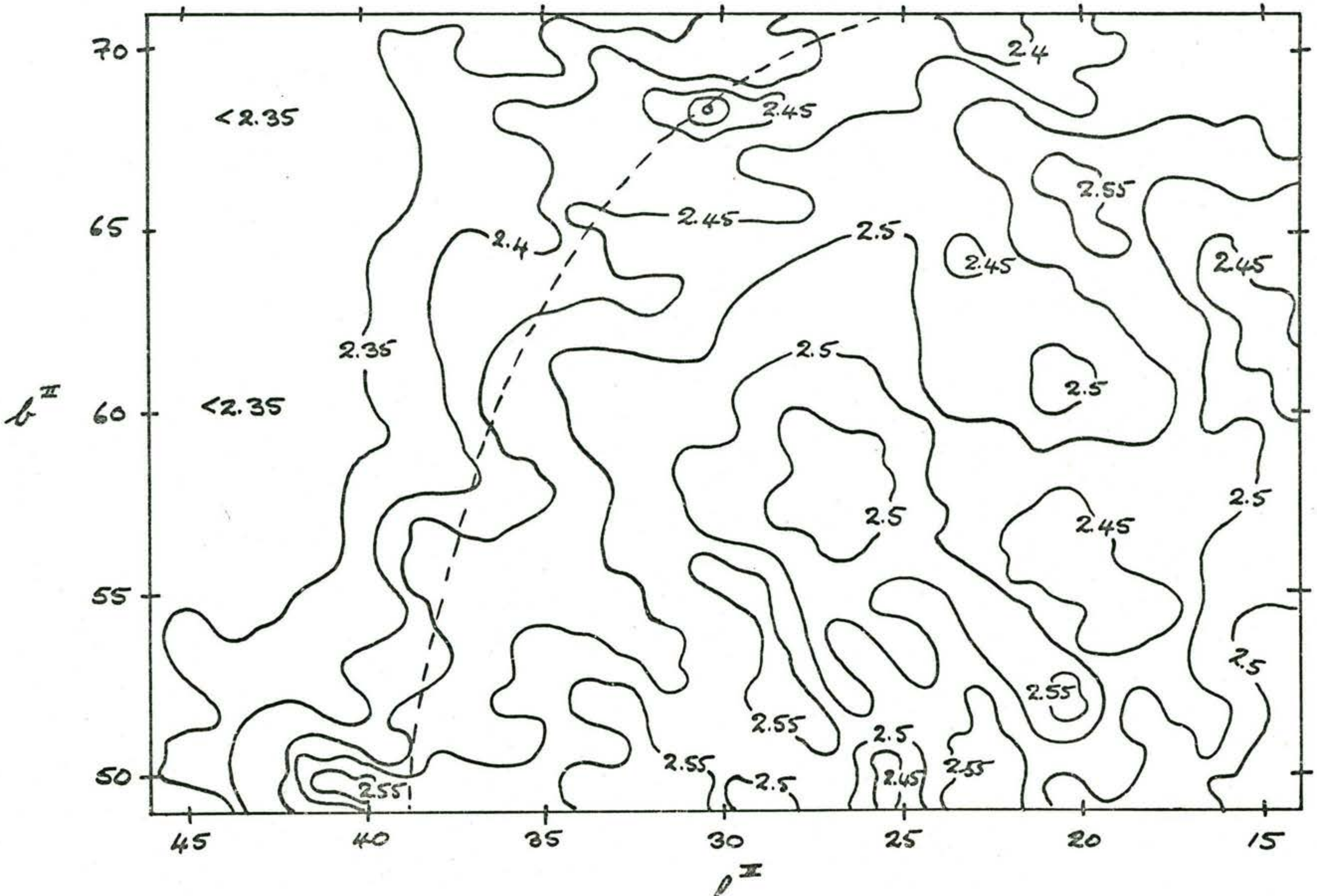

FIGURE 5.1 (Cont'd)

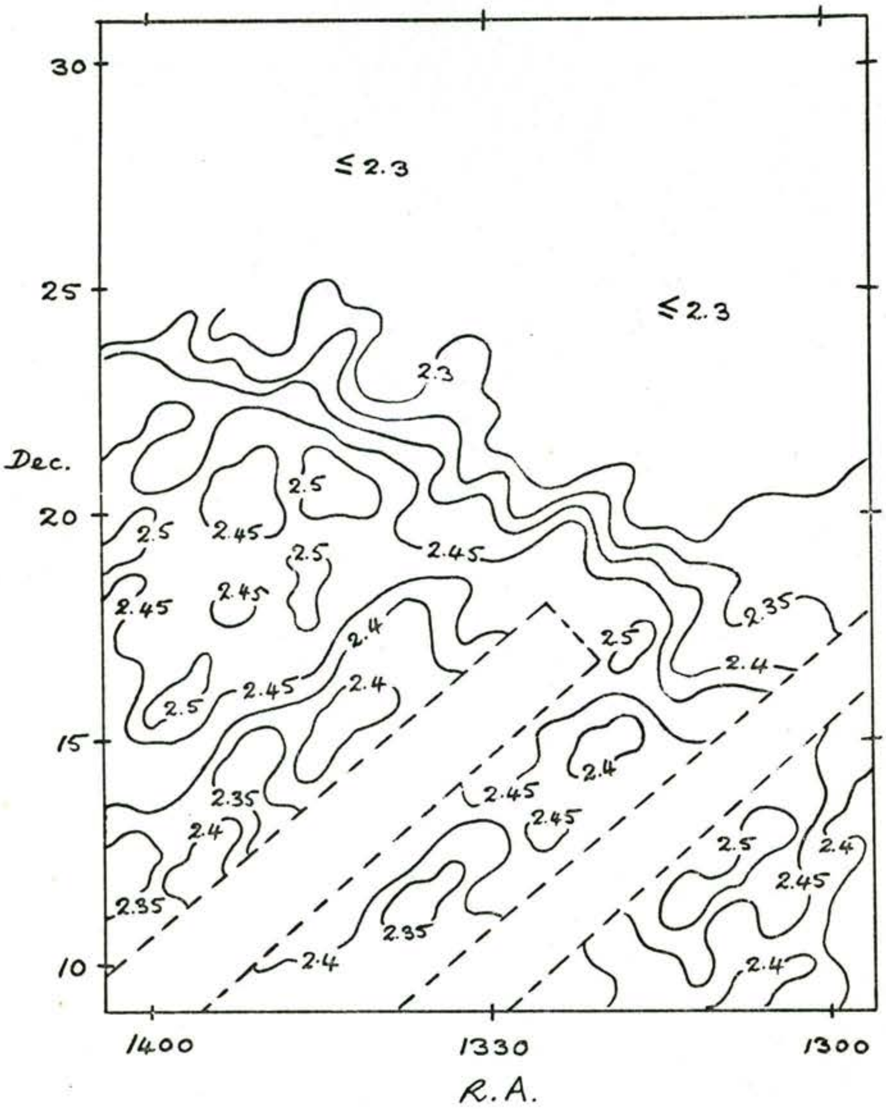

FIGURE 5.1 (Cont'd)

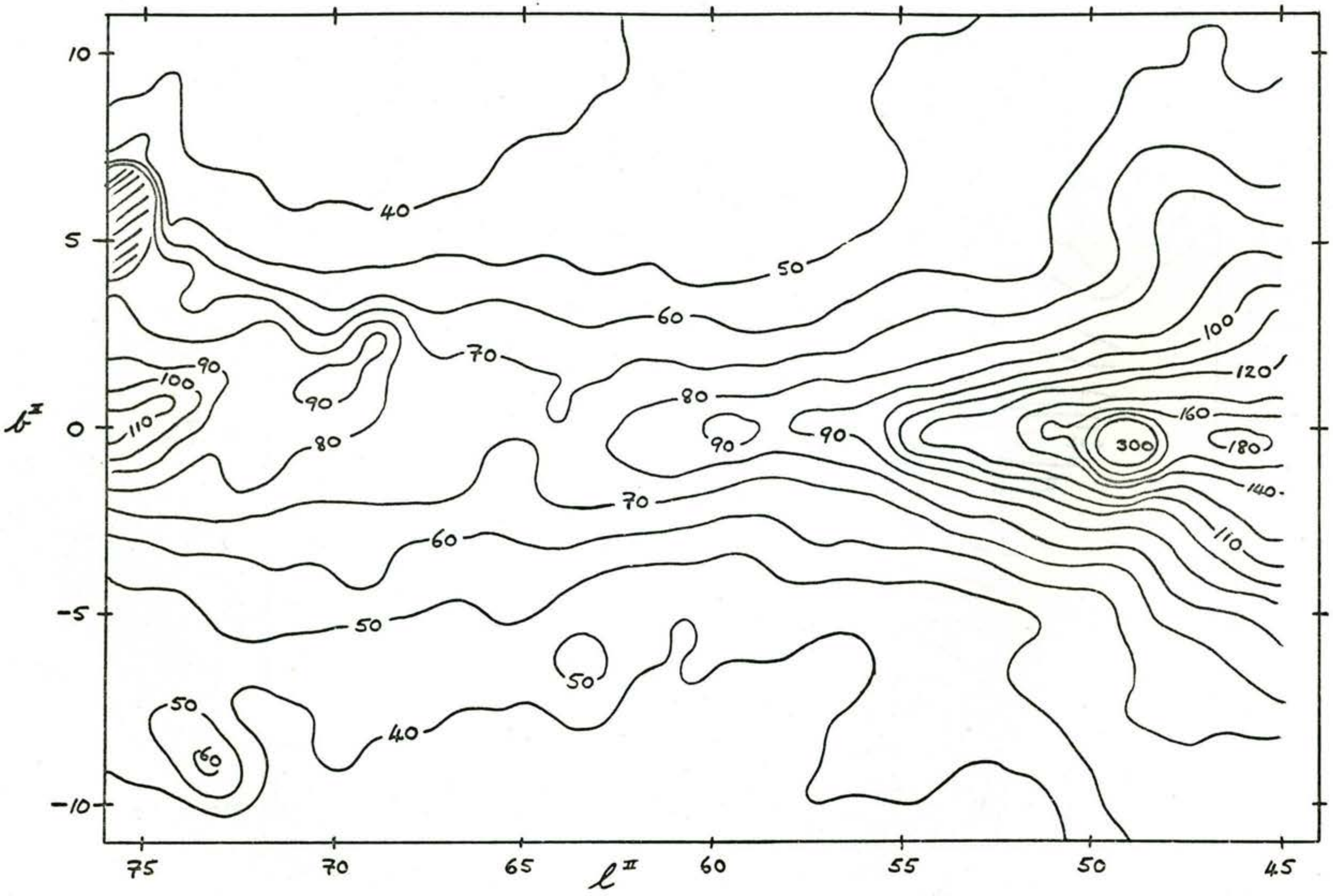
10
5
0
-5
-10
b^{II}
75
70
65
ℓ^{II}
60
55
50
45
40
50
60
70
80
90
100
110
90
80
70
60
50
90
90
100
120
160
300
180
140
110
50
40
50
60

FIGURE 5.2

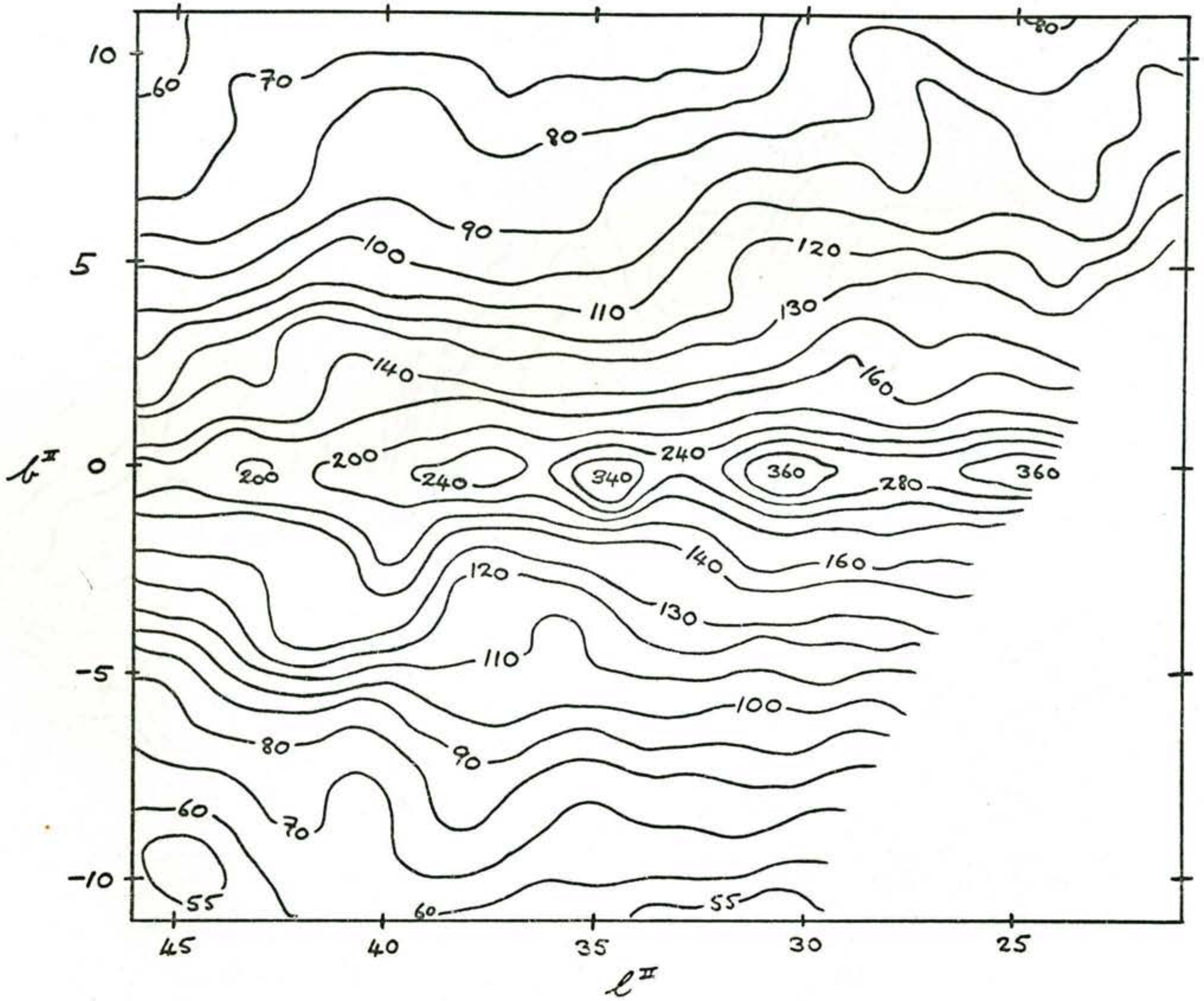

FIGURE 5.2 (Cont'd)

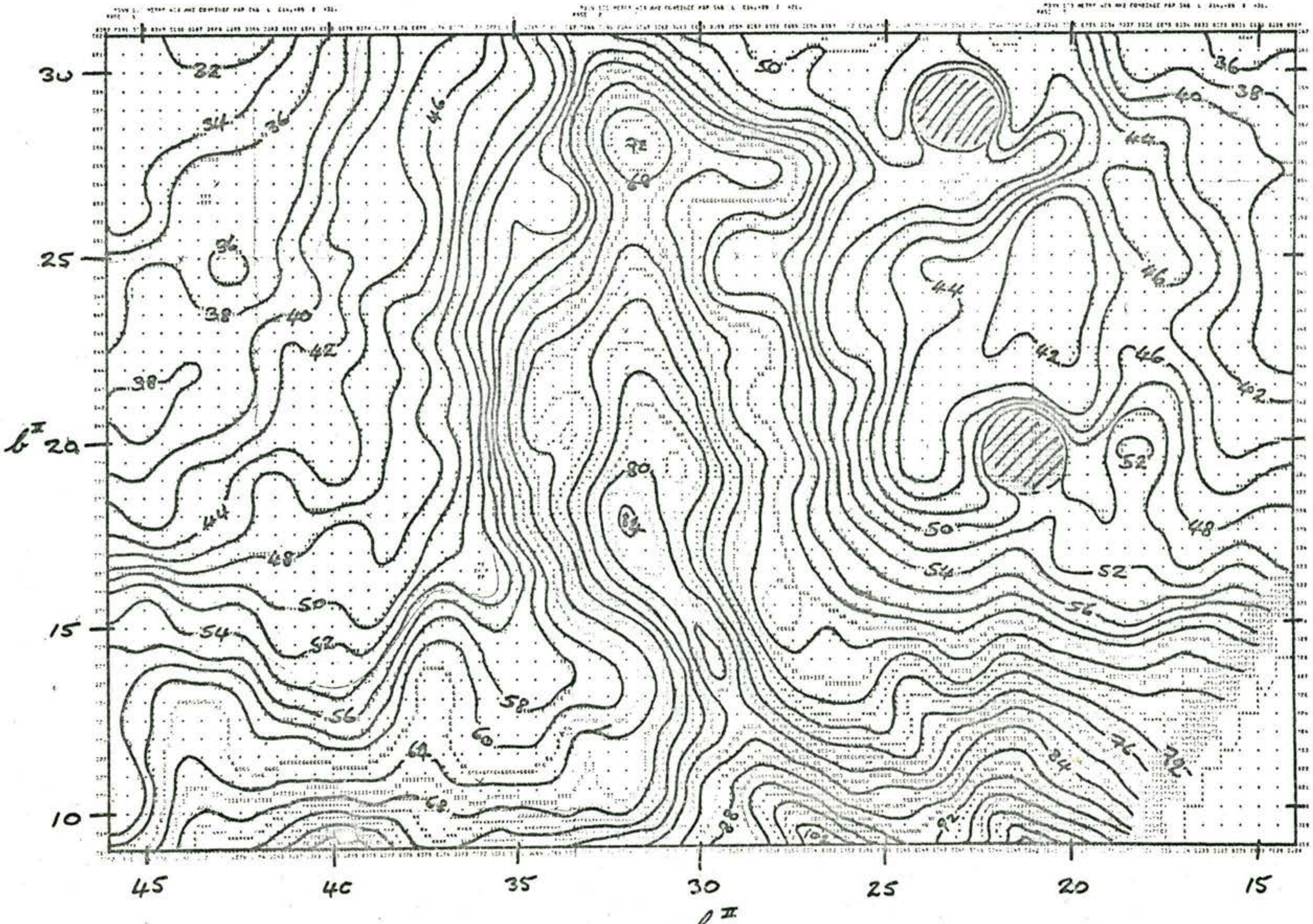

FIGURE 5.2 (Cont'd)

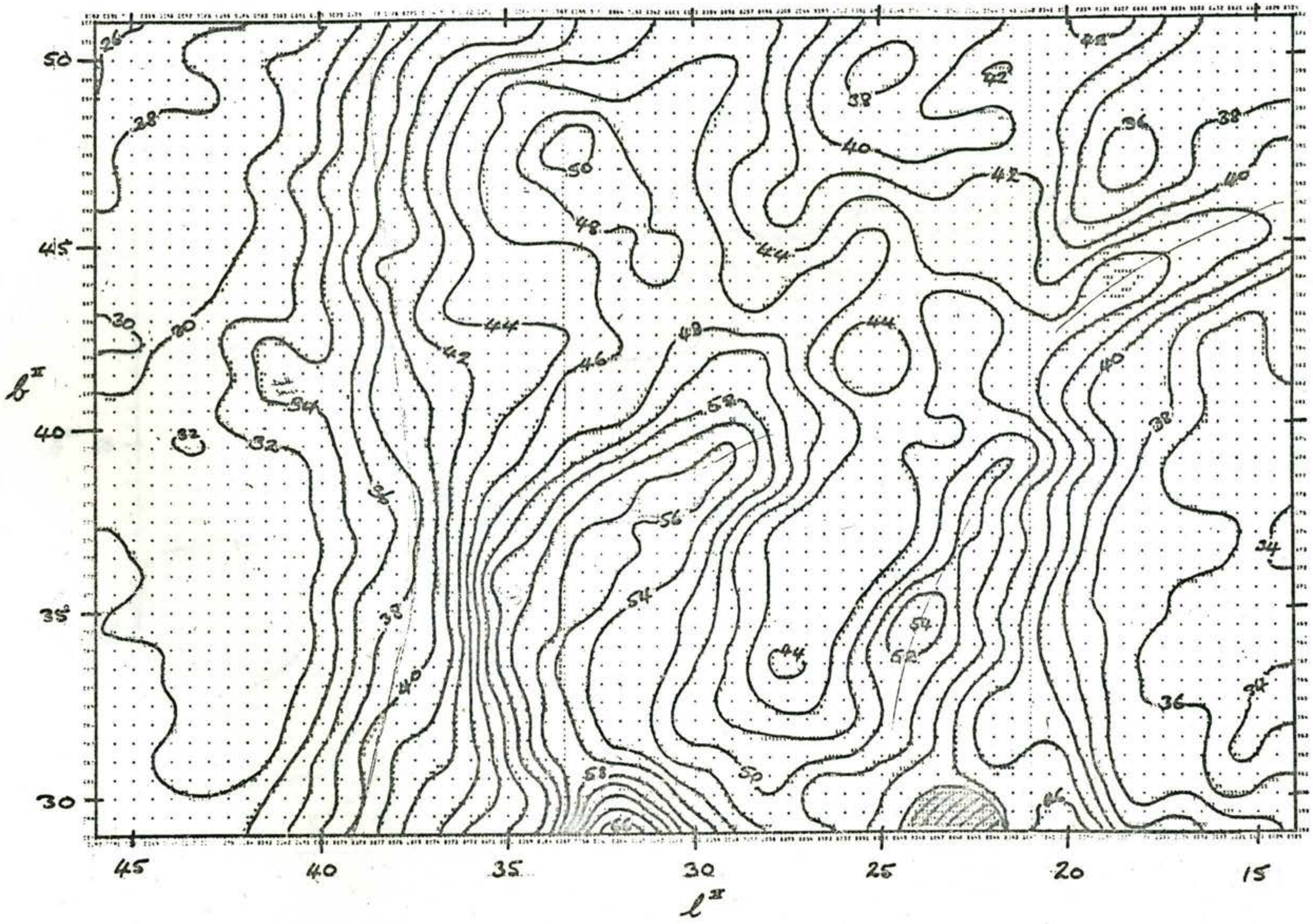

FIGURE 5.2 (Cont'd)

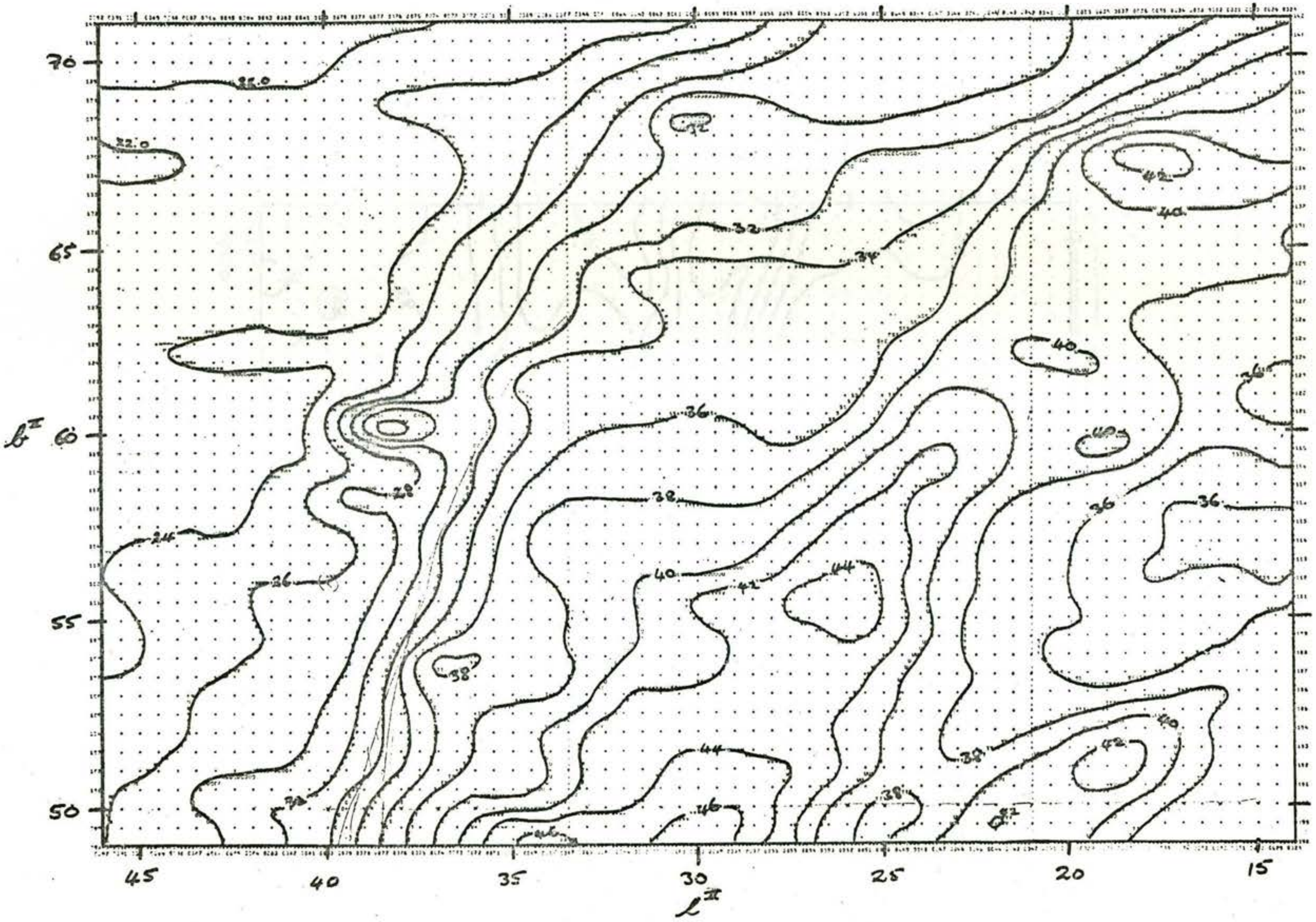

FIGURE 5.2 (Cont'd)

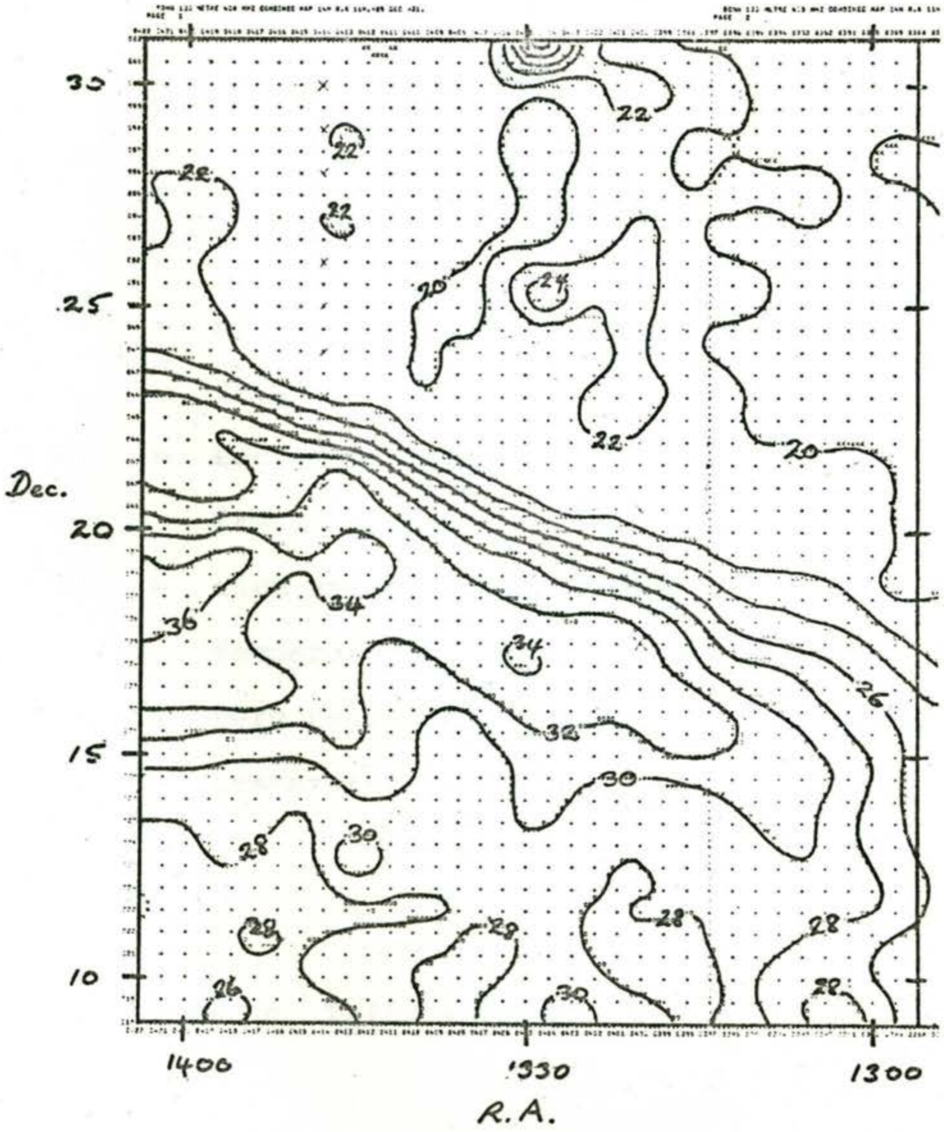

FIGURE 5.2 (Cont'd)

5.4 Accuracy of the Spectrum Maps

The accuracy of the spectrum maps is governed only by the absolute accuracy of the two brightness temperatures used to determine spectral index. The measured brightness temperature may be expressed in the following way:

$$T'(f) = P(f)\ (T(f) + Q(f)) \qquad \ldots\ 5.6$$

where $T'(f)$ = measured brightness temperature at frequency f

$T(f)$ = source brightness temperature at frequency f

$P(f)$ = term representing error in brightness temperature scale

$Q(f)$ = term representing error in brightness temperature zero

Also

$$T(f) = T_G(f) + T_E(f) + T_3 \qquad \ldots\ 5.7$$

where $T_G(f)$ = galactic component

$T_E(f)$ = nonthermal extragalactic component

T_3 = thermal extragalactic component

Using Equations 5.6 and 5.7, the following equation results:

$$T'(f) = P(f_1) / P(f_2) \cdot K_G \cdot T'(f_2) + P(f_1) \cdot \\ \cdot \Big[(K_E - K_G)\, T_E(f_2) + (1 - K_G)\, T_3 + \\ + Q(f_1) - K_G Q(f_2) \Big] \qquad \ldots\ 5.8$$

or

$$K_G' \equiv T'(f_1) / T'(f_2) \\ = P(f_1)/P(f_2)\, K_G + P(f_1)/T'(f_2) \cdot \\ \cdot \Big[(K_E - K_G)\, T_E(f_2) + (T_3 + Q(f_1) - K_G\, (T_3 + Q(f_2)) \Big] \\ \ldots\ 5.9$$

The maps of so-called galactic spectral index, (Figure 5.1), are effectively maps of the quantity log K_G', with the factor T_3 set equal to zero and the quantities $T'(f_1)$ and $T'(f_2)$ representing measured brightness temperatures after subtraction of the 3 K thermal extragalactic component. Hence, an investigation of the errors in these maps need only examine factors which would tend to make K_G' different from the true galactic spectrum, K_G. These factors are shown in Equation 5.9.

As would be expected, any errors in the brightness temperature scale at either frequency have a direct multiplying effect on the spectral ratio. The 408 MHz survey brightness temperature scale is claimed to be correct to better than 10%, whilst the 820 MHz survey has a figure of 6%. This leads to a maximum error of ±0.2 in an absolute spectral index of 2.5. Although this is a rather large uncertainty in the absolute spectral index, it is constant across the map and therefore will not mask any spatial variations of spectral index. This is, however, not the case with the other terms in Equation 5.9. Due to these terms an error is introduced, the effect of which varies with the level of brightness temperature.

Using the results of Bridle (1967), and an estimate of 2.5 for the galactic spectral index, a value for the term $(K_E - K_G)\ T_E(f_2)$ of about 0.4 is obtained. The effect of this term is to give higher values for the measured spectrum in regions of low brightness temperature. There appears to be no evidence for such an effect in the maps of Figure 5.1. As the term $T'(820)$ is never less than 2 K, the error in spectral index due to this term is always less than 0.1.

The remaining terms in Equation 5.9 show the effect of errors in the zero levels of the two surveys. It is of interest to determine the magnitude of these zero errors required to explain some of the features on the spectrum maps. Assuming that the brightness temperature scales of the two surveys are correct, Equation 5.9 reduces to:

$$K_G' = T'(408)/T'(820) = K_G + Z/T'(820) \quad \ldots \; 5.10$$

where $Z = Q(408) - K_G Q(820) + \left[(K_E - K_G)\, T_E(820) \approx 0.4\right]$

Because of the limited variation of K_G, in the following discussion Z is assumed to be a constant.

In the region above $b_{II} = 60^\circ$ there is a direct correlation between spectral index and brightness temperature. As the brightness temperature increases so does the spectral index. By taking points from this region and substituting in Equation 5.10, it is found that a value of Z of approximately -6 K is required to explain the spectral index variations. The spectral index across this region is then approximately 2.7. Such a zero error can be explained in terms of the quoted zero level errors of the two surveys, which require Z to lie in the range ±7 K.

If such a large zero error is in fact present, a correlation between spectral index and brightness temperature should be obvious in brighter regions of the spectrum maps. This is seen to be not always the case. For example, along the line of $l_{II} = 32^{\circ}$, from $b_{II} = 18^{\circ}$ to $b_{II} = 50^{\circ}$, the value of $T'(820)$ increases from 7 K to 14 K, however the spectrum is very constant, lying between 2.5 and 2.55. If the value of Z = -6 K is applied in this region, the spectral index is found to change gradually from 2.65 at $(l_{II}, b_{II}) = (32^{\circ}, 18^{\circ})$ to 2.75 at $(32^{\circ}, 50^{\circ})$. This is exactly what would be expected if the zero level error was estimated incorrectly.

These results could imply that there is position dependent zero level error in one of the surveys. There seems to be no reason to suspect this in the 820 MHz survey. However, at 408 MHz, a declination dependent term could be present due to incorrect ground radiation removal. To test this, a T-T plot was made of the region $b_{II} = 50^{\circ}$, $l_{II} = 15^{\circ}$ to $l_{II} = 40^{\circ}$.

It can be seen from Equation 5.10, that if $T'(408)$ is plotted against $T'(820)$ for a number of positions, contained within a region of constant spectral index, a straight line should result, the slope of which is the spectral index. Furthermore, the intercept on the $T'(408)$ axis is the quantity Z. This method has been used by a number of authors in studying spectral index (e.g. Turtle et al. (1962), Yates (1968), Landecker (1969)).

The region mentioned above is at approximately the same declination as the region $b_{II} \geq 60^{\circ}$. In the spectrum maps, the spectral index is roughly constant, and the range of brightness temperature is small enough, that a value of Z = -6 K produces a small change in spectrum across the region (< 0.06). Hence it was assumed that this is a region of constant galactic spectral index, which is required to make the T-T plot meaningful. A least squares method was used to find the line of best fit to the temperature pairs, the result being:

$$T'(408) = 6.06\ (\pm 0.3) \cdot T'(820) - 1.4\ (\pm 3.0)$$

hence $K_G = 6.06 \pm 0.3$; $\beta = 2.58 \pm 0.7$; $Z = -1.4 \pm 3.0$

This result would appear to rule out the existence of a zero error as large as -6 K. Furthermore, the spectral index so determined is close to the value in the spectrum maps, which would be expected if there is no significant zero error.

To test this method further, a number of other T-T plots were made of regions in the spectrum maps where the spectral index appears constant. The results of the least squares best fit straight lines in these regions are shown in Table 5.1. In all cases, the spectral index found from the slope of the T-T plot (the so-called differential spectral index) is the same (within 0.05) as the absolute spectral index shown in the spectrum maps. This fact, combined with the values of Z obtained, would appear to rule out the existence of any large zero error in the regions covered.

TABLE 5.1

ℓ_{II}	b_{II}	δ	K_G	β	Z
15° - 40°	50°	10° - 25°	6.06 ± 0.3	2.58 ± 0.07	-1.4 ± 3.0
25° - 37°	18°	1° - 11°	5.76 ± 0.13	2.51 ± 0.04	+2.1 ± 1.7
32°	18° - 50°	8° - 20°	6.01 ± 0.10	2.57 ± 0.02	-1.1 ± 1.2
20° - 31°	10°	-7° - 3°	6.16 ± 0.28	2.61 ± 0.06	+0.6 ± 4.6
37°	3° - 11°	5° - 9°	6.22 ± 0.09	2.62 ± 0.02	+1.0 ± 1.5

To summarize, it has been shown that the second term in Equation 5.9 is smaller than is required to be able to explain the structure apparent in the spectral index maps of Figure 5.1. Hence the conclusion is that the spectral structure shown is real.

5.5 Discussion of Spectrum Maps

If a comparison is made between the spectrum maps of Figure 5.1 and the 408 MHz brightness temperature maps of the same area (Figure 5.2), it is immediately apparent that there is relatively very little structure to be seen in the spectrum maps. The galactic plane, at $b_{II} = 0^{\circ}$, stands out plainly, but at high galactic latitudes, in theregion of the North Polar Spur, the spectrum maps show very little small scale structure.

A detailed discussion of the spectral properties of these two regions now follows.

5.5.1 North Polar Spur

The North Polar Spur is the most prominant large scale, high latitude feature of the radio sky.

It is seen as a region of enhanced emission, bounded by a steep outer edge, which is plainly seen on the 408 MHz survey maps, running from R.A. 13 00 to 16 00 at a declination of approximately $+20^{\circ}$, and then at lower galactic latitudes along a line of constant galactic longitude of approximately 35°. Regions situated towards the galactic centre, from the edge, are considered to be inside the North Polar Spur.

In the spectrum maps of Figure 5.1, the outer edge of the North Polar Spur, shown as a broken line, follows very closely the $\beta = 2.45$ contour. This line marks a very definite change in the spectral index. Inside the spur, the spectrum is approximately constant at around 2.5, falling to 2.45 at the end of the ridge at RA 13 30. Beyond the edge, it falls abruptly with the corresponding fall in brightness temperature. A similar, but less marked decrease in spectral index occurs on the other side of the main ridge of the spur, in the area around $l^{II}, b^{II} = 17^{\circ}, 28^{\circ}$.

The North Polar Spur shows a profusion of fine structure, mainly in the form of elongated ridges both parallel and perpendicular to the outer edge. These ridges were first reported by Haslam, Large and Quigley (1964) and have been catalogued by Holden (1969) and

Berkhuijsen (1971). The convolved 408 MHz maps of Figure 5.2 show a number of these ridges, for example at l^{II}, b^{II} = 31°, 38° and l^{II}, b^{II} = 24°, 35°. There is no corresponding structure to be seen in the spectrum maps. The position of the most prominent feature of the spur, the narrow neck, at l^{II}, b^{II} = 30°, 15°, is indicated in the spectrum map. There is evidence here of corresponding structure in the spectrum, running parallel to the narrow neck. To either side of this feature there are very steep temperature gradients which are not always resolved by the 37' arc beam of the 408 MHz survey, nor, according to Holden (1969), by the 25' arc beam of the 178 MHz survey of Caswell, Crowther and Holden (1967). It is possible that the structure appearing in the spectrum maps is due to small errors in the convolution process, accentuated by these very steep temperature gradients, and so care should be exercised in interpreting this as real variations in spectral index. The conclusion must be that the spectral index shows very little spatial variation, and none that can be definitly linked with intensity features.

The spectral index maps show that the average spectral index inside the spur is somewhat greater than that of the underlying background. This is further illustrated by the T-T plots shown in Figure 5.3, where forthe same temperature at 408 MHz, the 820 MHz temperature of points inside the spur is less than for points outside. Exactly the opposite effect was found by Berkhuijsen (1971) in a spectral comparison of the 820 MHz survey with the 240 MHz survey of Haslam et al. (1964). She made a number of T-T plots, at constant latitude, between longitudes 15° and 45°, and concluded that for the same temperature at 240 MHz, the 820 MHz temperature inside the spur was higher, indicating a lower total spectrum inside the spur. The same result was obtained by Landecker (1969) in his total spectrum maps between 85 MHz and 150 MHz. He also finds a relatively low spectrum on the main ridge of the spur. The differences between the present results and those of Landecker could be explained in terms of a variation in spectral index with frequency. However, the discrepancy between the 240 - 820 comparison and the 408 - 820 comparison is not so readily explained.

In an attempt to explain this discrepancy, a total spectrum map between 240 and 408 was made. The 240 MHz map was made available in computer readable form by Dr. G. Haslam. The equivalent 408 MHz maps were convolved to the 1.4° x 1.0° resolution of the 240 MHz survey, and then a point by point spectrum was taken,

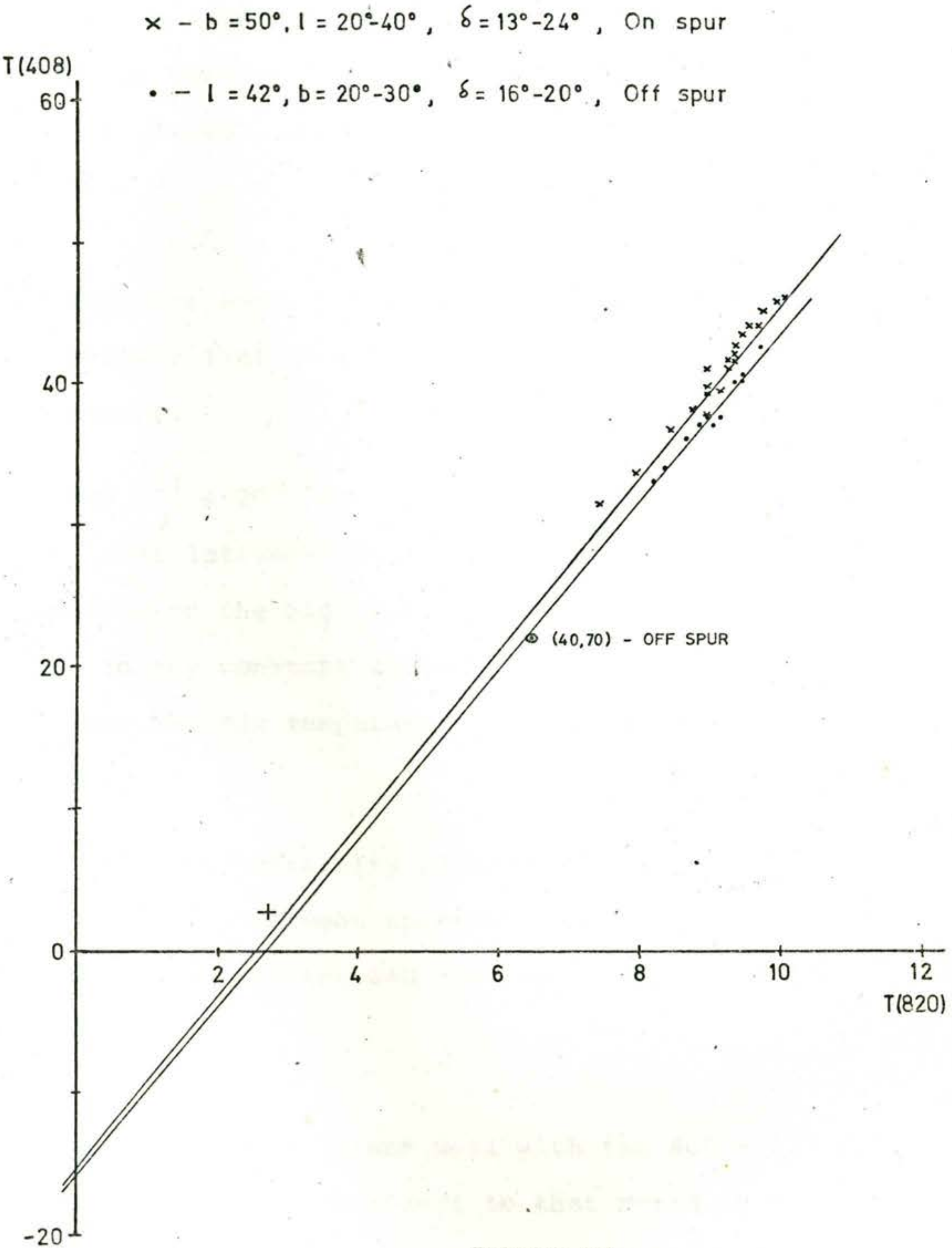
× – b = 50°, l = 20°-40°, δ = 13°-24°, On spur
• – l = 42°, b = 20°-30°, δ = 16°-20°, Off spur
T(408)
60
40
20
0
-20
2
4
6
8
10
12
T(820)
(40,70) - OFF SPUR

FIGURE 5.3

resulting in a spectral index map covering the region $l^{II} = 15^{\circ}$ to 45° and $b^{II} = 10^{\circ}$ to 30°. This map is difficult to interpret due to the fact that the 240 MHz map was not absolutely calibrated. However, the following general conclusions can be drawn from this comparison.

1. Inside the spur, there is no small scale spectral structure that corresponds to any of the intensity features.
2. Above $b^{II} = 20^{\circ}$, regions on the edge of the ridge at lower latitudes have a lower spectral index than regions on the high latitude side. This cannot be due to any constant zero error in the 240 MHz survey, as the 240 MHz temperatures of the two regions are equal.
3. In the lower intensity regions, there is a direct relationship between spectral index and intensity indicating that the 240 MHz temperatures are too high.

The first point agrees well with the 408 - 820 comparison. No similar effect to that noted in 2. is found in the 408 - 820 spectral maps. This does, however, agree with the results of Berkhuijsen, although she has interpreted them as differences in the spectral index of regions on and outside the main ridge of the spur. They would appear to be rather differences in the spectrum of regions to either side of the ridge peak but still on the ridge, as noted in 2. In fact Figure 7 from Berkhuijsen (1971), reproduced here as Figure 5.4, shows the opposite effect to that stated by that author. For equal temperatures at 240 MHz, the region inside the ridge (e.g. at $l^{II} = 36^{\circ}$) has a lower 820 MHz temperature than the region outside. This is equivalent to a higher spectral index inside the spur, as found in the 408 - 820 comparison. Berkhuijsen also states that the differential spectrum between 240 MHz and 820 MHz is the same inside and outside the spur. This is not the case between 408 MHz and 820 MHz. A T-T plot of points along $b^{II} = 27^{\circ}$ from $l^{II} = 15^{\circ}$ to 45° gives the following best fit straight lines.

a) All points $T'_{408} = 6.43 \cdot T'_{820} - 6.6$, $\beta = 2.67$

b) On ridge $T'_{408} = 6.19 \cdot T'_{820} - 3.6$, $\beta = 2.61$

c) Outside ridge $T'_{408} = 5.62 \cdot T'_{820} - 1.0$, $\beta = 2.47$

The large zero error in a) indicates that it is probably not valid to attempt to fit a straight line to

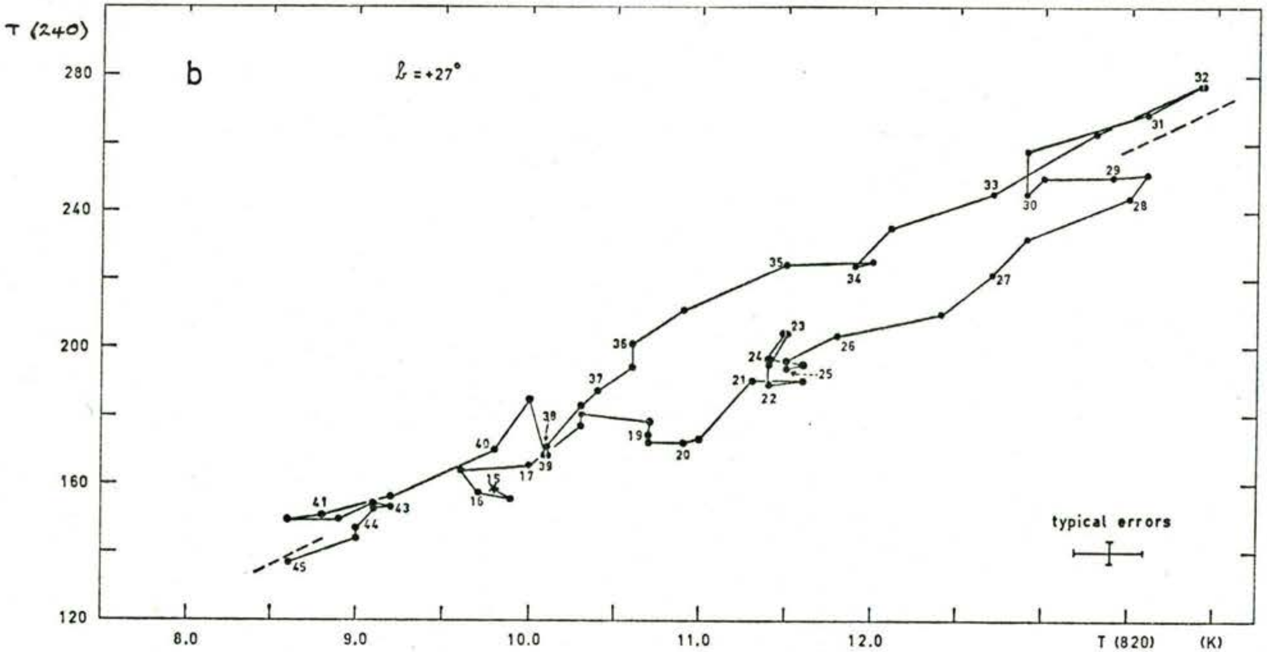

Fig. 7. Brightness temperatures at 240 MHz plotted against brightness temperatures at 820 MHz of points at two constant latitudes in the North Polar Spur (Loop I), between $l = 15°$ and $45°$. Longitudes of points are indicated. The mean line through a plot is shown by the broken lines

FIGURE 5.4

all points, as done by Berkhuijsen (1971). The difference in differential spectrum between b) and c) agrees well with the spectral index maps. The fact that the effect noted in 2. (above) only occurs in comparisons using the 240 MHz survey must cast doubt on the accuracy of this survey in this region.

In the region R.A. = 13 00 - 14 00, the edge of the spur is very well defined on the intensity map of Figure 5.2. Also the background is relatively flat so that the increase in temperature going onto the spur can be accurately measured, at both 408 MHz and 820 MHz. The differential spectral index of this step is found to be 2.80 ± 0.05. Because of the smooth background in this area, this is probably the best estimate that can be made of the spectral index of the radiation from the spur alone.

In the region of the spur, the present spectrum maps appear in general quite different from those of Landecker (1969) between 85 MHz and 150 MHz. For example, the region of low spectrum just off the ridge at $(l^{II}, b^{II}) = (20^{o}, 25^{o})$ on the present maps appears as a region of high spectrum on Landecker's maps. His measurements generally do not extend far enough north in declination to give a spectrum of the region outside the edge of the spur, although there are indications that this could have a higher spectrum. Once again, this is the opposite to what is found in the present spectrum maps. As there appears to be very little small scale structure in the spectral index, it would be difficult to explain these differences in terms of a resolution effect. The conclusion must be that the spectral index of the spur is frequency dependent, being lower than the general background between 85 MHz and 150 MHz, and higher than the background between 408 MHz and 820 MHz.

5.5.2 The Spectral Index at Low Galactic Latitudes

From the edge of the map at $l^{II} = 26^{\circ}$ up to $l^{II} = 55^{\circ}$, the galactic plane is seen clearly on the spectral maps as a band of low spectral index, approximately 3° wide in latitude. When the strong low spectrum sources at $l^{II} = 31^{\circ}$ and 35.5° are removed, the width of the low spectrum feature is seen to remain fairly constant with longitude, although it gradually becomes weaker with increasing longitude. This would imply that the thermal radiation from extended ionised hydrogen falls more steeply with increasing longitude than the non-thermal radiation. The fact that the feature extends out to 55° indicates that the extended HII is contained within a disk which has approximately the same radius as the non-thermal disk (Baldwin (1966)).

At $l^{II} = 57^{\circ}$, the spectral trough disappears and the spectrum on the plane is the same as at higher latitudes. At $l^{II} = 60^{\circ}$ there is once again a region of low spectrum, corresponding in position with the thermal source W55 (Westerhout (1958)). At higher longitudes, there is no apparent structure in the spectral maps at $b^{II} = 0^{\circ}$.

A feature of the low latitude spectral index away from the galactic plane is the region of relatively high spectrum in the region $25^{\circ} < l^{II} < 45^{\circ}$, $+3^{\circ} < b^{II} < 12^{\circ}$. The spectral index reaches its highest value in this region. On the negative latitude side of the galactic plane, the equivalent region has a significantly lower average spectral index. At higher latitudes, the spectrum on opposite sides of the galactic plane is approximately the same. It is perhaps significant that this region of high spectral index lies approximately at the point where the North Polar Spur appears out of the galactic plane. Although this region lies mostly outside the edge of the spur, it has been suggested in the past (Holden (1969)) that there is evidence of structure beyond this edge that is associated with the spur. In the region of high spectral index which lies outside the edge of the spur, there is no evidence of any corresponding intensity feature on the 408 MHz maps, although the ridge at (37°, $+13^{\circ}$) emerges from this region and appears to join the spur edge at approximately $b^{II} = 19^{\circ}$.

5.6 Conclusions

A map has been produced of Spectral Index between 408 MHz and 820 MHz. An investigation has been made of the accuracy of this map, with the conclusion that the map gives a true representation of the spatial variation of the spectral index of the galactic background radiation.

The results show that, except for the larger features (the galactic plane and the north polar spur), there is no correlation between brightness temperature features and spectral variations.

The north polar spur has been shown to have a higher spectrum than the background, a fact which disagrees with earlier results at lower frequencies.

An interesting region of high spectral index has been found at low galactic latitudes below the narrow neck of the north polar spur.

CHAPTER 6

THE STRUCTURE OF GALACTIC RADIO RADIATION AT 408 MHZ

6.1 Introduction

This chapter contains a discussion of the structure of the galactic radio radiation at 408 MHz as revealed in the Bonn Survey and the first part of the Southern Sky Survey. These two surveys are, on the present day scale, medium resolution surveys. Although it would be of great interest to map large areas of the sky at high resolution and high sensitivity, the time required to complete such surveys is not available on modern radiotelescopes. Hence the high resolution surveys must be confined to relatively small areas. It is in regions outside these restricted areas where the medium resolution surveys provide their most useful information. The discussion in this chapter will concern itself mainly with these regions.

6.2 The Galactic Plane

The galactic plane appears on the Bonn 408 MHz survey in the latitude (l^{II}) range 24° to 90°. The width of the radiation from the galactic plane decreases with increasing longitude to a minimum at approximately 57°, after which itincreases once again onto the Cygnus X complex at $l^{II} > 70°$.

The decrease at $l^{II} = 55°$ has been interpreted by Baldwin (1967) as the direction which the line of sight is tangential to the central non-thermal disk. Alternatively, Mills (1959) has suggested that the non-thermal radiation is mainly confined to the spiral arms, so that steps would be seen in the non-thermal radiation at directions where the line of sight is tangential to the edge of the arms. The step at $l^{II} = 55°$ then agrees well with the edge of the Sagittarius arm at $l^{II} = 51°$ (Burton (1970)). Mathewson et al. (1962) made a search for such steps in the non-thermal radiation and concluded that there was no good correlation with the spiral structure determined from measurements of HI. Komesaroff (1966) interpreted the non-thermal step at $l^{II} = 326°$ as the outer edge of a ring like structure, rather than a conventional spiral structure. He also reported a non-thermal step at $l^{II} = 34°$ as the other edge of this ring. The present observations at 408 MHz show no evidence for a step at 34°, nor do the 820 MHz studies of Berkhuijsen (1971). She attempted a comparison of the continuum profile at

$b^{II} = 0^{\circ}$ with the HI brightness between -150 km s^{-1} and $+150$ km s^{-1} from Burton (1970). The only really convincing correlation was found at $l^{II} = 55^{\circ}$, where the pronounced continuum step, mentioned above, occurs. Otherwise, the results were confused by the intense small diameter sources along the galactic plane. Meaningful results in this direction will probably only be obtained when the contribution from these sources is first subtracted before the comparison is made. For this purpose, the present results lack sufficient resolution. However, this has been done by Green (1974), private communication, but the results are not yet available.

6.3 The North Polar Spur

A number of medium resolution surveys of the North Polar Spur region have been made (e.g. Haslam, Large and Quigley (1964), Large, Quigley and Haslam (1966), Caswell, Crowther and Holden (1967), Berkhuijsen (1972)) and from these surveys certain distinct features have been recognised. These are the northern edge, the narrow neck, the ridges and the steps.

6.3.1 The Northern Edge

The northern edge of the spur appears on the 408 MHz maps along its whole length from (R.A., Dec.) = (13 00, +15°) to (17 50, +8°). From (13 25, +20°) to (14 00, +23°) the edge appears to be unresolved by the 37' arc beam. Holden (1969) reports that at 178 MHz the edge in this region is generally resolved. Hence the size of structure of the edge must be between 11' arc and 20' arc. The positions of the edge at 38 MHz (Williams, Kenderdine and Baldwin (1966)), 178 MHz and 408 MHz have been measured in this region and are found to agree within the measurement errors. Later than 14 00 the edge is generally resolved at 408 MHz until it becomes very sharp again at (16 50, +17°). At (17 00, +15°), the outer edge bulges out beyond a smooth continuation of its path up to that point and does not join it again until the narrow neck at (17 55, +5°).

6.3.2 The Ridges

The very complicated structure within the outer edge of the spur has been classified by previous authors in terms of ridges and steps. The ridges have been catalogued and investigated by Holden (1969). She concluded that most of the ridges reported by earlier workers are associated with three main ridges. These are the main ridge of the spur, bounded on the northern side by the outer edge, and two minor ridges which she called South Ridge 1 and South Ridge 2. The positions of these two ridges, as given by Holden, are:

South Ridge 1: (16 40, +8°) through (15 40, +9°) to (15 00, +5°)
South Ridge 2: (14 30, +10°) through (13 00, +5°) to (12 30, -1°)

Both these ridges appear on the 408 MHz maps, although South Ridge 2 does not extend further west than (13 50, +10°). The associations suggested by Holden between ridges from previous authors and these three main ridgesare generally born out by the 408 MHz results. There are, however, a number of ridges on the 408 MHz maps that appear to be distinct from the three main ridges.

There is a very narrow prominant ridge extending from (17 00, +7°) to (16 45, +3°). This region has not been observed at 178 MHz, but the ridge is plainly visible on the 820 MHz maps of Berkhuijsen (1972). At the lower end the edges appear to be unresolved at 408 MHz.

A very much broader ridge extends from (17 15, -4°) to (16 45, $+3^{\circ}$). This ridge is also present in the 240 MHz maps of Haslam et al. (1964) and the 820 MHz maps of Berkhuijsen. The southern edge of this ridge appears to join the southern edge of South Ridge 1 and together they form the southern boundary of the radiation of the spur. The ridges reported by Large et al. (1966), south of this edge, are not substantiated by either the 178 MHz or 408 MHz maps.

A ridge appears at 408 MHz at (15 30, $+13^{\circ}$), which is between South Ridge 1 and the main ridge of the spur. This ridge is very faint at 178 MHz, but was included in the list of ridges given by Large et al. Gradients were also observed in this region by Merkelijn and Davis (1967) at 1415 MHz. It may be that this ridge is connected with a projection from the main ridge of the spur at (16 20, $+14.5^{\circ}$). It is interesting to note that if the path followed by this ridge is extended eastwards, it meets the western end of South Ridge 2, as given by Holden. Apart from this very tenuous association, it would appear that this "central" ridge is an important feature distinct from the three main ridges of Holden.

6.3.3 The Steps

Holden also reported the existence of steps within the spur. These features, which are distinct from the ridges, had not been recognised before owing to the lower resolution of previous surveys. The steps appeared on the 178 MHz maps of Caswell et al. (1967) as sharp gradients of intensity joining two relatively flat regions. They were found to be typically 6° in length and merging into the general background at either end. Holden gives a list of the more prominent steps which have been investigated using the 408 MHz maps, with the following results.

(a) (13 16, +19°) to (14 00, +24°): This is part of the outer edge of the spur and can be followed far beyond (14 00, +24°) where it runs off the map of Caswell et al. It seems unreasonable to classify this part of the outer edge as a separate feature even though the temperature gradients are particularly sharp in this region.

(b) (13 48, +20°) to (14 20, +20°): This is part of the steep northern edge of the main ridge of the spur. It would appear to be much larger than stated by Holden, and in fact joins onto step (d) (see below).

(c) (14 24, 15°) to (14 48, 15°): At (14 25, 15°) there is a slightly steeper portion of the gradual gradient up onto the main northern ridge, but it does not extend for any length at 408 MHz.

(d) (14 40, 19.5°) to (15 12, 19.5°): See (b) above.

(e) (15 24, 07°) to (15 48, 07°): This is a part of the southern edge of the southern ridge, the continuation of which was effected by the sidelobes of HerculesA in the 178 MHz maps.

(f) (15 32, 16.5°) to (15 44, 16.5°): This is a part of the southern edge of the northern ridge, which extends to about (15 00, 18°) at 408 MHz. There is a similar gradient appearing on the 408 MHz maps just to the south of (f) centred at (15 35, 11.5°). There is no evidence of this feature on the 178 MHz maps.

(g) (16 20, 09°) to (16 36, 09°): This is the northern edge of the narrow ridge, which Holden likened to the narrow neck of the spur. The 408 MHz and 178 MHz results agree well.

(h) (16 24, 13°) to (16 36, 13°): This is the southern edge of a ridge of which the northern edge at

(16 25, 16.5°) is a similar step which is not as apparent on the 178 MHz maps.

(i) (16 28, 19°) to (17 16, 19°): On the 408 MHz maps there is a temperature gradient on this region, but no apparent step.

(j) (16 28, 19°) to (17 16, 19°): This is a particular steep part of the outer edge

(k) (17 00, 13.5°) to (17 20, 11°): This is the northern edge of the main ridge of the spur and joins onto the steps (o) and (q).

(l) (17 00, 11.5°) to (17 12, 10.5°): There is no evidence of a step here but there is a step like feature running south from (17 00, 12°) to (17 00, 8°). This region has been effected by sidelobe responses in the 178 MHz maps. It is possible that this gradient is associated with the prominent ridge mentioned previously.

(m) (17 28, 15.5°) to (17 44, 15.5°): There is no apparent step at 408 MHz in this region beyond the outer edge of the spur.

(n) (17 24, 7.5°) to (17 52, 2.5°): This is the southern edge of the main ridge of the spur, and extends down to at least declination 0°.

(o) (17 32, 12°) to (17 52, 09°): See (k) above.

(p) (17 36, 8.5°) to (17 52, 08°): A feature inside the main ridge, probably extending through to meet step (k) at (17 20, 11°).

(q) (17 52, 06°) to (18 00, 03°): See (k) above.

(r) (18 00, 03°) to (18 12, 03°): Holden states that this step is probably associated with the galactic disk radiation, although it could be continuation of the step (q) and the outer edge.

This completes the list of prominent steps as given by Holden. This is by no means a complete list as there are many other steep gradients associated with the spur similar to those discussed above. What is clear from the 408 MHz maps is that these steps are in almost every case part of a much larger feature, usually being the edges of prominent ridges. This argues against

Holden's statement that the steps are distinct features of the radiation of the spur.

6.3.4 The Narrow Neck

The Narrow Neck of the spur is seen as an intense narrow ridge at (17 55, $+3.5^\circ$). The two edges appear to be unresolved, but the feature has a somewhat flattened peak, showing that its width is of the order of 1°. Holden concluded that there was no evidence of continuation of the spur below $b^{II} = 11^\circ$, but Berkhuijsen et al. (1971) claim to be able to follow it down to $b^{II} = 8^\circ$ at 408 MHz and $b^{II} = 6^\circ$ at 820 MHz. The present 408 MHz maps also show a spur like feature extending from $(l^{II}, b^{II}) = (25^\circ, +6^\circ)$ to meet the lower end of the narrow neck at $(28.5^\circ, +11^\circ)$, although it must be noted that a similar spur occurs at somewhat lower longitude and appears not be associated with the spur.

6.3.5 The Small Circle of the North Polar Spur

It has long been known that the main ridge of the North Polar Spur is a very good fit to a small circle whose parameters have been recently given as;

radius 58° centred at $(l^{II}, b^{II}) = (329^{\circ}, +17.5^{\circ})$ (Salter (1970)). The apparent circular geometry of the spur led to the proposal that it is a remnant of a supernova outburst. This theory has received some support recently e.g. Berkhuijsen et al. (1971), Berkhuijsen (1973). However, a problem with this theory is that it predicts that the spur should also be visible along its small circle path at negative latitudes, which has not been observed to be the case. Yates (1968) has claimed to have found a feature which he associates with the spur at southern latitudes, but his observations lack the resolution needed to make this association conclusive.

The first observing session of the 408 MHz southern sky survey covers a portion of the small circle path of the North Polar Spur, and represents the highest resolution survey of this region, to date. Initial maps made of the region R.A. = 04 30 to 11 00, dec. = -55° to -85° have been examined for any structure that might be associated with the small circle of the spur, with negative results. It must be added, however, that as this area covers only a small section of the small circle path, and as there are many supernova remnants known with incomplete shells (e.g. Cygnus Loop - Appendix 2) this fact cannot be used as direct evidence that the spur is not a supernova remnant. Later stages of the southern sky survey have covered the complete small circle path at negative latitudes, and should give a definite answer to this question.

6.4 Loop II

The existence of Loop II (also known as the Cetus Arc) was first proposed by Large, Quigley and Haslam (1962). The path of the small circle of Loop II (Berkhuijsen, Haslam, and Salter (1971)) can be followed for a part of its length on the Bonn 408 MHz maps.

At the $l^{II} = 50^{\circ}$ end, the small circle enters the map at (21 15, -7°) and passes through (20 45, 0°) to (20 15, $+20^{\circ}$). A narrow ridge is seen on the 408 MHz maps at (20 55, 0°) and runs approximately along this small circle. This ridge is remarkable for its very steep southern edge, which is reminiscent of the very sharp gradients occuring in the North Polar Spur. Another ridge, at (20 50, $+6.5^{\circ}$), also has sharp edges, but appears to run approximately perpendicular to the small circle path. This ridge, as well as the northern edge of the previous ridge, also appear on

178 MHz maps of Caswell et al. (1967). If these gradients are in fact associated with Loop II, it is the first time that such small scale structure has been found in any of the large galactic loops other than the North Polar Spur.

At the $l^{II} = 160^{\circ}$ end of the arc, a broad increase in brightness temperature is seen (e.g. around 02 40, $+22^{\circ}$)), but there is no apparent fine structure. It should be noted that the 408 MHz maps, as presented here, are not ideally suited to following such broad low brightness features. This could be better achieved by smoothing the maps down to a lower resolution as was done for the spectral index determination in Chapter 5. In their present form, the maps are useful for searching for fine structure in known features.

6.5 Loop IV

The existence of Loop IV was first suggested by Salter (1970). He found that a small circle could be fitted to a number of ridges found on the maps of Large et al. (1966) and Seeger et al. (1965). One of these ridges is covered by the present 408 MHz maps and is in fact the South Ridge 2 discussed in Section 6.3.2. In the region R.A. < 13 15, the ridge observed at 408 MHz is a good fit to the small circle proposed by Salter. However, for R.A. > 13 15, the ridge appears to deviate markedly from the small circle path. Holden (1969) claims to be able to follow this ridge even further to the west, up to (R.A., dec.) = (14 30, $+10^{\circ}$), which is even further away from the proposed small circle path. These results would seem to indicate that this ridge is in fact part of the North Polar Spur. If this is in fact the case, then it must raise doubts as to the existence of Loop IV. No other structure along the proposed small circle path is seen in the 408 MHz maps, although this can not be taken as evidence against the existence of Loop IV. Spoelstra (1973) has shown, using Van der Laan's (1962) model of an expanding sphere in a magnetoionic medium, that only parts of the loop will be seen, depending on the angle between the line of sight and the direction of the magnetic field in the undisturbed medium.

6.6 Small Loop Structures

As well as the large galactic loops, having radii of the order of 40°, a number of smaller loops have been found, with radii around 2°. These are, the Lupus Loop (Milne (1970)), the Monoceros Loop (Haslam and Salter (1971)) and the Origem Loop (Berkhuijsen (1974)). The Bonn 408 MHz maps are ideally suited to the study of such low surface brightness, extended sources, so a search has been made of the maps for loop type features. Two possible candidates have been found, these being:

1. The feature centred at (18 55, $+21^{\circ}$). This feature is shown in Figure 6.1. The proposed path of the loop is shown by a broken line. The crosses mark the position of small diameter sources taken from the 4C catalogue (Gower, Scott and Wills (1967)). At low declinations, the feature is confused by the galactic plane emission, and so the path cannot be as easily followed as is the case with the northern ridge. For this reason it is difficult to calculate a flux for the entire loop. The feature is also seen on the 178 MHz maps of Caswell et al. (1967), where the increased resolution does not show any new structure. The agreement between the two maps is extremely good.

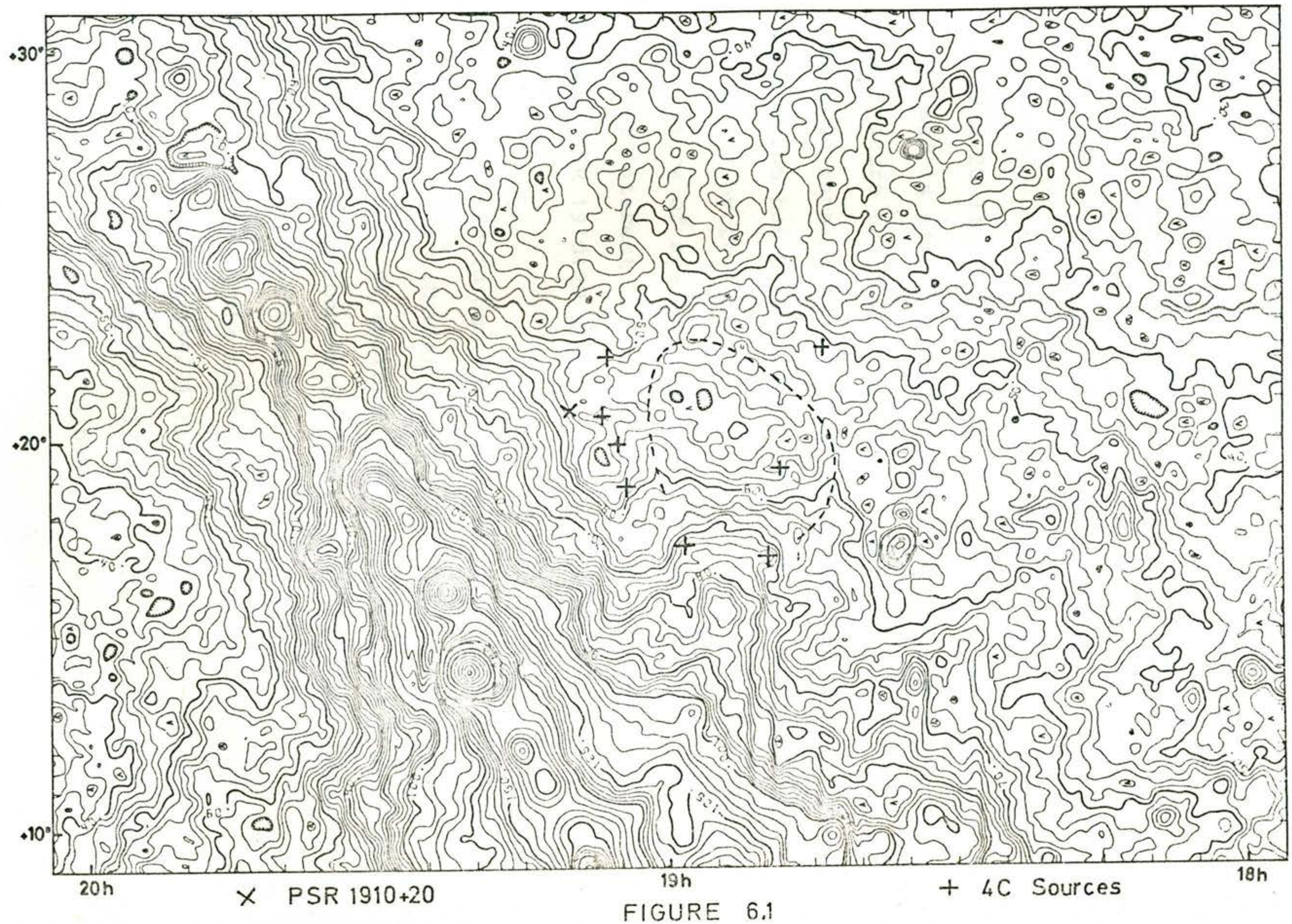

FIGURE 6.1

The fact that the loop is not a circle is not important in light of the fact that many non-circular shell sources are found (e.g. HB 21 - see Appendix 2).

It is of interest to note that a number of pulsars are found in proximity to this feature. The pulsar PSR 1910+20 lies only 2° outside the loop (see Figure 6.1), and is similarly positioned with respect to this feature as the pulsar PSR 0611+22 is to the supernova remnant IC 443 (Schönhardt (1973)). An association has been suggested between PSR 0611+22 and IC 443 by Davies et al. (1972), based on the coincidence of age and distance of these two sources. It is of interest to perform a similar comparison between PSR 1910+20 and the proposed loop.

PSR 1910+20 is quoted to have a dispersion measure of 84 parsec/cm^3 (Davies et al. (1972)), which places it at a distance of approximately 3 kpc (Taylor & Manchester (1974)). If the loop were also at this distance, then its linear diameter would be approximately 260 pc, which places it in the same class as the large galactic loops. Berkhuijsen (1973) has shown that such loops appear to fit reasonably well to the empirical relationship for supernova remnants between the average surface brightness and the linear diameter as derived by

Ilovaisky and Lequeux (1972). Substituting the diameter of 260 pc in this relationship gives an average surface brightness at 1 GHz of the order of 10^{-23} W m^{-2} $sterad^{-1}$ Hz^{-1}. This reduces to an average brightness temperature at 408 MHz of the order of 0.5 K. This would appear to be a somewhat low estimate of the loop brightness. It should be noted, however, that Berkhuijsen found values of 10^{-22} W m^{-2} $sterad^{-1}$ Hz^{-1} for the large galactic loops, which reduces to an average 408 MHz brightness temperature of about 5 K. This is more in agreement with the present small loop, which implies that this loop, if situated at the pulsar distance, would be a reasonable fit to the relationship derived by Berkhuijsen to include the large galactic loops. The conclusion mustbe that an association between the pulsar PSR 1910+20 and the loop cannot be completely discounted.

2. The area of emission at (19 38, +2°). This feature appears as a narrow ridge joining two prominent spurs. In this sense, it is similar to Loop II, but on a very much smaller angular scale. The path of the loop is lost in the galactic plane emission, and therefore cannot be completed, however the diameter is probably about 5°. There are no pulsars in proximity to this feature.

REFERENCES

Adgie, R.L., and Gent, H.: 1966, Nature 209, 549.

Baldwin, J.E.: 1967, I.A.U. Symposium no. 31, 337.

Berkhuijsen, E.M.: 1971, Astron. & Astrophys. 14, 359.

Berkhuijsen, E.M.: 1972, Astron. Astrophys. Suppl. 5, 263.

Berkhuijsen, E.M.: 1973, Astron. & Astrophys. 24, 143.

Berkhuijsen, E.M.: 1974, Astron. & Astrophys. 35, 429.

Berkhuijsen, E.M., Haslam, C.G.T., and Salter, C.J.: 1971, Astron. & Astrophys. 14, 252.

Bridle, A.H.: 1967, Mon. Not. R. astr. Soc. 136, 219.

Burton, W.B.: 1970, Astron. Astrophys. Suppl. 2, 261.

Caswell, J.L., Crowther, J.W., and Holden, D.J.: 1967, Mem. R. astr. Soc. 72, 1.

Condon, E.U.: 1941, Westinghouse Research Report, SR-105.

Davies, J.G., Lyne, A.G., and Seiradakis, J.H.: 1973, Nature Phys. Sci. 244, 84.

Fisher, R.E.: 1973, Trans. IEEE, MTT-21, 355.

Frater, R.H.: 1964, Rev. Sci. Instrum. 35, 810.

Green, A.J.: 1974, Astron. Astrophys. Suppl. 18, 267.

Gower, J.F.R., Scott, P.F., and Wills, D.: 1967, Mem. R. astr. Soc. 71, 49.

and Pilkington, J.D.H., and Scott, P.F.: 1965, Mem. R. astr. Soc. 69, 183.

Haslam, C.G.T.: 1974, Astron. Astrophys. Suppl. 15, 333.

Haslam, C.G.T., Large, M.I., and Quigley, M.J.S.: 1964, Mon. Not. R. astr. Soc. 127, 273.

Haslam, C.G.T., Quigley, M.J.S., and Salter, C.J.: 1970, Mon. Not. R. astr. Soc. 147, 405.

Haslam, C.G.T., Wilson, W.E., Graham, D.A., and Hunt, G.C.: 1974, Astron. Astrophys. Suppl. 13, 359.

Holden, D.J.: 1969, Mon. Not. R. astr. Soc. 145, 67.

Horton, P.W., Conway, R.G., and Daintree, E.J.: 1969, Mon. Not. R. astr. Soc. 143, 245.

Ilovaisky, S.A., and Lequeux, J.: 1972, Astron. & Astrophys. 18, 169.

Jones, E.M.T.: 1954, IRE Trans. Ant. & Prop. AP-2, 119.

Landecker, T.L.: 1969, Ph.D. Thesis, University of Sydney.

Large, M.I., Quigley, M.J.S., and Haslam, C.G.T.: 1962, Mon. Not. R. astr. Soc. 124, 405.

Large, M.I., Quigley, M.J.S., and Haslam, C.G.T.: 1966, Mon. Not. R. astr. Soc. 131, 335.

Komesaroff, M.M.: 1966, Aust. J. Phys. 19, 75.

Kraus, J.D.: 1966, "Radio Astronomy", McGraw-Hill.

Mathewson, D.S., Broten, N.W., and Cole, D.J.: 1966, Aust. J. Phys. 19, 93.

Mathewson, D.S., and Healey, J.R.: 1963, IAU-URSI Symposium No. 20, 245.

Mathewson, D.S., Healey, J.R., and Rome, J.M.: 1962, Aust. J. Phys. 15, 354.

Mathewson, D.S., and Milne, D.K.: 1965, Aust. J. Phys. 18, 635.

Merkelijn, J.K., Davis, M.M.: 1967, Bull. astr. Inst. Netherl. 19, 246.

Mills, B.Y.: 1959, "Paris Symposium on Radio Astronomy", Stanford Univ. Press, p. 431.

Pauliny-Toth, I.I.K., and Shakeshaft, J.R.: 1962, Mon. Not. R. astr. Soc. 124, 61.

Price, R.M.: 1969, Aust. J. Phys. 22, 641.

Salter, C.J.: 1970, Ph.D. Thesis, University of Manchester.

Schönhardt, R.E. 1973, Nature Phys. Sci. 243, 62.

Seeger, Ch.L., Westerhout, G., Conway, R.G., and Hoekema, T.: 1965, Bull. astr. Inst. Netherl. 18, 11.

Spoelstra, T.A.Th.: 1973, Astron. & Astrophys. 24, 149.

Stankevich, K.S., Wielebinski, R., and Wilson, W.E.: 1970, Aust. J. Phys. 23, 529.

Taylor, J.H., and Manchester, R.N.: 1974, "The Five College Radio Astronomy Observatory Pulsar List".

Thaddeus, P.: 1972, Ann. Rev. Astron. & Astrophys. 10, 305.

Turtle, A.J., Pugh, J.F., Kenderdine, S., and Pauliny-Toth, I.I.K.: 1962, Mon. Not. R. astr. Soc. 124, 297.

Van der Laan, H.: 1962, Mon. Not. R. astr. Soc. 124, 125.

Westerhout, G.: 1958, Bull. astr. Inst. Netherl. 14, 215.

Williams, P.J.S., Kenderdine, S., and Baldwin, J.E.: 1966, Mem. R. astr. Soc. 70, 53.

Yates, K.W.: 1968, Aust. J. Phys. 21, 167.

Yates, K.W., Wielebinski, R., and Landecker, T.L.: 1967, Aust. J. Phys. 20, 595.

Zinz, W., and Haslam, C.G.T.: 1972, Kleinheubacher Berichte 15, 385.

APPENDIX 1

Reprinted from the
AUSTRALIAN JOURNAL OF PHYSICS

RADIO SKY BACKGROUND STUDIES USING THE MOON AS A SCREEN

By K. S. Stankevich,* R. Wielebinski,†‡ and W. E. Wilson†

[*Manuscript received November* **3,** 1969]

Abstract

The Moon is a celestial object of well-defined temperature and size which in its passage through the Galaxy screens various areas of galactic emission. Measurements of the background temperature using the Moon as a screen have been made at 408 and 635 MHz with the 210 ft radio telescope at Parkes. The measurements required the determination of accurate temperature differences at both frequencies and of an absolute beam temperature at a selected calibration point. The results indicate small-scale spectral variations in the vicinity of the galactic plane. A new upper limit is set on the intensity of emission which may originate in an ionized intergalactic plasma at decimetre wavelengths.

I. Introduction

The measurement of absolute radio sky background temperatures presents many problems. The sky temperatures to be measured at microwave frequencies are low, often much below the temperature of the commonly used liquid nitrogen reference. Even when the instrumental calibration problems have been overcome there remains the major problem of the antenna reception characteristic. An antenna receives contributions from a solid angle of 4π sr, the reception level being determined by the antenna polar pattern. Absolute calibrations have been made by Pauliny-Toth and Shakeshaft (1962) at 404 MHz using a 7·5 m diameter paraboloidal reflector. The derivation of absolute full-beam brightness temperatures from antenna temperatures required elaborate corrections for contributions from the ground, from the side lobes, and from the atmosphere. A major achievement in this field was the determination of the 3°K cosmic background (black body) temperature at 4080 MHz by Penzias and Wilson (1965) using a 20 ft horn-reflector antenna. Other observers have confirmed the existence of this quasi-thermal component from millimetre to decimetre wavelengths, invariably using horn antennas (for a summary of results see Wolfe and Burbidge 1969). The reason for the use of horn antennas is the low and highly predictable side lobe structure. However, mechanical problems have so far prevented the construction of horn antennas with very narrow beamwidths.

To overcome the many limitations of absolute temperature measurements, a method using the Moon to screen the radio background was conceived. A set of

---

* Division of Radiophysics, CSIRO, P.O. Box 76, Epping, N.S.W., 2121; on leave from the Gorki Radiophysical Research Institute, Gorki, U.S.S.R.

† School of Electrical Engineering, University of Sydney, Sydney, N.S.W. 2006.

‡ Present address: Max-Planck-Institut für Radioastronomie, Argelanderstrasse 3, Bonn 53, Germany.

Aust. J. Phys., 1970, **23,** 529–39

measurements can be made with the Moon in the beam and after the Moon has moved away from the original observing position. Additional knowledge required is the absolute temperature of a calibration point and the characteristics of the Moon. By a careful choice of observing points and reference points, an absolute background temperature investigation is possible, with the resolution of the lunar disk (diameter $\sim \frac{1}{2}°$) without any of the questionable assumptions which are normally required in absolute calibrations. For many investigations, such as that of the small-scale structure of the galactic emission and of the smoothness of the radio background, narrow beams are essential. For such investigations the lunar screen method is ideal, resulting in an effective beam of $\frac{1}{2}°$ with no side lobes.

A number of investigations can be made once absolute temperatures have been found at two radio frequencies with a $\frac{1}{2}°$ beam. Variations of the galactic background spectral index have been reported at metre wavelengths by Bridle (1967) with a $17° \times 12°$ beam and by Landecker and Wielebinski (1968) at somewhat higher frequencies using a $3° \cdot 5$ beam. To achieve these results in both cases scaled antennas were used which overcame the polar pattern difficulties.

Recent theoretical investigations have speculated on the existence and nature of an intergalactic ionized gas. The mean density of matter in the universe calculated by averaging the material in galaxies gave $\rho \simeq 10^{-30}$ to 10^{-31} g cm^{-3} (van den Bergh 1961). The interpretation of experimental data of the expansion of the universe based on the theory of general relativity (Sandage 1962) showed the density to be near the critical value $\rho_c \simeq 2 \times 10^{-29}$ g cm^{-3}. Consequently an argument has been developed (Doroshkevich, Zeldovich, and Novikov 1967) suggesting the existence of an intergalactic plasma. The work of Weymann (1966) on such an intergalactic plasma predicts a change of spectrum of this emission in the decimetre wavelength region. This discrepancy was predicted to be as much as 10–20% from a thermal 3°K black body spectrum at 1000 MHz, with a gradual increase in discrepancy at lower frequencies. An experimental observation by Howell and Shakeshaft (1967) at decimetre wavelengths placed an upper limit of 2°K for this emission, in addition to the 3°K cosmic microwave background radiation.

The detection of the 3°K cosmic background radiation by Penzias and Wilson (1965) led to the explanation of a "primordial fireball" by Dicke *et al.* (1965). Alternative explanations have recently been investigated by Parijsky (1968) and Wolfe and Burbidge (1969), who attribute the 3°K cosmic background to the emission of many extragalactic sources with unusual spectra. In this case it is important to measure the spectrum of the cosmic background with an aerial of high resolution.

In this paper the method of measurement and results of observations using the Moon as a screen are presented. The radio telescope used for the measurements was the Parkes 210 ft reflector at frequencies of 408 and 635 MHz. In addition, a horn antenna was used at 408 MHz to obtain an absolute temperature for a calibration point. The observations were made in February and May 1969 in directions near the galactic centre. The results indicate small-scale spectral variations in the galactic radio emission. A small upper limit can be placed on the likely contribution from an interplanetary plasma in the decimetre wavelength region. The lunar screen method seems quite suitable for many astronomical investigations and we wish to propose the use of Mars for similar investigations on an even finer scale.

II. Method of Measurement

Measurements of the temperature of the Moon (Fig. 1) made at the Gorki Radiophysical Institute (Troitzky and Krotikov 1968), using the method of comparing the Moon's radiation with the radiation from a cooled black body absorber, show that the Moon has a constant effective temperature in the decimetre wavelength region ($T_{\rm m} = 225 \pm 1 \cdot 3\,^{\circ}{\rm K}$). It was also shown that for wavelengths longer than 3 cm no polarization effects exist. This result allows the use of the Moon as a screen whose temperature is constant.

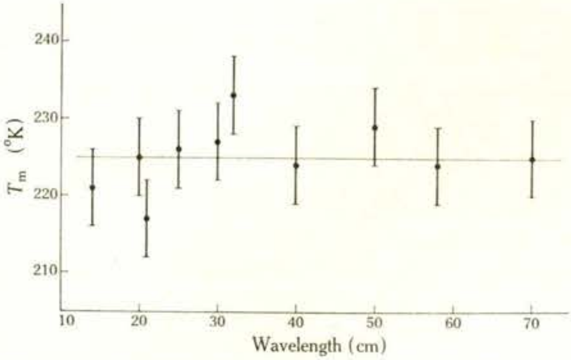

Fig. 1.—Brightness temperature $T_{\rm m}$ of the Moon in the decimetre wavelength region.

Let us consider the separate antenna temperature contributions in a lunar screen experiment. When the Moon is in the main beam of a radio telescope the antenna temperature $T_{\rm A}({\rm m})$ is made up by

$$T_{\rm A}({\rm m}) = T_{\rm A}^{\rm m} + T_{\rm A}^{\rm s} + T_{\rm A}^{\rm a}\,, \tag{1}$$

where $T_{\rm A}^{\rm m}$ is the antenna temperature due to the solid angle $\Omega_{\rm m}$ of the lunar disk, $T_{\rm A}^{\rm s}$ is the side lobe contribution coming from a solid angle $4\pi - \Omega_{\rm m}$, and $T_{\rm A}^{\rm a}$ is the atmospheric contribution from the solid angle $\Omega_{\rm m}$.

Pointing the antenna a little away from the Moon, a reference temperature $T_{\rm A}({\rm r})$ is obtained:

$$T_{\rm A}({\rm r}) = T_{\rm A}^{\rm b}({\rm r}) + T_{\rm A}^{\rm s} + T_{\rm A}^{\rm a}\,, \tag{2}$$

where $T_{\rm A}^{\rm b}({\rm r})$ is the brightness temperature of the point r in the solid angle $\Omega_{\rm m}$. The difference of the two measurements gives

$$\Delta_1 = T_{\rm A}({\rm m}) - T_{\rm A}({\rm r})\,. \tag{3}$$

The above temperature deflection can be accurately determined, as described in Section III.

A further set of measurements of the point m and the reference point r is then made after the moon has moved far away. These measurements yield the deflection

Δ_2 given by

$$\Delta_2 = T'_{\mathrm{A}}(\mathrm{m}) - T_{\mathrm{A}}(\mathrm{r}) \,, \tag{4}$$

where $T'_{\mathrm{A}}(\mathrm{m})$ is the antenna temperature due to the background radiation at the point m in the solid angle Ω_{m}.

The difference between the two deflections is

$$\Delta = \Delta_1 - \Delta_2 = T_{\mathrm{A}}(\mathrm{m}) - T'_{\mathrm{A}}(\mathrm{m}) \,. \tag{5}$$

If the background radiation is uniform over the solid angle Ω_{m}, then

$$\begin{aligned} \Delta &= (T_{\mathrm{m}} - T_{\mathrm{b}}) \exp(-\gamma) \Big(\int_{\Omega_{\mathrm{m}}} F \,\mathrm{d}\Omega \Big/ \int_{4\pi} F \,\mathrm{d}\Omega \Big) \eta \,, \\ &= (T_{\mathrm{m}} - T_{\mathrm{b}}) \exp(-\gamma)(1 - \beta_{\mathrm{m}})\eta \,, \end{aligned} \tag{6}$$

where T_{m} is the absolute temperature of the Moon, T_{b} the absolute background beam temperature, F the antenna polar pattern, γ the atmospheric absorption, η the antenna efficiency, and β_{m} a scattering factor. It is possible to determine T_{b} from equation (6). At decimetre wavelengths the background temperature T_{b} is of the same order as the Moon temperature T_{m} only at low galactic latitudes. So far no assumption has had to be made about the actual antenna polar pattern. To derive the antenna parameters required in (6) a measurement at high galactic latitude is necessary. A high latitude point is chosen from known surveys of the Galaxy with uniform background distribution, where the Moon can be observed some days after the galactic plane crossing. The absolute temperature of this calibration point has also to be measured, e.g. by use of a horn antenna technique.

When the observations of this calibration point are applied to (6), we have

$$(1 - \beta_{\mathrm{m}})\eta = \Delta_{\mathrm{c}} \exp(\gamma_{\mathrm{c}}) / \{T_{\mathrm{m}} - T_{\mathrm{b}}(\mathrm{c})\} \,, \tag{7}$$

where $T_{\mathrm{b}}(\mathrm{c})$ is the brightness temperature of the calibration point with beam Ω_{m} and γ_{c} is the atmospheric contribution at the calibration point. If $\gamma = \gamma_{\mathrm{c}}$, which can be achieved by using the same zenith angle, the combination of (6) and (7) gives

$$T_{\mathrm{b}} = T_{\mathrm{m}} - (\Delta/\Delta_{\mathrm{c}})\{T_{\mathrm{m}} - T_{\mathrm{b}}(\mathrm{c})\} \,. \tag{8}$$

III. Equipment and Calibration Procedures

The aerial used in this investigation was the 210 ft (64 m) fully steerable paraboloidal reflector at Parkes. The feeds for the observing frequencies, 408 and 635 MHz, were orthogonal single $\frac{1}{2}\lambda$ dipoles placed $\frac{1}{4}\lambda$ below the reflecting screen. The dipoles were matched to 50 Ω by adjustment of the dipole length and of the dipole–reflector spacing, using at first a General Radio admittance bridge. Subsequent matching was made using the bridge and reflection techniques incorporated in the receivers.

The receiver for 408 MHz is shown as a block diagram in Figure 2. The dipole feed was joined to a double-stub matching unit MU1 by means of a short length of low-loss cable. A coaxial switch allowed the receiver to be connected to either the feed or to a termination immersed in liquid nitrogen (Wielebinski 1967*a*). The varactor diode switch VS was driven from the switching waveform generator by a 1·2 kHz square wave. The receiver was connected via a matching unit (MU2) to a liquid nitrogen reference termination every half switching cycle. The directional coupler DC2 is the essential part of a reflection matching system. In the matching procedure the varactor switch is first terminated on both sides by two high quality 50 Ω terminations. The matching unit MU3 is adjusted until in both switch positions the reflection is the same and at least 40 dB below open circuit reflection. The inputs are then reconnected to the switch and matched using matching units MU1 and MU2. The preamplifier, a transistor cascode stage with 2 dB noise value, was isolated from input impedance variations by the circulator. The succeeding stages of mixer and 30 MHz i.f. amplifier (8 MHz wide) were followed by a wide dynamic range square law detector and a synchronous demodulator. The antenna temperature deflections were recorded on a Rikadenki pen recorder.

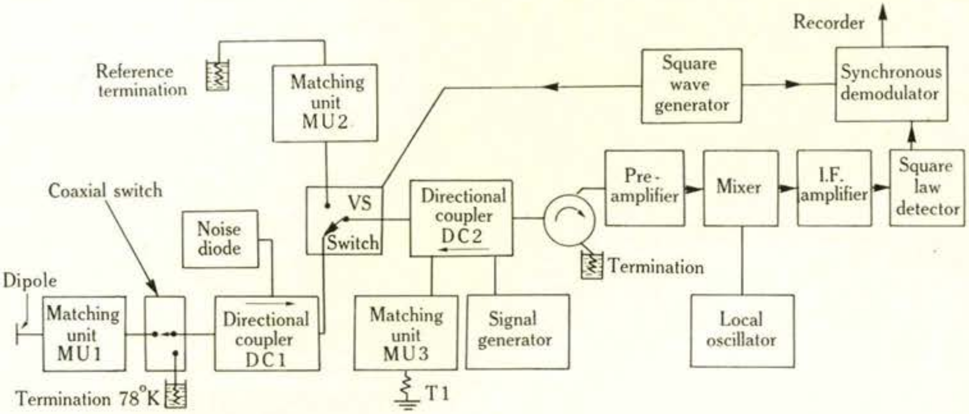

Fig. 2.—Block diagram of the receiver for 408 MHz.

The 635 MHz receiver followed the same general outline, except that the low noise preamplifier was a parametric amplifier with 10 MHz bandwidth. The matching was achieved by using both a General Radio admittance bridge and reflectometer techniques.

The noise temperature calibration was derived from a well-matched liquid nitrogen termination and a set of 1, 2, and 3 dB attenuators (Weinschel model 50). The procedure for temperature calibration is first to replace the feed by the matched termination. Subsequent insertion of the matched attenuators allows the derivation of the temperature scale by the well-known formula

$$T_{\mathrm{e}} = \alpha T_{\mathrm{i}} + (1-\alpha) T_0 , \tag{9}$$

where T_{e} is the effective temperature, T_{i} the input temperature, T_0 the temperature of the lossy components (attenuators), and α the attenuation coefficient. The use of three attenuators allowed extrapolation of the calibration curve of the 408 MHz receiver to give the effective temperature of the liquid nitrogen termination, inclusive of lossy components, as

$$T_{\text{term}} = 79 \pm 0\cdot 5\,^{\circ}\text{K}.$$

During the observations the following procedure was used. At the beginning of each observing period a session of impedance matching was carried out. Each termination was measured (five in number for the two frequencies), using a *GR* admittance bridge, and found to be matched to better than 1·05 vswr. Prior laboratory measurements had been made using a time-domain reflectometer to select the most suitable matched terminations. The aerials were then measured and stub tuner adjustments made to produce a vswr of the order of 1·05 at the receiver through the connecting low-loss cable. A selected liquid nitrogen termination was used as a temperature standard throughout the experiment, replacing the feeds at both 408 and 635 MHz. If the admittance measurements showed a satisfactory match, observations would start. The coaxial switch allowed remote connection to a reference load for monitoring of the zero level. Noise calibrations through the directional coupler DC1 allowed the monitoring of the receiver gain. If either of the two monitoring parameters changed by more than 2% the observations were discontinued and the matching procedures repeated.

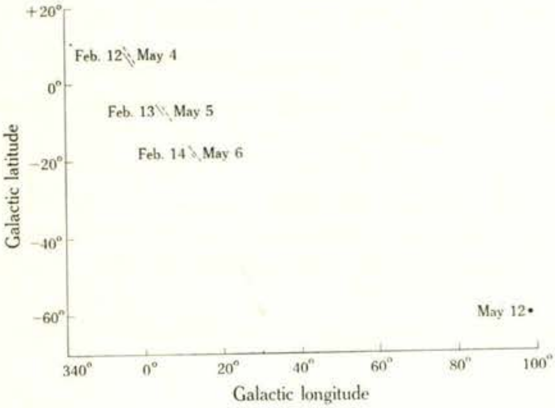

Fig. 3.—Galactic coordinates of points at which measurements and calibration were done at 408 and 635 MHz.

The calibration with 1, 2, and 3 dB attenuators gives a temperature range of some 100 °K. Four points are available for linearity determination. The Moon deflection and the reference point deflection are essentially within this dynamic range with the exception of some reference points where the antenna temperature falls somewhat below the liquid nitrogen reference temperature. The linearity of the 408 MHz receiver was found to be excellent and numerous calibrations showed little scatter. It appears that relative temperatures in this dynamic range could be measured to an accuracy of 2%. The linearity of the 635 MHz receiver required corrections over the dynamic range used in this experiment. However, individual transfer characteristics showed reproducible tendencies if the local oscillator frequency was kept constant. An accuracy of 3% was deduced for the 635 MHz receiver.

An additional measurement required in the lunar screen method is an absolute background temperature at one of the observing frequencies, if the spectral index is well known. This was derived at 408 MHz using a pyramidal horn available at Parkes. The horn has an aperture of $6 \cdot 1\lambda \times 4 \cdot 5\lambda$ with a slant height of some 10λ. The polar diagram of this horn has been investigated thoroughly as part of a solar calibration at 408 MHz (Landecker 1967; Wielebinski 1967*b*). The method of measurement and calibration is essentially the same as described for the lunar screen experiment. The values of horn losses, south celestial pole temperature, and ground contribution were derived partly from the work of Price (1969), Landecker (unpublished), and more recent measurements at Parkes. The value of absolute sky temperature deduced for the calibration point $\alpha = 0^h$, $\delta = 0°$ is $T_b(408) = 20 \pm 1$ °K.

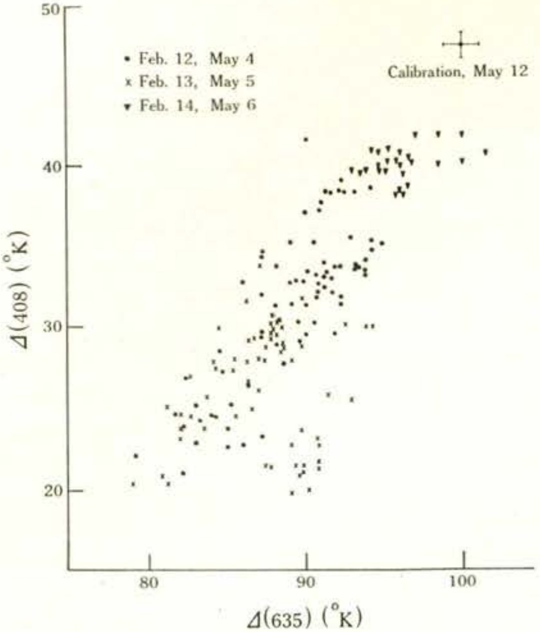

Fig. 4.—Differential antenna temperatures $\Delta = T_A(\mathrm{m}) - T'_A(\mathrm{m})$ at 408 MHz as a function of temperatures at 635 MHz for different galactic coordinates. The error in the estimation of the antenna temperature is shown by the length of the cross bars of the calibration point.

IV. Observations

The observations were made during February 12–16, 1969 and May 5–7, 1969. In both these observing sessions the Moon crossed the galactic plane in the vicinity of the galactic centre. The path of the Moon across the Galaxy and during the observations is shown in Figure 3. For calibration purposes measurements were made on May 12, 1969 in the direction $l^{\mathrm{II}} = 98° \cdot 5$, $b^{\mathrm{II}} = -60°$ ($\alpha = 0^h$, $\delta = 0°$).

During the observations a Moon point and a reference point were measured alternately every 5 min. The temperature deflections were recorded on a chart recorder. After every second point a reference measurement was made by switching to the liquid nitrogen termination in place of the antenna. At the same time a noise generator deflection was measured for gain stability checking. An impedance measuring and adjusting procedure was carried at the beginning and end of each observing session and on three or four occasions throughout its duration of some 5 hr. It was found that the impedance remained well matched during the useful observing time and would contribute negligible error to the measured antenna temperatures. In Figure 4 the whole set of observations is plotted in the form $\Delta(408)$ versus $\Delta(635)$. Corrections had to be applied to the deflection temperatures for variations of the Moon's diameter, but the diameter did not change by more than 2% near the galactic plane. At the calibration point the lunar diameter change was 5%. The antenna temperature of the Moon was found from the calibration point to be $\Delta_c = 47\cdot5 \pm 0\cdot7$ °K at 408 MHz and $\Delta_c = 100 \pm 1$ °K at 635 MHz. This allows the determination of the antenna pattern function

$$1/(1-\beta_m)\eta = \{T_m - T_b(c)\}/\Delta_c\,, \tag{10}$$

which was found to have the values 4·32 at 408 MHz and 2·17 at 635 MHz. Using this correction it is possible to calculate the absolute brightness temperature of the screened background using equation (8).

V. Results

For analysis of the results we consider the summation of the brightness temperature over the various emitting regions in the beam. This summation is done in a manner analogous to that used by Turtle *et al.* (1962) for spectrum separation. For wavelengths λ_1 and λ_2 the brightness temperatures $T_b(\lambda)$ are

$$\left.\begin{aligned} T_b(\lambda_1) &= T_g(\lambda_1)+T_e(\lambda_1)+T_r \\ \text{and}\qquad T_b(\lambda_2) &= n_g T_g(\lambda_1)+n_e T_e(\lambda_1)+T_r\,, \end{aligned}\right\} \tag{11}$$

where T_g is the galactic background temperature, T_e is the extragalactic nonthermal contribution, and T_r is the extragalactic component with a black body spectrum, while the ratios n_g and n_e are derived from the spectral relations

$$n_e = (\lambda_2/\lambda_1)^{\beta_e}\,, \qquad n_g = (\lambda_2/\lambda_1)^{\beta_g}\,,$$

where β_e and β_g are the temperature spectral indices of extragalactic and galactic emission respectively.

From (11)

$$T_b(\lambda_2) = n_g T_b(\lambda_1) + (n_e - n_g)T_e(\lambda_1) + (1-n_g)T_r\,. \tag{12}$$

In (12) the slope of the $T_b(\lambda_2)$ versus $T_b(\lambda_1)$ diagram determines the ratio n_g of the galactic background radiation. The intercept of (12) on the $T_b(\lambda_2)$ axis yields a temperature T^* given by

$$T^* = (n_e - n_g)T_e(\lambda_1) + (1-n_g)T_r\,. \tag{13}$$

The value of this intercept can be used (with known values of n_e, n_g, and $T_e(\lambda_1)$) to derive the black body component T_r.

The spectral index for the galactic background emission determined from the slope of the majority of measured points shown in Figure 4 gives $\beta_g = 2\cdot5 \pm 0\cdot2$. These measurements took no account of the radio polarization of the galactic emission on the measured directions. Deviations from the mean slope can represent either real small-scale spectral changes in the galactic emission or intense polarization. However, observations of polarization in the direction of the Moon's path (Mathewson and Milne 1965) indicate polarization temperatures less than 3° K at 408 MHz. Some sets of measured points deviate from the mean brightness temperature by as much as 40°K at 408 MHz and 10°K at 635 MHz; at 408 MHz this is 10 times higher than the maximum measured polarization temperatures. An inescapable conclusion is that small-scale spectral variations have been found in the vicinity of the galactic plane. In addition to these spectral variations a group of points in Figure 4 is well away from the main group. The spectral index for these points is found to be $\beta = 3\cdot3$. To explain this result by polarization only, more than 20% polarization would be required.

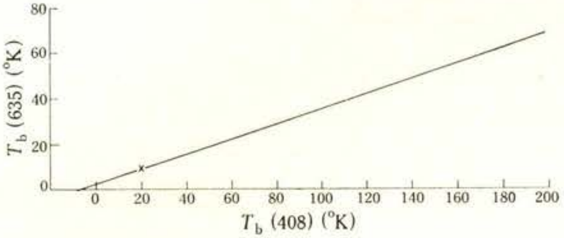

Fig. 5.—Brightness temperatures $T_b(408)$ at 408 MHz as a function of the brightness temperatures $T_b(635)$ at 635 MHz for the case $\beta = 2\cdot5$. The cross is the calibration point in Figure 4.

The spectral index found by Howell and Shakeshaft (1967) in the direction of the north galactic pole in a similar frequency range using broad beam horn antennas was $\beta = 2\cdot8 \pm 0\cdot1$. If we assume that this spectral index is true for the nonthermal component of galactic emission in the region of the present measurements a separation of a nonthermal part $Af^{-2\cdot8}$ and a thermal component $Bf^{2\cdot0}$ requires the solution of

$$\frac{Af_1^{-2\cdot8} + Bf_1^{2\cdot0}}{Af_2^{-2\cdot8} + Bf_2^{2\cdot0}} = \left(\frac{f_1}{f_2}\right)^{-2\cdot5}. \tag{14}$$

The above equation will be satisfied if the thermal component is not more than 4% of the nonthermal radiation.

Figure 5 shows the intercept region of the graph in Figure 4. The intercept on the $T_b(408)$ axis has been drawn for the case of $\beta_g = 2\cdot5$. The intercept determines the value of T^* as given in equation (13). A value of the extragalactic spectral index $\beta_e = 2\cdot8$ has been derived by Shimmins and Day (1968) for the frequency range 178–2650 MHz. The extragalactic component due to radio sources was determined by Pooley and Ryle (1968) at 408 MHz to be $2\cdot30 \pm 0\cdot5$°K for $\beta_e = 2\cdot8$ and $2\cdot8 \pm 0\cdot7$°K for $\beta_e = 2\cdot75$.

For our observations,

$$(n_e - n_g)T_e(635) = 0 \cdot 3 \pm 0 \cdot 2\,^\circ\mathrm{K}\,,$$

and therefore the above term in (13) will be used only in error determination.

The intercept for $\beta = 2 \cdot 5$ as shown in Figure 5 gives

$$T^* = -6^\circ = (1 - n_g)T_r\,,$$

which results in $T_r = 3^\circ$K. The value of this component T_r is only weakly dependent on the value adopted for the galactic spectrum. We compute that for $\beta = 2 \cdot 3$, $T^* = -5^\circ$K and $T_r = 2 \cdot 9^\circ$K, while, for $\beta = 2 \cdot 7$, $T^* = -7^\circ$K and $T_r = 3^\circ$K. A change of values of lunar temperature and/or of the calibration point absolute temperature by $\pm 1^\circ$K does not produce significant changes of T_r from $T_r = 3^\circ$K. Taking the maximum error of increased lunar temperature and decreased calibration temperature, we find a peak variation of $0 \cdot 5^\circ$K, giving a final result of $T_r = 3 \pm 0 \cdot 5\,^\circ$K in the decimetre wavelength range, which is in good agreement with the mean value of $2 \cdot 68^\circ$K for centimetre and millimetre observations (see, for example, Wolfe and Burbidge 1969).

The results derived from the observational method of using the Moon as a screen give us information on small-scale spectral variations of the radiation near the galactic plane and on the absolute value of the cosmic background in the decimetre wavelength range. The spectral variations are significantly greater than the total which could be attributed to sources, polarization of the background, and measurement errors. The conclusion reached is that the spectrum of the galactic emission varies on a scale of $\frac{1}{2}^\circ$. The cosmic background result of $3 \cdot 0 \pm 0 \cdot 5\,^\circ$K agrees with published values, however, setting a new low upper limit for any intergalactic plasma contribution in the decimetre wavelength range. It is suggested that no contribution from a hot intergalactic plasma is apparent in this frequency range.

VI. Acknowledgments

We thank Dr. E. G. Bowen and Mr. J. G. Bolton for permission to use the Parkes radio telescope. One of us (K.S.S.) wishes to thank the Division of Radiophysics, CSIRO, for its hospitality and the School of General Studies, Australian National University, for financial support. The absolute calibration program is supported at the School of Electrical Engineering, University of Sydney, by an ARGC grant. One of us (W.E.W.) is supported by a Commonwealth Postgraduate Scholarship. We thank Mr. T. L. Landecker for the determination of an accurate south pole temperature and Mr. B. Jones for assistance with observations. Finally, we wish to thank Dr. B. J. Robinson for his support of the research program and for reading the manuscript.

VII. References

van den Bergh, S. (1961).—*Z. Astrophys.* **53**, 219.

Bridle, A. H. (1967).—*Mon. Not. R. astr. Soc.* **136**, 219.

Dicke, R. H., Peebles, P. J. E., Roll, P. G., and Wilkinson, D. T. (1965).—*Astrophys. J.* **142**, 414.

Doroshkevich, A. G., Zeldovich, Ye. B., and Novikov, I. D. (1967).—*Astr. Zh.* **44**, 295.

Howell, T. F., and Shakeshaft, J. R. (1967).—*Nature, Lond.* **216**, 753.

Landecker, T. L. (1967).—*Proc. astr. Soc. Aust.* **1**, 61.

Landecker, T. L., and Wielebinski, R. (1968).—*Proc. astr. Soc. Aust.* **1**, 210.

Mathewson, D. S., and Milne, D. K. (1965).—*Aust. J. Phys.* **18**, 635.

Parijsky, Y. N. (1968).—*Astr. Zh.* **45**, 279.

Pauliny-Toth, I. I. K., and Shakeshaft, J. R. (1962).—*Mon. Not. R. astr. Soc.* **124**, 61.

Penzias, A. A., and Wilson, R. W. (1965).—*Astrophys. J.* **142**, 419.

Pooley, G. G., and Ryle, M. (1968).—*Mon. Not. R. astr. Soc.* **139**, 515.

Price, R. M. (1969).—*Aust. J. Phys.* **22**, 641.

Sandage, A. (1962).—"Problems of Extragalactic Research." p. 350. (Macmillan: New York.

Shimmins, A. J., and Day, G. A. (1968).—*Aust. J. Phys.* **21**, 377.

Troitzky, V. S., and Krotikov, V. D. (1968).—*Radiophysics USSR* **11**, 1135.

Turtle, A. T., Pugh, J. F., Kenderdine, S., and Pauliny-Toth, I. I. K. (1962).—*Mon. Not. R. astr. Soc.* **124**, 297.

Weymann, R. (1966).—*Astrophys. J.* **145**, 567.

Wielebinski, R. (1967*a*).—*Proc. Instn Radio Engrs Aust.* **28**, 273.

Wielebinski, R. (1967*b*).—*Proc. astr. Soc. Aust.* **1**, 62.

Wolfe, A. M., and Burbidge, G. R. (1969).—*Astrophys. J.* **156**, 345.

MAX-PLANCK-GESELLSCHAFT
zur Förderung der Wissenschaften e. V.
M.P.I. f. Radioastronomie, Bonn

Sonderdruck Nr. 47

Das Spektrum der Radiostrahlung

von

R. Wielebinski u. W. E. Wilson

Sonderdruck aus „Mitteilungen der Astronomischen Gesellschaft Nr. 31 (1972)"

R. Wielebinski und W. E. Wilson (Max-Planck-Institut für Radioastronomie, Bonn): Das Spektrum der Radiostrahlung.

Messungen des Radiospektrums stellen den Ausgangspunkt zum Aufbau von Modellen der galaktischen Radiostrahlung dar. In jüngster Zeit führte eine verbesserte Meßtechnik zu wesentlich genaueren Spektrumswerten. Eine der wichtigen Folgen der neueren Messungen war die Entdeckung von Variationen im Spektralindex in verschiedenen Richtungen. In letzter Zeit wurden viele neue Beobachtungen veröffentlicht, wovon einige, vielleicht stärker als bisher vermutet, Variationen im Spektralindex zeigten.

In dieser Arbeit wird eine Reihe neuer Messungen beschrieben. Deren Ergebnisse werden zum Vergleich und zur Bestimmung von Differenzen in anderen veröffentlichten Resultaten herangezogen. Auch die Implikationen für die Beobachtungen kosmischer Strahlung werden behandelt.

Einleitung

Die genaue Bestimmung des Radiospektrums war immer schon von großem astronomischen Interesse, da man die Mechanismen der Radiostrahlung aufgrund von Spektralindexwerten untersuchen konnte. Ein Vergleich der frühen Surveys (z. B. Komesaroff, 1961) ergab einen Spektralwert von $\beta = 2{,}6 \pm 0{,}2$ ($\mathrm{T} \propto \lambda^{\beta}$). Schon früher hatten Adgie und Smith (1956) darauf hingewiesen, daß das Spektrum mit Antennen gemessen werden sollte, deren Größe im konstanten Verhältnis zur Wellenlänge ist. Dabei wird das Problem des Antennendiagramms eleminiert, da derart abgestimmte Antennen identische Keulen haben.

Diese Methode wurde von einigen Beobachtern mit Antennen mit kleiner Auflösung in Cambridge (Purton 1966, Andrew 1966) und in Sydney (Yates, Wielebinski 1966) angewendet. Aus diesen Messungen ging klar hervor, daß der Temperatur-Spektralindexwert $\beta = 2{,}6 \pm 0{,}1$ für die Wellenlängen von 10 bis 100 MHz war, wobei bei zunehmender Frequenz die Indexwerte auch zunahmen. Das Mikrowellenspektrum der Radiostrahlung nahe der galaktischen Ebene wurde von Penzias und Wilson (1966) bestimmt durch Vergleiche von Surveys bei 960 MHz und 1390 MHz mit Schnitten durch die galaktische Ebene bei 4080 MHz, wobei $\beta = 2{,}9$ gefunden wurde.

Eine Bestätigung dieser möglichen Indexvariationen gelang durch mühsame und genau geplante Messungen. Die ersten positiven Beobachtungen kamen von Bridle (1967) und Landecker und Wielebinski (1969). Ihre Untersuchungen des Spektrums ergaben, daß die Strahlung aus hohen galaktischen Breiten von Stelle zu Stelle bedeutende Unterschiede aufwies. Eine vollständige Analyse einer Serie von genau geeichten Surveys bei 1 m Wellenlänge und mittlerer Auflösung (Berkhuijsen, 1971) bestätigte die früheren Ergebnisse. Eine besonders praktische Methode zum Studium des Spektrums entwickelter Stankevitch et al. (1970). Diese Methode benutzte die Scheibe des Mondes, um die Hintergrundstrahlung zu blokkieren. Bei Benutzung von 2 nahen Frequenzen wurde dadurch eine genaue Bestimmung des Spektrums erreicht. Spektralindexvariationen von $\beta = 2{,}1$ aus der Richtung der galaktischen Ebene, wo HII-Regionen in der Keule vorhanden sind, bis $\beta = 3{,}3$ wurden in dem Experiment beobachtet. In den niedrigen Wellenlängenbereichen wurden Satelliten benutzt (Alexander et al. 1969), die das Spektrum bis hinunter zu 400 kHz maßen.

Messungen mit Hornantennen

Über einen Zeitraum von 3 Jahren haben wir mit Hornantennen im Zenit von Sydney und Parkes ($\delta = -34°$) gemessen, und zwar bei 408 MHz, 716,5 MHz und 1424 MHz. Messungen bei der Frequenz von 408 MHz wurden von Landecker (1969) durchgeführt. Jedes dieser Hörner hatte eine Öffnung von $6{,}1\,\lambda \times 4{,}1\,\lambda$ und eine Länge von etwa $10\,\lambda$. Die 3 dB Keulenbreite war 13°. Eine verkleinerte Version dieser Hornantennen wurde für 9,2 GHz gebaut und genau im Antennenlabor untersucht. Das so bestimmte gesamte Antennendiagramm wurde mit den 'E' und 'H' Ebenen jedes einzelnen Horns für sich verglichen. Die Kenntnis des gesamten Antennendiagramms ermöglicht die Korrektion von Nebenzipfelwirkungen und die Berechnung der 'full-beam' Strahlungstemperatur. Die Genauigkeit der Meßmethode verschlechterte sich allmählich von 408 MHz bis 1424 MHz, besonders für niedrige Antennentemperaturen. Die gesammelten Ergebnisse der gemessenen Antennentemperaturen finden sich in der beigefügten Liste.

Die Analyse dieser Ergebnisse folgt der Methode, die Turtle et al. (1962) beschrieben. Da sich die Antennentemperatur aus Einwirkungen aus dem galaktischen Vordergrund, außergalaktischen Quellen sowie kosmischem Mikrowellenhintergrund zusammensetzt, ergibt erst ein „Differenzialspektrum" eine für galaktische Studien bedeutungsvolle Ziffer. Das Differenzialspektrum erhält man, indem man die Antennentemperaturen zweier Frequenzen miteinander vergleicht. Es sollte betont werden, daß diese Methode keine genauen Nullinien benötigt. Die Ergebnisse von Vergleichen der in Liste gegebenen Resultate befinden sich in Abb. 1 und 2. Der Spektralindex ändert sich und eine Reihe von unterschiedlichen Spektralgebieten sind in Abb. 1 und 2 erkennbar. Bei $\delta = -34°$ von RA 1615 bis RA 1800 ist die galaktische Ebene in der Antennenkeule. Dort werden niedrigere Werte des Spektralindexes beobachtet. Von RA 1800 bis 1900 beobachtet man einen zunehmenden Spektralindex. Doch bei höheren galaktischen Breiten werden für RA 1930 bis 2130 sehr hohe Spektralindexe festgestellt.

Es ist klar, daß in der Richtung der galaktischen Ebene der gemessene Spektralindex niedriger sein kann wegen der Mischung von Strahlung aus HII-Region und nicht-thermischer Strahlung in der Antennenkeule. Eine Berechnung kann in der Tat zeigen, daß nur 4 % der gesamten Strahlung aus optisch dünnen thermischen

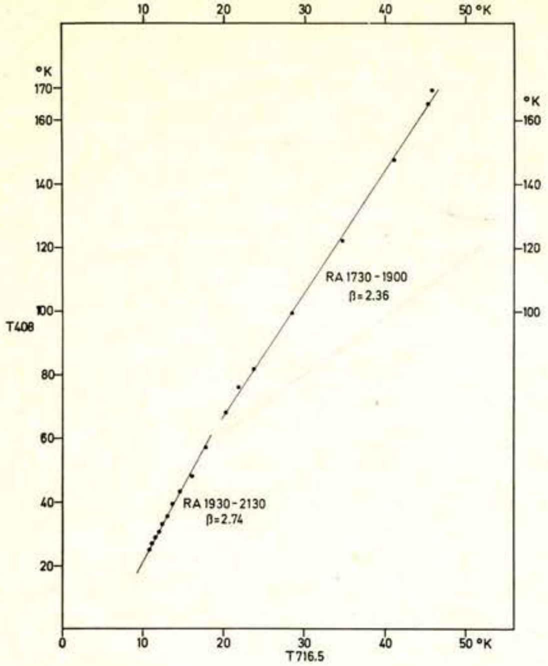

Abb. 1: Differenzialspektrumdiagramm 408 MHz – 716,5 MHz

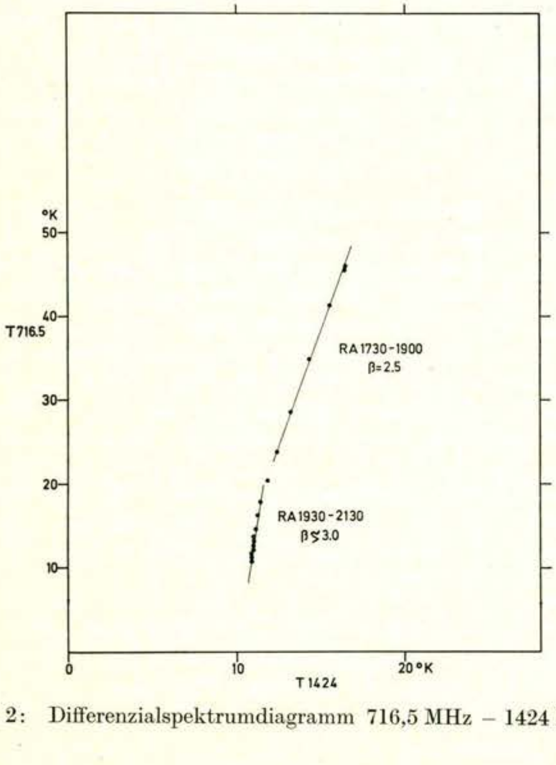

Abb. 2: Differenzialspektrumdiagramm 716,5 MHz – 1424 MHz

Tabelle I

1968/70 Horn Messungen $\delta = -34°$

Absolute Antennentemperaturen

α	408 MHz	716.5 MHz	1424 MHz
15^h15^m	56.6	16.5	
15 30	61.5	17.7	11.4
15 45	67.3	19.5	11.5
16 00	76.2	21.8	11.6
16 15	87.1	24.3	11.9
16 30	99.7	27.6	12.4
16 45	115.7	32.0	13.6
17 00	135.4	37.0	14.6
17 15	155.5	42.5	15.6
17 30	169.0	46.0	16.4
17 45	164.9	45.6	16.4
18 00	146.8	41.2	15.5
18 15	122.2	34.9	14.3
18 30	98.8	28.6	13.4
18 45	81.4	23.8	12.4
19 00	67.9	20.2	11.8
19 15	56.8	17.8	11.4
19 30	48.8	16.1	11.2
19 45	42.9	14.6	11.1
20 00	38.8	13.7	11.0
20 15	35.1	13.1	11.0
20 30	32.8	12.5	11.0
20 45	30.4	12.1	11.0
21 00	28.6	11.6	10.9
21 15	26.9	11.2	10.9
21 30	25.1	10.9	10.9

Regionen mit $\beta = 2{,}1$ nötig sind, um eine Abnahme des Differenzialspektrumindexes von $\beta = 2{,}9$ auf $\beta = 2{,}5$ (Stankevitch et al. 1970) zu bewirken. Andererseits sind die hohen Werte des Spektralindexes, $\beta \geqq 3{,}0$, schwer zu erklären. Doch scheint das nur ein „mittlerer" Wert zu sein, da kürzlich von Webster (private Mitteilung) in dem Nordpolarsporn Gebiet ein Spektralindexwert von 3,8 beobachtet worden ist.

Vergleich mit anderen Ergebnissen

Jahrelang war es üblich, ein kontinuierliches Spektrum zu zeichnen, indem man Beobachtungen von Satelliten aus unterhalb 10 MHz an die der Bodenstationen oberhalb 10 MHz anschloß. Das war solange möglich, wie Antennenkeulen genügend breit waren, um Indexvariationen auszugleichen. Zumindest bei höheren Frequenzen scheint eine ganze Anzahl von Spektralindices möglich, je nach der Beobachtungsrichtung. Die zusammengefaßten Ergebnisse werden in Abb. 3 gezeigt. Die Ergebnisse bei niedrigen Wellenlängen stammen von Satellitenmessungen von Alexander et al. (1969), der feststellte, daß $\beta = 2{,}0$ bei 4 MHz ist. Die Spektralindexwerte im Frequenzbereich 10 MHz bis 100 MHz stammen aus Arbeiten von Yates und Wielebinski (1966) und Andrew (1966). Bei mittlerer Auflösung ergaben Vergleiche von genau geeichten Surveys eine Anzahl von Indexwerten, die in Abb. 3 zu sehen sind (Landecker und Wielebinski 1970, Berkhuijsen 1971). Ergebnisse aus Cambridge (Howell, 1970) sind auch benutzt worden.

Abb. 3

	Frequenz MHz	Keule	Art der Messung
(1) Komesaroff	19,7 85 240 400 910 1390	1°	Survey
(2) Andrew	10 13,1 17,5 26,5 38	~120°	Scaled antenna
(3) Purton	38 81,5 178 404	15° × 50°	Scaled antenna
(4) Yates and Wielebinski	14,1 20 30 48,5 85	~120°	Scaled antenna
(5) Bridle	13,1 17,5 81,5	17° × 12°	Scaled antenna
(6) Landecker und Wielebinski	85 150	35°	Survey
(7) Stankevitch et al.	408 635	1/2°	Monddeckung
(8) Penzias und Wilson	81,5 408 960 1390 4080	0.7°	Survey
(9) Howell			Scaled horn
(10) Wielebinski und Wilson	408 716,5 1424	13°	Scaled horn
(11) Alexander et al.	0,2 – 9,2	180° – 10°	Satellit
(12) Webster	610 – 1420		Scaled horn

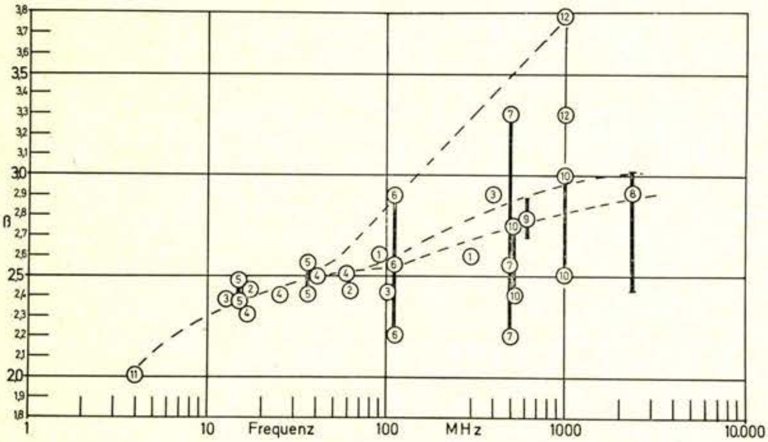

Abb. 3: Gesammelte Spektralindexwerte

Zusammenhang mit kosmischen Teilchen

Die Theorie der Synchrotronstrahlung (z. B. Ginsburg und Syrovatskij, 1965) stellt den Zusammenhang zwischen dem Energiespektrum kosmischer Elektronen und dem Spektralindex der Radiostrahlung her. Wenn das Energiespektrum der kosmischen Elektronen

$$N(E)\,dE = k\,E^{-\gamma}\,dE$$

ist, wobei γ der Elektronenspektralindex ist, dann ergibt sich, daß der Spektralindex α der Radiostrahlung ($\beta = \alpha + 2$)

$$\alpha = \frac{\gamma - 1}{2} \text{ ist.}$$

Ein Elektronenspektrum mit konstantem Exponenten γ über einen weiten Energiebereich resultiert in Radioemission mit konstantem Spektralindex β. Umgekehrt bedeutet eine beobachtete Variation in β eine Variation in α, solange Elektronengeschwindigkeiten eine Gaußsche Verteilung haben. Der Anstieg des Spektralindex β wurde von Turtle (1963) untersucht und durch einen ,,Bruch" im Elektronenenergiespektrum erklärt. Doch die Energieabweichung, die benötigt wird, um den Temperaturspektralindexwechsel von $\beta = 2{,}6$ bei niedrigeren Frequenzen zu $\beta = 3{,}8$ bei höheren Frequenzen zu erklären, erfordert den Wechsel von γ von 2,2 zu 4,6. Solche Variationen wurden bis jetzt (Daniel, 1969) bei keiner Beobachtung entdeckt. Diese Überlegungen wurden von Webster (1970) mit dem gleichen Ergebnis untersucht. Eine Erklärung für den Anstieg ist noch nicht vorhanden.

Referenzen

ADGIE, R. und SMITH, F. G.: Observatory **76**, 181, 1956

ALEXANDER, J. K., BROWN, L. W., CLARK, T. A., STONE, R. G. und WEBER, R. R.: Ap. J. **157**, L163, 1969

ANDREW, B. H.: Mon. Not. Roy. Astr. Soc. **132**, 79, 1966

BERKHUIJSEN, E.: Ph. D. Thesis, Leiden, 1971

BRIDLE, A. H.: Mon. Not. Roy. Astr. Soc. **136**, 219, 1967

DANIEL, R. R.: 'Cosmic Ray Studies', Tata Institute, Bombay, 1969

GINSBURG, V. L. und SYROVATSKIJ, S. I.: 'The Origin of Cosmic Rays' Pergamon Press New York, 1964

HOWELL, T. F.: Astrophys. Lett. **6**, 45, 1970

KOMESAROFF, M. M.: Aust. J. Phys. **14**, 515, 1961

LANDECKER, T. L.: Ph. D. Thesis, Sydney, 1969

LANDECKER, T. L. und WIELEBINSKI, R.: Proc. Astron. Soc. Aust. **1**, No. 5, 210, 1969

LANDECKER, T. L. und WIELEBINSKI, R.: Aust. J. Phys., Astr. Supp. No. 16, Oct. 1970

PENZIAS, A. A. und WILSON, R. W.: Ap. J. **146**, 666, 1966

PURTON, C. R.: Mon. Not. Roy. Astr. Soc. **133**, 463, 1966

STANKEVITCH, K. S., WIELEBINSKI, R. und WILSON, W. E.: Aust. J. Phys. **23**, 529, 1970

TURTLE, A. J., PUGH, J. F., KENDERDINE, S. und PAULINY-TOTH, I. I. K.: Mon. Not. Roy. Astr. Soc. **124**, 297, 1962

TURTLE, A. J.: Mon. Not. Roy. Astr. Soc. **126**, 405, 1963

WEBSTER, A. S.: Astrophys. Letters **5**, 189, 1970

YATES, W. K. und WIELEBINSKI, R.: Aust. J. Phys. **19**, 389, 1966

APPENDIX 2

Max-Planck-Gesellschaft zur Förderung der Wissenschaften E. V.
M. P. I. f. Radioastronomie, Bonn

Sonderdruck Nr. 3, Ser. A

Astron. & Astrophys. 28, 197 – 201 (1973)

Radio Observations of the Cygnus Loop at 2.7 and 10.7 GHz

N. J. Keen, W. E. Wilson, C. G. T. Haslam, D. A. Graham and P. Thomasson

Max-Planck-Institut für Radioastronomie, Bonn

Received June 28, 1973

Summary. Observations of the Cygnus Loop supernova remnant, made with the 100-meter radio telescope at 2.7 GHz and 10.7 GHz, reveal much new detail, and appear to confirm the conclusion of Kundu and Becker (1972) that radio emission from the source is predominantly of non-thermal origin. A detailed 10.7 GHz map of the small area around the radio maximum in NGC 6992, indicates only limited correspondence between radio and optical features at a resolution of ~ 1 arc min. An exceptional point source, located in the northern portion of the Cygnus Loop, has a flat spectrum and is time-variable at 10.7 GHz. This object appears to be physically associated with the supernova remnant.

Key words: supernova remnant – non-thermal radio frequency emission – variable component

---

Introduction

The Cygnus Loop supernova remnant has recently been classified as a thermal source of X-ray emission by Gorenstein *et al.* (1971), Tucker (1971) and Cox (1972). Parker (1964) treated it as a thermal source of optical emission. All recent radio measurements, however, indicate spectral indices steeper than −0.5 at frequencies above 1 GHz (Kundu, 1969; Moffat, 1971; Kundu and Becker, 1972); hence, radio emission at these frequencies appears to be predominantly of non-thermal origin. This paper reports total flux measurements, made with the 100-meter radio telescope of the Max-Planck-Institut für Radioastronomie. The observations covered the whole source at 2.7 GHz, and several portions of the source at 10.7 GHz.

Observations

The observations were performed at 2.7 GHz in July 1972, and at 10.7 GHz in November 1972. Cooled parametric amplifiers and load-switching were used at both frequencies. A noise calibration was injected into the antenna arm of the receiver every second Dicke switch period, so that the receiver could be calibrated continuously. The total receiver noise temperatures were approximately 90 K at 2.7 GHz and 130 K at 10.7 GHz, with i.f. bandwidths of 50 and 30 MHz at 2.7 GHz and 10.7 GHz respectively. Further details of the receiving system are given by Keen and Zimmermann (1973). A linearly polarised feed was set at a different position angle for each scan through a given region. The half-power beamwidths were 4.8 arc min at 2.7 GHz and 1.25 arc min at 10.7 GHz. The pointing accuracy of the antenna was < 8 arc sec during night observations. Aperture efficiency was 49 per cent at 2.7 GHz and 43 per cent at 10.7 GHz. Brightness temperatures, fluxes and telescope pointing were determined from the calibration sources 3 C 48, 3 C 286 (pointing only) and 3 C 380 at 2.7 GHz, and 3 C 410 (pointing only) and NGC 7027 at 10.7 GHz.

Scans were taken in right ascension. At 2.7 GHz, scans at 2 arc deg per minute were separated by 2 arc min in declination. At 10.7 GHz, scans at 0.5 arc deg per minute were separated by 0.5 arc min in declination. Five scans were made at each declination at 2.7 GHz, and 20 scans at 10.7 GHz. The final maps (Figs. 1 and 2) are the sums of individual maps. The maps correspond to total intensity, that is, Stokes' parameter I. Total errors caused by non-linear baseline drifts are estimated as contributing together < 30 per cent of a contour interval at both frequencies. The r.m.s. noise on the final maps is < 0.01 K of brightness temperature at both frequencies.

Results at 2.7 GHz

The 2.7 GHz map is shown in Fig. 1. Unresolved sources are listed in Table 1 together with fluxes and spectral indices (defined by $S \propto f^{\alpha}$) deduced from the 408 MHz measurements by Colla *et al.* (1970) and Colla *et al.* (1972), and the 1.4 GHz measurements of Moffat (1971): position errors are 0.5 arc min and spectral errors 6 per cent. The most outstanding

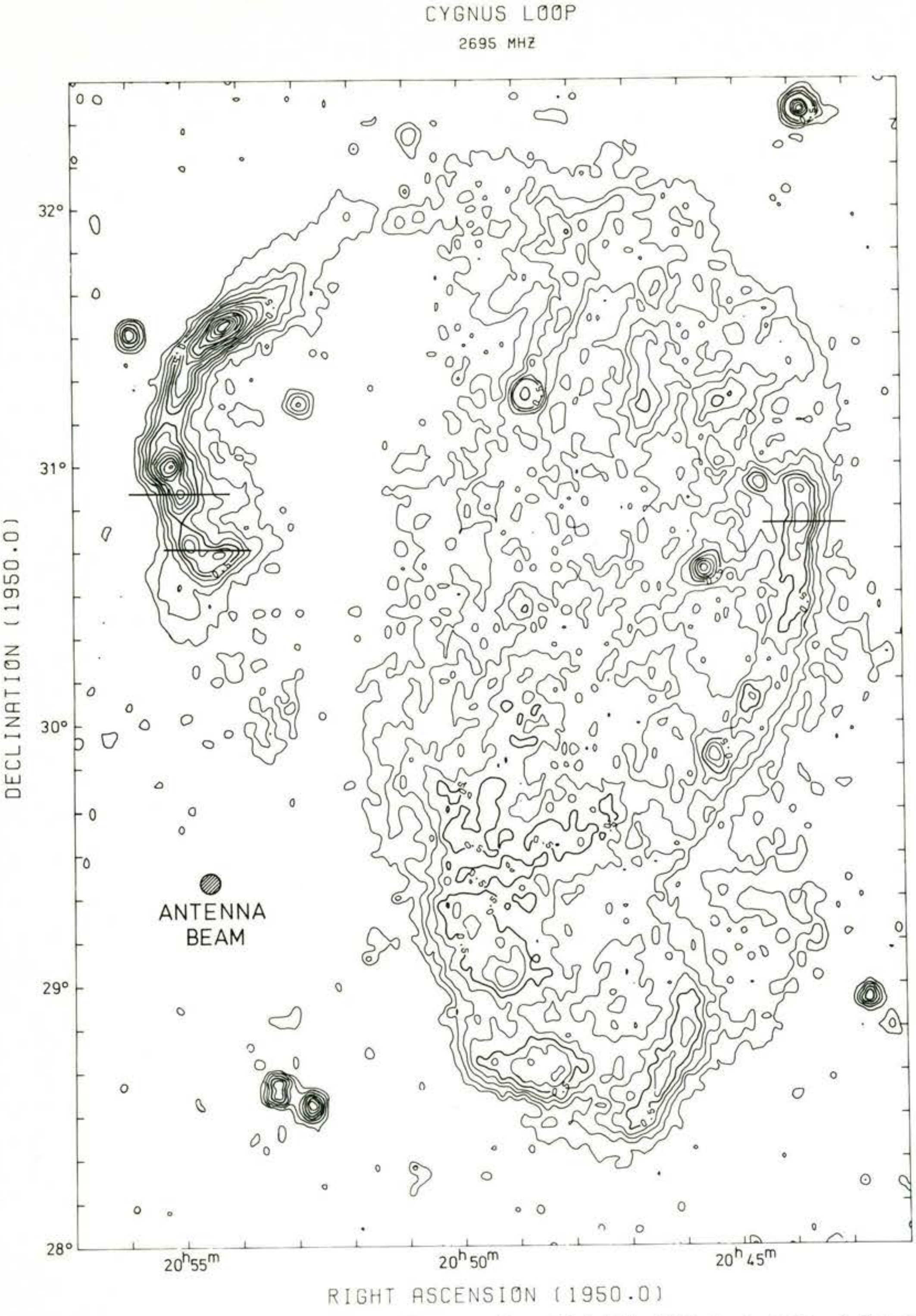

Fig. 1. Total intensity map of the Cygnus Loop at 2.7 GHz. The contour interval is 0.1 K in T_b. The horizontal lines indicate locations of sample scans at 10.7 GHz

difference between Fig. 1 and previous radio frequency maps is the greater wealth of detail. A further new result is that in regions corresponding to strong optical filaments, the contours are definitely steeper towards the outside of the source. The general form of the radiation suggests a circular ring, with a possible "secondary remnant" which has broken through the southern perimeter. This secondary loop may be material from the main ring, which has expanded out along the direction of the local interstellar magnetic field, or which has encountered a lower-density region of the interstellar medium and consequently been decelerated less than the remainder of the loop. The appearance of a secondary ring is not unique to the Cygnus Loop: 2.7 GHz observations of HB 21, made with the 100-meter radio telescope, show a definite inner ring of radiation located towards the south-eastern boundary.

Results at 10.7 GHz

The 10.7 GHz observations were confined to limited regions of the Cygnus Loop, because of the weak signal. Three different observations were performed:

1. The area around the 2.7 GHz maximum of NGC 6992 was mapped, and is shown in Fig. 2. On a scale of 1 arc min, there is only a fair correspondence between radio and optical emission.
2. A series of scans were made at a few locations where the 5 GHz observations of Kundu and Becker (1972) suggest steep slopes in the radio emission. The locations of these scample scans are shown in Fig. 1: no variations > 0.2 K in brightness temperature were detected.
3. Two small and relatively intense point sources were observed, one within the northern portion of the Cygnus Loop, and one just outside. Both sources are discussed in the next section.

Table 1. Unresolved sources in the Cygnus Loop, with flux >0.2 f.u. at 2.7 GHz

Source	Position (1950.0)		Flux Density			Spectral
	R.A.	Dec.	S_{408}	S_{1400}	S_{2695}	index α
			($\times 10^{-26}$ Wm^{-2}Hz^{-1})			($S \propto f^{\alpha}$)
CL 1	$20^{h}42^{m}40^{s}.6$	$28^\circ 57'.0$	0.98		0.27	-0.68
CL 2[a]	20 43 47.3	32 22.7	1.66		0.74	-0.48
CL 3	20 45 34.9	30 35.7	1.04		0.48	-0.41
CL 4[a]	20 48 47.3	31 16.5	0.6		0.58	-0.02
CL 5	20 52 44.9	28 32.4	1.72		0.35	-0.84
CL 6	20 52 54.3	31 14.3	—	0.27	0.19	-0.55
CL 7	20 55 56.6	31 30.6	1.21	0.63	0.35	-0.52[b] -0.91[c]

[a] 5 GHz positions from Westerbork (van der Laan and Duin, private communication)

CL 4 $\begin{cases} 20^{h}48^{m}47.35^{s} \\ 31^\circ 16' 10.3'' \end{cases}$ CL 2 $\begin{cases} 20^{h}43^{m}47^{s}.53 \\ 32^\circ 22' 50''.6 \end{cases}$

[b] Between 408 MHz and 1.4 GHz

[c] Between 1.4 GHz and 2.7 GHz

Discussion

Figure 3 shows the 2.7 GHz map of the area around the maximum of NGC 6992, together with the identical region at 10.7 GHz convolved to the same resolution as the 2.7 GHz. The spectral index for brightness temperature is -2.4, so that the thermal contribution at 10.7 GHz is small.

The source Cygnus Loop 4, hereafter CL 4, was measured at both frequencies. The spectrum of CL 4 is shown in Fig. 4, and includes interferometer measurements performed at other radio observatories. The error bars shown at 10.7 GHz represent the range of apparent variations in flux which occur between five observations over a period of fifteen weeks. The

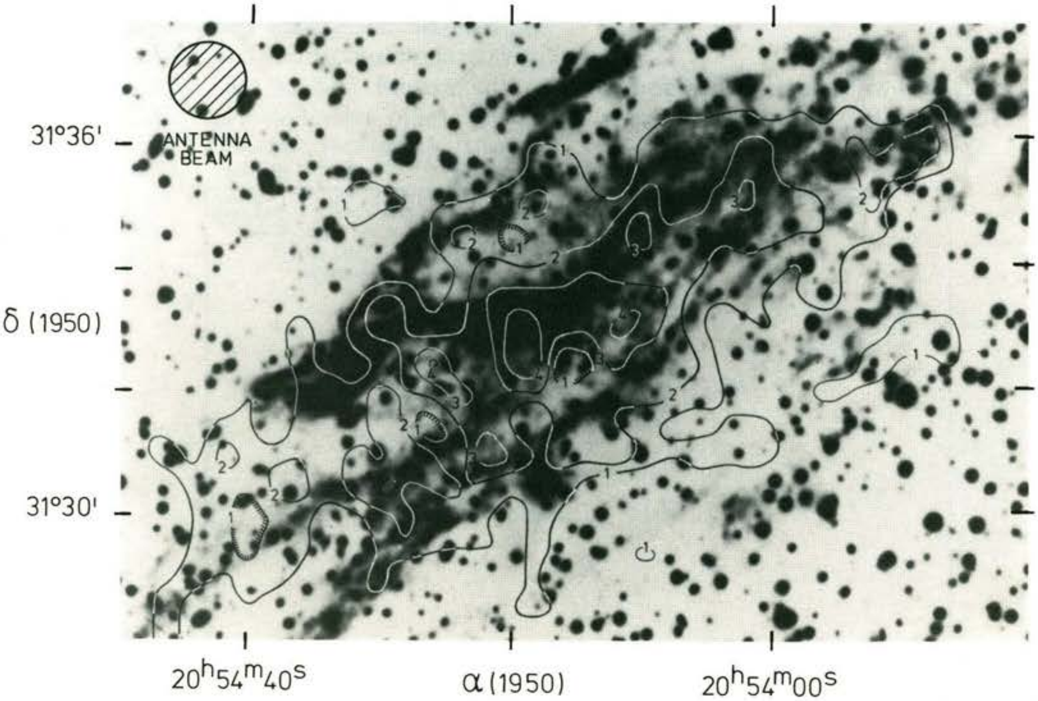

Fig. 2. Total intensity map of a small region of NGC 6992 at 10.7 GHz. The contour interval is 0.035 K in T_b. The radio contours are superimposed on a copy of W. C. Miller's colour photograph

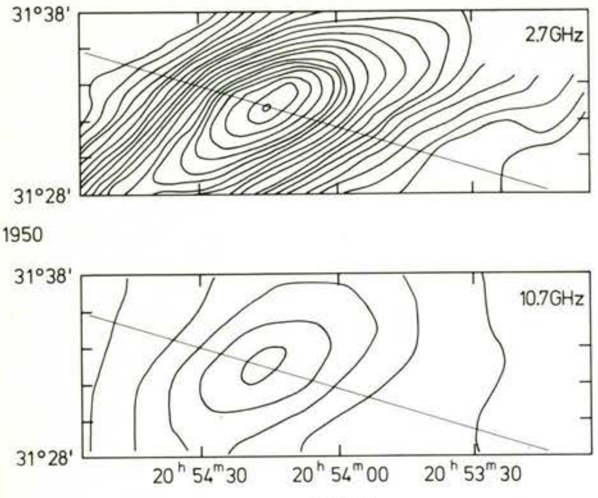

Fig. 3. The region shown in Figure 2, at 2.7 (upper) GHz and 10.7 GHz (lower) with identical angular resolution (4.8 arc min beam). Contour intervals are 0.05 K and 0.012 K in T_b respectively. Lines through the source maximum indicate sections for spectral index estimate

individual measurements at 10.7 GHz are shown in Fig. 5. Since the source is unresolved at 8 GHz with an interferometer baseline of 2.7 km (Kundu and Becker, private communication), the angular size is < 1.5 arc sec, corresponding to a brightness temperature of > 2800 K.

Duin (private communication) has drawn attention to an optical source on the blue Palomar Sky Survey plate, whose position is:

$$\alpha_{1950} = 20^h48^m47.55^s \pm 0.15^s$$

$$\delta_{1950} = 31°16'\,11.0'' \pm 2''$$

which agrees remarkably well with the radio position of CL 4 obtained at 5 GHz with the Westerbork synthesis radio telescope (van der Laan, private communication). On the other hand, X-ray emission maps of the Cygnus Loop by Stevens and Garmire (1973) and Rappaport (private communication) indicate no significant emission at the location of CL 4.

Whilst it is uncertain whether the intense variable source CL 4 belongs to the Cygnus Loop, a bridge of emission is apparent at 2.7 GHz, connecting the source to the main northern filamentary structure. Furthermore, if the source is situated in the Cygnus Loop ($d \approx 770$ pc), its diameter at 8 GHz is $<$ one light week, which is consistent with the time scale of its variability. It is unlikely that the variation could be attributed to a telescope pointing error, or to receiver or atmospheric problems, since simultaneous measurements of source CL 2 showed no variations.

The source CL 2 is situated 30 arc min outside the north-western boundary of the Cygnus Loop. The estimated number of extragalactic sources with flux $\geqq 0.35$ f.u. at 10 GHz is 200 (± 40) per steradian (Pauliny-Toth, private communication). This value corresponds to 1 or 2 such sources in the area mapped at 2.7 GHz, so that the source is probably extragalactic. Duin (private communication) reports a flux of 0.53 f.u. at 5 GHz, and the source appears to be unresolved by the Westerbork instrument (diameter < 3 arc sec).

The H I velocity profiles of Henderson (1967) for $l^{II} = 75°$ show a small, irregular cloud at a radial velocity of 12 km s^{-1}, which extends from the extremity of the Cygnus Loop to the approximate location of the source CL 2. Furthermore, an H I depletion occurs between $b^{II} = -7°$ and $-8°$, which corresponds to the approximate boundaries of the Cygnus Loop. Kazès (private communication) has made H I measurements on the eastern side of the Cygnus Loop, with the Nançay radio telescope. He finds neutral hydrogen

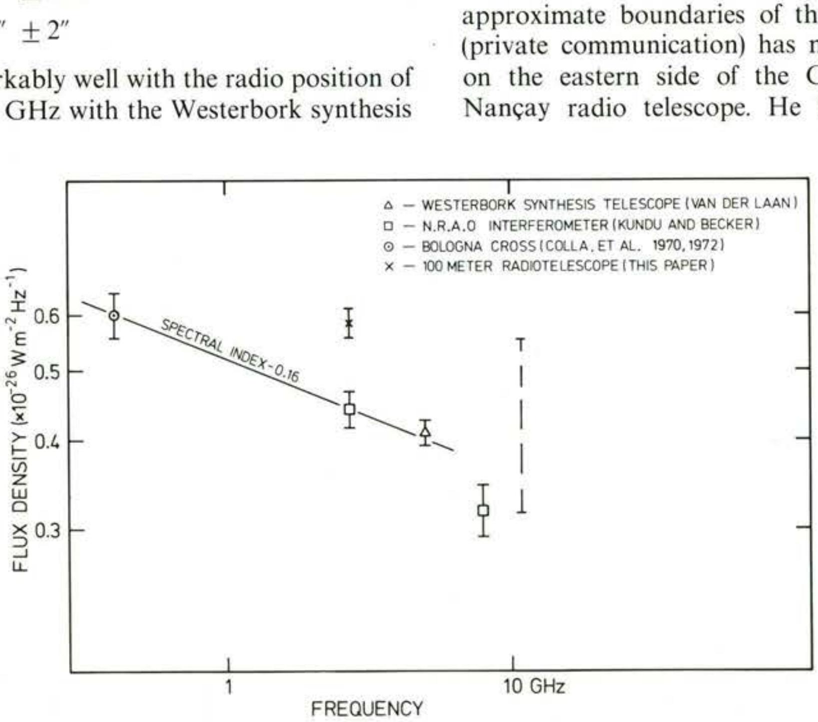

Fig. 4. The spectrum of source CL 4 between 408 MHz and 10.7 GHz

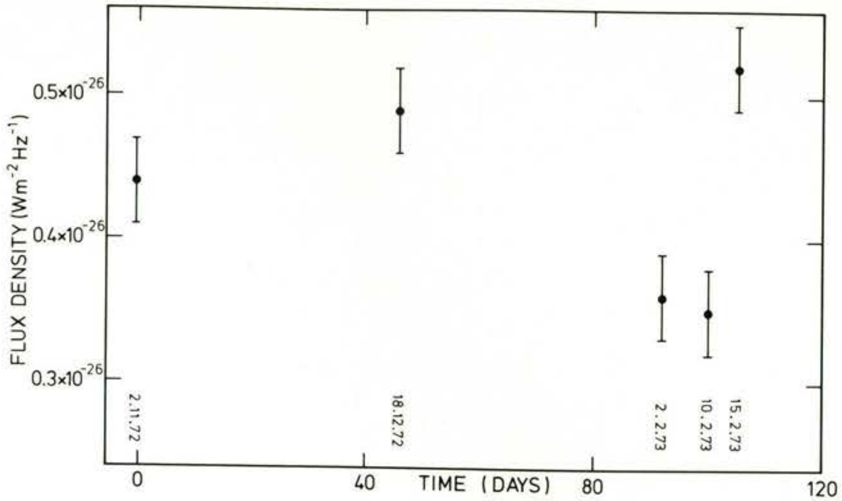

Fig. 5. Time variability of source CL 4 at 10.7 GHz

outside the boundaries of the radio shell. The intensity of the H I emission appears to be low immediately ahead of the shock-front, increasing fairly uniformly to the ambient interstellar value several *pc* ahead of the front. A more detailed interpretation of the Nançay results is difficult, because of the very broad antenna beam in declination.

Acknowledgements. We would like to express our gratitude to the telescope operators and technicians at the 100-meter radiotelescope, and to our colleagues at the Max-Planck-Institut für Radioastronomie, the National Radio Astronomy Observatory, the Astronomy Program at the University of Maryland, the Observatoire de Meudon and the Sterrewacht te Leiden, for supplementary measurements of sources CL 2 and CL 4. We are also grateful to P. Charles, R. M. Duin, M. R. Kundu and H. van der Laan for stimulating discussions, and to D. Downes for suggestions and improvements to the manuscript.

References

Colla, G., Fanti, C., Fanti, R., Ficarra, A., Formiggini, L., Gandolfi, E., Grueff, G., Lari, C., Padrielli, L., Roffi, G., Tomasi, P., Vigotti, M. 1970, *Astron. & Astrophys. Suppl.* **1**, 281

Colla, G., Fanti, C., Fanti, R., Ficarra, A., Formiggini, L., Gandolfi, E., Lari, C., Marano, B., Padrielli, L., Tomasi, P. 1972, *Astron. & Astrophys. Suppl.* **7**, 1

Cox, D. P. 1972, *Astrophys. J.* **178**, 169

Gorenstein, P., Harris, B., Gursky, H., Giacconi, R., Novick, R., Vanden Bout, P. 1971, *Science* **172**, 369

Henderson, A. P. 1967, University of Maryland, Ph. D. Thesis

Kundu, M. R. 1969, *Astrophys. J.* **158**, L 103

Kundu, M. R., Becker, R. H. 1972, *Astron. J.* **77**, 459

Keen, N. J., Zimmermann, P. 1973, *Nachrichtentechnische Zeitschrift* **26**, Heft 3, 124

Moffat, P. H. 1971, *Monthly Notices Roy. Astron. Soc.* **153**, 401

Parker, R. A. R. 1964, *Astrophys. J.* **139**, 493

Stevens, J. C., Garmire, G. P. 1973, *Astrophys. J.* **180**, L 19

Tucker, W. H. 1971, *Science* **172**, 372

N. J. Keen
W. E. Wilson
C. G. T. Haslam
D. A. Graham
P. Thomasson
Max-Planck-Institut für Radioastronomie
D-5300 Bonn
Federal Republic of Germany

Accepted for publication by Astronomy and Astrophysics.

Research Note (Main Journal)

High Resolution Measurements of the Supernova HB 21 at a Frequency of 2.7 GHz

C.G.T. Haslam

N.J. Keen

W.E. Wilson

D.A. Graham

P. Thomasson

Max-Planck-Institut für Radioastronomie, D-5300 Bonn, Auf dem Hügel 69, Federal Republic Germany

Summary Total brightness temperature measurements of HB 21 at 2.7 GHz show a structure very similar to that reported by Hill at 1.4 GHz at similar angular resolution. The spectral index over large parts of the source is approximately 2.8.

Key words Supernova remnant - brightness temperature - spectral index.

High Resolution Measurements of the Supernova HB 21
at a Frequency of 2.7 GHz

Continuum observations of the supernova HB 21 were performed in July 1972, using the 100-meter radiotelescope of the MPI für Radioastronomie, at a frequency of 2.7 GHz. The observations were performed using a cooled parametric amplifier, with which a total system temperature of approximately 90 K was achieved. Declination scans were taken in such a way as to ensure that all parts of the source were mapped at least four times, at various position angles of the linearly polarised feed horn. The resultant total power map is shown in Figure 1. Brightness temperature calibration procedures have been described in an earlier paper (Keen et al., 1973).

The angular resolution of 4.5 arc minutes was considerably higher than that of Kundu, Becker and Velusamy (1973) and Erkes and Dickel (1969), and hence considerably more structure is apparent. Detailed polarisation information was not available for the measurements reported here, although comparisons of data taken at various position angles indicated no notable small-scale divergences from the map of Kundu et al.

Comparison of Figure 1 with the 1.4 GHz results of Hill (1974) reveal close structural similarities. Figure 2 shows four cuts through the source, obtained from the results of Hill and our Figure 1. Over significant areas, or in regions with important structure, spectral indices obtained from Figure 2 and from the two maps yield values $\beta = 2.8 \pm 0.15$ ($T \propto \lambda^{\beta}$). In a few regions of low signal-to-noise ratio, extreme values between 0.5 and 1.1 occur, although the significance of these extremes of spectral index is questionable. The only notable exception is the strong source at the northern perimeter, which has a spectral index of 0.5. This range of spectral indices is considerably at variance with those of Erkes and Dickel at lower angular resolution, for reasons which are not apparent. However, comparisons of Figure 1 with the 5 GHz map of Kundu (1971) support our spectral estimates.

Noteworthy in Figure 1 is an inner ring of radiation, near to the southern extremity of the source. This is also evident in the maps of Kundu and Hill, and appears to have a spectral index typical for the source - as is illustrated in Figure 2(d).

Acknowledgements. We are grateful for the support and enthusiasm of the telescope operators during these observations.

Captions for Figures

Figure 1 Total power map of HB 21 at 2.7 GHz. The position of the profile in Figure 2(d) is shown by the broken line.

Figure 2 Four brightness temperature profiles of the source. For the first three, radial scans are taken from the centre at $\alpha = 20^h43^m20^s$, $\delta = 50^\circ 29'$, at the position angles given (measuring anticlockwise on the source). The fourth profile is taken at $\ell^{II} = 88^\circ 30'$, which passes through the two maxima of the southern ring source. The 1.4 GHz values are from Hill (1974).

References

Erkes, J.W., Dickel, J.R. 1969, Astron. J. 74, 840

Hill, I.E. 1974, Mon. Not. R. astr. Soc. 169, 59

Keen, N.J., Wilson, W.E., Haslam, C.G.T., Graham, D.A., Thomasson, P. 1973, Astron. & Astrophys. 28, 197

Kundu, M.R. 1971, Astrophys. J. 165, L55

Kundu, M.R., Becker, R.H., Velusamy, T. 1973, Astron. J. 78, 170

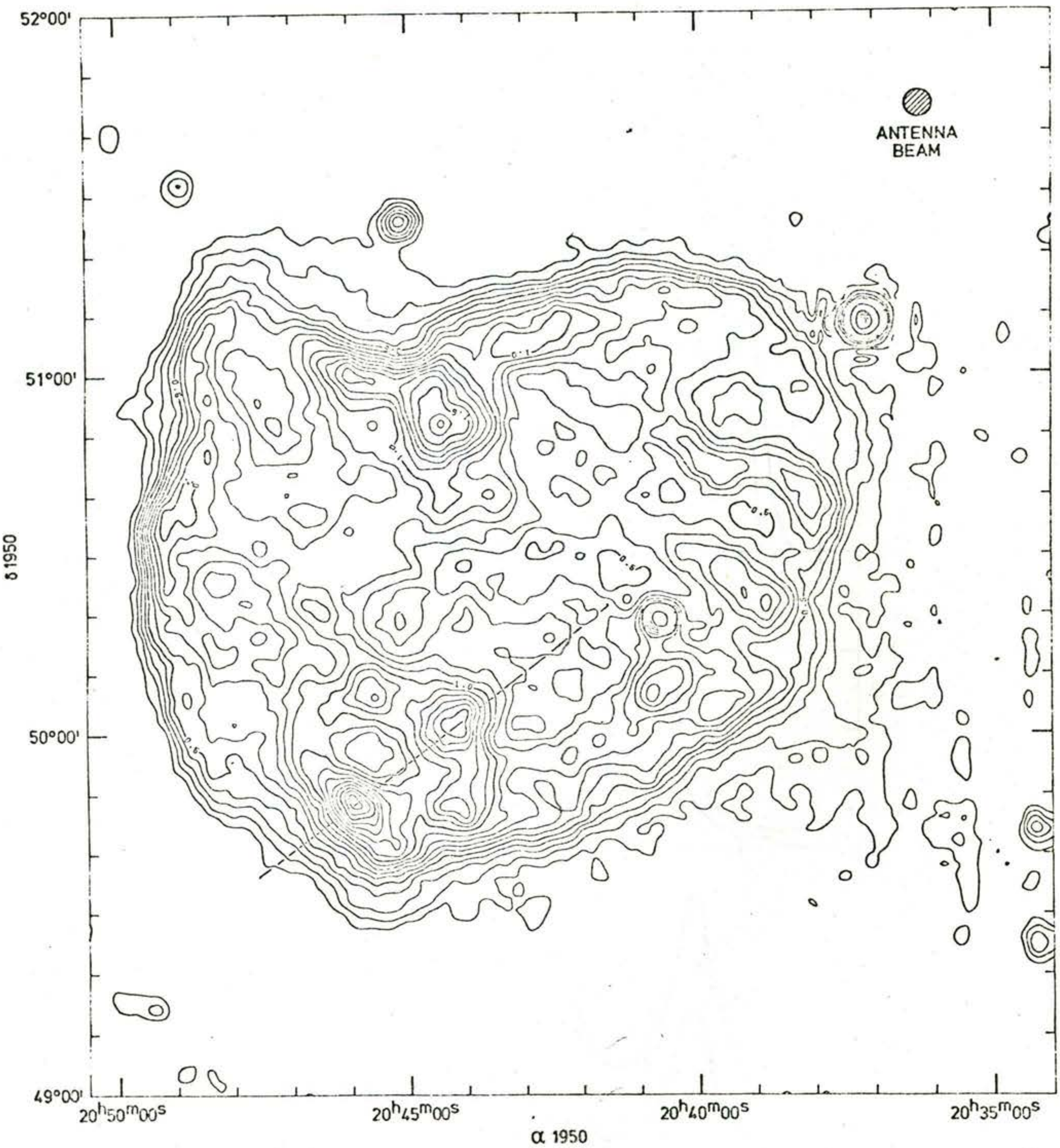
52°00'
51°00'
50°00'
49°00'
δ 1950
ANTENNA
BEAM
0.1
0.5
1.0
20h50m00s
20h45m00s
20h40m00s
20h35m00s
α 1950

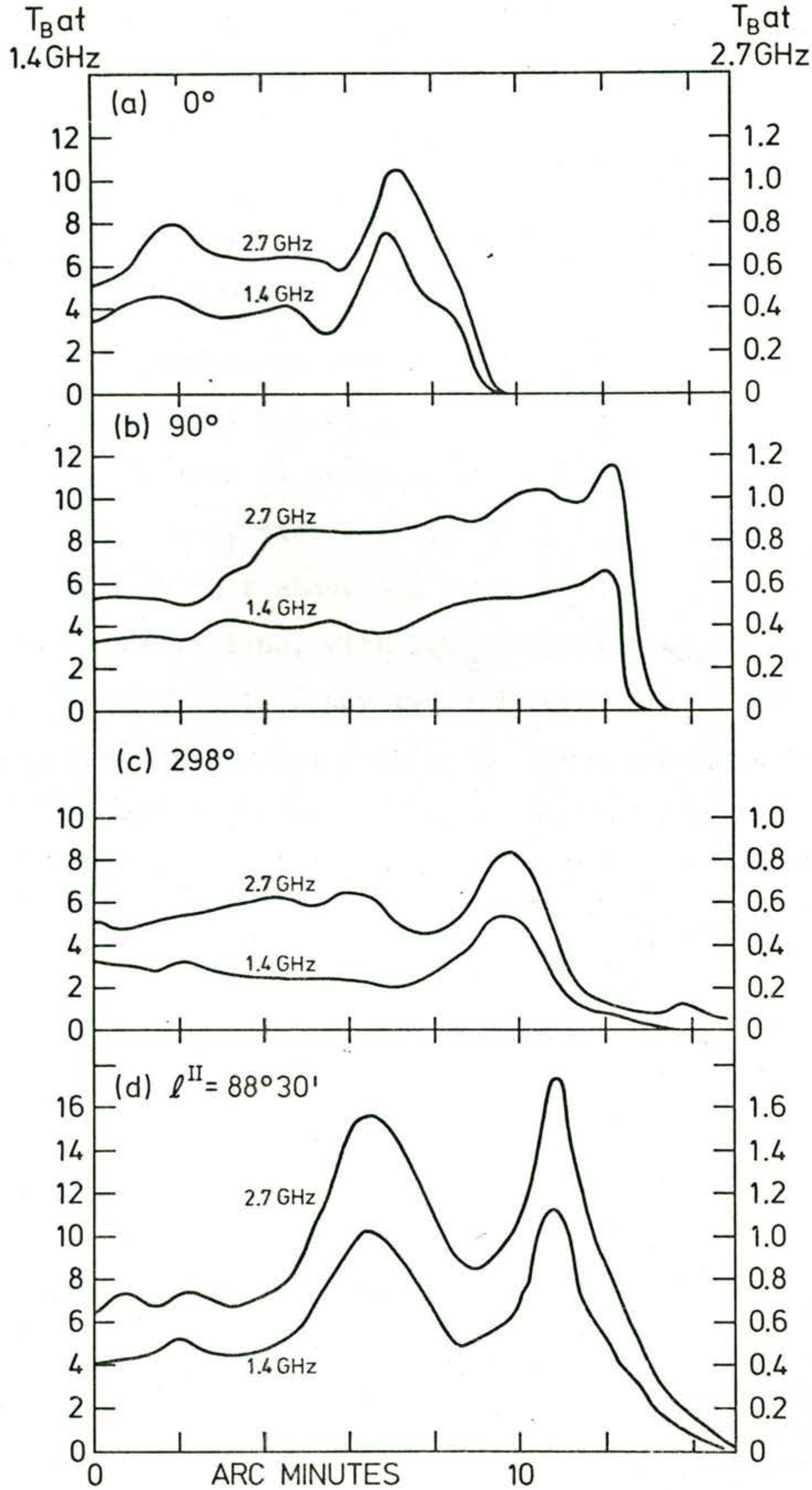

T_B at 1.4 GHz
T_B at 2.7 GHz
(a) 0°
(b) 90°
(c) 298°
(d) ℓ^II = 88°30'
2.7 GHz
1.4 GHz
0
2
4
6
8
10
12
14
16
0.2
0.4
0.6
0.8
1.0
1.2
1.4
1.6
0
10
ARC MINUTES

APPENDIX 3

The Bonn 408 MHZ Survey Maps

The complete survey is presented in the form of contour maps in equatorial coordinates, Epoch 1950.0. The contours are drawn in units of brightness temperature, step 2 K to 100 K, step 5 K to 150 K, step 10 K to 300 K and step 50 K above 300 K. Each fifth contour is drawn as a heavy line, with its value printed along it (where space permits). Any twofold ambiguity is resolved by a mark which appears within the lower contour. The maps are drawn in blocks of 2 hours right ascension by 20° declination.

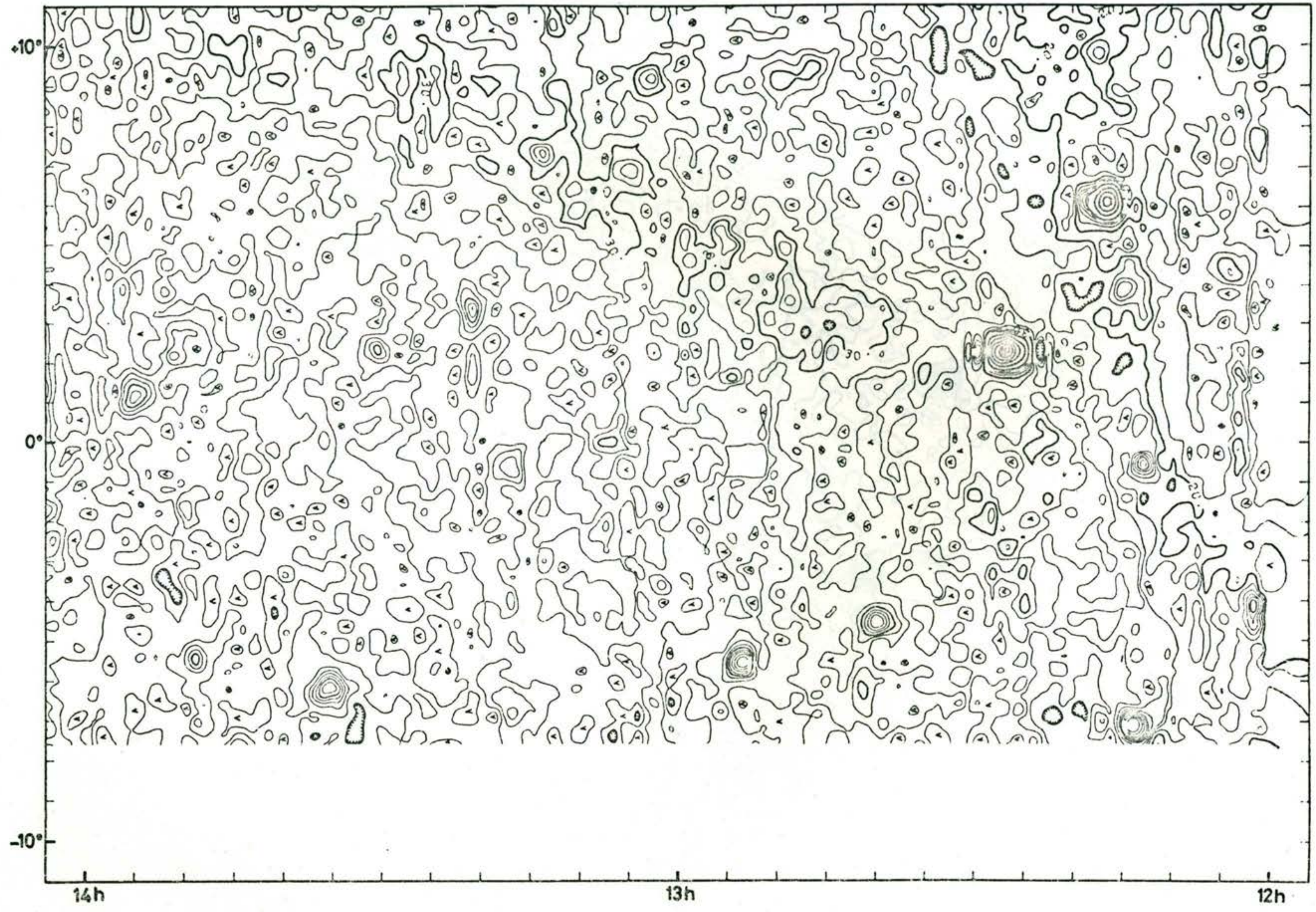
+10°
0°
-10°
14h
13h
12h
30
30
30
20
20


+30°
+20°
+10°
Virgo A
14h
13h
12h

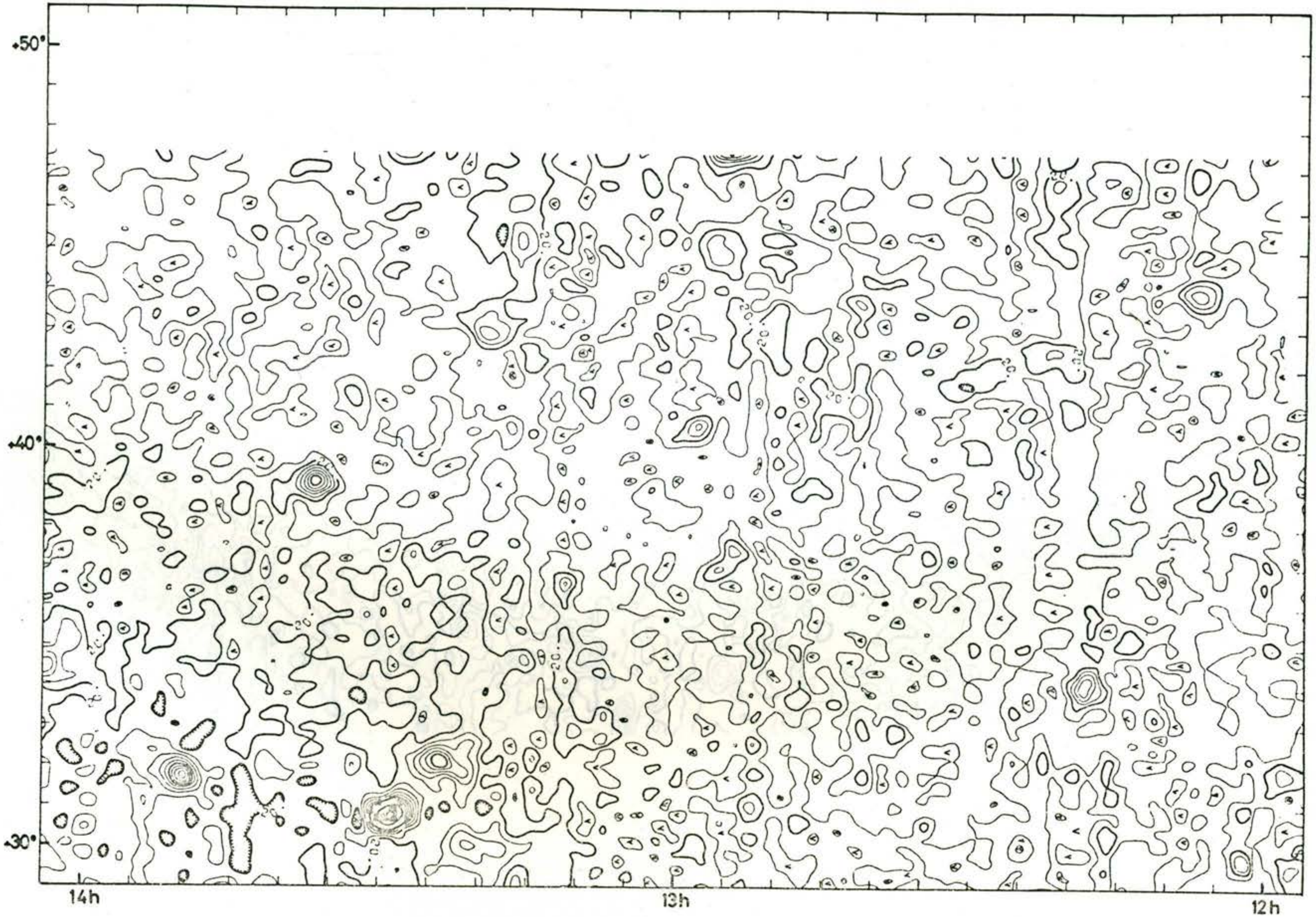
+50°
+40°
+30°
14h
13h
12h
20

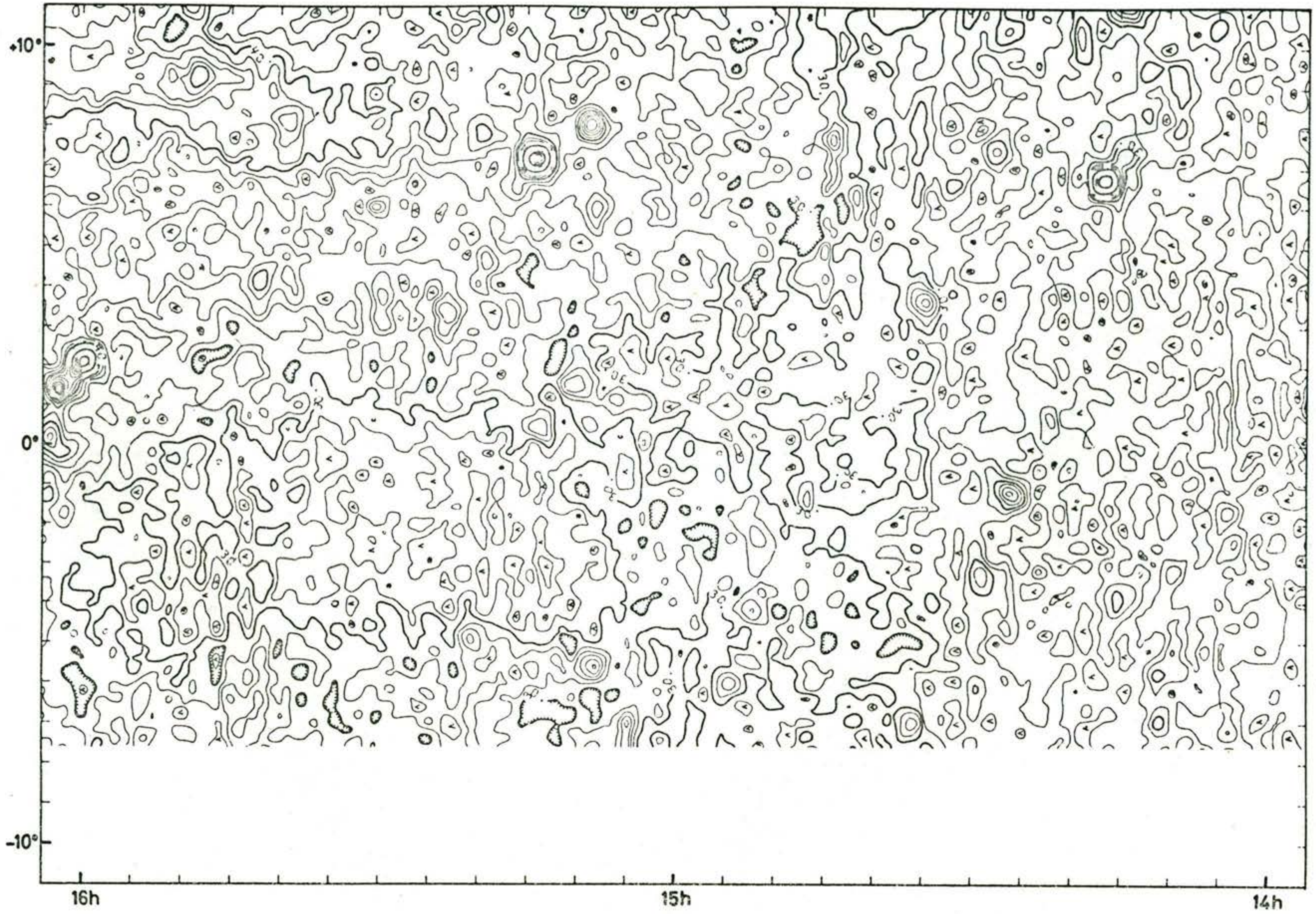
+10°
0°
-10°
16h
15h
14h
30


+30°
+20°
+10°
16h
15h
14h
30
40
30
40
40
40
30
30
30
30

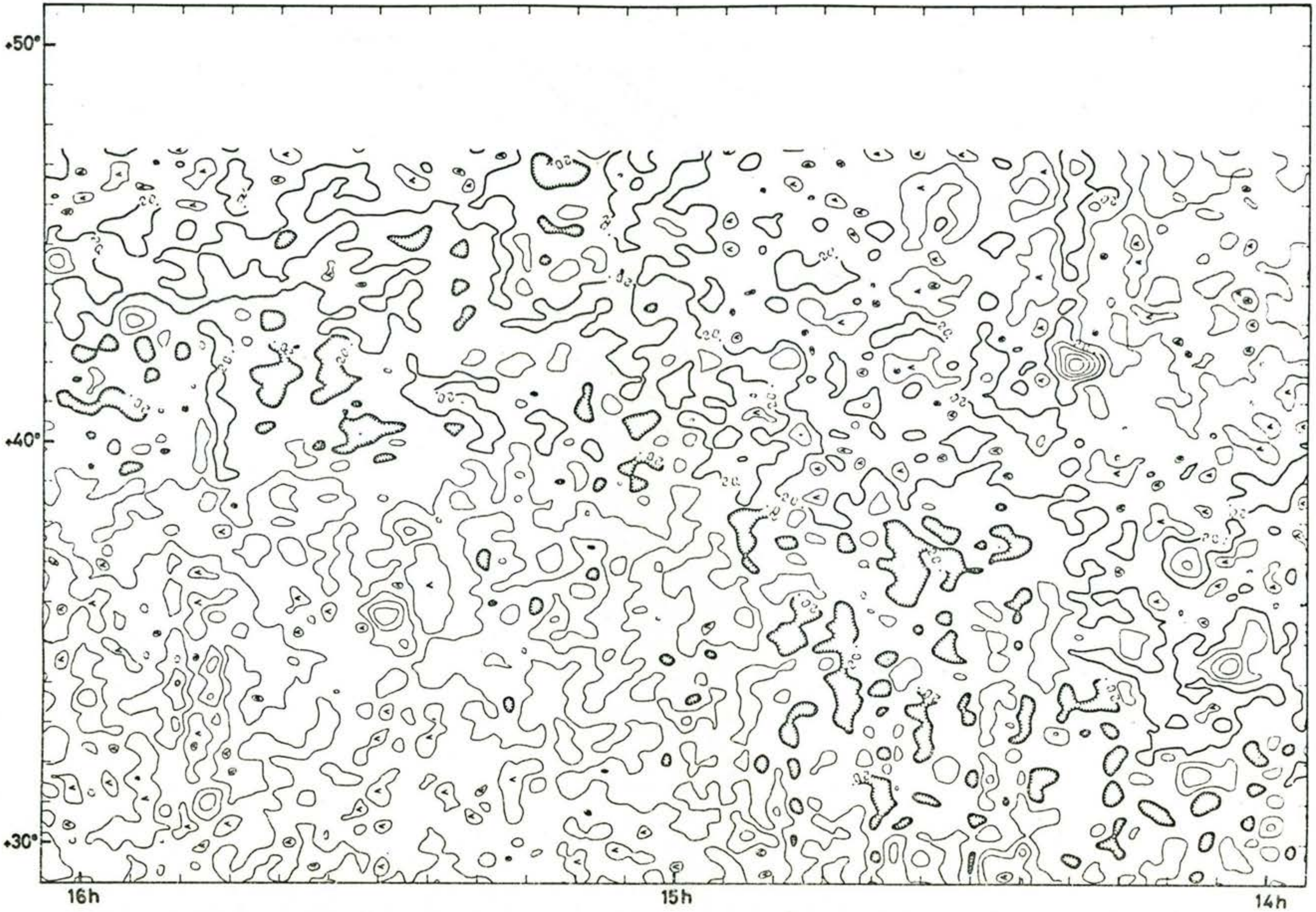
+50°
+40°
+30°
16h
15h
14h

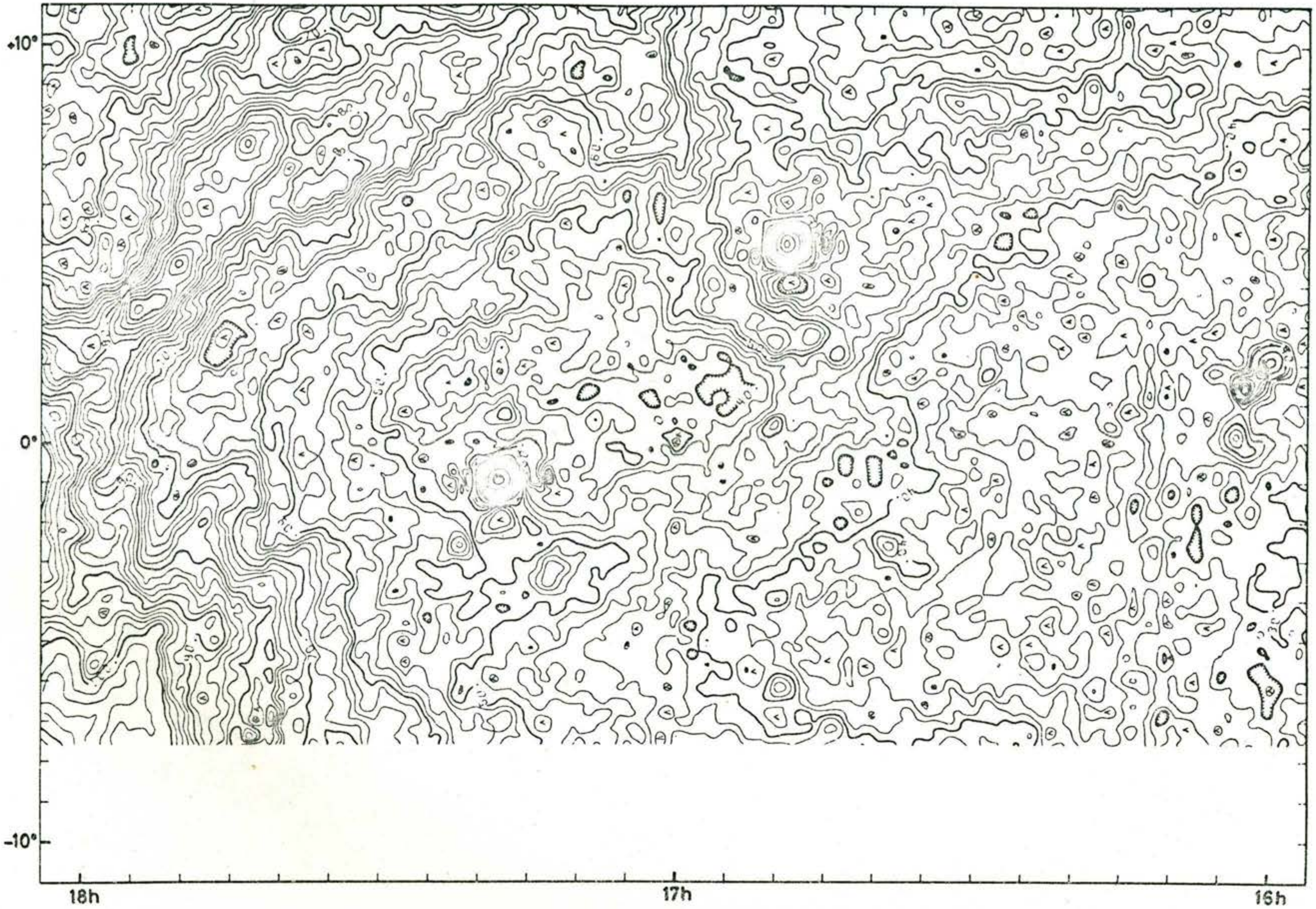
+10°
0°
-10°
18h
17h
16h

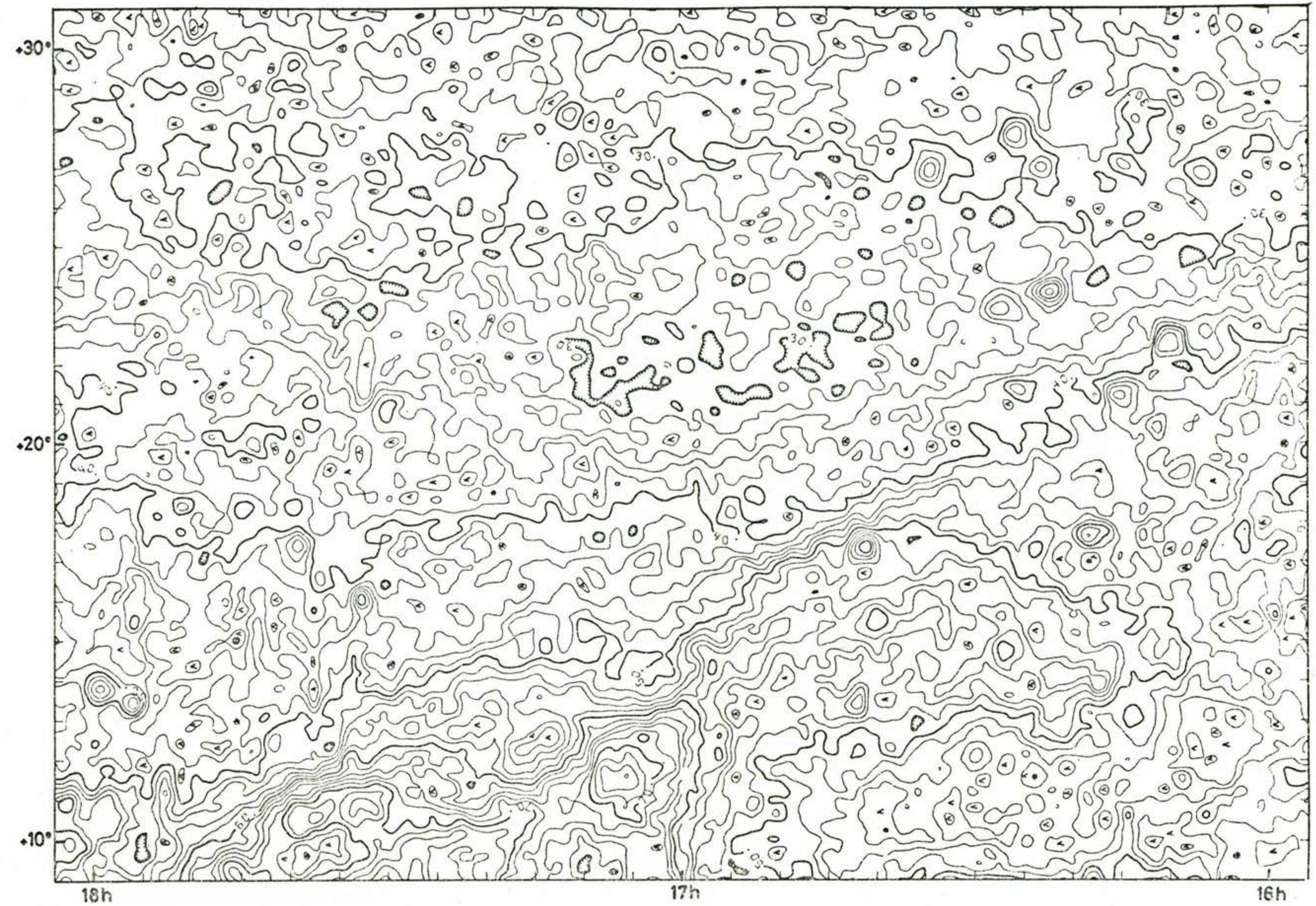
+30°
+20°
+10°
18h
17h
16h


+50°
+40°
+30°
18h
17h
16h
20

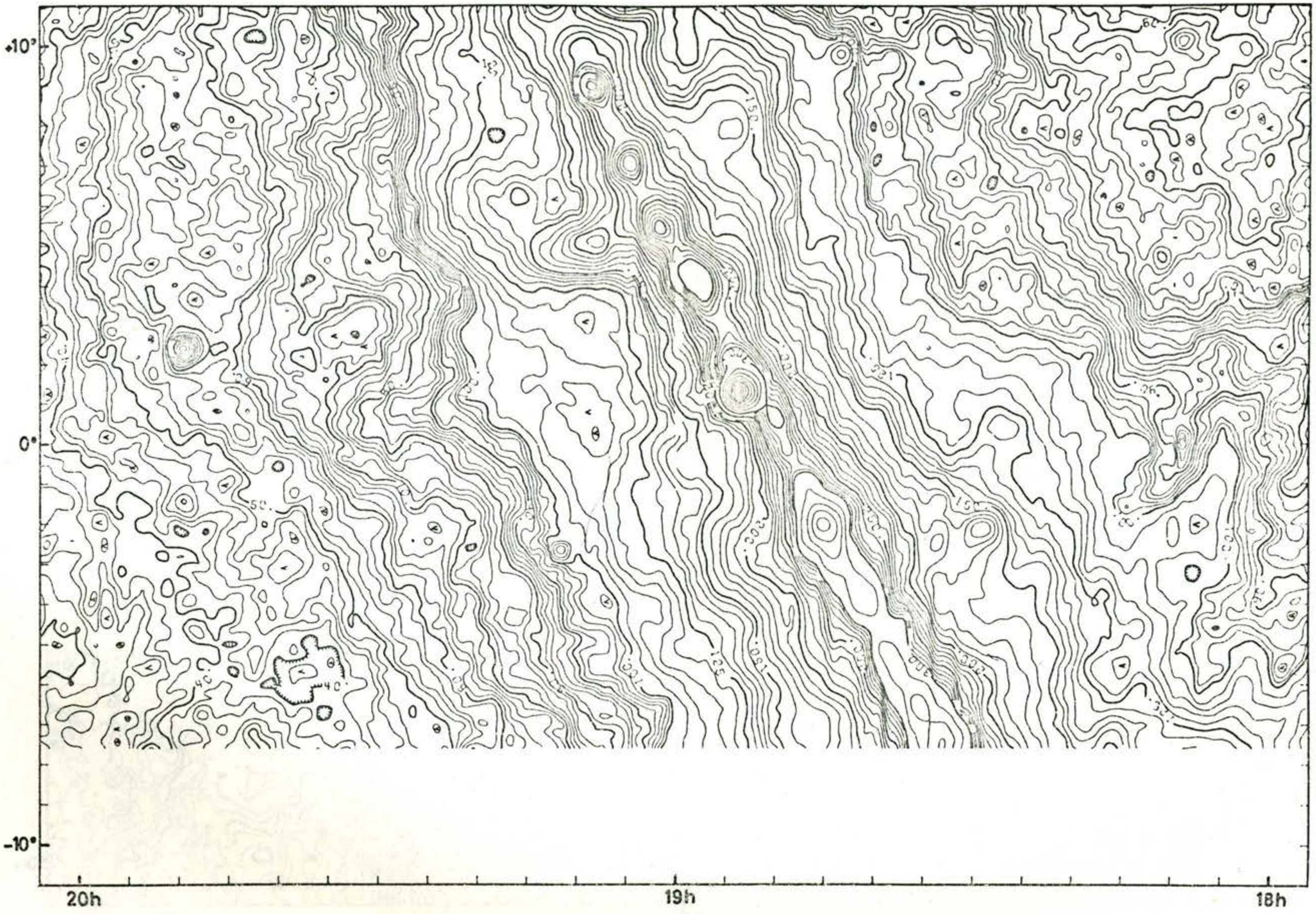
+10°
0°
-10°
20h
19h
18h
150
125
200
100
50
40

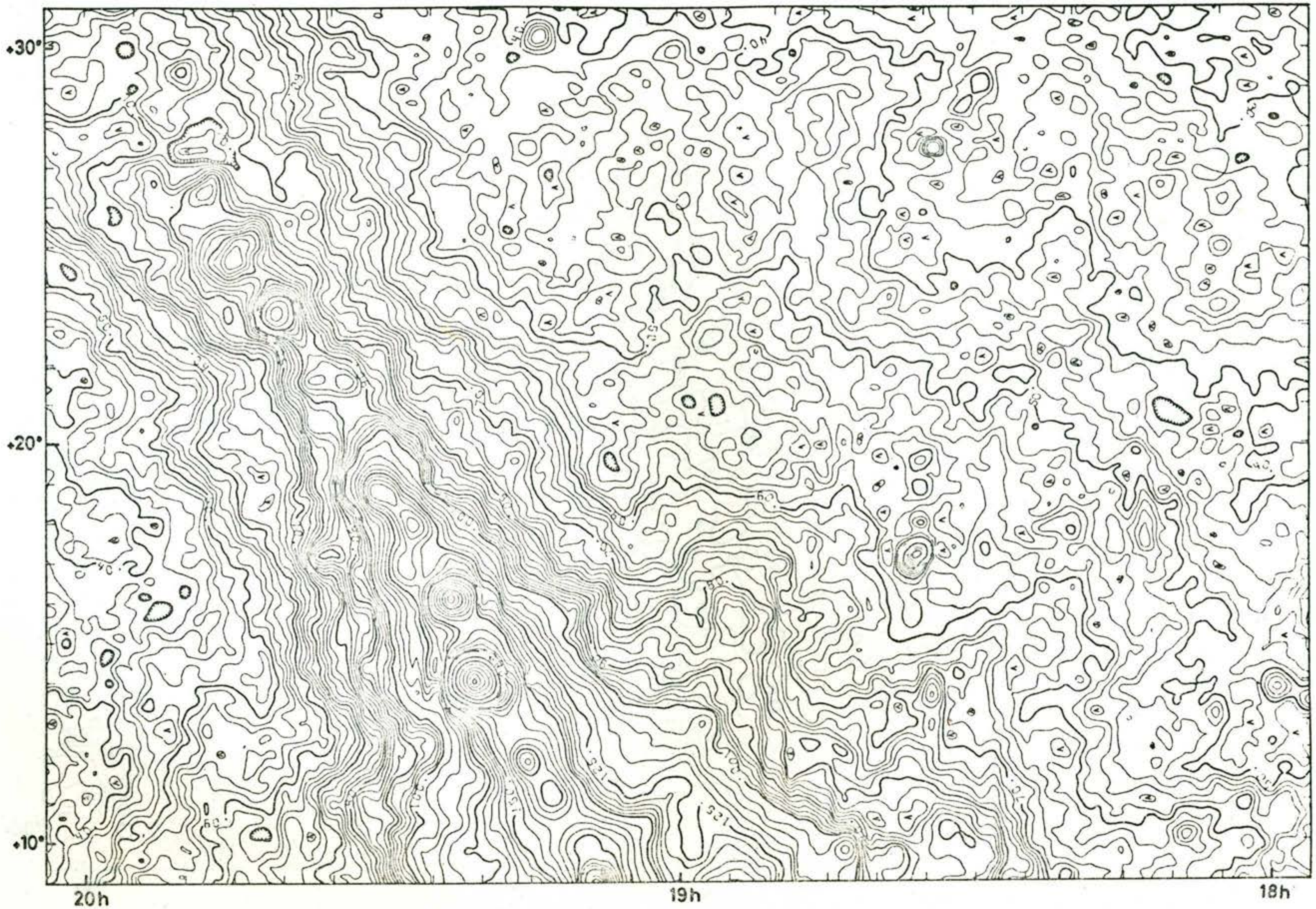

+30°
+20°
+10°
20h
19h
18h

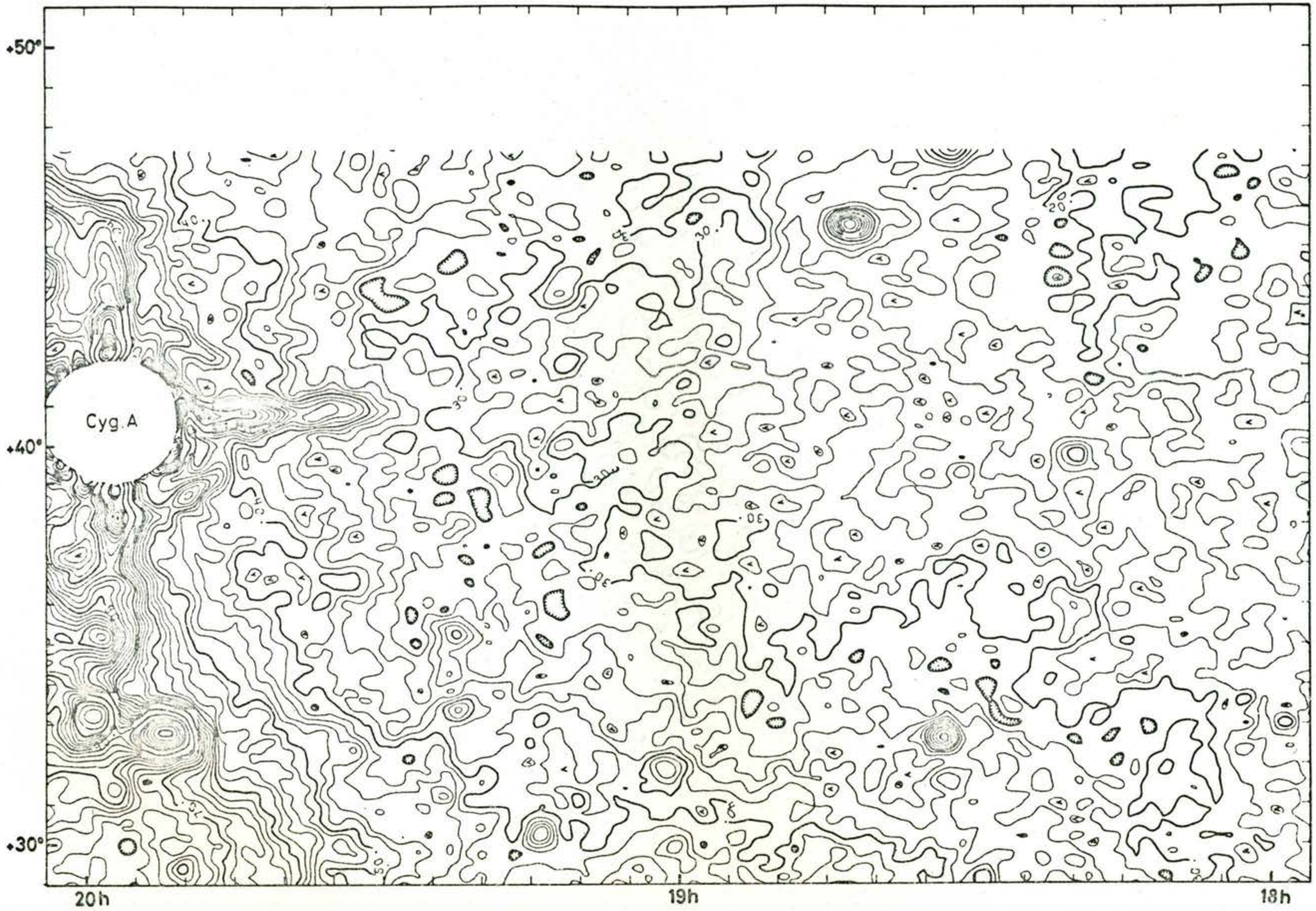
+50°
+40°
+30°
20h
19h
18h
Cyg. A
20
30
40
50

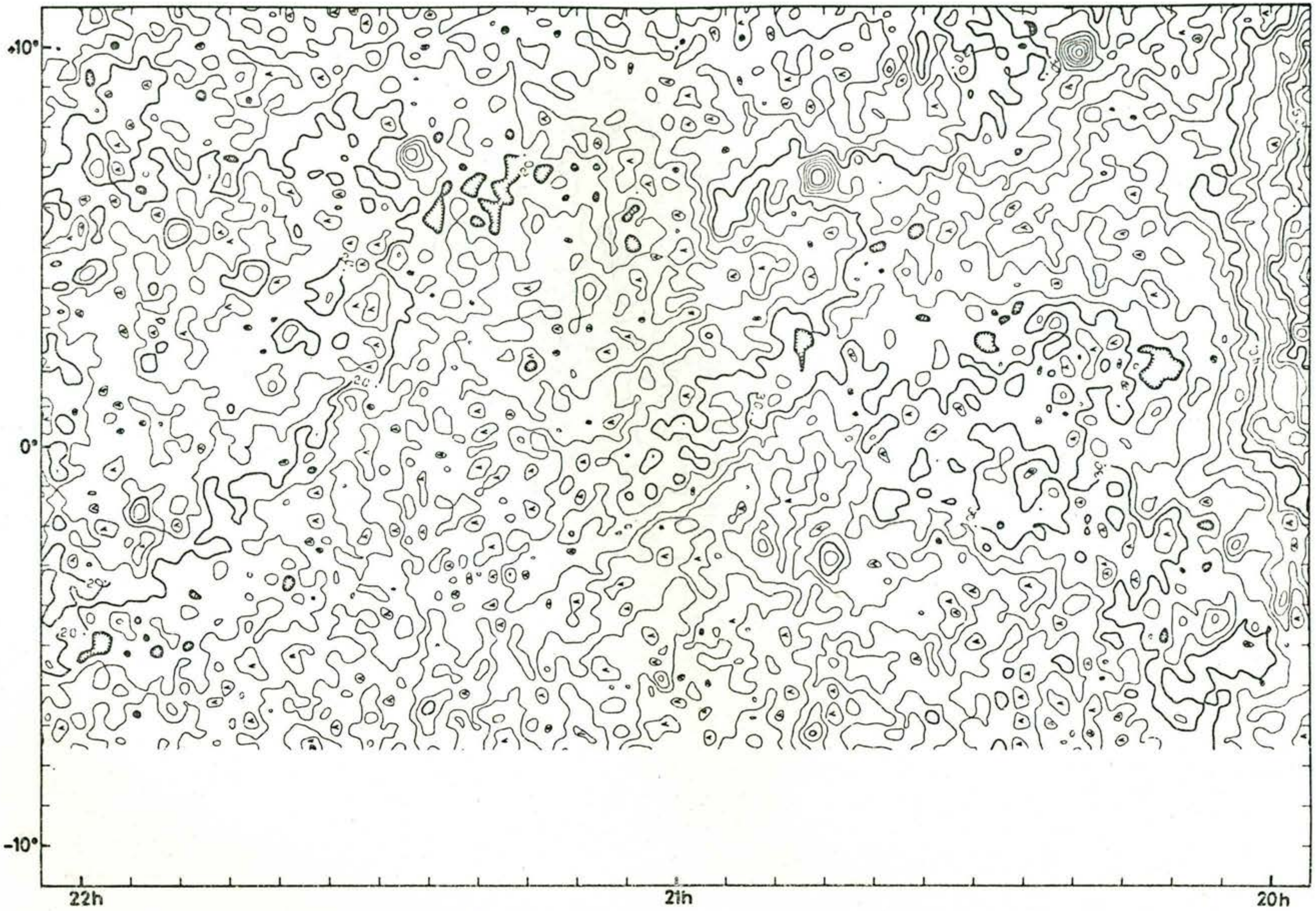
+10°
0°
-10°
22h
21h
20h
20
20
20
30
30
30


+30°
+20°
+10°
22h
21h
20h

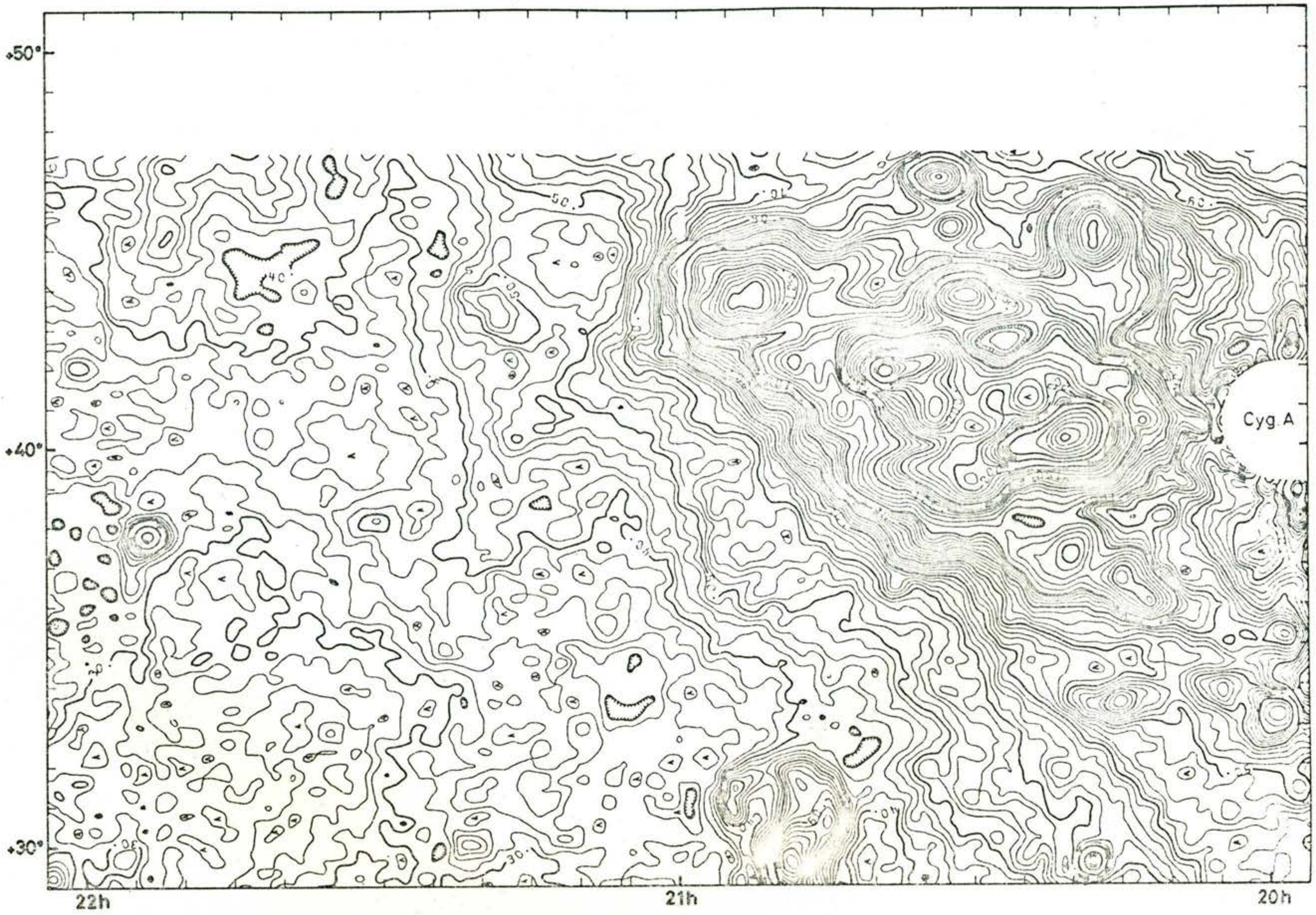
+50°
+40°
+30°
22h
21h
20h
Cyg A
40
50
60
30

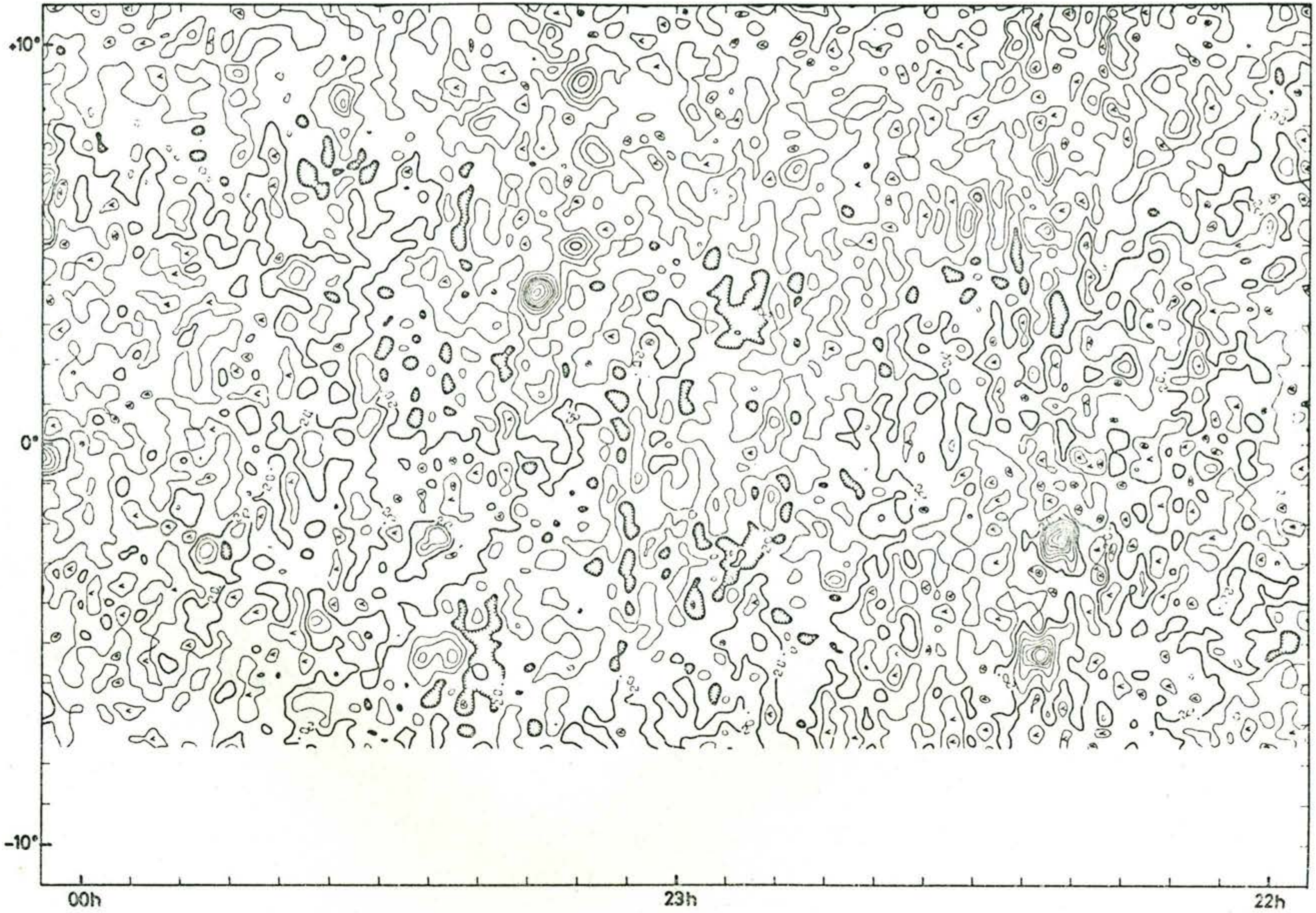
+10°
0°
-10°
00h
23h
22h

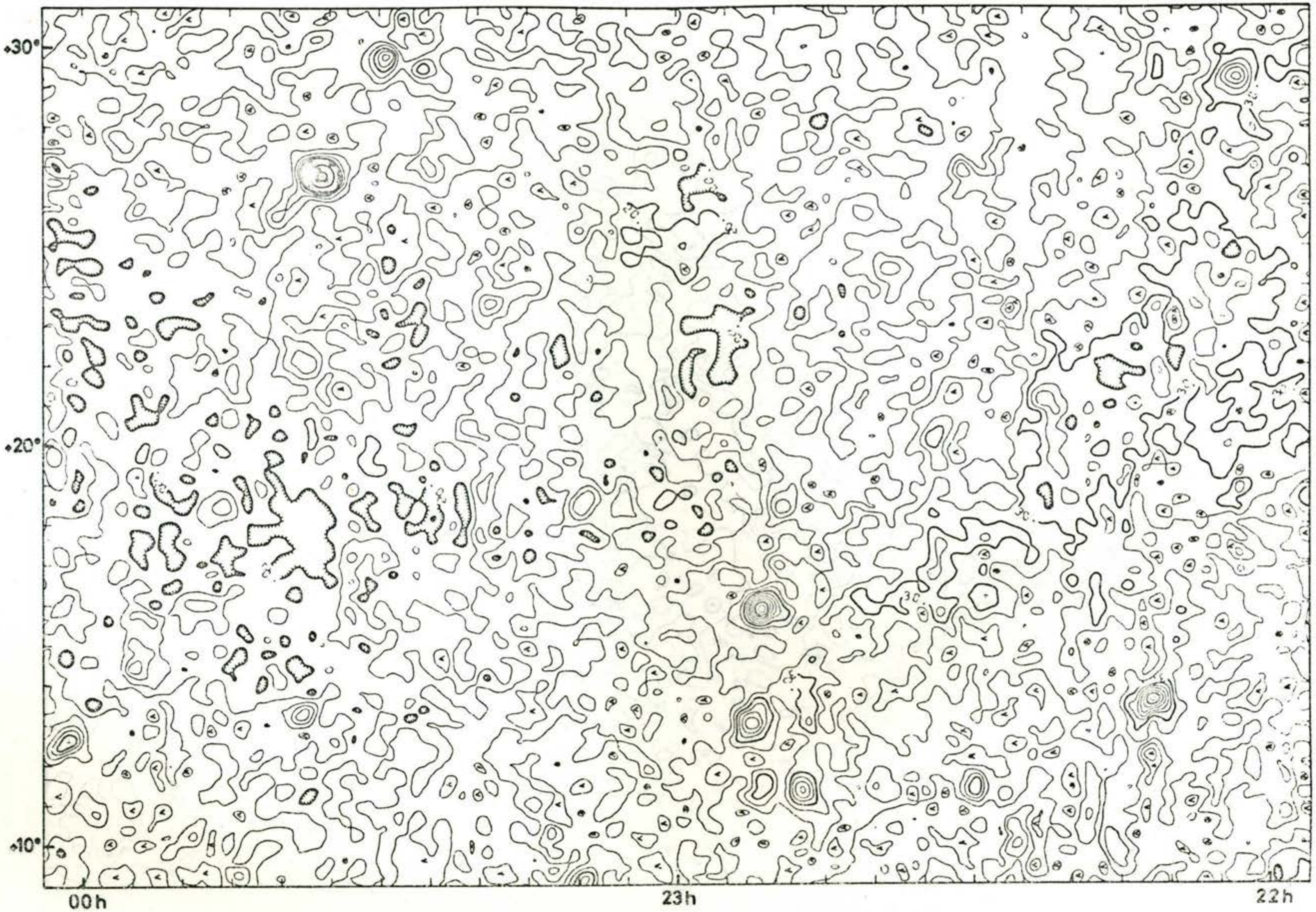
+30°
+20°
+10°
00h
23h
22h
3σ

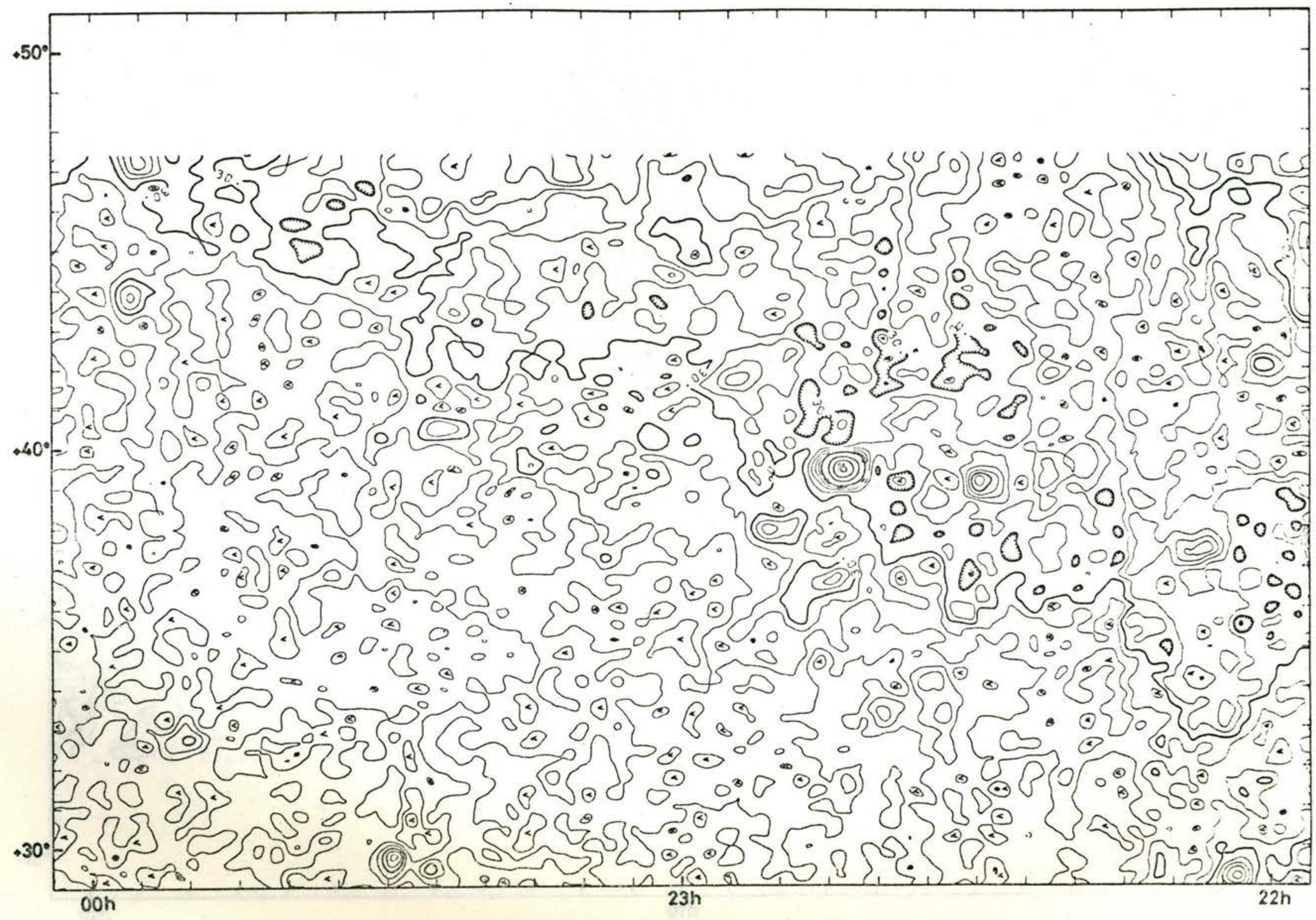
+50°
+40°
+30°
00h
23h
22h

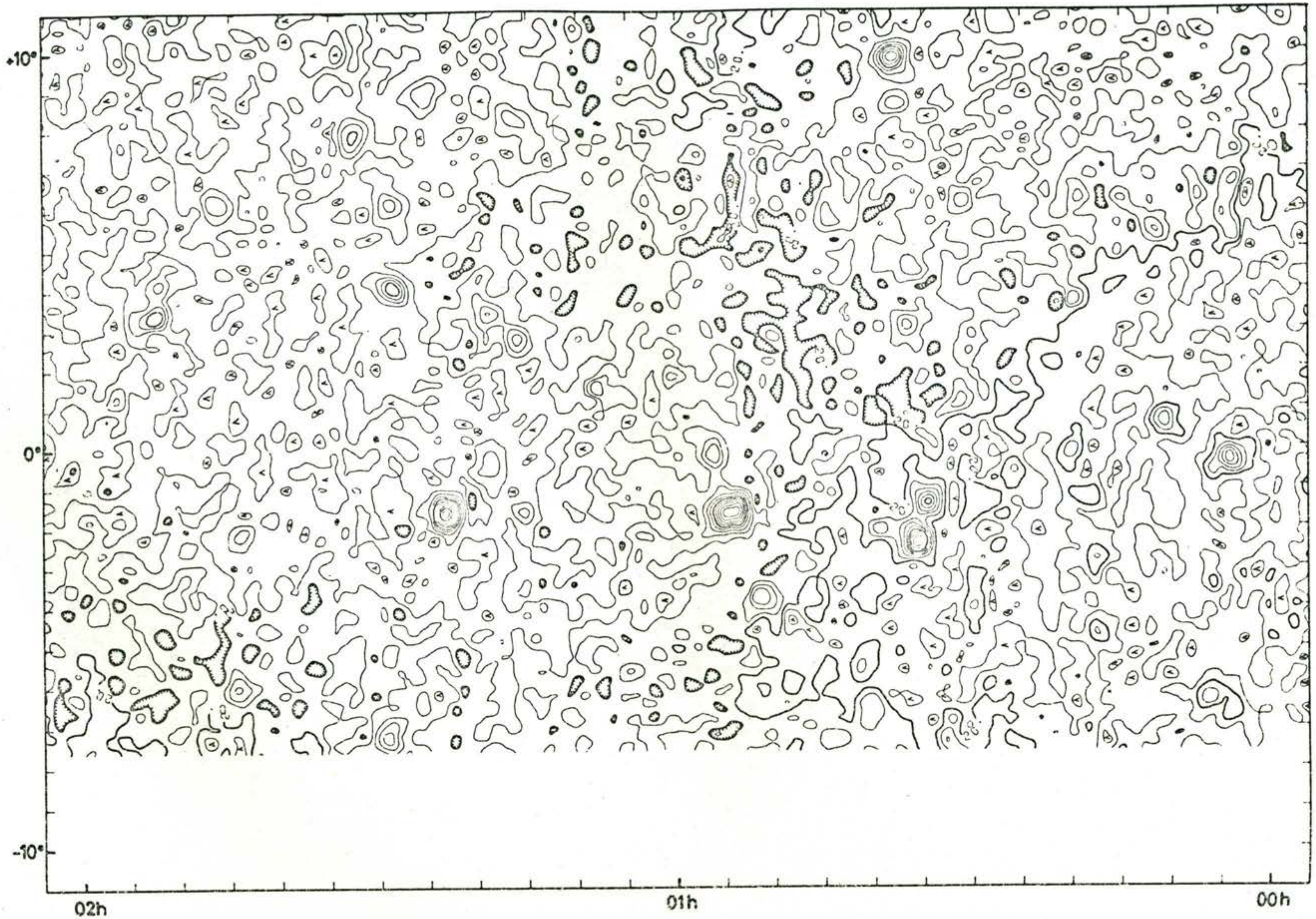
+10°
0°
-10°
02h
01h
00h

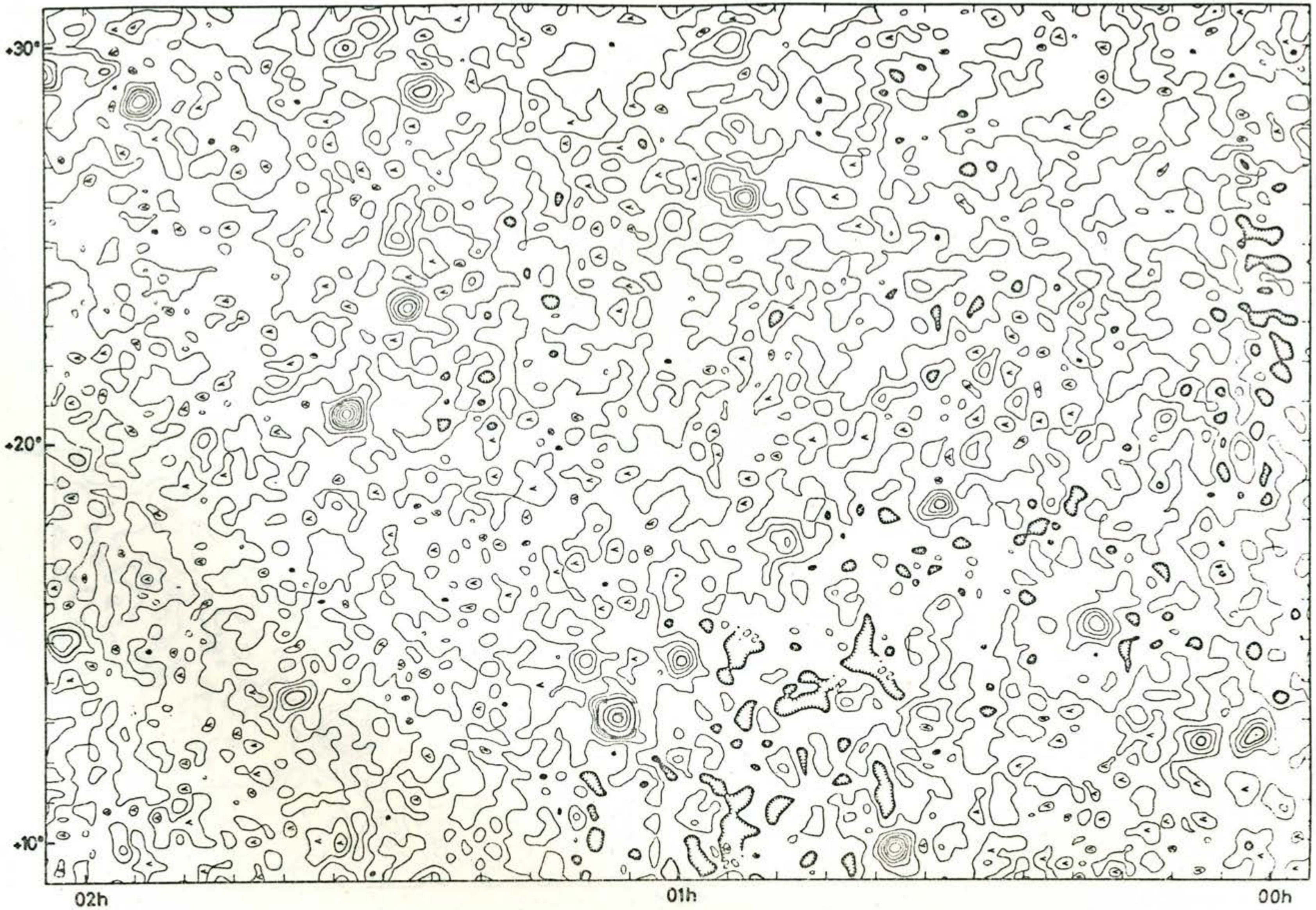
+30°
+20°
+10°
02h
01h
00h

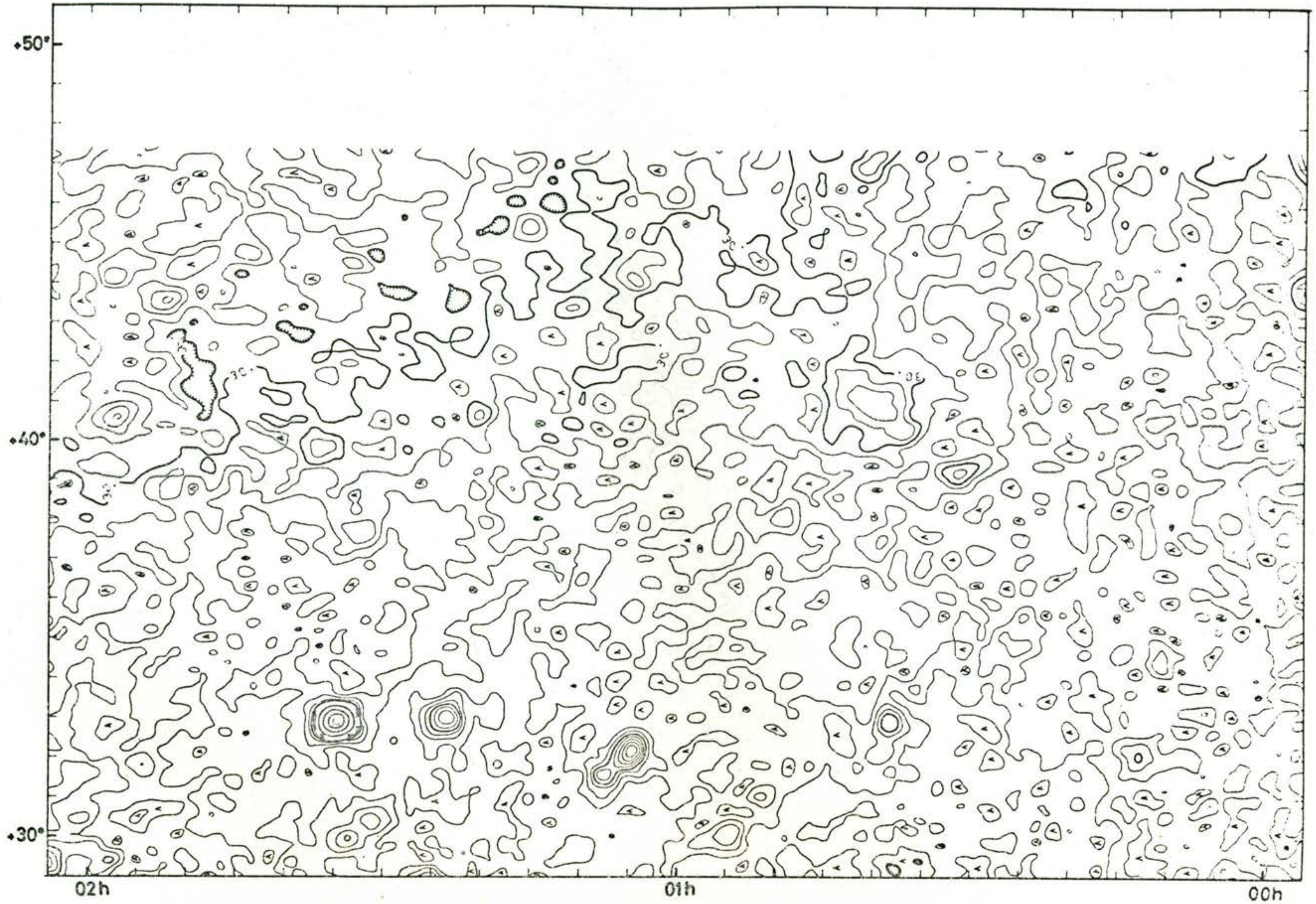
+50°
+40°
+30°
02h
01h
00h

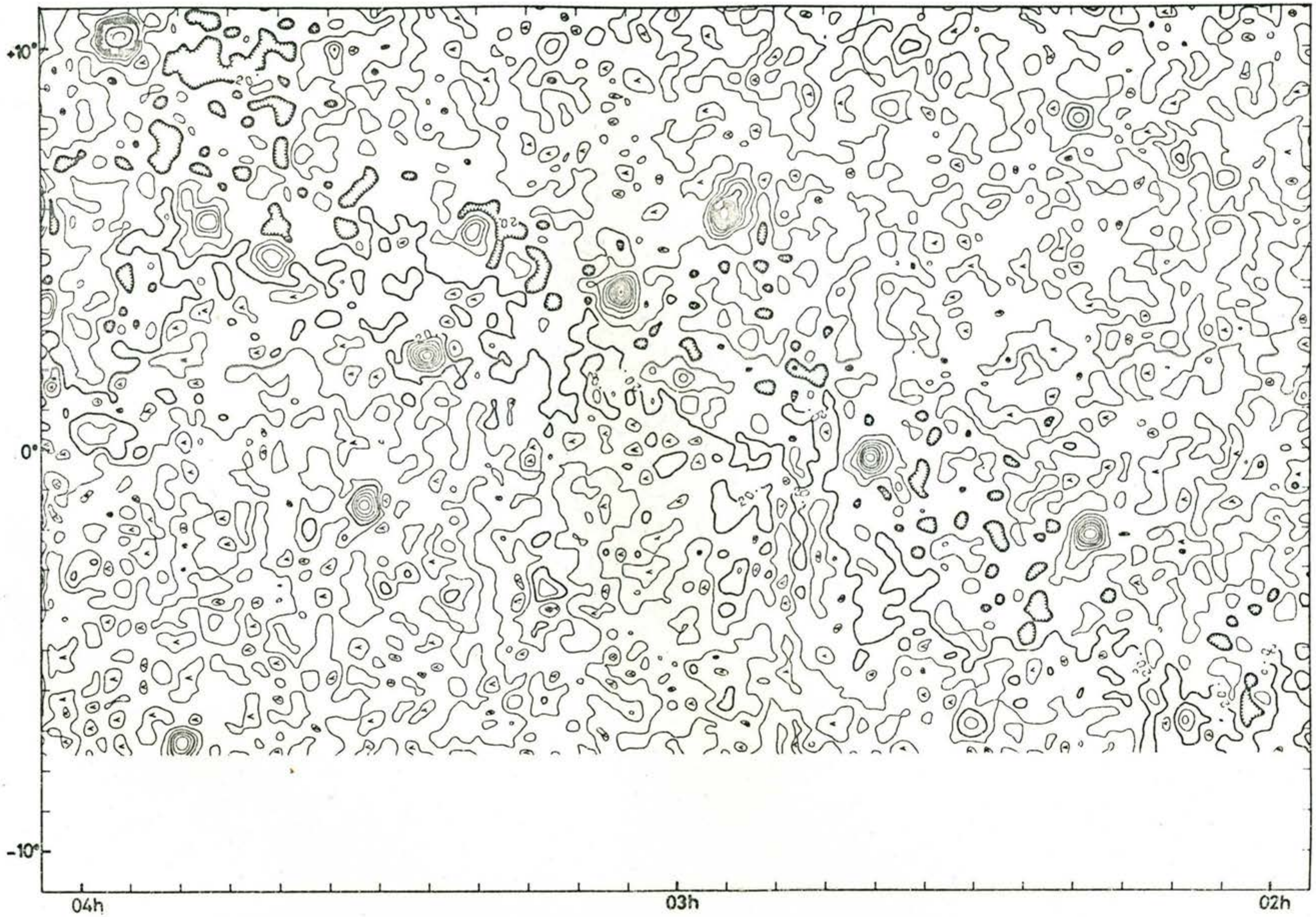
+10°
0°
-10°
04h
03h
02h
20

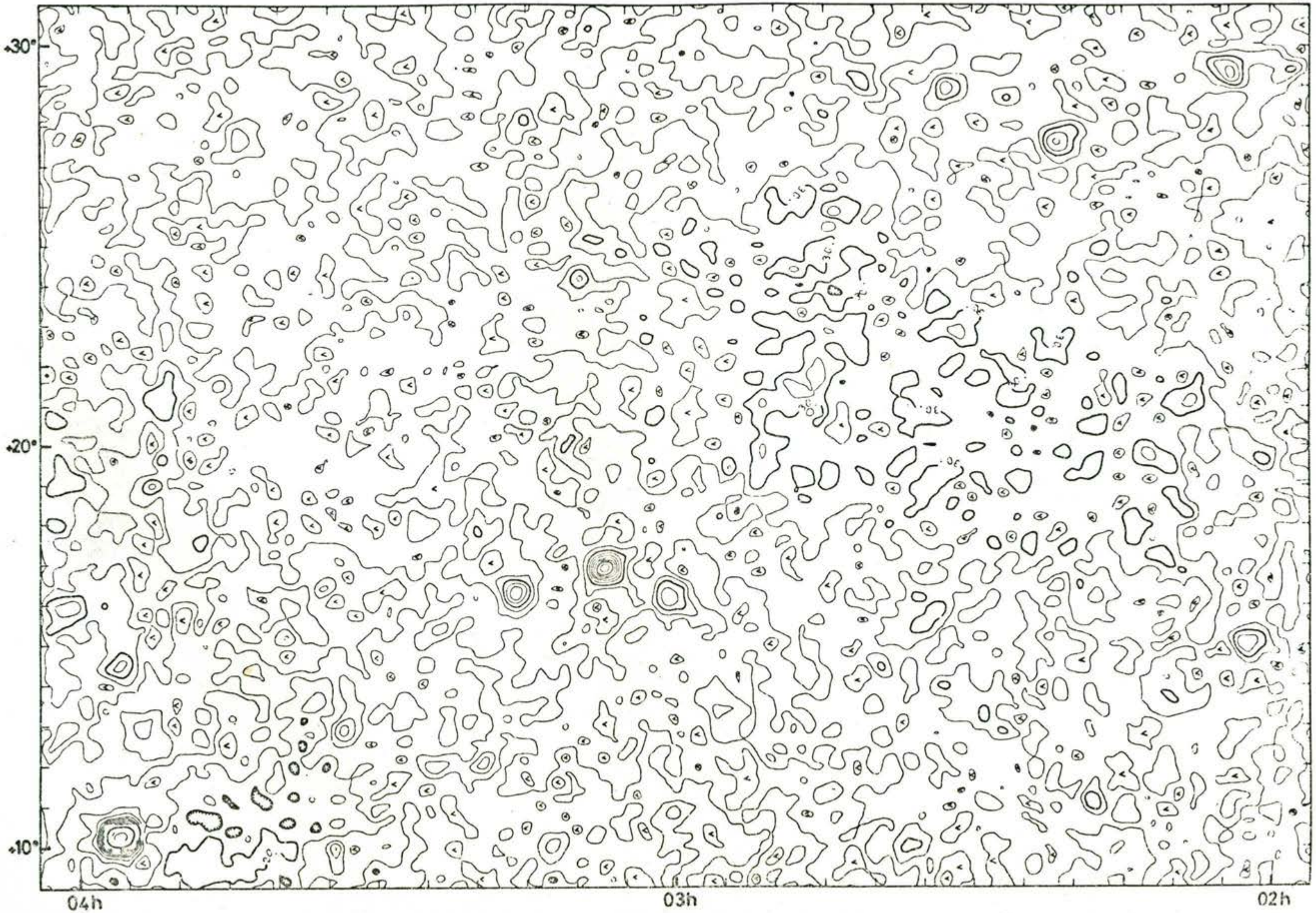
+30°
+20°
+10°
04h
03h
02h

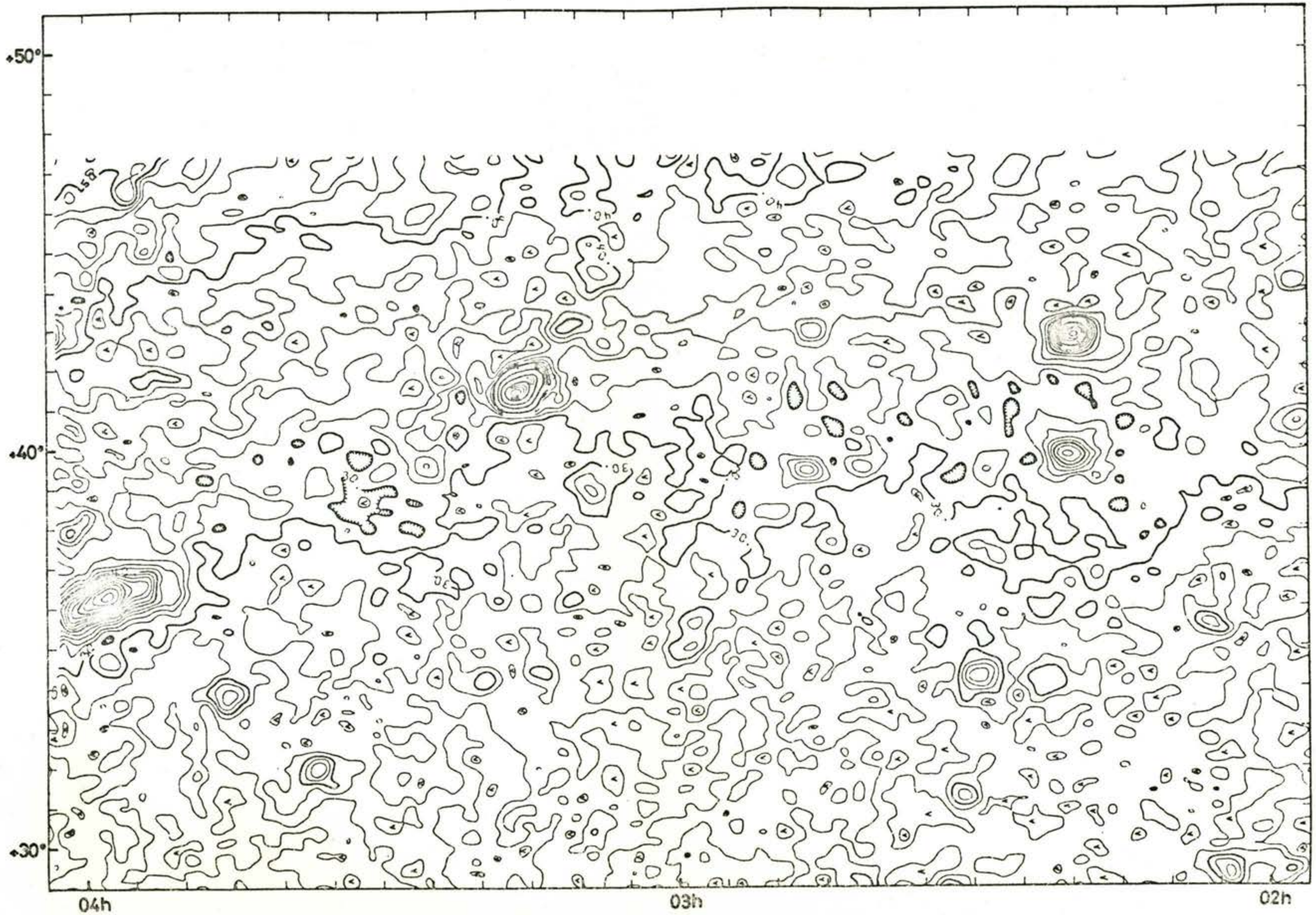
+50°
+40°
+30°
04h
03h
02h

APPENDIX 3 (CONTINUED)

The Bonn 408 MHZ Survey in new galactic coordinates Any ambiguity in the contour levels may be resolved by reference to the equatorial maps.

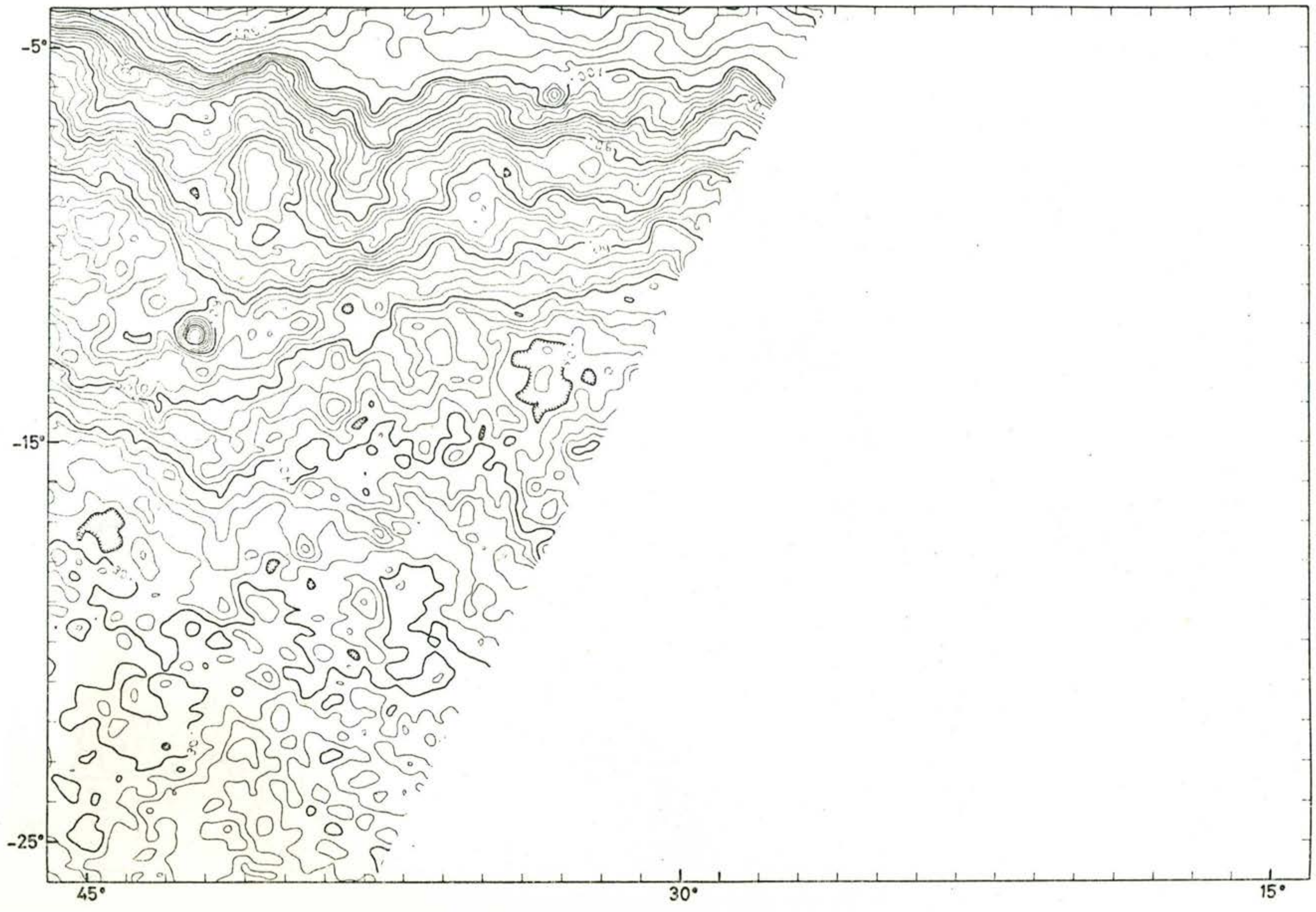
-5°
-15°
-25°
45°
30°
15°
100
30

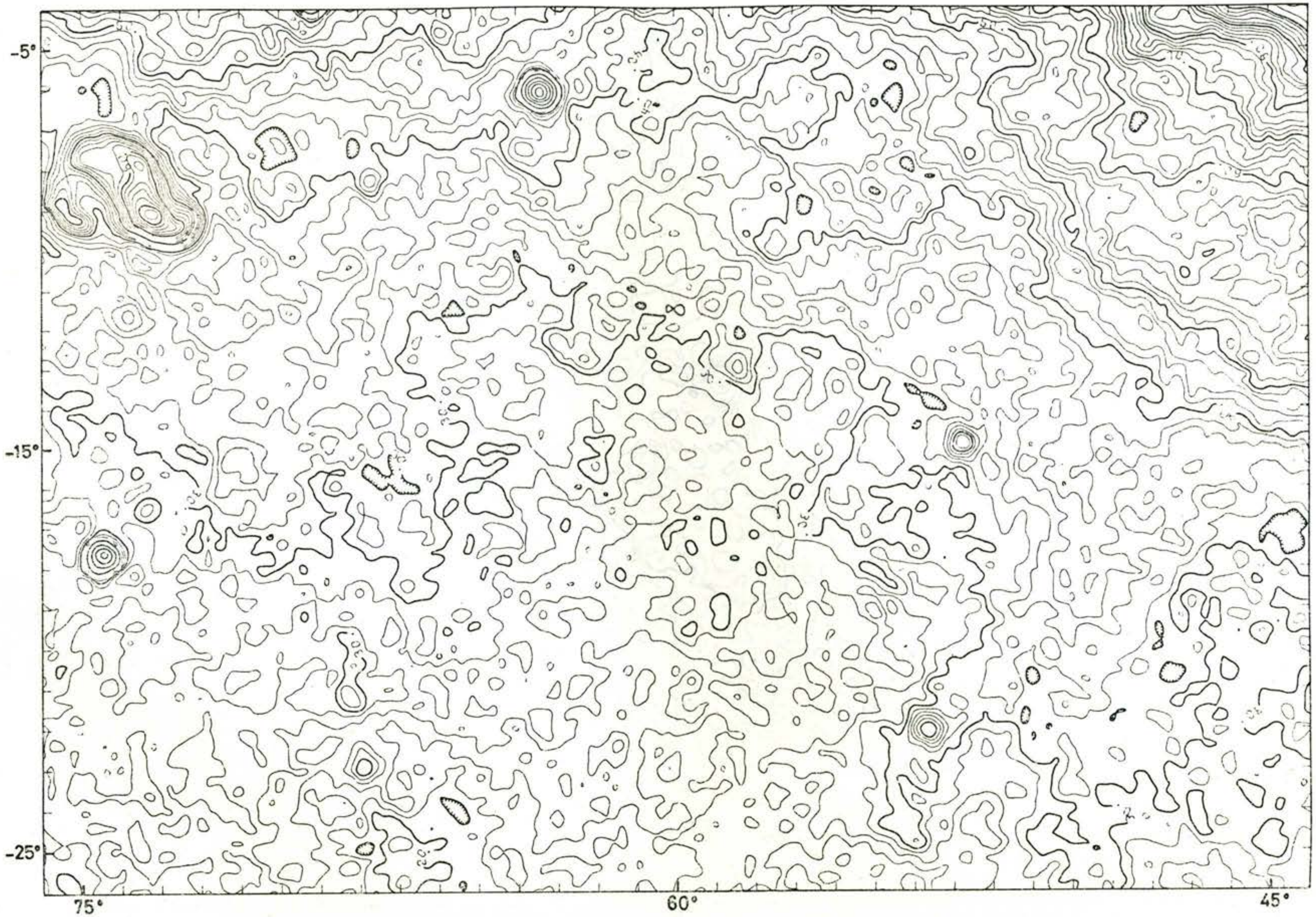
-5°
-15°
-25°
75°
60°
45°
30
40

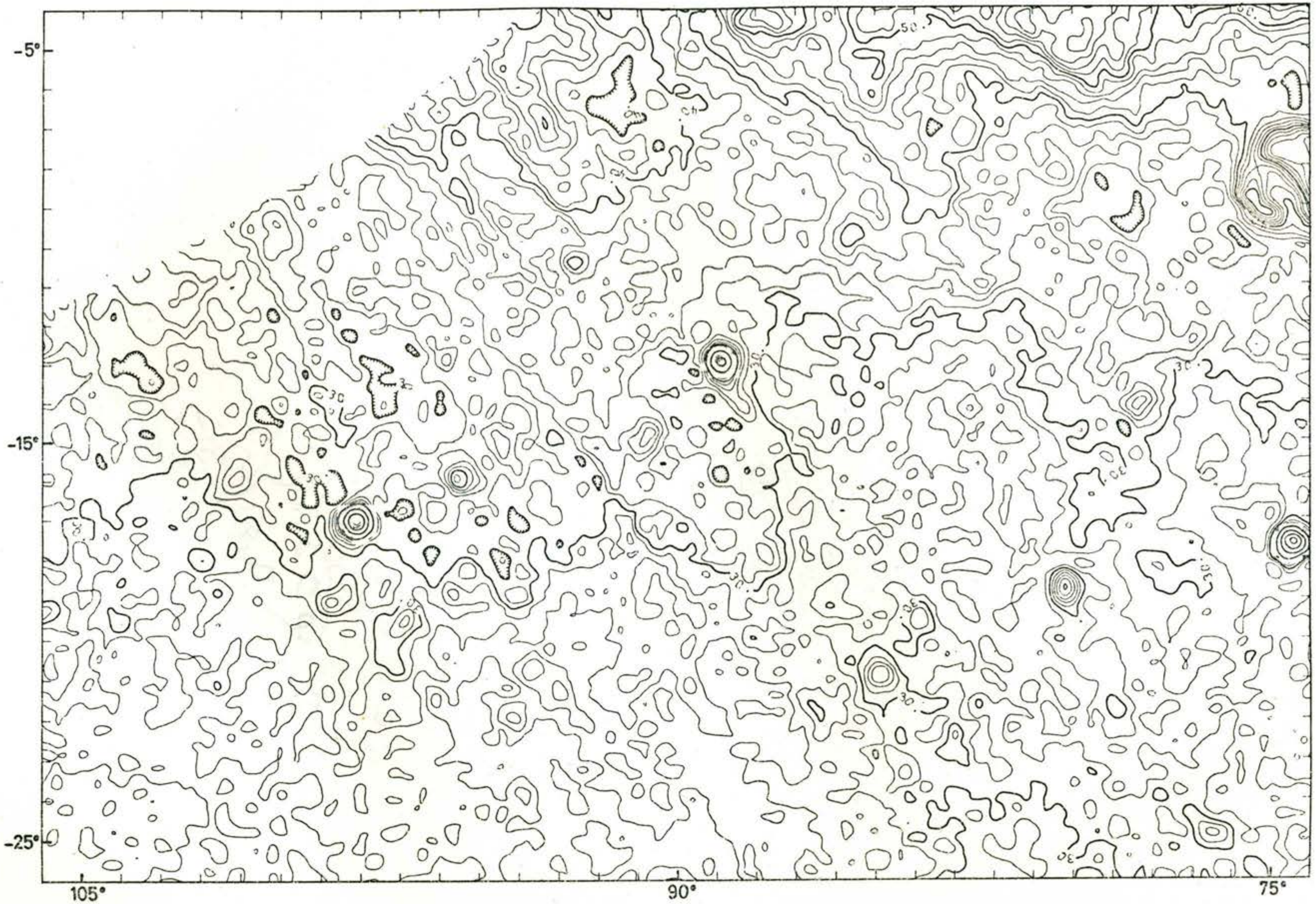
-5°
-15°
-25°
105°
90°
75°
50
40
30

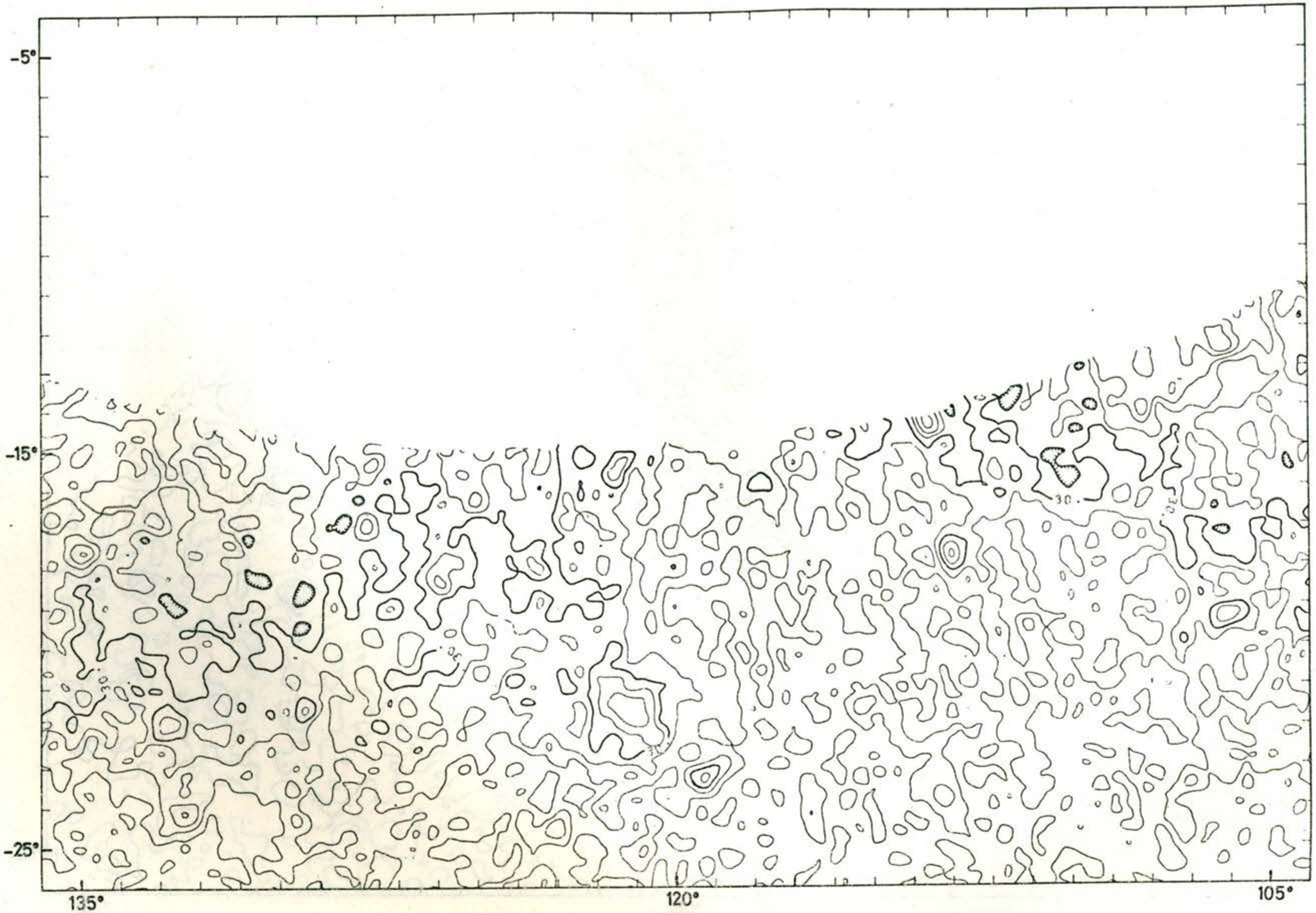

-5°
-15°
-25°
135°
120°
105°
30
30
30
30
30

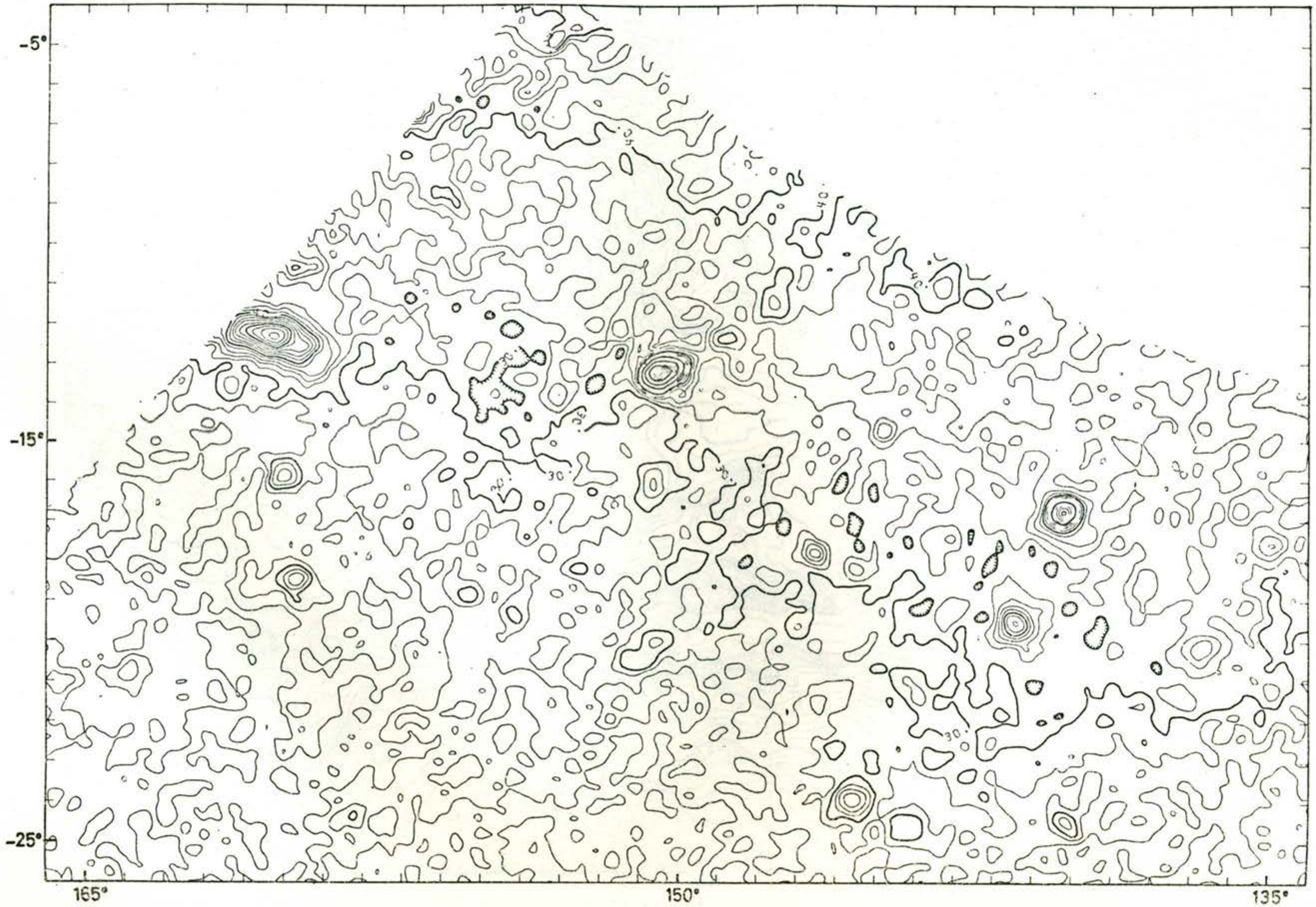
-5°
-15°
-25°
165°
150°
135°
30
40

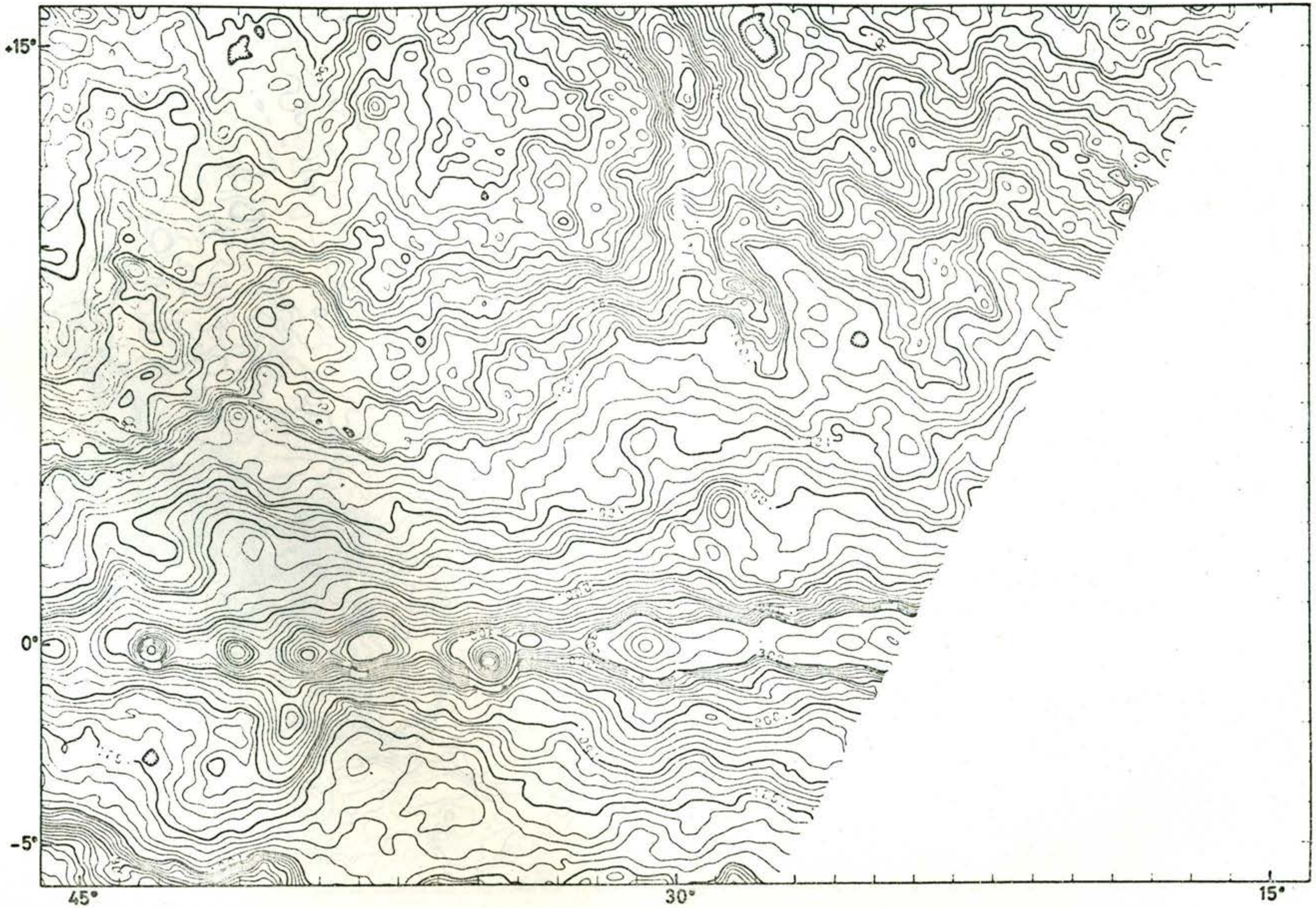
+15°
0°
-5°
45°
30°
15°

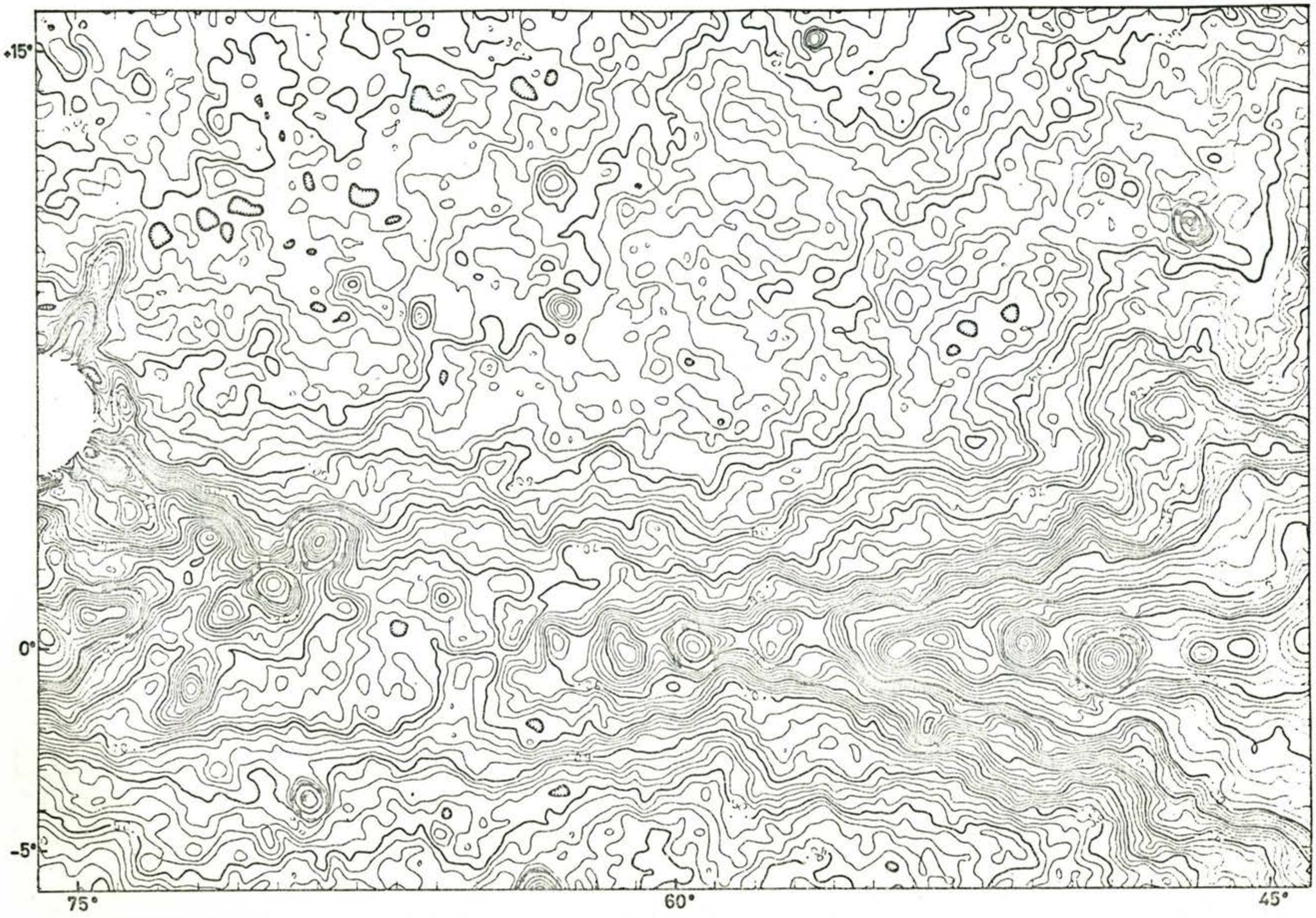
+15°
0°
-5°
75°
60°
45°


+35°
+25°
+15°
45°
30°
15°


+35°
+25°
+15°
75°
60°
45°

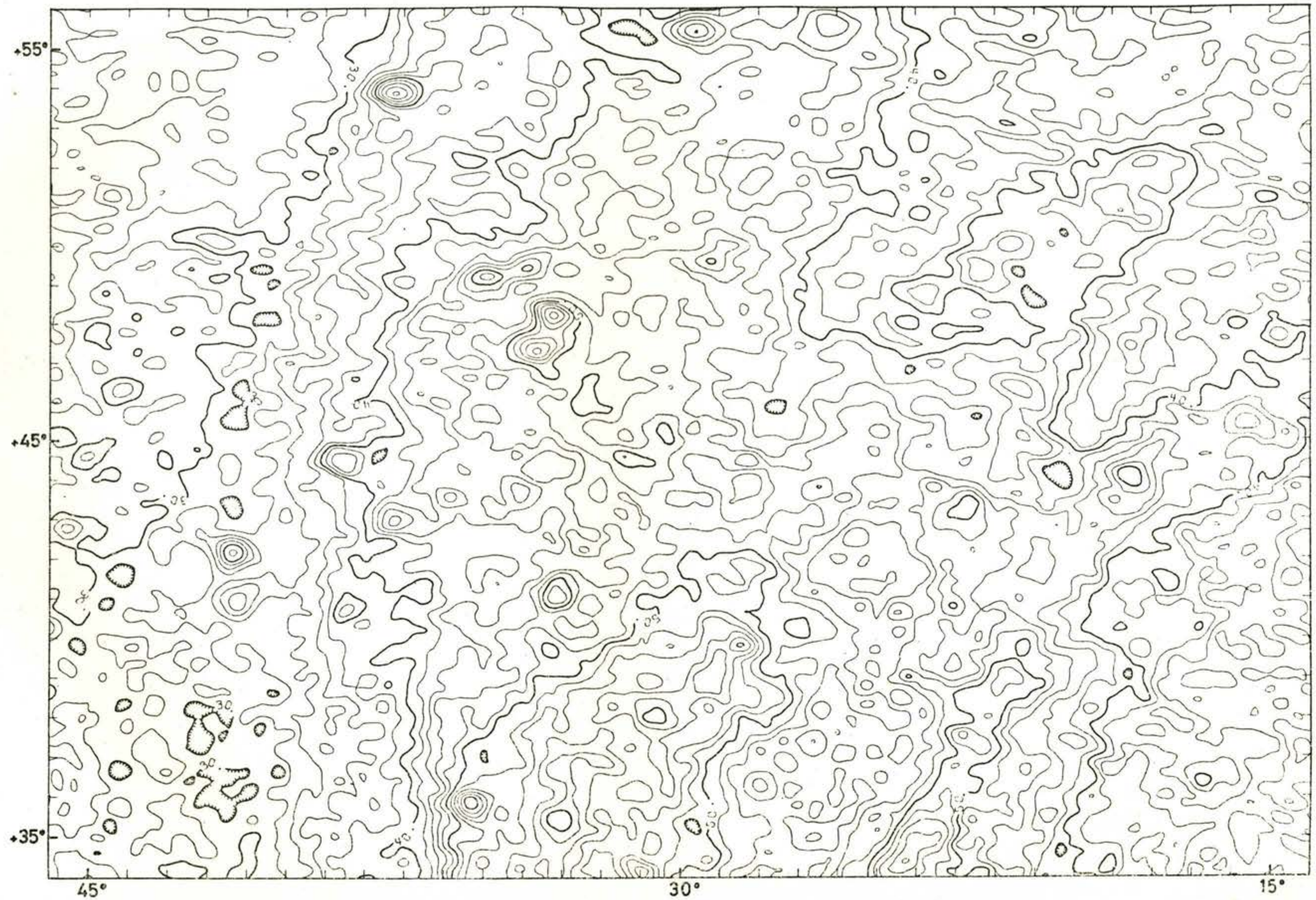
+55°
+45°
+35°
45°
30°
15°
30
40
30
40
30